

A Hybrid ALE-Fixed-Grid Approach for Fluid-Structure Interaction

Shadan Shahmiri

Bericht Nr. 22 (2014)
Lehrstuhl für Numerische Mechanik
Professor Dr.-Ing. Wolfgang A. Wall
Technische Universität München

Berichte können bezogen werden über:



Lehrstuhl für Numerische Mechanik
Technische Universität München
Boltzmannstrasse 15
D-85747 Garching bei München
<http://www.lnm.mw.tum.de>

Alle Rechte, insbesondere das der Übersetzung in andere Sprachen, vorbehalten. Ohne Genehmigung des Autors ist es nicht gestattet, dieses Buch ganz oder teilweise auf photomechanischem, elektronischem oder sonstigem Wege zu kommerziellen Zwecken zu vervielfältigen.

All rights reserved. In particular the right to translate the text of this thesis into another language is reserved. No part of the material protected by this copyright notice may be reproduced or utilized in any form or by any means, electronic or mechanical, including photocopying, recording or by any other information storage and retrieval system, without written permission of the author.

TECHNISCHE UNIVERSITÄT MÜNCHEN

Lehrstuhl für Numerische Mechanik

A Hybrid Fixed-Grid-ALE Approach for Fluid-Structure Interaction

Shadan Shahmiri

Vollständiger Abdruck der von der Fakultät für Maschinenwesen der Technischen Universität München zur Erlangung des akademischen Grades eines

Doktor-Ingenieurs (Dr.-Ing.)

genehmigten Dissertation.

Vorsitzender: Univ.-Prof. dr.ir. Daniel J. Rixen

Prüfer der Dissertation:

1. Univ.-Prof. Dr.-Ing. Wolfgang A. Wall
2. Univ.-Prof. Marek Behr, Ph.D.

Rheinisch-Westfälische Technische Hochschule (RWTH) Aachen

Die Dissertation wurde am 7. Mai 2014 bei der Technischen Universität München eingereicht und durch die Fakultät für Maschinenwesen am 11. Juli 2014 angenommen.

Abstract

In the present work a finite element based hybrid ALE-fixed-grid fluid-structure interaction (FSI) approach for simulation of complex two- and three-dimensional FSI problems involving large structural deformations is developed. The two main features of the proposed FSI method are as follows: first, it is able to deal with large and complex structural deformations. Second, it provides a proper resolution of the flow features at structural surface throughout the simulation, which is essential in order to resolve steep gradients in normal direction for high Reynolds number flow. In this approach, the structure, which is described in Lagrangian formulation, is surrounded by a surface layer of deformable stretched fluid elements based on an Arbitrary-Eulerian-Lagrangian (ALE) formulation. This deformable fluid patch, which is embedded in the fixed-grid Eulerian background fluid domain, moves and deforms with the structure, and provides an appropriate boundary layer mesh over the simulation time. The surface coupling between the two fluid domains is imposed weakly using a stabilized formulation at the common fluid-fluid interface. In other words, overlapping meshes are used without introducing overlapping solutions. The structure and the moving fluid are coupled in the same way as in classical ALE-based FSI approaches.

The method is derived in two main steps: First, a stable and robust extended finite element (XFEM)-based embedded fluid formulation for viscous as well as convective dominated flows is introduced. It is built from the following essential ingredients: since the fluid patch ends in the middle of background elements, an XFEM-based approach is introduced to model a sharp separation between active and inactive regions on background grid. Boundary conditions on the embedded interface are imposed weakly using Nitsche's formulation. Nitsche's stabilization parameter is determined via a local eigenvalue problem, which provides a reliable, and an automatic computation of Nitsche stabilization parameter for any element's shape or form, or polynomial orders. Face-oriented stabilizations are applied to take control over ghost values, balance fluid instabilities in the interface zone, and to improve the system conditioning. To overcome the instabilities caused by the convective mass transport across the fluid-fluid interface, additional inflow stabilization terms are introduced. A detailed numerical analysis of the stabilized embedded fluid formulation shows the optimal error convergence in viscous and convective cases, independent of the size of cut elements, or the position of the interface. This formulation is applied to moving interfaces, introducing a new XFEM time-integration approach, which results in a robust and stable solution over time.

In the next step, the structural equations are coupled with the proposed embedded fluid formulation into a monolithic FSI system. Solving such nonlinear FSI system with Newton-Raphson scheme in a straightforward way leads to further complexities regarding the Eulerian description of fixed-grid background fluid in combination of moving fluid patch. In order to avoid these complexities, a novel FSI approach stated as *relaxing ALE approach* is proposed. The key idea of relaxing ALE approach is that the position of the internal fluid-fluid interface does not change during the Newton-Raphson scheme, and it is updated only at the end of each time step.

Two- and three-dimensional numerical examples are presented to validate the proposed approach, and to demonstrate its superior performance. These examples prove that robust, stable and accurate solution is achieved independent of the position of internal fluid-fluid interface or the complexity of the form of fluid patch. Furthermore, the method provides feasibility of resolving steep gradients within the boundary layer around the structural surface, in addition to

handling the large deformation of structure with ease. Thus, the present FSI approach is best suited for complex real-world FSI problems.

Zusammenfassung

In dieser Arbeit wurde ein neuer Ansatz zur Simulation von komplexen zwei- und dreidimensionalen Problemen der Fluid-Struktur-Interaktion (FSI) entwickelt, der insbesondere für Fälle großer Strukturdeformationen geeignet ist. Das auf Finiten Elementen basierende Verfahren verwendet zwei gekoppelte Fluidfelder, die jeweils auf dem Arbitrary-Lagrangian-Eulerian(ALE)- und Euler-Ansatz beruhen. Die vorgestellte Methode hat folgende charakteristische Merkmale: Einerseits werden beliebig große und komplexe strukturelle Verformungen zufriedenstellend behandelt. Dabei bietet das Verfahren andererseits eine stetig präzise Auflösung von Strömungseigenschaften entlang der Strukturoberfläche. Diese Eigenschaft ist grundlegend für die Erfassung hoher wandnormaler Gradienten von Strömungen hoher Reynolds-Zahl. Im vorgestellten Ansatz wird das Strukturgebiet, das wie üblich in Lagrangescher Beschreibung gegeben ist, von einer Schicht grenzschichtspezifisch gestreckter Fluidelemente auf ALE-Basis umhüllt. Dieses Netz aus verformbaren Fluidelementen wird in ein Hintergrundgitter aus Fluidelementen in Euler-Betrachtung eingebettet. Das ALE-Netz folgt den Bewegungen und Deformationen des Strukturfelds über den gesamten Simulationszeitraum hinweg und stellt so eine dauerhaft hohe Auflösung des Grenzschichtbereichs sicher. Die oberflächenbasierte Kopplung zwischen den beiden Fluidnetzen wird schwach erfüllt, unter Verwendung einer stabilisierten Formulierung an der gemeinsamen Grenzfläche. Somit werden überlappende Netze genutzt, ohne dass überlappende Lösungen eingeführt werden. Die Kopplung zwischen Struktur und ALE-Fluid erfolgt in gleicher Weise wie bei klassischen ALE-basierten FSI-Ansätzen. Im folgenden soll die Methode in zwei Schritten hergeleitet werden. Zunächst wird eine stabile und robuste Fluidformulierung vorgestellt, die auf der eXtended Finite Element Method (XFEM) beruht und sowohl für viskos als auch für konvektiv dominierte Strömungen gültig ist. Dabei wird der XFEM-basierte Ansatz gewählt, um im Hintergrundgitter zwischen aktiven und inaktiven, vom ALE-Gitter bedeckten Regionen zu unterscheiden, da diese an beliebiger Stelle innerhalb eines Hintergrundelements auftreten können. Die Kontinuität entlang der Fluid-Fluid Grenzfläche wird unter Verwendung der Nitsche-Methode schwach erfüllt. Der Stabilisierungsparameter der Nitsche-Kopplung wird über die Lösung eines lokalen Eigenwertproblems ermittelt. Dies bietet eine verlässliche Bestimmung des Nitsche-Parameters für Elemente beliebiger Art, Geometrie oder polynomialer Ordnung. Um die Werte von Freiheitsgraden im inaktiven Fluidbereich zu kontrollieren, Instabilitäten an der Grenzfläche zu vermeiden und die Kondition des Systems zu verbessern, werden flächenorientierte ("face-oriented") Stabilisierungsterme angewendet. Um Instabilitäten auszugleichen, die aus konvektivem Massentransport über die Fluid-Fluid-Grenzfläche herrühren, werden zusätzliche Einstromterme eingeführt. Eine detaillierte numerische Analyse der stabilisierten eingebetteten Fluidformulierung zeigt optimale Fehlerkonvergenz sowohl in viskos als auch in konvektiv dominierten Fällen. Diese ist außerdem unabhängig von der Größe geschnittener Hintergrundelemente oder der Position der Fluid-Fluid-Grenzfläche. Die Formulierung wird schließlich mithilfe eines neuen Ansatzes zur XFEM-Zeitintegration auf Fälle mit bewegten Grenzflächen erweitert. Damit kann eine robuste und stabile Lösung über die Zeit erreicht werden. Der zweite große Schritt umfasst die Vereinigung der Strukturgleichungen mit der vorgeschlagenen eingebetteten Fluidformulierung zu einem monolithischen FSI-System.

Die Lösung solcher nichtlinearer FSI-Probleme mit einem Newton-Raphson-Verfahren in der üblichen Art führt zu Schwierigkeiten, die sich aus der Kombination der gewählten Euler-Beschreibung im Hintergrundgitter mit bewegten eingebetteten Netzen ergibt. Um dies zu vermeiden, wird ein neuer Lösungsansatz entwickelt: Das "Relaxing ALE"-Prinzip. Der Grundgedanke hier ist, dass sich die Position der eingebetten Fluid-Fluid-Grenzfläche während der Newton-Raphson-Iteration nicht ändert und erst am Ende des jeweiligen Zeitschritts aktualisiert wird. Am Ende dieser Ausarbeitung werden zwei- und dreidimensionale Beispiele vorgestellt, um den neuen FSI-Ansatz zu validieren und seine Vorteile aufzuzeigen. Diese Beispiele zeigen, dass eine robuste, stabile und präzise Lösung unabhängig von der geometrischen Form oder der Position des eingebetteten Fluidnetzes erreicht werden kann. Der neue Ansatz bietet somit die Möglichkeit, hohe Gradienten innerhalb der Grenzschicht an der Strukturoberfläche aufzulösen, während er gleichzeitig große Strukturdeformationen zulässt. Die vorgestellte Methode ist daher hervorragend für komplexe FSI-Probleme der realen Welt geeignet.

Danksagung

Die vorliegende Arbeit wurde in den Jahren 2009 bis 2014 während meiner Tätigkeit als wissenschaftliche Mitarbeiterin am Lehrstuhl für Numerische Mechanik der Technischen Universität München (TUM) erarbeitet und verfasst. Die Arbeit lag der Fakultät für Maschinenwesen der Technischen Universität München (TUM) im Sommersemester 2014 als Dissertation vor. An dieser Stelle möchte ich mich bei all jenen bedanken, die mich in diesen Jahren intensiver Arbeit unterstützt haben.

An erster Stelle möchte ich ganz herzlich bei meinem Doktorvater, Herrn Prof. Dr. Wolfgang A. Wall, für die Möglichkeit der Anfertigung dieser Doktorarbeit, seine Unterstützung, sein Vertrauen in mich und für das von ihm geschaffene produktive Arbeitsumfeld bedanken. Dankbar bin ich auch den weiteren Mitgliedern der Prüfungskommission, Herrn Prof. Dr. Daniel J. Rixen und Herrn Prof. Marek Behr, Ph.D., für ihre Zeit und Mühe und die schnelle Erstellung des Gutachtens.

Ein ganz besonders Dankeschön geht an meine Münchner Kollegen, von den ich viel gelernt habe und mit denen ich eine sehr wertvolle Zeit verbracht habe. Sie haben für mich die Promotionszeit zu einem unvergesslichen Lebensabschnitt gemacht, an den ich mich mit Freude erinnern werde. Insbesondere möchte ich mich bei meinen Kollegen der XFEM-Gruppe, Benedikt Schott, Sudhakar Yogaraj, Raffaella Kruse und Ursula Rasthofer für deren Unterstützung, Hilfestellung und die vielen wertvollen Diskussionen bedanken. Meine ehemaligen Kollegen Dr. Axel Gerstenberger und Dr. Ulrich Küttler haben mich auch in den ersten zwei Jahren der Promotion sehr unterstützt und viele wertvolle Anregungen geliefert. Ebenso danke ich Susanna Tinkl, Dr. Caroline Danowski, Matthias Mayr, Dr. Volker Gravemeier, Karl-Robert Wichmann, Hamman de Vaal, Christian Roth, Julien Gillard, Dr. Markus Gitterle und Dr. Florian Henke für die wertvolle Zusammenarbeit. Danke ich auch denjenigen Kollegen, die mir bei der technischen Fertigstellung des Manuskripts geholfen haben.

Zuletzt gebührt mein ganz herzlicher Dank meinen Eltern und meiner Schwester Shanly für deren uneingeschränkten Unterstützung und ihren Rückhalt in schwierigen Situationen. Ohne sie wäre die Anfertigung der vorliegenden Arbeit nicht möglich gewesen.

München, September 2014

Shadan Shahmiri

Contents

1	Introduction	1
1.1	Motivation	1
1.2	Coupling strategies to fluid-structure interaction simulations	2
1.3	Principal approaches to fluid-structure interaction simulations	2
1.3.1	Arbitrary-Lagrangian-Eulerian (ALE)-based FSI approaches	2
1.3.2	Fixed-grid FSI approaches	3
1.3.3	Hybrid FSI approaches	5
1.4	Research objective	6
1.4.1	Requirements	7
1.4.2	Proposal for hybrid ALE-fixed-grid FSI approach	9
1.5	Outline	10
2	Governing Equations	13
2.1	System of references	13
2.2	Structure	13
2.2.1	Kinematics	14
2.2.2	Constitutive equation	14
2.2.3	Balance of linear momentum	15
2.2.4	Weak formulation	16
2.2.5	Discretization	16
2.2.6	Linearization	17
2.3	Fluid	18
2.3.1	Kinematics	18
2.3.2	Constitutive equation	18
2.3.3	Conservation of mass	19
2.3.4	Conservation of linear momentum	19
2.3.5	Incompressible Navier-Stokes equations	19
2.3.6	ALE form of the incompressible Navier-Stokes equations	20
2.3.7	Weak formulation	21
2.3.8	Discretization	22
2.3.9	Stabilization	24
2.3.10	Linearization	26
2.4	Fluid grid motion	27
2.5	Coupled fluid-structure problem	28
2.5.1	Problem definition	28
2.5.2	Coupling conditions	29

3	An XFEM-based embedded fluid formulation	31
3.1	Problem definition	31
3.2	An XFEM-based formulation for background fluid field	34
3.2.1	Introduction to Extended Finite Element Method (XFEM)	34
3.2.2	Volume-cell representation of background fluid domain	37
3.2.3	A DOF-management algorithm for complex topologies	40
3.2.4	Numerical integration	41
3.3	Enforcement of fluid-fluid interface conditions	43
3.3.1	Overview of different methods	45
3.3.2	Nitsche’s method	47
3.3.3	Mixed/hybrid Cauchy stress-based method (MHCS)	56
3.3.4	Mixed/hybrid viscous stress-based method (MHVS)	62
3.3.5	Comparison of different methods	67
3.4	Extension to convection-dominated flow	71
3.5	Face-oriented fluid stabilizations	74
3.6	Fluid stabilization at the interface	77
3.7	Convergence study with two-dimensional Kim-Moin flow	78
3.7.1	Analysis of different parameters	80
3.7.2	Analysis of different methods for weak enforcement of coupling conditions	85
3.7.3	Analysis of different stabilization techniques	86
3.7.4	Analysis of inflow stabilizations for convection dominated flow	88
3.7.5	Summary	91
3.8	Moving embedded fluid	93
3.9	Numerical examples	100
3.9.1	Benchmark computations	100
3.9.2	Two-dimensional cylinder Benchmark with higher Reynolds number	102
3.9.3	Two-dimensional flow over a moving cylinder	108
3.9.4	Two-dimensional moving snake with prescribed motion	108
3.9.5	Three-dimensional moving snake with prescribed motion	112
4	A hybrid ALE-fixed-grid monolithic FSI approach	115
4.1	Problem definition	115
4.2	Semi-discrete formulation of coupled FSI system	116
4.3	Linearization of coupled FSI system	121
4.3.1	Modified structure field	122
4.3.2	Modified fluid field	122
4.3.3	Fluid-structure coupling conditions	123
4.4	Monolithic FSI system	125
4.4.1	Structure-split	128
4.4.2	Fluid-split	129
4.5	Relaxing ALE approach	130
4.6	Numerical examples	133
4.6.1	Pseudo one-dimensional FSI example	134
4.6.2	Two-dimensional compressing structure	136
4.6.3	Two-dimensional bending structure	138

4.6.4	Three-dimensional bending structure	142
4.6.5	Three-dimensional freely moving snake	145
5	Summary and Outlook	153
A	Appendix	157
A.1	Derivation of a lower bound of the Nitsche parameter for Stokes problem . . .	157
A.2	Convergence study with two-dimensional Kim-Moin flow	160
	Bibliography	163

Nomenclature

Abbreviations

FSI	fluid-structure interaction
ALE	Arbitrary-Lagrangian-Eulerian
SUPG	Streamline-Upwind/Petrov-Galerkin
PSPG	Pressure-Stabilizing/Petrov-Galerkin
LPS	local projection-based stabilization
LBB	Ladyzhenskaya-Babuška-Brezzi
FEM	finite element method
XFEM	extended finite element method
DOF	degrees of freedom
GFEM	generalized finite element method
MHCS	mixed/hybrid Cauchy stress-based
MHVS	mixed/hybrid viscous stress-based
RE	Reynolds number

Subscripts and superscripts

$(\cdot)^s, (\cdot)^s$	refers to structure field
$(\cdot)^b, (\cdot)^b$	refers to background fluid subdomain
$(\cdot)^e, (\cdot)^e$	refers to embedded fluid subdomain
$(\cdot)^g, (\cdot)^g$	refers to embedded fluid grid
$(\cdot)^{ff}$	refers to embedded fluid formulation
$(\cdot)_h$	refers to spatial discretization
$(\cdot)^{FF}, (\cdot)_{FF}$	refers to fluid-fluid interface
$(\cdot)^{FSI}, (\cdot)_{FSI}$	refers to fluid-structure interface
$(\cdot)^{n+1}$	refers to current time step
$(\cdot)^n$	refers to previous time step
$(\cdot)_x$	refers to Eulerian formulation
$(\cdot)_\chi$	refers to ALE formulation
$(\cdot)_I$	refers to interior degrees of freedom far from FSI interface
$(\cdot)_\Gamma$	refers to FSI degrees of freedom
$(\cdot)_{def}$	refers to solution on deformed mesh (Relaxing ALE approach)
$(\cdot)^S$	refers to standard unknowns of final fluid-fluid system
$(\cdot)^I$	refers to interface unknowns of final fluid-fluid system

Reference systems

\mathbf{X}	Lagrangian framework
\mathbf{x}	Eulerian framework
χ	ALE framework

Mathematical symbols and operators

$(\cdot, \cdot)_{\Omega}$	L^2 -inner product on domain Ω
$(\cdot, \cdot)_{\Omega(t^{n+1})}$	L^2 -inner product on moving domain Ω at t^{n+1}
$\langle \cdot, \cdot \rangle_{\Gamma}$	L^2 -inner product on boundary Γ
$\langle \cdot, \cdot \rangle_{\Gamma(t^{n+1})}$	L^2 -inner product on moving boundary Γ at t^{n+1}
$\langle \cdot, \cdot \rangle_{\partial\Omega_N}$	L^2 -inner product on Neumann boundary $\partial\Omega_N$
Grad	material gradient operator
∇	spatial gradient operator
Div	material divergence operator
$\nabla \cdot$	spatial divergence operator
R	discrete residual operator
R^{std}	discrete residual operator for standard Galerkin terms
R^{stab}	discrete residual operator for stabilized fluid formulation
$()^{\text{T}}$	transpose of a tensor
$()^{-1}$	inverse of a tensor
\mathbf{I}, \mathbf{I}	identity tensor, identity matrix
det	determinant
tr	trace operator
ln	natural logarithm
$\dot{(\cdot)}$	first time derivative
$\ddot{(\cdot)}$	second time derivative
$[[\cdot]]$	jump operator
$\{\cdot\}, \langle \cdot \rangle$	weighted interface average operators
$\{\cdot\}_m$	mean average operator
Q^1	polynomial of order at most one
δ_{i0}	Kronecker delta

Spatial and Time Discretization

N_i	shape function for node i
n	time step index
Δt	time step size

Structure

$\delta \mathbf{d}^s$	virtual displacement
γ, β	Newmark's method parameters
α_m, α_f	generalized- α method parameters
ρ_∞	spectral radius in high frequency limit
$t^{n+1-\alpha_f}, t^{n+1-\alpha_m}$	generalized- α intermediate time points

Fluid

\mathbf{v}	virtual velocity
q	virtual pressure
θ	one-step- θ parameter
Θ	time factor
\mathbf{u}^{hist}	history values

ALE

$\delta \mathbf{d}^g$	virtual mesh displacement
-----------------------	---------------------------

Function spaces

\mathcal{W}_d	trial space for structural displacements
\mathcal{V}_d	test space for structural displacements
V_h^d	discrete trial and test space for structure field
\mathcal{W}_u	trial space for fluid velocity
\mathcal{W}_p	trial space for pressure
V_h	discrete trial and test space for velocity
Q_h	discrete trial and test space for pressure
V_h^b	discrete trial and test space for background fluid velocity
Q_h^b	discrete trial and test space for background fluid pressure
V_h^e	discrete trial and test space for embedded fluid velocity
Q_h^e	discrete trial and test space for embedded fluid pressure
S_h^b	discrete discontinuous space of additional stress field $\bar{\boldsymbol{\sigma}}_h^b$
\mathcal{W}_λ	trial space for FSI Lagrange multipliers
\mathcal{V}_λ	test space for FSI Lagrange multipliers

Fields and associated parameters

Structure

\mathbf{d}^s	displacement
$\dot{\mathbf{d}}^s$	first material time derivative of displacement (velocity)
$\ddot{\mathbf{d}}^s$	second material time derivative of displacement (acceleration)
\mathbf{d}_0^s	initial displacement
$\dot{\mathbf{d}}_0^s$	initial velocity

\mathbf{b}^s	body force
$\bar{\mathbf{h}}^s$	Neumann traction vector
\mathbf{F}	deformation gradient tensor
J	determinant of deformation gradient tensor
\mathbf{R}	rotation tensor
\mathbf{U}	stretch tensor
\mathbf{C}	right Cauchy-Green tensor
\mathbf{E}	Green-Lagrange strain tensor
\mathbf{S}	second Piola-Kirchhoff stress tensor
$\boldsymbol{\sigma}^s$	Cauchy stress tensor
Ψ	strain-energy function
Ψ_{SVK}	strain-energy function for St.-Venant-Kirchhoff material
Ψ_{NH}	strain-energy function for Neo-Hookean material
λ^s, μ^s	Lamé parameters
E	Young's modulus
ν^s	Poisson's ratio
ρ^s	density
$\mathbf{N}^s, \mathbf{n}^s$	unit normal vectors in reference and current configurations

Fluid

\mathbf{u}	velocity
p	pressure
p_{kin}	kinematic pressure
$\dot{\mathbf{u}}$	acceleration
$\boldsymbol{\epsilon}(\mathbf{u})$	strain rate tensor
$\boldsymbol{\sigma}$	Cauchy stress tensor
$\boldsymbol{\tau}$	shear stress tensor
μ	dynamic viscosity
ν	kinematic viscosity
ρ^f	density
\mathbf{n}^f	outward pointing normal vector of fluid boundary
\mathbf{u}^0	initial velocity
$\bar{\mathbf{h}}$	Neumann traction vector
\mathbf{b}^f	body force
\mathbf{c}	ALE convective velocity
τ^m, τ_s	residual-based stabilization parameters
h	characteristic element length
\mathbf{r}_h^m	discrete residual of momentum equation
\mathbf{r}_h^c	discrete residual of continuity equation

ALE

\mathbf{d}^g	mesh displacement
\mathbf{u}^g	mesh velocity

Domains, boundaries and meshes

Structure

Ω_0^s	reference (material) configuration
Ω^s	current (spatial) configuration
$\partial\Omega_D^s$	Dirichlet partition of boundary
$\partial\Omega_N^s$	Neumann partition of boundary
\mathcal{T}^s	structure mesh

Fluid

Ω^f	whole fluid domain
Ω_0^f	fluid domain at initial time
$\partial\Omega_D^f$	Dirichlet partition of boundary
$\partial\Omega_N^f$	Neumann partition of boundary
Ω^b	physical background fluid subdomain
Ω_K^b	physical fluid volume for cut element K
Ω^{b-}	void/fictitious background fluid subdomain
$\partial\Omega_N^f$	Neumann partition of boundary of background fluid subdomain
Ω^e	embedded fluid subdomain
\mathcal{T}^b	whole background fluid mesh
\mathcal{T}^e	embedded fluid mesh

ALE

Ω^{ALE}	ALE domain
$\partial\Omega^{\text{ALE}}$	Dirichlet partition of boundary

Interfaces

Γ^{FF}	fluid-fluid interface
Γ^{FSI}	fluid-structure interface

Embedded fluid formulation

\mathbf{n}^b	outward pointing normal vector of background fluid subdomain
\mathbf{n}^e	outward pointing normal vector of embedded fluid subdomain

XFEM

$\hat{\psi}$	Heaviside function
\mathcal{T}^Γ	set of cut elements
\mathcal{T}^*	set of cut elements unified with elements of physical background fluid
V	volume-cell
f	facet

Ω_K^b	physical fluid volume for cut element K
Ω_K^e	embedded fluid K adjacent to fluid-fluid interface
Γ_K^{FF}	boundary segment of element K at fluid-fluid interface
$\text{supp}\{N_n\}$	support of shape functions of node n
PATH_C	connection between volume-cells via facets
C	connection of active fluid volume-cells
C_n	set of connections of active fluid volume-cells
$ C_n $	number of connections of active fluid volume-cells
Nitsche	
α'	Nitsche stabilization parameter
β_n	switch of symmetric or non-symmetric viscous part of Nitsche's formulation
κ_b, κ_e	weights of average operators
meas	geometric measure
C_K^b	Nitsche's inverse inequality parameter (background element weighting)
C_K^e	Nitsche's inverse inequality parameter (embedded element weighting)
δ, α	constants included in definitions of Nitsche stabilization parameter
MHCS and MHVS	
$\bar{\sigma}^b$	additional discontinuous stress field on background fluid
$\bar{\tau}^b$	additional discontinuous virtual stress field on background fluid
β_v	switch of symmetric or non-symmetric viscous part of MHVS method
n	MHVS stabilization parameter
Stabilizations	
j_{GP}	ghost-penalty operator
α_{GP}	ghost-penalty parameter
\mathcal{F}_G	set of cut faces of background fluid mesh
h_F	maximal distance from face F to the opposite faces
β_h	advective velocity across fluid-fluid interface
γ_{adv}	convective inflow stabilization constant
\mathcal{F}_E	interior faces of embedded fluid mesh
\mathcal{F}_B	interior faces of background fluid mesh
j_p, j_{stream}	face-oriented stabilization operators
$\gamma_p, \gamma_\alpha, \gamma_s$	face-oriented stabilization parameters
\mathbf{n}^F	normal vector with respect to the face F
$j_{\text{intv}}, j_{\text{intp}}$	fluid stabilization operators at fluid-fluid interface
$\gamma_{\text{intp}}, \gamma_{\text{pc}}, \alpha_{\text{intv}}$	parameters of fluid stabilization operators at fluid-fluid interface
$\delta_{br}, \delta_{er}, \delta_{ef}$	switches between residual and face-oriented stabilizations
Moving interface	
$\tilde{\mathbf{u}}_h^{b,n}$	interpolated background fluid vector
$\mathbf{u}_h^{*b,n}$	constrained interpolated background fluid vector

System matrices and vectors

Structure

M^s	mass matrix
F_{int}^s	vector of internal forces
F_{ext}^s	vector of external forces
d^s	vector of discrete nodal values for displacement
\dot{d}^s	vector of discrete nodal values for velocity
\ddot{d}^s	vector of discrete nodal values for acceleration
r^s	discrete residual vector
S	structural matrix
Δd^s	displacement increments

Fluid

M^F	mass matrix
C^F, K^F, G^F	standard Galerkin matrices
S^{SUPG}	matrix of SUPG contributions
S^{PSPG}	matrix of PSPG contributions
S^{BV}	matrix of bulk viscosity contributions
f_b^F, f_N^F	vector of body forces and Neumann conditions
f_{hist}^F	vector of history values of previous time step
r^{stab}	stabilized residual vector
$u, \Delta u$	discrete nodal velocity and velocity increments
$p, \Delta p$	discrete nodal pressure and pressure increments
r^b	background fluid residual vector
r^e	embedded fluid residual vector

ALE

A	ALE matrix
$d^g, \Delta d^g$	discrete nodal mesh displacement and mesh displacement increments

Nitsche

G^c	Nitsche consistency matrices
G^a	Nitsche adjoint consistency matrices
G^α	Nitsche penalty matrices

MHCS and MHVS

G	boundary coupling matrices of stress-based methods
K	volume coupling matrices of stress-based methods
r_σ^b	residual vector of additional stress field
C	coupling matrices of stress-based methods after condensation
$c^{e,K}, c^{b,K}$	residual vectors of the coupling terms after condensation

Fluid-fluid system

\underline{G}	matrix of Nitsche terms and convective inflow stabilizations
\underline{S}	matrix of fluid stabilization terms

FSI system

r^{FSI}	residual of nonlinear FSI problem
r^s, r^{ff}	residuals of structure and fluid fields
r^{kin}	residual of kinematic coupling condition
λ	vector of discrete nodal values of FSI Lagrange multipliers
$\Delta\lambda$	FSI Lagrange multiplier increments
$r_\lambda^s, r_\lambda^{\text{ff}}$	FSI contributions of structure and fluid residuals
F^{ff}	fluid-fluid matrix
$u_{\Gamma}^{\text{ff}}, \Delta u_{\Gamma}^{\text{ff}}$	vector and increments of interior DOFs of fluid-fluid formulation
$u_{\Gamma}^{\text{ff}}, \Delta u_{\Gamma}^{\text{ff}}$	vector and increments of FSI-DOFs of fluid-fluid formulation
$C_{\text{FS}}, C_{\text{SF}}$	FSI coupling matrices
J	Jacobian matrix
Δx	incremental solution vector
τ	switch of first or second order transformation of ALE displacements
$\Delta d_{\Gamma,p}^s$	structure predictors
x_{def}^{n+1}	current solution of FSI problem on deformed mesh (Relaxing ALE approach)

Fluid-structure interaction

$d_{\Gamma^{\text{FSI}}}^s$	displacement at fluid-structure interface
$u_{\Gamma^{\text{FSI}}}^e$	embedded fluid velocity at fluid-structure interface
$d_{\Gamma^{\text{FSI}}}^g$	embedded grid displacement at fluid-structure interface
$u_{\Gamma^{\text{FSI}}}^g$	embedded grid velocity at fluid-structure interface
λ	Lagrange multiplier field
$\delta\lambda$	virtual Lagrange multiplier field
$h_{\Gamma^{\text{FSI}}}^e$	traction field of embedded fluid at fluid-structure interface
$h_{\Gamma^{\text{FSI}}}^s$	traction field of structure fluid at fluid-structure interface
Γ_K^{FSI}	fluid-structure interface segments
a, b	time integration factors
λ	nodal values of discrete Lagrange multipliers

1 Introduction

1.1 Motivation

Fluid-structure interaction (FSI), which is one of the most important and challenging multi-physics phenomena, can be defined as an interaction of a flow field with a movable or deformable structure. FSI plays a significant role in many engineering and scientific fields. Some exemplary engineering systems, where the FSI problems are considered as an essential factor are aircraft wings, turbine blades, bridges, airbags or tent-roofs. FSI also appears in many biological problems, such as various arterial and venous circulatory blood flows, respiration of air by the lungs, cellular immersion, red blood cells in blood plasma and swimming jelly fish.

FSI problems are most often too complex to obtain an analytical solution to their model equations. Furthermore, it is not always possible to carry out an experiment to a specific problem, since such experiments are often too costly or the required facilities are limited. Thus, for complex problems often numerical simulations are the only way to investigate the fundamental physics involved in the interaction of fluid and structure. In many scientific and engineering fields, numerical simulations accompany experimental results, to eliminate or reduce the necessity of performing experiments. Hence, development and application of efficient and accurate numerical methods for complex FSI problems have gained great attention over the last decades.

The present work concentrates on the development of a new FSI approach particularly suited for the interaction of incompressible flow with deformable, compressible or incompressible structures, undergoing large deformations. The two main features of the proposed FSI method are as follows: first, it is able to deal with unlimited and complex structural deformations. Second, a proper mesh resolution around the structural surface, constructed a priori, is preserved during the whole simulation time. This makes the method best suited for real-world FSI problems, since having a boundary layer mesh around the structural surface, where boundary layers, are usually present, and flow separation and re-attachment could occur, is an important prerequisite for achieving reliable results for complex FSI problems. A possible application for the FSI approach developed in this thesis is, for example, the modeling of the interaction of flapping biofilm streamers, which are clusters of microbial aggregates connected to a tail elongated from the cluster in the direction of the flow, with the fluid surrounding them, see e.g. Taherzadeh et al. [166] and Coroneo et al. [53]. Other attractive engineering applications are, for instance, flows around and/or induced by rotating components, such as a submarine or a rotating propeller.

FSI methods can be classified by various factors. Important features for classifying FSI methods are, e.g. the principal FSI approaches, i.e. the formulations of structure and fluid field and the way quantities at the common fluid-structure interface are transferred, or the coupling strategies. In the following, first, a short overview of the coupling strategies is given. Afterwards, an overview of the most important existing principal FSI approaches, which motivate the development of the new FSI approach in this thesis, and their key features are provided. For the sake

of clarity, the principal FSI approaches, discussed in the following, are subdivided into three main groups, classical ALE-based FSI approaches, fixed-grid FSI approaches and hybrid FSI approaches.

1.2 Coupling strategies to fluid-structure interaction simulations

The coupling strategies are an important factor for classifying FSI methods. Regarding coupling strategies, the FSI methods can be divided into two main groups, staggered or partitioned schemes and monolithic schemes. Partitioned methods are based on the evaluation of the single fields and transferring the coupling information between the fields. One type of partitioned methods are weak coupling methods, where each field is solved only once in every time step. It has been shown that these approaches are applicable for compressible flow problems, e.g. aeroelasticity, see Farhat [68]. However, weak coupling methods are unstable for incompressible flows as a result of the well-known artificial added-mass effect, shown by Causin et al. [44] and Förster et al. [74]. On the other hand, strong coupling methods iterate the field solvers until a converged solution in every time step is achieved. The coupling is, for example, based on classical Dirichlet/Neumann algorithm. Several acceleration schemes have been introduced to improve the convergence behavior of strong coupling methods. Strong coupling methods are covered in detail, e.g. in Fernández and Moubachir [71], Küttler and Wall [121], Le Tallec and Mouro [125], Mok and Wall [141], and Küttler and Wall [122]. Another class of coupling schemes are monolithic schemes, which are also strong coupling methods, see e.g. Heil [99], Küttler [120], Klöppel et al. [117] and Mayr et al. [135]. In contrast to partitioned methods, monolithic schemes solve the entire FSI problem in a global system simultaneously. For challenging FSI problem, the use of a monolithic approach is either essential or it outperforms partitioned schemes in terms of robustness, performance and computational costs. Some example of these challenging FSI problems are channels with flexible walls, see Heil [99], or biological problems like the modeling of human red blood cells, see Klöppel and Wall [116]. A comparison and performance analysis between partitioned and monolithic schemes can be found in Heil et al. [100] and Küttler et al. [123]. To solve the global FSI system, in Heil [99] block preconditioned Newton-Krylov schemes were suggested. Gee et al. [81] proposed efficient preconditioners based on algebraic multigrid techniques. For an overview of strong coupling FSI schemes the interested reader is referred to Küttler et al. [123].

1.3 Principal approaches to fluid-structure interaction simulations

1.3.1 Arbitrary-Lagrangian-Eulerian (ALE)-based FSI approaches

Arbitrary-Lagrangian-Eulerian (ALE)-based FSI methods are the most popular and most widely used approaches in commercial and research FSI-codes. The formulation of the flow field is based on an ALE formulation, whereas the structure is described in a Lagrangian framework.

The ALE formulation of the fluid field allows for solving the flow field on a deformable grid, which undergoes the same deformation as the structure at the common fluid-structure interface. The deformation of the fluid mesh inside the domain is arbitrary and extended from the motion of the fluid at the interface with an appropriate grid motion algorithm, which minimizes the discretization error and avoids distorted elements as much as possible. The ALE-based FSI approach can be traced back to the early works by, e.g. Belytschko et al. [23], Belytschko and Kennedy [25], Hirt et al. [104], Hughes et al. [108] and Donea et al. [63]. A noteworthy advantage of the ALE-based approach is that the position of the structure within the fluid domain is known a priori and, therefore, a proper fine mesh can be constructed near the structural surface to resolve the flow features around it. However, large structural deformations can distort the fluid mesh such that re-meshing and mesh-updating become unavoidable. Hence, the optimal fluid mesh around the structure can often not be preserved.

This shortcoming of the ALE-based FSI algorithm was the motivation for developing alternative FSI approach, the so-called fixed-grid methods, which is discussed in the forthcoming section.

1.3.2 Fixed-grid FSI approaches

Fixed-grid FSI approaches use formulations on a fixed Eulerian grid formulation to describe the fluid field, as usual for fluid problems without moving interfaces. The key idea of fixed-grid approaches is that the structure moves independently of the fluid grid. Therefore, unlimited and complex deformations of the structure are basically possible. The fluid-structure interface is usually described explicitly by the surface of the structure or implicitly, e.g. via level-set functions. It divides the fluid domain into two subdomains, the actual physical fluid subdomain and a void/fictitious fluid subdomain, which has no physical meaning and is covered by the structure field. The fictitious fluid subdomain may be treated differently depending on the actual fixed-grid approach. The coupling conditions at the fluid-structure interface need to be enforced weakly, since the fluid-structure interface is usually not aligned with element boundaries, but located in fluid element interiors. In the forthcoming paragraphs, some of the most important fixed-grid FSI approaches are briefly outlined.

Immersed boundary (IB) method and its derivations are one of the earliest classes of the fixed-grid FSI approaches. The IB method was originally developed by Peskin [145] to simulate blood flow and muscle contraction in a beating heart, see also Peskin [146]. Other similar approaches such as extended immersed boundary methods or immersed finite element methods were developed later by, for example, Wang and Liu [176] and Zhang et al. [182], or other variations such as in Leveque and Calhoun [129] and Lee and Leveque [126]. For an overview of IB methods see, e.g. Mittal and Iaccarino [138]. The key idea of the IB method is that the computation of the flow is extended into the fictitious fluid subdomain. The fluid velocities on the fictitious subdomain are interpolated into the structure domain to evaluate the structural deformation. The structural elastic forces are then interpolated back into the fluid domain, which result in additional body forces in the fluid equations. IB methods have been considered as a useful tool for biomechanical problems, where the flow with immersed soft boundaries has to be modeled.

The Distributed Lagrange Multiplier/Fictitious Domain (DLM/FD) methods (see, e.g. Baaijens [4], De Hart et al. [57], Glowinski et al. [86, 87], Van Loon et al. [170] and Yu [181]) which have some similarities to IB methods, are another class of fixed-grid approaches. As for IB meth-

ods, in the DLM/FD approach the fluid-structure coupling takes place between the fictitious fluid subdomain and the structure, i.e. also for DLM/FD the coupling between fluid and structure is a volumetric coupling. In this approach, the fluid and structure degrees of freedom are solved usually in a monolithic system with an additional Lagrange multiplier unknown to enforce the kinematic coupling between the fictitious fluid subdomain and the structure. Hence, the fictitious subdomain is forced to undergo the same deformation as the structure.

However, the most IB and DLM/FD methods are not appropriate approaches for FSI problems, which require an accurate representation of the quantities at the interface, since the methods do not deliver accurate and sharp representations of the stress jumps over the fluid-structure interface. Furthermore, for IB methods exists some mesh-size dependencies between fluid and structure to achieve an accurate kinematic matching between them. Moreover, since the interaction between fluid and structure fields is a volumetric coupling, the structure is affected by an artificial viscosity or it is forced to be incompressible, see Wall et al. [174]. For a more detailed overview of the mentioned fixed-grid approaches, the interested reader is referred to Wall et al. [174] and Gerstenberger and Wall [83]. Other fixed-grid approaches using level-set functions, often based on finite-difference or finite-volume methods, are given, for example, in Fedkiw et al. [70] or Cirak and Radovitzky [50].

The shortcomings of the methods explained above were the motivation for developing a new fixed-grid approach for two-dimensional FSI problems based on an extended finite element method (XFEM) and Lagrange multipliers (LM) by Gerstenberger and Wall [84]. The XFEM, originally introduced by Belytschko and Black [22] and Moës et al. [139] for crack problems, makes it possible to model a jump across interfaces. Lagrange multipliers are used to enforce the coupling condition weakly along the interface. The XFEM-based FSI approach is able to represent a sharp interface between physical and fictitious fluid subdomains. Thus, discontinuities in velocity and pressure fields and the derivatives like stresses across the fluid-structure interface are represented accurately. This is an important aspect to preserve the conservation properties at the interface and avoid any incorrect energy transfer across the interface. Furthermore, no mesh-size dependencies between structure and fluid fields exist and the mesh sizes can be chosen independently. Moreover, due to the surface coupling along the interface, the influences of the fictitious subdomain are eliminated. This approach was extended to three-dimensional problems by Gerstenberger and Wall [85] and Gerstenberger [82] by using a mixed/hybrid formulation, where an additional discontinuous stress field is defined on the background fluid field to enforce the coupling condition along the fluid-structure interface. Legay et al. [128] described an XFEM-based approach for FSI problems and free surfaces using a level-set function and Lagrange multipliers. Other XFEM-based space-time approaches for FSI problems were proposed by Legay and Kölke [127], Zilian and Legay [185], and Kölke and Legay [118]. Another fixed-grid approach introduced by Baiges and Codina [10] is referred to as a fixed-grid ALE approach. In this method, as in other fixed-grid approaches, the background fluid is defined on a fixed mesh but, additionally, the method makes use of an ALE formulation to deal with the difficulties arising due to the Eulerian formulation of the fluid domain in combination of moving boundaries.

An important issue for ensuring reliable simulations of complex FSI problems is a proper resolution of the flow features around the structural surface. The above-mentioned XFEM-based fixed-grid approach allows in fact for large deformations of the structure, but unlike in ALE-based methods, it is not possible to generate an appropriate mesh around the structure. Particularly for high Reynolds number flow, having a boundary layer mesh around the structural

surface is essential. The inability of existing fixed-grid approaches to match this requirement usually prevents them from being used for complex FSI problems in real-world applications. A rather straightforward solution would be a local, adaptive mesh refinement and coarsening combined with error estimator-based and/or heuristics-based refinement indicators, as described in Gerstenberger and Wall [83] for two-dimensional FSI problems. An overview of adaptive embedded mesh techniques is given by Löhner et al. [130]. However, such an adaptive approach becomes rather inefficient for three-dimensional problems involving large motions of the structural surface, since either larger regions often have to be refined and/or the mesh updates may have to be done very often during the simulation. Furthermore, the refinement usually occurs simultaneously in each spatial direction and, therefore, it is almost impossible to efficiently resolve the boundary layers by using extremely stretched elements, particularly in the three-dimensional case.

In the forthcoming section, an overview of most important approaches, which make use of two fluid meshes and allow for constructing surface layer of fitted fluid mesh around the structure, is given. These approaches are classified into hybrid FSI approaches, in this work.

1.3.3 Hybrid FSI approaches

Chimera methods, originally introduced by Steger et al. [159], make use of overlapping fluid meshes to model FSI problems with large structural deformation. The structure is surrounded by a surface-fitted moving fluid patch, which is located in a fixed-grid background fluid mesh. The Chimera method was proposed for flexible mesh generation of the flow simulation around rigid bodies such as flow around a complex space-shuttle vehicle or an unsteady flow around a helicopter. Other Chimera-like methods were developed later, for example, by Meakin and Suhs [136], Vázquez et al. [171], Wang and Parthasarathy [177] or Houzeaux and Codina [107]. To treat flexible structures, the ALE-Chimera method, based on a combination of ALE and Eulerian fluid formulations, was proposed by Gamnitzer and Wall [80], see also Wall et al. [175]. In the ALE-Chimera method the structure is surrounded by a surface-fitted ALE fluid mesh, which moves and deforms with the structure. In contrast to the ALE-based approach, the ALE fluid does not cover the entire fluid domain, but rather moves with the structure in the fixed-grid background fluid. Therefore, on the one hand, large deformation of the structure is possible and, on the other hand, the ALE mesh allows for an accurate resolution of the structural surface. However, the Chimera schemes have some drawbacks. They make use of the overlapping zone of two fluid domains to get a converged solution after iterating between the fluid domains. The solution of the both fluid regions are matched by a weak Dirichlet/Neumann coupling. This introduces an additional iteration step over the overlapping fluid grids to obtain the fluid solution. Beside this additional cost, there is a dependency on the size of the overlapping domain; this region has to be large enough to achieve a converged solution.

As an extension to the two-dimensional XFEM/LM-based fixed-grid FSI approach by Gerstenberger and Wall [84], described in Section 1.3.2, a hybrid Lagrange-multiplier based overlapping mesh approach combining ALE and fixed-grid Eulerian formulations was proposed by Gerstenberger and Wall [83] for two-dimensional FSI problems. In this approach, as in the ALE-Chimera approach, a fine surface layer of deformable fluid elements based on ALE formulation is added to the structural surface, which moves and deforms with the structure. The ALE-based fluid patch captures the flow near the fluid-structure interface with an appropriate fine mesh. This

fine layer of flexible fluid elements is then embedded into the fixed-grid background fluid mesh. However, in contrast to the ALE-Chimera approach, the coupling between the two fluid subdomains is a weak surface coupling based on the XFEM/LM-method, i.e. no iterations between the two fluid domains are performed. The structure and the fluid patch are coupled based on the classical ALE-based method described above. A similar approach for three-dimensional stationary FSI problems, however, with a fixed interface between two fluid domains, was recently introduced by Massing et al. [133].

An example of a non-overlapping mesh approach, which also enables constructing surface layer of fitted fluid mesh around the structure is the shear-slip method proposed by Behr and Tezduyar [20]. The shear-slip method is able to handle flow problems with moving interfaces including regularly large deformations, i.e. straight-line translations or rotations. The fluid mesh is divided into three subdomains, two stationary meshes and an instationary thin mesh between them. At each time step, the elements in a thin zone of the fluid mesh undergo 'shear' deformation to the nearest nodes of the stationary mesh. The thin zone is subsequently remeshed by a 'slip' of the connectivity of the nodes. This approach was applied to three-dimensional flow problems with rotating mechanical components in Behr and Tezduyar [21]. Another non-overlapping mesh approach based on a non-uniform rational B-spline (NURBS) was proposed by Bazilevs and Hughes [15] for the computation of the flow around rotating components. Also here, the method consists of a fluid subdomain which surrounds the structure and rotates with it. The moving fluid patch is then located in a stationary fluid subdomain. The interface between the rotating and stationary fluid, which has a circular or cylindrical form, keeps its form throughout the simulation.

An attractive approach for mesh tying of non-matching fluid discretizations at an arbitrary interface based on a dual mortar method (see e.g. Wohlmuth [178]), was recently proposed by Ehrl et al. [66]. The dual mortar method is based on dual Lagrange multipliers, which are constructed according to biorthogonality condition and can thus be condensed easily from the global system of equations. This approach can be extended to FSI problems with locally large structural deformations, e.g. rotations. A fine fluid patch surrounds the structure, which is then coupled to a bigger fluid domain based on the dual mortar approach. To maximize the feasible deformation of the structure, the patch and background fluid domains are both described in ALE formulation. Since the patch fluid mesh slides at the background mesh, the connectivity of the nodes has to be recomputed in every time step. A similar approach to this is the sliding mesh method introduced by Klöppel [115]. The sliding mesh approach is a pure ALE-based FSI approach with only one fluid domain, which allows large structural rotations in a sliding of the fluid grid on the structural surface.

A general sketch of three main FSI approaches developed at the Institute of Computational Mechanics at the Technische Universität München to date, described in this section, ALE-based FSI approach, fixed-grid FSI approach and XFEM/LM-based hybrid ALE-fixed-grid method, is given in Figure 1.1.

1.4 Research objective

The method developed in this thesis and outlined in the following is aiming at a robust, accurate and efficient general FSI approach for complex two- and three-dimensional problems, in

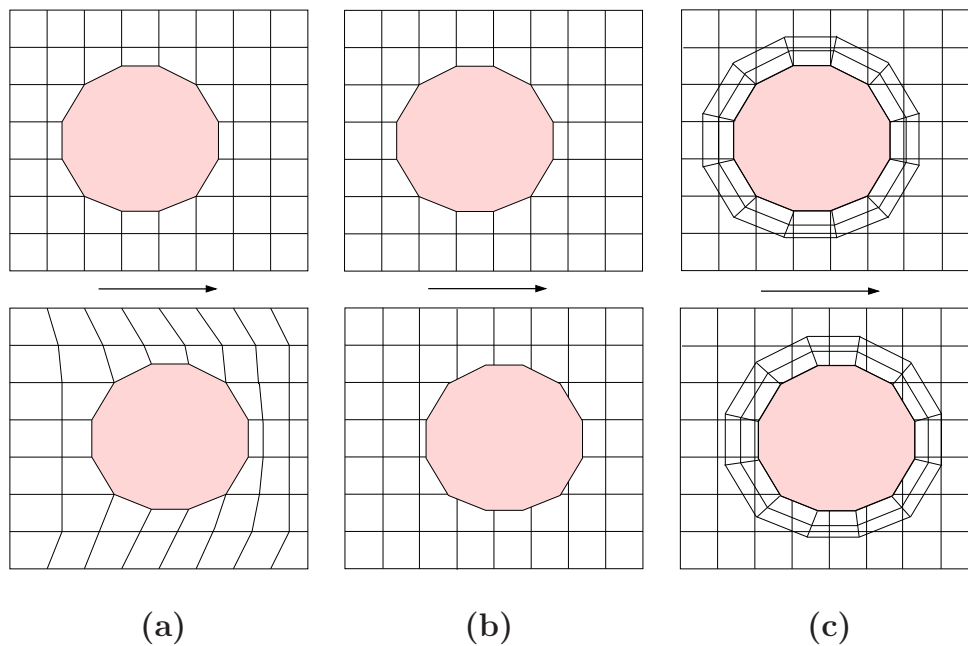


Figure 1.1: Stretch of possible FSI approaches: **(a)** ALE-based FSI approach **(b)** Fixed-grid FSI approach **(c)** Hybrid ALE-fixed-grid FSI approach.

particular, the interaction of incompressible flow with deformable, compressible or incompressible structure, without any limitations regarding models and approaches in individual fields. The structure should be able to undergo large and complex deformations, involving a proper resolution of the flow features around its surface throughout the simulation. Fixed-grid methods are counted among the most interesting approaches when dealing with large deformations of the structure, since they allow for unlimited and complex deformation of the structure without any distorted fluid elements or remeshing procedures. Among them, the XFEM-based methods have very desirable properties, such as surface coupling between fluid and structure without any influence of the fictitious fluid on the structure, and a sharp representation of the quantities at the interface. However, a combination of a fixed-grid approach with a proper resolution of the flow features around the structural surface throughout the simulation applicable for complex three-dimensional problems is still missing. Hence, in this thesis a three-dimensional robust, accurate and stable hybrid ALE-fixed-grid FSI approach, inspired by the XFEM-based hybrid approach for two-dimensional FSI problems of Gerstenberger and Wall [84], allowing for large structural deformations in combination with a deformable fluid mesh around the structure is developed. The deformable fluid mesh follows the structural deformation and, therefore, captures the flow near the fluid-structure interface throughout the whole simulation.

1.4.1 Requirements

In the following, based on the explanation given above, the most important requirements for developing such a hybrid ALE-fixed-grid FSI approach for complex three-dimensional FSI problems are highlighted.

Lagrangian formulation of the structure The structure domain should be modeled using a Lagrangian formulation, exploiting the existing implementations. Moreover, it should be able to deal with existing structural models and approaches without introducing any restrictions.

No mesh-size dependencies As mentioned above, a drawback of Chimera methods is that they make use of the overlapping zone to get a solution after iterating between both fluid domains. However, to get a converged solution, the overlapping domain should be large enough. To have an appropriate fitted mesh around the structure individual for each particular FSI problem, it is essential to eliminate the limitations regarding the mesh-size dependencies between the patch fluid and the fixed-grid background fluid. Hence, a surface coupling between the patch fluid and the background fluid is desired without introducing overlapping solutions as in Chimera methods.

No extra cost due to fictitious fluid As aforementioned, solving the fictitious fluid introduces an extra cost in the global system. A FSI approach is desired with no influence of the fictitious fluid, i.e. no extra cost in terms of introducing a redundant solution in the overlapping region.

Stable, accurate and robust coupling between two fluid subdomains To apply a deformable fluid patch in complex three-dimensional FSI problems it is crucial to satisfy high demands on the weak coupling between the background fluid and patch fluid. This coupling needs to be stable, accurate, robust and independent of the position of the internal fluid-fluid interface between two fluid subdomains or the complexity of the form of the patch fluid. After all, a smooth transition of the solution across the fluid-fluid interface has to be achieved for any interface position. Thus, developing a stabilized embedded fluid formulation, which results in a robust and accurate solution for every position of the fluid-fluid interface in viscous as well as convective dominated flow is essential.

Stable and robust solution over time In contrast to ALE formulations, where the grid of the fluid domain is deformed with the moving boundary and provides an appropriate description for it, the Eulerian formulation is naturally inappropriate for moving interfaces, as the fluid grid is generally not aligned with the interface. This leads to an inconsistency, since integrals on the time dependent background fluid involve values from the last time step, which change their degrees of freedom over time. Thus, to deal with this inconsistency, developing an appropriate and efficient XFEM time-integration approach to handle the Eulerian fixed-grid background fluid in combination with moving interfaces is crucial. This time-integration approach together with the stabilized embedded fluid formulation should provide a stable, accurate and robust solution throughout the simulation, aiming at a smooth transition of the velocity and pressure fields across the fluid-fluid interface at any time.

Monolithic solution scheme The structural equations together with the fluid-fluid system need to be solved in a monolithic scheme, i.e. without any iterations between the fixed-grid background fluid, the fluid patch and the structure. However, the combination of the Eulerian background fluid together with the moving fluid patch results in further complexities with respect to solving the global nonlinear problem monolithically with a Newton-Raphson scheme. It leads

to a global system, which changes its degrees of freedom in every Newton step. The reason is that a new position of the fluid-fluid interface gives rise to a new physical and fictitious background fluid mesh and, thus, new degrees of freedom arise and some degrees of freedom are removed in every Newton step. Moreover, the missing values of the previous Newton step, which are required in the present Newton step have to be reconstructed with the XFEM time-integration approach aforementioned. This process brings in a perturbation in every Newton step, which would prevent any convergence or result in a poor convergence behavior of the Newton-Raphson scheme. Hence, an algorithm is required to deal with this problem. The achieved accuracy of the solution of the monolithic hybrid FSI approach should be equivalent to the well-established monolithic ALE-based approach.

1.4.2 Proposal for hybrid ALE-fixed-grid FSI approach

This thesis describes a hybrid ALE-fixed-grid FSI approach for complex two- and three-dimensional FSI problems with large structural deformation, which combines the advantages of fixed-grid and ALE-based FSI methods, addressing all aforementioned requirements. The structure is described as usual in a Lagrangian formulation, which is surrounded by a surface layer of deformable fluid elements based on an ALE formulation. This deformable fluid patch, which is then embedded in the fixed-grid Eulerian background fluid, deforms with the structure and provides an appropriate boundary layer mesh throughout the simulation. The coupling between the structure and the moving fluid is handled in the same way as classical ALE-based FSI approaches. The surface coupling between the two fluid domains is imposed weakly using a stabilized formulation. Thus, in other words, overlapping meshes are used without introducing overlapping solutions. The most important ingredients of the presented method are given in the following:

- As the embedded fluid subdomain ends in the middle of the background fluid elements, the first step toward the stabilized embedded fluid formulation is to decouple the background fluid into a physical and a fictitious subdomain, i.e. to describe a jump from the physical values of the background fluid to zero along the fluid-fluid interface. For this purpose, an XFEM-based formulation, using a flexible framework for handling multiple degrees of freedom for nodes of a fixed-grid background mesh is presented, see also Schott and Wall [154] and Shahmiri et al. [156, 157].
- The coupling between the physical background fluid and the embedded fluid is then imposed weakly along the fluid-fluid interface. For this purpose, a stabilized embedded fluid formulation for viscous as well as convective dominated flow independent of the position of the fluid-fluid interface is proposed. The essential ingredients of the embedded fluid formulation are as following: The coupling condition on the fluid-fluid interface is imposed weakly using Nitsche's formulation (Nitsche [144]), and the Nitsche parameter is determined via a local eigenvalue problem. Face-oriented and ghost-penalty stabilizations, according to Burman and Hansbo [38] and Burman et al. [42] are applied to control the ghost values at the interface zone adequately, balance fluid instabilities at the interface zone for both viscous and convective dominated flows, and, control the conditioning of the system. To overcome the instabilities caused by convective mass transport across the fluid-fluid interface, additional inflow stabilization terms at the fluid-fluid interface are introduced, see also Shahmiri et al. [156].

- For time discretization of the embedded fluid formulation, finite difference schemes are employed. To deal with the inconsistency of the combination of Eulerian fixed-grid background fluid and moving fluid-fluid interface, a new XFEM time-integration approach is developed. This approach, together with the stabilized embedded fluid formulation, results in a stable and robust solution for any time, see also Shahmiri et al. [156].
- The structure and the fluid patch are coupled in same way as the ALE-based FSI approach. This allows the use of coupling algorithms originally developed for classical ALE-based FSI approaches. The whole system is solved in a monolithic system as presented, for example, in Gee et al. [81]. For the monolithic system, the fluid-fluid interface is an internal interface, which is hidden in the fluid system, and does not affect the FSI coupling directly. To solve the monolithic FSI system and deal with the Eulerian description of the background fluid combined with the moving fluid patch, a relaxing ALE approach is proposed.

To conclude, all the ingredients mentioned above result in a novel hybrid ALE-fixed-grid FSI approach to perform reliable simulations of complex two- and three-dimensional FSI problems. The proposed FSI approach is implemented in the multiphysics research-code BACI (Wall and Gee [173]), written in C++ and developed at the Institute of Computational Mechanics at the Technische Universität München. The parallel framework is based on the open-source libraries of Trillinos by Sandia National Laboratories, see Heroux et al. [103].

1.5 Outline

The methods and the algorithms presented in this thesis are organized in the same order as the important ingredients required for the monolithic hybrid ALE-fixed-grid FSI approach mentioned above, starting with the finite element formulation of individual fields and the XFEM-based embedded fluid formulation, and ending with the hybrid ALE-fixed-grid FSI approach. Thus, the remainder of the presented work is organized as follows:

In Chapter 2 the basic concepts of continuum mechanics, governing equations and the spatial and temporal discretization of single fields are reviewed. Then a hybrid fluid-structure formulation including its coupling conditions is proposed, which allows for separately considering of the coupling at the fluid-fluid interface and at the fluid-structure interface in the forthcoming chapters.

Chapter 3 concentrates on the stabilized embedded fluid formulation. An embedded fluid formulation based on an extended finite element method (XFEM) for transient problems and stationary interface is developed step-by-step, which is applied to moving interfaces afterwards. First, an XFEM-based formulation for the fixed-grid background fluid subdomain is presented. Afterwards, the focus is shifted to the weak enforcement of coupling conditions on the fluid-fluid interface. In this context, different coupling methods and various stabilization terms are discussed, and finally a stabilized embedded fluid formulation independent of the position of fluid-fluid interface for viscous and convective dominated flows is introduced. The proposed formulation is then extended to moving interfaces by introducing a new XFEM time-integration approach for the Eulerian background fluid. The proposed stabilized embedded fluid formulation is validated for the case of stationary as well as moving embedded fluid.

Chapter 4 combines the stabilized embedded fluid formulation, proposed in Chapter 3, and the structure field into a coupled FSI system, which is solved in a monolithic scheme. The challenge of solving the derived monolithic FSI system in combination of moving embedded fluid and fixed-grid background fluid is explained, and a new method stated as *relaxing ALE approach* is introduced. Numerical examples validate the hybrid ALE-fixed-grid FSI approach and show the ability and performance of the proposed method.

The conclusion in Chapter 5 reviews the achievements and the key points necessary for developing the hybrid ALE-fixed-grid FSI approach. Furthermore, it provides directions for future work.

2 Governing Equations

In this chapter, first, a short introduction to the systems of reference is given. Afterwards, in Section 2.2, the basic concepts of continuum mechanics and governing equations for structure field are reviewed. The Section 2.3 focuses on fluid field, containing the governing equations for incompressible flow of a Newtonian fluid in an Eulerian and Arbitrary-Lagrangian-Eulerian (ALE) description. Subsequently, Section 2.4 contains a short introduction to fluid grid motion. Finally, the new hybrid ALE-fixed-grid fluid-structure interaction (FSI) approach will be introduced and the related coupling conditions will be presented.

2.1 System of references

An important consideration before simulating any numerical method is an appropriate choice of a reference system. The methods of continuum mechanics make use of three different reference systems: the material or Lagrangian formulation, the spatial or Eulerian formulation and the Arbitrary-Lagrangian-Eulerian (ALE) formulation, a term that was introduced by Hirt et al. [104]. Usually the structure is described in time-dependent Lagrangian formulation, where the position and physical properties of the particles are described in terms of the material coordinates. For pure fluid problems the time-independent Eulerian description is used, where the observer is spatially fixed and watches the fluid passing. The ALE formulation is introduced to deal with fluid problems involving moving boundaries like in classical ALE-based FSI approach. In ALE framework the mesh follows the motion of the boundary, while it deforms arbitrarily in the domain, i.e. the mesh moves with a velocity independent from the fluid. In the present work, the three named reference systems are employed. The structure is as usual described in Lagrangian formulation, denoted as \mathbf{X} . The fluid domain is divided in two parts, which are described in Eulerian and ALE reference systems, denoted as \mathbf{x} and $\boldsymbol{\chi}$, respectively. For a detailed description of the reference systems the interested reader is referred to Wall [172] and Donea and Huerta [62].

2.2 Structure

This section contains a brief introduction to basic structural continuum equations. The field of structural mechanics is covered by a huge amount of literature. For a detailed explanation of structural mechanics the reader is referred to the classical textbooks, for example, by Crisfield [54, 55], Wriggers [179] and Zienkiewicz and Taylor [183].

2.2.1 Kinematics

A structural deformation is mostly described in Lagrangian or material formulation. To describe the deformation of a structure two frames of reference have to be introduced. The reference or initial configuration Ω_0^s describes the domain occupied by all material points \mathbf{X} at the time $t = 0$. On the other hand, the current configuration Ω_t^s denotes the momentary position \mathbf{x} at an arbitrarily time t . The displacement \mathbf{d}^s in current configuration is then defined as

$$\mathbf{d}^s = \mathbf{x} - \mathbf{X}. \quad (2.1)$$

The deformation gradient tensor \mathbf{F} relates a line element $d\mathbf{X}$ in the reference configuration \mathbf{X} to a line element $d\mathbf{x}$ in current configuration \mathbf{x} as

$$d\mathbf{x} = \mathbf{F}d\mathbf{X}. \quad (2.2)$$

The deformation gradient \mathbf{F} can be split into a volume-preserving rigid body motion part \mathbf{R} (an orthogonal rotation tensor), and a volume-changing stretch part \mathbf{U} , the so-called stretch tensor, as

$$\mathbf{F} = \mathbf{R} \cdot \mathbf{U}. \quad (2.3)$$

The symmetric right Cauchy-Green tensor \mathbf{C} is defined as

$$\mathbf{C} = \mathbf{F}^T \cdot \mathbf{F} = \mathbf{U}^T \cdot \mathbf{R}^T \cdot \mathbf{R} \cdot \mathbf{U} = \mathbf{U}^T \cdot \mathbf{U}, \quad (2.4)$$

which does not contain the rotational part of the deformation any more. It describes the mapping of the squares of the line elements between reference and current configuration

$$d\mathbf{x} \cdot d\mathbf{x} = d\mathbf{X} \cdot \mathbf{C} \cdot d\mathbf{X}. \quad (2.5)$$

The Green-Lagrange strain tensor is a very common strain measure in nonlinear solid mechanics. It is defined as

$$\mathbf{E} = \frac{1}{2}(\mathbf{F}^T \cdot \mathbf{F} - \mathbf{I}), \quad (2.6)$$

in the reference configuration. The Green-Lagrange strain tensor \mathbf{E} is $\mathbf{0}$ in the undeformed configuration.

2.2.2 Constitutive equation

The second Piola-Kirchhoff stress tensor \mathbf{S} is defined as

$$\mathbf{S} = (\det \mathbf{F}) \mathbf{F}^{-1} \cdot \boldsymbol{\sigma}^s \cdot \mathbf{F}^{-T}, \quad (2.7)$$

where $\boldsymbol{\sigma}^s$ defines the physical Cauchy stresses of the structure. In this work, hyper-elastic materials are used, which implies the existence of a strain-energy function Ψ . A formulation of hyper-elastic materials reads as

$$\mathbf{S} = 2 \frac{\partial \Psi}{\partial \mathbf{C}} = \frac{\partial \Psi}{\partial \mathbf{E}}. \quad (2.8)$$

Particularly, in the present work, the St.-Venant-Kirchhoff and Neo-Hookean materials are employed. The former describes a linear relation between \mathbf{S} and \mathbf{F} , while for a Neo-Hookean

material a nonlinear stress-strain relationship is obtained. The St.-Venant-Kirchhoff material is based on a quadratic strain energy function

$$\Psi_{\text{svk}} = \frac{\lambda^s}{2} (\text{tr } \mathbf{E})^2 + \mu^s \mathbf{E} : \mathbf{E}, \quad (2.9)$$

with λ^s and μ^s representing the Lamé parameters, which are related with the Young's modulus E and Poisson's ratio ν^s via

$$\lambda^s = \frac{E\nu^s}{(1 + \nu^s)(1 - 2\nu^s)} \quad (2.10)$$

and

$$\mu^s = \frac{E}{2(1 + \nu^s)}. \quad (2.11)$$

The strain-energy function for the Neo-Hookean materials is given as

$$\Psi_{\text{NH}} = \frac{\mu^s}{2} (\text{tr } \mathbf{C} - 3) - \mu^s \ln J + \frac{\lambda^s}{2} (\ln J)^2 \quad (2.12)$$

with J defined as determinant of the deformation gradient tensor, $J = \det \mathbf{F}$.

2.2.3 Balance of linear momentum

The dynamic equilibrium at a structural point in reference configuration is defined as

$$\rho^s \ddot{\mathbf{d}}^s - \text{Div}(\mathbf{F}\mathbf{S}) = \rho^s \mathbf{b}^s \quad \text{in } \Omega_0^s \times (0, T), \quad (2.13)$$

where $\ddot{\mathbf{d}}^s = \frac{d^2 \mathbf{d}^s}{dt^2}$ is the second material time derivative in the Lagrangian reference system. The equation (2.13) states an equilibrium between the forces of inertia, internal forces, and an external body force \mathbf{b}^s in the undeformed structure configuration Ω_0^s . Hereby, ρ^s denotes the structural density defined per unit undeformed volume and Div the divergence in the Lagrangian reference system. The primary unknown is the structural displacement \mathbf{d}^s . The internal forces are defined in terms of Piola-Kirchhoff stress tensor \mathbf{S} (2.7) and the deformation gradient \mathbf{F} (2.3). As initial condition at $t = 0$ the initial structural displacement and its first material time derivative, the velocity, have to be employed

$$\mathbf{d}^s(t = 0) = \mathbf{d}_0^s, \quad \dot{\mathbf{d}}^s(t = 0) = \dot{\mathbf{d}}_0^s \quad \text{in } \Omega_0^s. \quad (2.14)$$

The boundary conditions are decomposed into Dirichlet and Neumann boundary conditions, denoted as $\partial\Omega_D^s$ and $\partial\Omega_N^s$, respectively. The applied boundary conditions are given as

$$\mathbf{d}^s = \bar{\mathbf{d}}^s \quad \text{on } \partial\Omega_D^s \times (0, T), \quad (2.15)$$

$$(\mathbf{F}\mathbf{S}) \cdot \mathbf{N}^s = \bar{\mathbf{h}}^s \quad \text{on } \partial\Omega_N^s \times (0, T), \quad (2.16)$$

where $\bar{\mathbf{h}}^s$ is the traction vector and \mathbf{N}^s denotes the normal vector. Furthermore, the prescribed Dirichlet values are denoted as $\bar{\mathbf{d}}^s$. In the material configuration, the mass conservation is always fulfilled and will not be considered any further. The balance of linear momentum together with the constitutive equation and the kinematic equation define a system of coupled nonlinear partial differential equation of hyper-elastic structure dynamics.

2.2.4 Weak formulation

In order to derive a finite element approximation of the structural systems of equations, a weak form is required. After multiplication of balance of linear momentum (2.13) with the virtual displacements $\delta \mathbf{d}^s$ and integration by parts, the weak form can be stated as:

Find $\mathbf{d}^s \in \mathcal{W}_d$ such that for all $\delta \mathbf{d}^s \in \mathcal{V}_d$ holds

$$(\delta \mathbf{d}^s, \rho^s \ddot{\mathbf{d}}^s)_{\Omega^s} + (\text{Grad } \delta \mathbf{d}^s, \mathbf{FS})_{\Omega^s} = (\delta \mathbf{d}^s, \rho^s \mathbf{b}^s)_{\Omega^s} + \langle \delta \mathbf{d}^s, \bar{\mathbf{h}}^s \rangle_{\partial \Omega_N^s}. \quad (2.17)$$

The solution spaces and the corresponding test function spaces are defined as

$$\mathcal{W}_d := \{ \mathbf{d}^s \in [\mathbf{H}^1(\Omega^s)]^3 \mid \mathbf{d}^s|_{\partial \Omega_D^s} = \bar{\mathbf{d}}^s \}, \quad (2.18)$$

$$\mathcal{V}_d := \{ \delta \mathbf{d}^s \in [\mathbf{H}^1(\Omega^s)]^3 \mid \delta \mathbf{d}^s|_{\partial \Omega_D^s} = \mathbf{0} \}. \quad (2.19)$$

By $(\cdot, \cdot)_{\Omega^s}$ and $\langle \cdot, \cdot \rangle_{\partial \Omega_N^s}$, the standard inner products over the reference domain and Neumann part of the boundary are denoted.

2.2.5 Discretization

For the spatial discretization of the structural system the finite element method is applied. A large amount of literature is available on finite element methods in structural mechanics. Some examples are Hughes [109] and Zienkiewicz and Taylor [183]. The weak form (2.17) is discretized in space by replacing the unknown field \mathbf{d}^s , the virtual displacement $\delta \mathbf{d}^s$ and the second material time derivative $\ddot{\mathbf{d}}^s$ by

$$\mathbf{d}_h^s(\mathbf{x}, t) = \sum_i^n N_i(\mathbf{x}) \mathbf{d}_i^s, \quad (2.20)$$

$$\delta \mathbf{d}_h^s(\mathbf{x}, t) = \sum_i^n N_i(\mathbf{x}) \delta \mathbf{d}_i^s, \quad (2.21)$$

$$\ddot{\mathbf{d}}_h^s(\mathbf{x}, t) = \sum_i^n N_i(\mathbf{x}) \ddot{\mathbf{d}}_i^s. \quad (2.22)$$

Hereby, the nodal values \mathbf{d}_i^s , $\delta \mathbf{d}_i^s$ and $\ddot{\mathbf{d}}_i^s$ from the corresponding discrete formulation spaces are interpolated by the trilinear shape functions $N_i(\mathbf{x})$ with n denoting the overall number of nodes. In the present work, eight-noded trilinear hexahedral (hex8) solid elements are used. Introducing the discrete approximations (2.20) into the weak form results in the following semi-discrete system of nonlinear differential equation in matrix notation

$$\mathbf{M}^s \ddot{\mathbf{d}}^s + \mathbf{F}_{\text{int}}^s(\mathbf{d}^s) - \mathbf{F}_{\text{ext}}^s = \mathbf{0}, \quad (2.23)$$

where \mathbf{M}^s denotes the structural mass matrix and $\mathbf{F}_{\text{int}}^s$ represents the nonlinear vector of internal forces, as it depends on the current displacement. Furthermore, the vector of external forces is denoted by $\mathbf{F}_{\text{ext}}^s$. For the time discretization of the structural system finite difference schemes are applied to the semi-discrete system (2.23). Particularly, the generalized- α method based on

a Newmark method is employed. The generalized- α scheme shifts the time point at which the discretized equations are evaluated to a generalized mid-point. While the Newmark method evaluates the discrete equation at the time point t^{n+1} , the generalized- α makes use of the intermediate points $t^{n+1-\alpha_f}$ and $t^{n+1-\alpha_m}$. The nodal displacements and the velocities at the new time step t^{n+1} are approximated by

$$\dot{\mathbf{d}}^{s,n+1} = \frac{\gamma}{\beta\Delta t}(\mathbf{d}^{s,n+1} - \mathbf{d}^{s,n}) - \frac{\gamma - \beta}{\beta}\dot{\mathbf{d}}^{s,n} - \frac{\gamma - 2\beta}{2\beta}\Delta t\ddot{\mathbf{d}}^{s,n}, \quad (2.24)$$

$$\ddot{\mathbf{d}}^{s,n+1} = \frac{1}{\beta\Delta t^2}(\mathbf{d}^{s,n+1} - \mathbf{d}^{s,n}) - \frac{1}{\beta\Delta t}\dot{\mathbf{d}}^{s,n} - \frac{1 - 2\beta}{2\beta}\ddot{\mathbf{d}}^{s,n}, \quad (2.25)$$

with the parameters $\gamma \in [0, 1]$ and $\beta \in [0, \frac{1}{2}]$. The displacements, the velocities and the accelerations, at mid-points are linear interpolations of the corresponding start and end vectors. They are defined as

$$\mathbf{d}^{s,n+1-\alpha_f} = (1 - \alpha_f)\mathbf{d}^{s,n+1} + \alpha_f\mathbf{d}^{s,n}, \quad (2.26)$$

$$\dot{\mathbf{d}}^{s,n+1-\alpha_f} = (1 - \alpha_f)\dot{\mathbf{d}}^{s,n+1} + \alpha_f\dot{\mathbf{d}}^{s,n}, \quad (2.27)$$

$$\ddot{\mathbf{d}}^{s,n+1-\alpha_m} = (1 - \alpha_m)\ddot{\mathbf{d}}^{s,n+1} + \alpha_m\ddot{\mathbf{d}}^{s,n}, \quad (2.28)$$

with the parameters $\alpha_f, \alpha_m \in [0, 1]$. The nonlinear equation of motion at the generalized mid-points becomes

$$\mathbf{M}^s\ddot{\mathbf{d}}^{s,n+1-\alpha_m} + \mathbf{F}_{\text{int}}^s(\mathbf{d}^{s,n+1-\alpha_f}) - \mathbf{F}_{\text{ext}}^{s,n+1-\alpha_f} = 0, \quad (2.29)$$

with

$$\mathbf{F}_{\text{ext}}^{s,n+1-\alpha_f} = (1 - \alpha_f)\mathbf{F}_{\text{ext}}^{s,n+1} + \alpha_f\mathbf{F}_{\text{ext}}^{s,n}. \quad (2.30)$$

2.2.6 Linearization

In order to solve the nonlinear system (2.29) using a Newton-Raphson method, the nodal forces $\mathbf{F}_{\text{int}}^s(\mathbf{d}^{s,n+1-\alpha_f})$, which are nonlinear in the displacements $\mathbf{d}^{s,n+1}$, e.g. in the case of using nonlinear material law, need to be linearized. The nonlinear discretized equation (2.29) evaluated at the generalized mid-point in residual form can be written as

$$\mathbf{r}^s(\mathbf{d}^{s,n+1}) = \mathbf{M}^s\ddot{\mathbf{d}}^{s,n+1-\alpha_m} + \mathbf{F}_{\text{int}}^s(\mathbf{d}^{s,n+1-\alpha_f}) - \mathbf{F}_{\text{ext}}^{s,n+1-\alpha_f} = 0. \quad (2.31)$$

Using Taylor expansion, the nonlinear residual is linearized at the end of time step at t^{n+1} as

$$\mathbf{r}^s(\mathbf{d}_{i+1}^{s,n+1}) = 0 = \mathbf{r}^s(\mathbf{d}_i^{s,n+1}) + \left. \frac{\partial \mathbf{r}^s(\mathbf{d}^{s,n+1})}{\partial \mathbf{d}^{s,n+1}} \right|_i \Delta \mathbf{d}_{i+1}^{s,n+1} + \text{h.o.t.} \quad (2.32)$$

Omitting the higher order terms (h.o.t.), the linear system

$$\left. \frac{\partial \mathbf{r}^s(\mathbf{d}^{s,n+1})}{\partial \mathbf{d}^{s,n+1}} \right|_i \Delta \mathbf{d}_{i+1}^{s,n+1} = -\mathbf{r}^s(\mathbf{d}_i^{s,n+1}) \quad (2.33)$$

is obtained, with $\Delta \mathbf{d}_{i+1}^{s,n+1}$ as unknowns. The matrix formulation of the linear system (2.33) reads as

$$\left[\mathbf{S} \right]_i^{n+1} \left[\Delta \mathbf{d}^s \right]_{i+1}^{n+1} = - \left[\mathbf{r}^s \right]_i^{n+1}. \quad (2.34)$$

After solving (2.34) for the displacement increments $\Delta \mathbf{d}_{i+1}^{s,n+1}$ in every iteration, the new displacements at iteration step $i + 1$ are updated as

$$\mathbf{d}_{i+1}^{s,n+1} = \mathbf{d}_i^{s,n+1} + \Delta \mathbf{d}_{i+1}^{s,n+1}. \quad (2.35)$$

2.3 Fluid

Within this section, the basic fluid equations in Eulerian and ALE framework will be introduced. The topic of continuum fluid mechanics is a very broad field. The intention of this section is to present the equations and notations which will be used in the present work, rather than giving a full description of continuum fluid mechanics. For general textbooks of continuum fluid mechanics the reader is referred for example to the books of Ferziger and Peric [72] and Lai et al. [124]. A more detailed presentations of the fundamental equations can also be found in Wall [172] and Gravemeier [88]. More information on the description of flow on Arbitrary-Lagrangian-Eulerian (ALE) framework can be obtained in Donea and Huerta [62], Donea et al. [64] and Wall [172]. Important textbooks on finite element methods on flow problems are for example Donea and Huerta [62], Gresho and Sani [89] and Zienkiewicz et al. [184]. In this section a standard finite element formulation for incompressible flow will be derived.

2.3.1 Kinematics

The Eulerian description, which is mostly used in fluid mechanics, is presented in the following. The velocity \mathbf{u} is the primary kinematic unknown of a flow problem. The acceleration of a fluid particle is given by the materiel time derivative of the velocity, which appears in the momentum equation. It is expressed by a local time derivative and a convective term as

$$\frac{D\mathbf{u}}{Dt} = \frac{\partial\mathbf{u}}{\partial t}\Big|_{\mathbf{x}} = \frac{\partial\mathbf{u}}{\partial t}\Big|_{\mathbf{x}} + \mathbf{u} \cdot \nabla\mathbf{u}. \quad (2.36)$$

Moreover, the symmetric part of the gradient of the velocity is called strain rate tensor, which is defined as

$$\epsilon(\mathbf{u}) = \frac{1}{2}(\nabla\mathbf{u} + (\nabla\mathbf{u})^T), \quad (2.37)$$

with ∇ indicating the spatial derivatives with respect to fixed Eulerian framework \mathbf{x} .

2.3.2 Constitutive equation

The Cauchy stresses $\boldsymbol{\sigma}$ at a fluid point can be decomposed into the hydrostatic pressure p and the shear stress tensor $\boldsymbol{\tau}$

$$\boldsymbol{\sigma} = -p\mathbf{I} + \boldsymbol{\tau}. \quad (2.38)$$

The shear stress tensor $\boldsymbol{\tau} = f(\epsilon(\mathbf{u}))$ is a function of strain rate tensor. For a Newtonian flow the function $f(\epsilon(\mathbf{u}))$ is considered as a linear function. The constitutive equation is then defined as

$$\boldsymbol{\sigma} = -p\mathbf{I} + 2\mu\epsilon(\mathbf{u}), \quad (2.39)$$

where μ denotes the dynamic viscosity, which is equal to kinematic viscosity times fluid mass density $\mu = \nu\rho^f$. Furthermore, the kinematic pressure is defined as

$$p_{\text{kin}} = \frac{p}{\rho^f}. \quad (2.40)$$

2.3.3 Conservation of mass

A fundamental law of Newtonian mechanics is the conservation of mass contained in a material volume. For the incompressible fluid, where the density ρ^f is considered as a constant, the rate of the mass change should be directly related to the inflow and outflow boundaries, if no mass sources or sinks are present. This relation is given as

$$\int_{\Gamma} \mathbf{u} \cdot \mathbf{n}^f \, d\Gamma = 0, \quad (2.41)$$

where \mathbf{n}^f denotes the outward pointing normal of the boundary. The mass balance also terms the continuity equation in the fluid domain Ω^f , which is defined as

$$\nabla \cdot \mathbf{u} = 0 \quad \text{in} \quad \Omega^f \times (0, T). \quad (2.42)$$

2.3.4 Conservation of linear momentum

The balance of the linear momentum at a fluid particle inside the fluid domain Ω^f in Eulerian description is given by

$$\rho^f \frac{\partial \mathbf{u}}{\partial t} \Big|_{\mathbf{x}} + \rho^f \mathbf{u} \cdot \nabla \mathbf{u} = \nabla \cdot \boldsymbol{\sigma} + \rho^f \mathbf{b}^f \quad \text{in} \quad \Omega^f \times (0, T), \quad (2.43)$$

where \mathbf{b}^f denotes the body force. Inserting the constitutive equation (2.39) results in the Eulerian formulation of the momentum balance of the transient incompressible Navier-Stokes equations in the convective form

$$\rho^f \frac{\partial \mathbf{u}}{\partial t} \Big|_{\mathbf{x}} + \rho^f \mathbf{u} \cdot \nabla \mathbf{u} + \nabla p - 2\mu \nabla \cdot \boldsymbol{\epsilon}(\mathbf{u}) = \rho^f \mathbf{b}^f \quad \text{in} \quad \Omega^f \times (0, T), \quad (2.44)$$

with the strain rate tensor defined in (2.37).

2.3.5 Incompressible Navier-Stokes equations

The linear momentum (2.44) together with the conservation of mass (2.42) result in the transient nonlinear incompressible Navier-Stokes equations in Eulerian description

$$\rho^f \frac{\partial \mathbf{u}}{\partial t} \Big|_{\mathbf{x}} + \rho^f \mathbf{u} \cdot \nabla \mathbf{u} + \nabla p - 2\mu \nabla \cdot \boldsymbol{\epsilon}(\mathbf{u}) = \rho^f \mathbf{b}^f \quad \text{in} \quad \Omega^f \times (0, T), \quad (2.45)$$

$$\nabla \cdot \mathbf{u} = 0 \quad \text{in} \quad \Omega^f \times (0, T). \quad (2.46)$$

The unknown fields are the velocity field \mathbf{u} and the pressure p . For the Navier-Stokes equations appropriate initial and boundary conditions have to be prescribed. As an initial condition a velocity field in initial fluid domain Ω_0^f

$$\mathbf{u}(t = 0) = \mathbf{u}^0 \quad \text{in} \quad \Omega_0^f \quad (2.47)$$

is required, which has to satisfy $\nabla \cdot \mathbf{u} = 0$ to achieve a well posed problem. For the pressure field there is no initial condition, as it rather acts like a Lagrange multiplier for the incompressibility condition. Thus, the role of the pressure is to adjust itself to satisfy the incompressibility

condition. The fluid boundary is split into Dirichlet and Neumann boundaries, indicated as $\partial\Omega_D^f$ and $\partial\Omega_N^f$, respectively. The boundary conditions on $\partial\Omega_D^f$ and $\partial\Omega_N^f$ are given as

$$\mathbf{u} = \bar{\mathbf{u}} \quad \text{on} \quad \partial\Omega_D^f \times (0, T), \quad (2.48)$$

$$\boldsymbol{\sigma} \cdot \mathbf{n}^f = \bar{\mathbf{h}} \quad \text{on} \quad \partial\Omega_N^f \times (0, T), \quad (2.49)$$

where $\bar{\mathbf{u}}$ denotes the prescribed velocity field, $\bar{\mathbf{h}}$ the traction vector and \mathbf{n}^f the outward pointing normal of the boundary.

2.3.6 ALE form of the incompressible Navier-Stokes equations

In this section, the incompressible Navier-Stokes equations will be introduced in Arbitrary-Lagrangian-Eulerian (ALE) description. For further discussion of the solution of the Navier-Stokes equations on an ALE mesh the reader is referred to Förster [73].

In a fluid-structure interaction (FSI) problem one has to deal with moving boundaries and changing domain. Hereby, the structural equations are given in Lagrangian formulation and, thus, can track the motion of the interface. In ALE-based FSI approaches this problem is solved by defining the fluid domain in ALE formulation, where the fluid mesh follows the movement of the boundary but it is not attached to the motion of the fluid particles inside the fluid domain Ω^f . This approach can be traced to the early works of Hirt et al. [104], Belytschko and Kennedy [25], Belytschko et al. [23], Hughes et al. [108] and Donea et al. [63].

Following Förster [73], the spatial coordinates of a particular point in $\mathbf{x} \in \Omega^f$ are given by a unique mapping

$$\mathbf{x} = \varphi(\boldsymbol{\chi}, t), \quad t \in (0, T) \quad (2.50)$$

where $\boldsymbol{\chi}$ denotes the reference system, which tracks the moving boundaries but moves arbitrarily inside the fluid domain. To derive the Navier-Stokes equations in ALE framework, the material time derivative should be expressed with respect to the deforming reference system. The material time derivative of $f(\mathbf{x}(\boldsymbol{\chi}, t), t)$ after applying the chain rule results in

$$\frac{Df}{Dt} = \left. \frac{\partial f(\boldsymbol{\chi}, t)}{\partial t} \right|_{\boldsymbol{\chi}} + \frac{\partial f(\boldsymbol{\chi}, t)}{\partial \boldsymbol{\chi}} \frac{\partial \boldsymbol{\chi}}{\partial t} \Big|_{\mathbf{x}} = \left. \frac{\partial f(\boldsymbol{\chi}, t)}{\partial t} \right|_{\boldsymbol{\chi}} + \frac{\partial f(\mathbf{x}, t)}{\partial \mathbf{x}} \frac{\partial \mathbf{x}}{\partial \boldsymbol{\chi}} \frac{\partial \boldsymbol{\chi}}{\partial t} \Big|_{\mathbf{x}}. \quad (2.51)$$

Assuming that f is equal to the spatial coordinate \mathbf{x} , then the material time derivative, i.e. the temporal change of the spatial position of a material point is the velocity \mathbf{u} . Considering (2.50) the velocity reads as

$$\mathbf{u} = \frac{D\mathbf{x}}{Dt} = \left. \frac{\partial \mathbf{x}(\boldsymbol{\chi}, t)}{\partial t} \right|_{\boldsymbol{\chi}} + \frac{\partial \mathbf{x}(\boldsymbol{\chi}, t)}{\partial \boldsymbol{\chi}} \frac{\partial \boldsymbol{\chi}}{\partial t} \Big|_{\mathbf{x}}. \quad (2.52)$$

The first term of (2.52), which denotes the temporal change of the spatial position of a reference point, is identified as the velocity of the reference system \mathbf{u}^g . Using the both equations (2.51) and (2.52) one can derive the ALE expression of the material time derivative of a function f as

$$\frac{Df}{Dt} = \left. \frac{\partial f(\boldsymbol{\chi}, t)}{\partial t} \right|_{\boldsymbol{\chi}} + (\mathbf{u} - \mathbf{u}^g) \cdot \nabla f. \quad (2.53)$$

The *ALE convective velocity* \mathbf{c} can now be introduced as the difference of the material velocity and the mesh velocity

$$\mathbf{c} = \mathbf{u} - \mathbf{u}^g. \quad (2.54)$$

The equation (2.53) is also named as *fundamental ALE equation* and denotes that the material time derivative of a quantity f is equal to the temporal change of f in the reference system χ and the transport of f due to a relative motion of the system expressed by a convective term. Using the fundamental ALE equation (2.53) an ALE formulation of the momentum balance equation (2.44) can be derived as

$$\rho^f \frac{\partial \mathbf{u}}{\partial t} \Big|_{\chi} + \rho^f \mathbf{c} \cdot \nabla \mathbf{u} = \nabla \cdot \boldsymbol{\sigma} + \rho^f \mathbf{b}^f \quad \text{in } \Omega^f \times (0, T). \quad (2.55)$$

In the ALE version of the linear momentum equation all spatial derivatives refer to the Eulerian system \mathbf{x} and the only quantity described in the reference system χ is the time derivative. The linear momentum (2.55) together with conservation of mass (2.42) result in the transient incompressible Navier-Stokes equations in ALE description

$$\rho^f \frac{\partial \mathbf{u}}{\partial t} \Big|_{\chi} + \rho^f \mathbf{c} \cdot \nabla \mathbf{u} + \nabla p - 2\mu \nabla \cdot \boldsymbol{\epsilon}(\mathbf{u}) = \rho^f \mathbf{b}^f \quad \text{in } \Omega^f \times (0, T), \quad (2.56)$$

$$\nabla \cdot \mathbf{u} = 0 \quad \text{in } \Omega^f \times (0, T). \quad (2.57)$$

2.3.7 Weak formulation

The weak formulation is obtained by multiplication of the strong form with appropriate test functions for velocity and pressure leading to the weighted residual. The weighted residual is integrated over the domain Ω^f . A sequenced partial integration results in a final weak form of the problem. The idea is to reduce the required order of differentiability for the solution fields and fulfill the equations in an integral sense. The weak form of the incompressible Navier-Stokes equation in Eulerian description after integration by parts, becomes

$$\begin{aligned} (\mathbf{v}, \rho^f \frac{\partial \mathbf{u}}{\partial t})_{\Omega^f} + (\mathbf{v}, \rho^f \mathbf{u} \cdot \nabla \mathbf{u})_{\Omega^f} + (q, \nabla \cdot \mathbf{u})_{\Omega^f} - (\nabla \cdot \mathbf{v}, p)_{\Omega^f} \\ + (\boldsymbol{\epsilon}(\mathbf{v}), 2\mu \boldsymbol{\epsilon}(\mathbf{u}))_{\Omega^f} = (\mathbf{v}, \rho^f \mathbf{b}^f)_{\Omega^f} + \langle \mathbf{v}, \bar{\mathbf{h}} \rangle_{\partial \Omega_N^f}, \end{aligned} \quad (2.58)$$

which is the base of spatial discretization as it will be discussed later in this section. It has to be pointed out that the sign of the weighted continuity equation $(q, \nabla \cdot \mathbf{u})_{\Omega^f}$ can be chosen arbitrarily. In (2.58), for stability reasons the sign is chosen opposite to the term $-(\nabla \cdot \mathbf{v}, p)_{\Omega^f}$. Similar to (2.58), the weak formulation of the Navier-Stokes equations in ALE formulation is given as

$$\begin{aligned} (\mathbf{v}, \rho^f \frac{\partial \mathbf{u}}{\partial t})_{\Omega^f} + (\mathbf{v}, \rho^f \mathbf{c} \cdot \nabla \mathbf{u})_{\Omega^f} + (q, \nabla \cdot \mathbf{u})_{\Omega^f} - (\nabla \cdot \mathbf{v}, p)_{\Omega^f} \\ + (\boldsymbol{\epsilon}(\mathbf{v}), 2\mu \boldsymbol{\epsilon}(\mathbf{u}))_{\Omega^f} = (\mathbf{v}, \rho^f \mathbf{b}^f)_{\Omega^f} + \langle \mathbf{v}, \bar{\mathbf{h}} \rangle_{\partial \Omega_N^f}. \end{aligned} \quad (2.59)$$

The trial space for the velocity and pressure are defined by

$$\mathcal{W}_u := \{ \mathbf{u} \in [\mathbf{H}^1(\Omega^f)]^3 \mid \mathbf{u}|_{\partial \Omega_D^f} = \bar{\mathbf{u}} \}, \quad (2.60)$$

$$\mathcal{W}_p := \mathbf{L}^2(\Omega^f). \quad (2.61)$$

In the case of a pure Dirichlet problem, i.e. if $\partial\Omega^f = \partial\Omega_D^f$ the pressure is defined up to a constant. In this case, the trial space for pressure changes to $L^2(\Omega^f)/\mathbb{R}$. The corresponding weighting functions are defined as

$$\mathcal{V}_u := \{\mathbf{v} \in [\mathbf{H}^1(\Omega^f)]^3 \mid \mathbf{v}|_{\partial\Omega_D^f} = \mathbf{0}\}, \quad (2.62)$$

$$\mathcal{V}_p := L^2(\Omega^f). \quad (2.63)$$

Hereby, for the integrals the usual notations for inner products, i.e. $(f, g)_{\Omega^f} = \int_{\Omega^f} f(x)g(x)d\Omega^f$ and $\langle f, g \rangle_{\partial\Omega_N^f} = \int_{\partial\Omega_N^f} f(x)g(x)dx$, are used.

2.3.8 Discretization

The incompressible Navier-Stokes equations need to be discretized in space and time. In the presented work, the finite element method is employed for the discretization of fluid equations in space and the finite difference method for the discretization in time. For the time discretization, the one-step- θ method is considered. The one-step- θ method applied to the general first order ordinary differential equation $\dot{y} = f(y, t)$ can be stated as

$$\frac{y^{n+1} - y^n}{\Delta t} = \theta f(y^{n+1}, t^{n+1}) + (1 - \theta)f(y^n, t^n), \quad (2.64)$$

where Δt denotes the time step and θ the one-step- θ parameter. For $\theta = 1$ the backward Euler scheme is obtained, for $\theta = 0$ the forward Euler scheme and for $\theta = \frac{1}{2}$ the trapezoidal rule or Crank-Nicolson scheme. While the backward Euler and forward Euler scheme are first order accurate, the Crank-Nicolson scheme is a second order accurate scheme and free of any spurious damping. Applying the one-step- θ scheme (2.64) to the weak form (2.58) it yields

$$\begin{aligned} & \left(\mathbf{v}, \frac{\rho^f}{\Theta} \mathbf{u}\right)_{\Omega^f} + \left(\mathbf{v}, \rho^f \mathbf{u} \cdot \nabla \mathbf{u}\right)_{\Omega^f} + \left(q, \nabla \cdot \mathbf{u}\right)_{\Omega^f} \\ & \quad - \left(\nabla \cdot \mathbf{v}, p\right)_{\Omega^f} + \left(\boldsymbol{\epsilon}(\mathbf{v}), 2\mu \boldsymbol{\epsilon}(\mathbf{u})\right)_{\Omega^f} \\ & = \left(\mathbf{v}, \frac{\rho^f}{\Theta} \mathbf{u}^{\text{hist}}\right)_{\Omega^f} + \langle \mathbf{v}, \bar{\mathbf{h}} \rangle_{\partial\Omega_N^f} + \left(\mathbf{v}, \rho^f \mathbf{b}^f\right)_{\Omega^f}, \end{aligned} \quad (2.65)$$

with $\Theta = \Delta t \theta$ denoting the time factor. In (2.65), to shorten the notation the index $n + 1$ is omitted. Furthermore, the history value \mathbf{u}^{hist} is defined as

$$\mathbf{u}^{\text{hist}} = \mathbf{u}^n + \Delta t(1 - \theta)\dot{\mathbf{u}}^n. \quad (2.66)$$

For the spatial discretization the standard (Bubnov-)Galerkin scheme is applied with the corresponding discrete spaces denoted as V_h and Q_h . In this work, for the finite element discretization, trilinear eight-noded hexahedral elements for velocity and pressure are used. To discretize the fluid, the same shape functions for both velocity and pressure fields are applied. The discretized velocity and pressure fields, \mathbf{u}_h and p_h , are given as

$$\mathbf{u}_h(\mathbf{x}) = \sum_i^n N_i(\mathbf{x})\mathbf{u}_i, \quad (2.67)$$

$$p_h(\mathbf{x}) = \sum_i^n N_i(\mathbf{x})p_i, \quad (2.68)$$

and the corresponding discrete test functions \mathbf{v}_h and q_h

$$\mathbf{v}_h(\mathbf{x}) = \sum_i^n N_i(\mathbf{x}) \mathbf{v}_i, \quad (2.69)$$

$$q_h(\mathbf{x}) = \sum_i^n N_i(\mathbf{x}) q_i. \quad (2.70)$$

Hereby, the values \mathbf{u} , p , \mathbf{v} and q are discretized by the trilinear shape functions $N_i(\mathbf{x})$ with n denoting the number of overall nodes. The discrete values are now applied to the semi-discrete weak formulation (2.65), resulting in a discrete formulation defined as:

Find $(\mathbf{u}_h, p_h) \in V_h \times Q_h$ such that $\forall (\mathbf{v}_h, q_h) \in V_h \times Q_h$ holds

$$\begin{aligned} & (\mathbf{v}_h, \frac{\rho^f}{\Theta} \mathbf{u}_h)_{\Omega^f} + (\mathbf{v}_h, \rho^f \mathbf{u}_h \cdot \nabla \mathbf{u}_h)_{\Omega^f} + (q_h, \nabla \cdot \mathbf{u}_h)_{\Omega^f} \\ & - (\nabla \cdot \mathbf{v}_h, p_h)_{\Omega^f} + (\boldsymbol{\epsilon}(\mathbf{v}_h), 2\mu \boldsymbol{\epsilon}(\mathbf{u}_h))_{\Omega^f} \\ & = \langle \mathbf{v}_h, \bar{\mathbf{h}} \rangle_{\partial\Omega_N^f} + (\mathbf{v}_h, \rho^f \mathbf{b}^f)_{\Omega^f} + (\mathbf{v}_h, \frac{\rho^f}{\Theta} \mathbf{u}_h^{\text{hist}})_{\Omega^f}. \end{aligned} \quad (2.71)$$

Moreover, the discrete residual terms in Eulerian formulation

$$\begin{aligned} R_{\mathbf{x},u}^{\text{std}}(\mathbf{u}_h, p_h) & := (\mathbf{v}_h, \frac{\rho^f}{\Theta} \mathbf{u}_h)_{\Omega^f} + (\mathbf{v}_h, \rho^f \mathbf{u}_h \cdot \nabla \mathbf{u}_h)_{\Omega^f} - (\nabla \cdot \mathbf{v}_h, p_h)_{\Omega^f} \\ & + (\boldsymbol{\epsilon}(\mathbf{v}_h), 2\mu \boldsymbol{\epsilon}(\mathbf{u}_h))_{\Omega^f} - \langle \mathbf{v}_h, \bar{\mathbf{h}} \rangle_{\partial\Omega_N^f} - (\mathbf{v}_h, \rho^f \mathbf{b}^f)_{\Omega^f} \\ & - (\mathbf{v}_h, \frac{\rho^f}{\Theta} \mathbf{u}_h^{\text{hist}})_{\Omega^f}, \end{aligned} \quad (2.72)$$

$$R_{\mathbf{x},p}^{\text{std}}(\mathbf{u}_h, p_h) := (q_h, \nabla \cdot \mathbf{u}_h)_{\Omega^f}, \quad (2.73)$$

are introduced. Linearization of (2.72) and (2.73) with respect to the unknowns \mathbf{u}_h and p_h , results in the contributions of the linearized system as it will be shown in Section 2.3.10. The resulting discrete nonlinear system can be written in matrix notation as

$$\frac{1}{\Theta} \mathbf{M}^F \mathbf{u}^{n+1} + [\mathbf{C}^F(\mathbf{u}) + \mathbf{K}^F] \mathbf{u}^{n+1} + \mathbf{G}^F \mathbf{p}^{n+1} = \mathbf{f}_b^F + \mathbf{f}_N^F + \mathbf{f}_{\text{hist}}^F, \quad (2.74)$$

$$-(\mathbf{G}^F)^T \mathbf{u}^{n+1} = 0. \quad (2.75)$$

The vectors of velocity and pressure unknowns at the time step t^{n+1} are denoted as \mathbf{u}^{n+1} and \mathbf{p}^{n+1} , respectively. The matrices \mathbf{M}^F , \mathbf{C}^F , \mathbf{K}^F , \mathbf{G}^F and $(\mathbf{G}^F)^T$ refer to mass matrix, convective matrix, viscous matrix, gradient operator and discrete divergence operator, respectively. The terms at the right side of (2.74) refer to the body forces, Neumann conditions and the values from the time step t^n .

The ALE formulation of the semi-discrete form of the Navier-Stokes equation differs from (2.71) in the convective term, which is defined in ALE formulation as

$$(\mathbf{v}_h, \rho^f \mathbf{c}_h \cdot \nabla \mathbf{u}_h)_{\Omega^f}. \quad (2.76)$$

Accordingly, the discrete residual term in ALE formulation are defined as

$$\begin{aligned} R_{\mathcal{X},u}^{\text{std}}(\mathbf{u}_h, p_h) &:= (\mathbf{v}_h, \frac{\rho^f}{\Theta} \mathbf{u}_h)_{\Omega^f} + (\mathbf{v}_h, \rho^f \mathbf{c}_h \cdot \nabla \mathbf{u}_h)_{\Omega^f} - (\nabla \cdot \mathbf{v}_h, p_h)_{\Omega^f} \\ &\quad + (\boldsymbol{\epsilon}(\mathbf{v}_h), 2\mu \boldsymbol{\epsilon}(\mathbf{u}_h))_{\Omega^f} - \langle \mathbf{v}_h, \bar{\mathbf{h}} \rangle_{\partial\Omega_N^f} - (\mathbf{v}_h, \rho^f \mathbf{b}^f)_{\Omega^f} \\ &\quad - (\mathbf{v}_h, \frac{\rho^f}{\Theta} \mathbf{u}_h^{\text{hist}})_{\Omega^f}, \end{aligned} \quad (2.77)$$

$$R_{\mathcal{X},p}^{\text{std}}(\mathbf{u}_h, p_h) := (q_h, \nabla \cdot \mathbf{u}_h)_{\Omega^f}. \quad (2.78)$$

2.3.9 Stabilization

The standard (Bubnov-)Galerkin scheme for incompressible flow suffers from two major instabilities, instability of convection-dominated flow and inf-sup instability in the case of equal order interpolations of velocity and pressure field. Different methods have been proposed to overcome these instabilities. A famous family of stabilization approaches are the residual-based methods. The well-known *Streamline-Upwind/Petrov-Galerkin (SUPG)* method, introduced by Brooks and Hughes [30], and *Pressure-Stabilizing/Petrov-Galerkin (PSPG)* method, by Hughes et al. [111] overcome the instabilities of standard Galerkin scheme. Furthermore, the interior penalty techniques of discontinuous Galerkin methods have been applied to continuous Galerkin methods leading to another class of stabilization methods, *edge-/face-oriented stabilization* schemes, introduced originally by Burman et al. [42]. These methods will be discussed in detail in Section 3.5. A comparison of these stabilization techniques and other methods as Local projection-based stabilization techniques (LPS), see e.g. Becker and Braack [18] and Braack and Burman [26], is given by Braack et al. [27]. In the following, the famous residual-based stabilizations will be presented.

The first type of instability is due to the presence of the convective term in the momentum equation. Such difficulties increase by convection dominated flow, i.e. for high values of the Reynolds number. In order to overcome this instability, the SUPG term

$$\sum_{\mathbf{e}} (\mathbf{u}_h \cdot \nabla \mathbf{v}_h, \tau^m \mathbf{r}_{\mathbf{x},h}^m)_{\Omega^f} \quad (2.79)$$

is added to the standard Galerkin terms. In (2.79), $\mathbf{r}_{\mathbf{x},h}^m$ represents the residual of the momentum equation in Eulerian description

$$\mathbf{r}_{\mathbf{x},h}^m = \rho^f \frac{\partial \mathbf{u}_h}{\partial t} \Big|_{\mathbf{x}} + \rho^f \mathbf{u}_h \cdot \nabla \mathbf{u}_h + \nabla p_h - 2\mu \nabla \cdot \boldsymbol{\epsilon}(\mathbf{u}_h) - \rho^f \mathbf{b}_h^f. \quad (2.80)$$

Furthermore, $\sum_{\mathbf{e}}$ denotes the sum of interior finite element domains. The stabilization parameter τ^m , which is inspired by Franca and Valentin [75] and Barrenechea and Valentin [12], is defined as

$$\tau^m = \frac{1}{\frac{1}{c_T \Delta t} \cdot \max(\xi_1, 1) + \frac{4\nu}{m_k h^2} \cdot \max(\xi_2, 1)}, \quad (2.81)$$

with

$$\xi_1 = \frac{4\nu c_T \Delta t}{m_k h^2}, \quad \xi_2 = \frac{m_k \|\mathbf{u}_h\| h}{2\nu}. \quad (2.82)$$

Hereby, m_k denotes a positive constant related to the element type (see Harari and Hughes [97]), and Δt and c_T denote the time step size and a constant depending on the numerical time-integration scheme (e.g. $c_T = \theta$ for one-step- θ), respectively. Moreover, the SUPG term in ALE framework reads as

$$\sum_e (c_h \cdot \nabla \mathbf{v}_h, \tau^m \mathbf{r}_{\mathbf{x},h}^m)_{\Omega^f} \quad (2.83)$$

with the residual of the momentum equation in ALE description defined as

$$\mathbf{r}_{\mathbf{x},h}^m = \rho^f \frac{\partial \mathbf{u}_h}{\partial t} \Big|_{\mathbf{x}} + \rho^f c_h \cdot \nabla \mathbf{u}_h + \nabla p_h - 2\mu \nabla \cdot \boldsymbol{\epsilon}(\mathbf{u}_h) - \rho^f \mathbf{b}_h^f. \quad (2.84)$$

The second numerical difficulty is the so-called *inf-sup* instability. The resulting matrix structure of the standard Galerkin (2.71) represents a saddle-point nature, due to the pressure field, which acts as a Lagrange multiplier term on the incompressibility constraint. Thus, a suitable choice of function spaces for velocity and pressure is necessary for the matrix to have a full rank. The requirement for such an appropriate choice is that the velocity and pressure spaces have to satisfy an inf-sup condition also named as *Ladyzhenskaya-Babuška-Brezzi* (LBB) condition, see Brezzi and Fortin [29]. To satisfy this condition, LBB-conforming finite elements have to be used. An example of stable velocity-pressure pairs are the Taylor-Hood elements, see Taylor and Hood [167]. If the choice of velocity and pressure spaces does not satisfy the inf-sup condition, this condition has to be circumvented, i.e. the standard Galerkin formulation needs to be stabilized. It has to be noted that the inf-sup instability appears for any Reynolds number. PSPG method, originally introduced by Hughes et al. [111], stabilizes the standard Galerkin scheme, by adding nonzero entries to the zero block of the system and eliminating the saddle-point structure of the system. A combination of residual-based stabilizations SUPG/PSPG in application of Navier-Stokes equations was introduced by Tezduyar et al. [168]. The PSPG stabilization term is defined as

$$\sum_e (\nabla q_h, \tau^m \mathbf{r}_{\mathbf{x},h}^m)_{\Omega^f}, \quad (2.85)$$

with the residual of the momentum equation given in (2.80), or as

$$\sum_e (\nabla q_h, \tau^m \mathbf{r}_{\mathbf{x},h}^m)_{\Omega^f}, \quad (2.86)$$

in ALE framework with the residual of the momentum equation given in (2.84).

Finally, for a better control of incompressibility condition in convection dominated flow, a *grad-div* stabilization term also called as *bulk viscosity* or *least-square incompressibility constraint* term, proposed by Hansbo and Szepessy [96],

$$\sum_e (\nabla \cdot \mathbf{v}_h, \tau^c \mathbf{r}_h^c)_{\Omega^f} \quad (2.87)$$

with the discrete residual of continuity equation

$$\mathbf{r}_h^c = \nabla \cdot \mathbf{u}_h \quad (2.88)$$

is added to the discrete Galerkin terms. The stabilization parameter τ^c is defined as

$$\tau^c = \frac{\|\mathbf{u}_h\|}{2} \cdot \min(\xi_2, 1), \quad (2.89)$$

where ξ_2 is provided in (2.82). All the stabilization parameters depend on the characteristic element length h . The choice of the element parameter is not defined very clear. An overview of different element length parameters can be found in Gamnitzer [79]. In the present work, for the SUPG method the stream length definition is chosen. It estimates the element length in direction of fluid velocity (see also Wall [172]). In the case of the PSPG and the least-square incompressibility constraint term, the volume-equivalent diameter, which is the variant based on a pure geometrical choice, is chosen (see Gamnitzer [79]).

Finally, the discrete nonlinear stabilized formulation in Eulerian framework can be defined as a combination of standard Galerkin terms, defined in (2.72) and (2.73) together with the contributions of residual-based stabilizations as

$$\begin{aligned} R_{\mathbf{x},u}^{\text{stab}}(\mathbf{u}_h, p_h) &= R_{\mathbf{x},u}^{\text{std}}(\mathbf{u}_h, p_h) + \sum_{\mathbf{e}} (\mathbf{u}_h \cdot \nabla \mathbf{v}_h, \tau^m \mathbf{r}_{\mathbf{x},h}^m)_{\Omega_f} \\ &\quad + \sum_{\mathbf{e}} (\nabla \cdot \mathbf{v}_h, \tau^c \mathbf{r}_h^c)_{\Omega_f}, \end{aligned} \quad (2.90)$$

$$R_{\mathbf{x},p}^{\text{stab}}(\mathbf{u}_h, p_h) = R_{\mathbf{x},p}^{\text{std}}(\mathbf{u}_h, p_h) - \sum_{\mathbf{e}} (\nabla q_h, \tau^m \mathbf{r}_{\mathbf{x},h}^m)_{\Omega_f}. \quad (2.91)$$

Accordingly, in ALE framework the discrete nonlinear stabilized formulation reads as

$$\begin{aligned} R_{\mathcal{X},u}^{\text{stab}}(\mathbf{u}_h, p_h) &= R_{\mathcal{X},u}^{\text{std}}(\mathbf{u}_h, p_h) + \sum_{\mathbf{e}} (\mathbf{c}_h \cdot \nabla \mathbf{v}_h, \tau^m \mathbf{r}_{\mathcal{X},h}^m)_{\Omega_f} \\ &\quad + \sum_{\mathbf{e}} (\nabla \cdot \mathbf{v}_h, \tau^c \mathbf{r}_h^c)_{\Omega_f}, \end{aligned} \quad (2.92)$$

$$R_{\mathcal{X},p}^{\text{stab}}(\mathbf{u}_h, p_h) = R_{\mathcal{X},p}^{\text{std}}(\mathbf{u}_h, p_h) - \sum_{\mathbf{e}} (\nabla q_h, \tau^m \mathbf{r}_{\mathcal{X},h}^m)_{\Omega_f}. \quad (2.93)$$

2.3.10 Linearization

For the Newtonian fluid with constant density the only nonlinear term is the convective term. Adding residual-based stabilization SUPG, adds an additional source of nonlinearity to the formulation. In the present work, the Newton-Raphson method is employed to solve the nonlinear system, which requires a full linearization of the terms. By applying a Taylor expansion to the nonlinear systems of equations, the stabilized fluid residual at the iteration step $i + 1$ is given as

$$\begin{bmatrix} \mathbf{r}_u^{\text{stab}} \\ \mathbf{r}_p^{\text{stab}} \end{bmatrix}_{i+1}^{n+1} = 0 = \begin{bmatrix} \mathbf{r}_u^{\text{stab}} \\ \mathbf{r}_p^{\text{stab}} \end{bmatrix}_i^{n+1} + \begin{bmatrix} \frac{\partial \mathbf{r}_u^{\text{stab}}}{\partial \mathbf{u}} & \frac{\partial \mathbf{r}_u^{\text{stab}}}{\partial \mathbf{p}} \\ \frac{\partial \mathbf{r}_p^{\text{stab}}}{\partial \mathbf{u}} & \frac{\partial \mathbf{r}_p^{\text{stab}}}{\partial \mathbf{p}} \end{bmatrix}_i^{n+1} \begin{bmatrix} \Delta \mathbf{u} \\ \Delta \mathbf{p} \end{bmatrix}_{i+1}^{n+1} + \text{h.o.t.} \quad (2.94)$$

Hereby, $\mathbf{r}_u^{\text{stab}}$ and $\mathbf{r}_p^{\text{stab}}$ denote the vectors of nonlinear stabilized fluid residuals. Omitting the higher order terms and using the matrix notations, the linearized system at step $i + 1$ and the

time step t^{n+1} reads as

$$\begin{bmatrix} \mathbf{M}^F + \mathbf{C}^F + \mathbf{S}^{\text{SUPG}} + \mathbf{S}^{\text{BV}} & \mathbf{G}^F + \mathbf{S}^{\text{SUPG}} \\ -(\mathbf{G}^F)^T + \mathbf{S}^{\text{PSPG}} & \mathbf{S}^{\text{PSPG}} \end{bmatrix}_i^{n+1} \begin{bmatrix} \Delta \mathbf{u} \\ \Delta \mathbf{p} \end{bmatrix}_{i+1}^{n+1} = \begin{bmatrix} r_u^{\text{stab}} \\ r_p^{\text{stab}} \end{bmatrix}_i^{n+1}. \quad (2.95)$$

In (2.95), the stabilization matrices are denoted as \mathbf{S}^{SUPG} , \mathbf{S}^{PSPG} and \mathbf{S}^{BV} . By summing up the standard Galerkin matrices, the linear system (2.95) can be written as

$$\begin{bmatrix} \mathbf{F}_{uu} + \mathbf{S}^{\text{SUPG}} + \mathbf{S}^{\text{BV}} & \mathbf{F}_{up} + \mathbf{S}^{\text{SUPG}} \\ \mathbf{F}_{pu} + \mathbf{S}^{\text{PSPG}} & \mathbf{S}^{\text{PSPG}} \end{bmatrix}_i^{n+1} \begin{bmatrix} \Delta \mathbf{u} \\ \Delta \mathbf{p} \end{bmatrix}_i^{n+1} = \begin{bmatrix} r_u^{\text{stab}} \\ r_p^{\text{stab}} \end{bmatrix}_i^{n+1}, \quad (2.96)$$

which has to be solved in every iteration step $i+1$ of each time step t^{n+1} . After solving (2.96) for the velocity and pressure increments, $\Delta \mathbf{u}_{i+1}^{n+1}$ and $\Delta \mathbf{p}_{i+1}^{n+1}$, in every iteration step, the new velocity and pressure at the iteration step $i+1$ are updated as

$$\mathbf{u}_{i+1}^{n+1} = \mathbf{u}_i^{n+1} + \Delta \mathbf{u}_{i+1}^{n+1}, \quad (2.97)$$

$$\mathbf{p}_{i+1}^{n+1} = \mathbf{p}_i^{n+1} + \Delta \mathbf{p}_{i+1}^{n+1}. \quad (2.98)$$

2.4 Fluid grid motion

In Section 2.3.6, the incompressible Navier-Stokes equations in ALE reference system have been presented. In ALE formulation, the deformation of the boundaries of the fluid domain follows the fluid motion at the boundary, while the deformation of the mesh inside the domain is arbitrary. There is no unique way to describe the fluid mesh motion inside the domain. However, having an appropriate algorithm, which minimizes the discretization error and avoids distorted elements is crucial. At the same time, the algorithm should allow for large deformation of the domain. Several approaches have been introduced in literature. As an example, spring-algorithms, which treat the edges of the fluid grid like a elastic spring and possibly add torsion springs to the nodes were proposed by Batina [13], Farhat et al. [69] and Degand and Farhat [58]. In the present work, a quasi-elastostatic pseudo-structure approach, is used, which will be discussed briefly in the following. For a detailed description of this approach and an overview of other methods the reader is referred to Wall [172]. In this approach the mesh is considered as an elastic body. The governing equations of the ALE field are based on the simple structure equation in spatial coordinates

$$\nabla \cdot \boldsymbol{\sigma}^g = \mathbf{0}, \quad \text{in } \Omega^{\text{ALE}} \quad (2.99)$$

$$\mathbf{d}^g = \bar{\mathbf{d}}^g, \quad \text{on } \partial\Omega^{\text{ALE}}. \quad (2.100)$$

In (2.100), $\bar{\mathbf{d}}^g$ describes the mesh displacement which is prescribed on the boundary. The stresses are calculated based on the simple St.-Venant-Kirchhoff material

$$\boldsymbol{\sigma}^g = \lambda^g \text{tr}(\boldsymbol{\epsilon}^g) \mathbf{I} + 2\mu^g \boldsymbol{\epsilon}^g, \quad (2.101)$$

with linear strain measure $\boldsymbol{\epsilon}^g$ defined as

$$\boldsymbol{\epsilon}^g(\mathbf{d}^g) = \frac{1}{2}(\nabla \mathbf{d}^g + (\nabla \mathbf{d}^g)^T). \quad (2.102)$$

The λ^g and μ^g are the Lamé constants, which are related to the material parameters Young's modulus E^g and Poisson's ratio ν^g . By multiplication of (2.99) with the virtual displacements $\delta \mathbf{d}^g$ the weak formulation is obtained as

$$(\delta \mathbf{d}^g, \nabla \cdot \boldsymbol{\sigma}^g)_{\Omega^e} = 0. \quad (2.103)$$

For the discretization of the weak form (2.103) trilinear eight-noded elements are used. The discrete fields \mathbf{d}_h^g and $\delta \mathbf{d}_h^g$ results from

$$\mathbf{d}_h^g(\mathbf{x}, t) = \sum_i^n N_i(\mathbf{x}) \mathbf{d}_i^g(t), \quad (2.104)$$

$$\delta \mathbf{d}_h^g(\mathbf{x}, t) = \sum_i^n N_i(\mathbf{x}) \delta \mathbf{d}_i^g(t), \quad (2.105)$$

with N_i denoting linear shape functions. Applying the discrete forms to the weak formulation the resulting ALE linear system reads as

$$[\mathbf{A}] [\mathbf{d}^g] = 0. \quad (2.106)$$

In the following section, the coupled fluid-structure problem and the problem definition including the required coupling conditions are discussed.

2.5 Coupled fluid-structure problem

A fluid-structure interaction (FSI) problem consists of the description of fluid and structure fields and the coupling conditions at their common interface. The FSI coupling is a surface coupling, where the interaction of fluid and structure fields only takes place at the shared interface. In the classical FSI approach the fluid domain is described in the ALE formulation. This allows the fluid mesh to attach to the structure at the common interface throughout the simulation. In the hybrid ALE-fixed-grid approach a mixed Eulerian-ALE formulation for the fluid field is used. The fluid domain is divided into two fluid subdomains with the same material properties; a moving embedded fluid subdomain and a fixed-grid background fluid subdomain. The embedded fluid subdomain, which is described in ALE formulation, surrounds the structure and follows the movement and deformation of it. Thus, at the FSI interface, which is the common interface between embedded fluid and the structure, the embedded fluid mesh has the same motion of the structure. This moving ALE-fluid is referred to as *embedded fluid* as it is embedded into the fixed-grid background fluid, which is described in Eulerian formulation. This section is devoted to a brief description of the setup of the hybrid ALE-fixed-grid FSI formulation including the problem definition and the coupling conditions.

2.5.1 Problem definition

In Figure 2.1, a general setup of the hybrid ALE-fixed-grid FSI approach is shown. Let $\Omega^f = \Omega^b \cup \Omega^e$ be the whole fluid domain. The fluid domain Ω^f is separated into a fixed-grid background

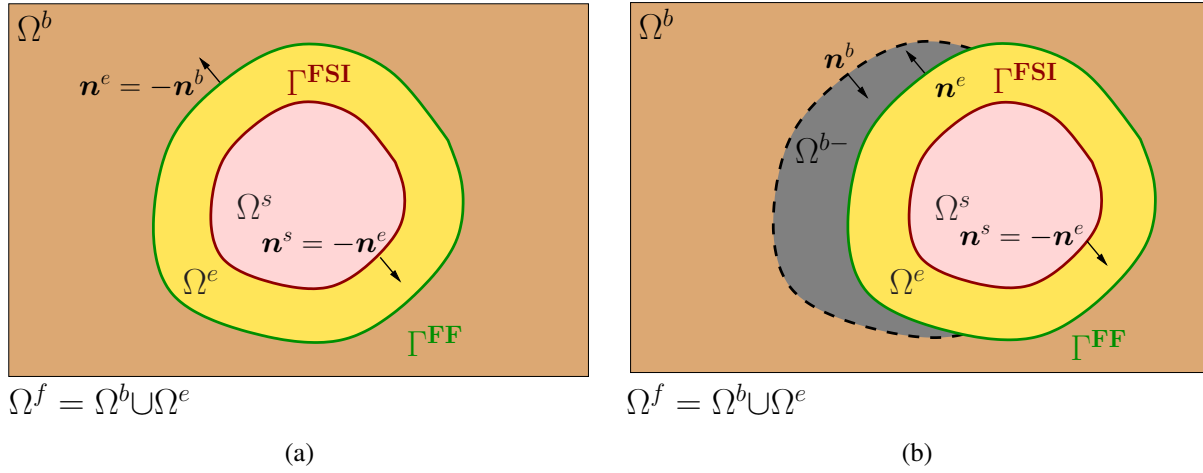


Figure 2.1: **(a)** The fluid domain Ω^f is divided into a background fluid subdomain Ω^b and an embedded fluid subdomain Ω^e via the fluid-fluid interface Γ^{FF} . The embedded fluid subdomain interacts with the structure domain Ω^s at the fluid-structure interface Γ^{FSI} . **(b)** The interface Γ^{FF} also divides the entire background fluid in a physical part Ω^b and an inactive void/fictitious part Ω^{b-} . The inactive void/fictitious fluid subdomain Ω^{b-} is covered by the embedded fluid subdomain Ω^e and the structure domain Ω^s .

fluid subdomain Ω^b and an embedded fluid subdomain Ω^e by fluid-fluid interface Γ^{FF} . Furthermore, the interface Γ^{FF} subdivides the background fluid into an active physical part identified with Ω^b and an inactive void/fictitious part Ω^{b-} , which is covered by Ω^e and Ω^s (see Figure 2.1b). The coupling of the two fluid subdomains, Ω^b and Ω^e , takes place only at the shared interface, Γ^{FF} . The fluid domain Ω^f interacts with the structure domain Ω^s at the fluid-structure interface Γ^{FSI} via the embedded fluid subdomain Ω^e .

2.5.2 Coupling conditions

The last part of this section, addresses the coupling conditions at both interfaces depicted in Figure 2.1, i.e. the fluid-fluid interface Γ^{FF} and the fluid-structure interface Γ^{FSI} . First the constraints at the physical fluid-structure interface Γ^{FSI} between embedded fluid subdomain Ω^e and structural domain Ω^s will be introduced. Then, the internal coupling conditions between embedded fluid subdomain Ω^e and background fluid subdomain Ω^b at the fluid-fluid interface Γ^{FF} will be provided. Besides the Dirichlet and Neumann boundaries, Γ^{FF} and Γ^{FSI} represent the third kind of boundary, where a surface coupling between different domains takes place. At both interfaces the domains are coupled through kinematic and dynamic coupling constraints.

Coupling conditions at the fluid-structure interface

At the physical fluid-structure interface Γ^{FSI} a no-slip condition as the kinematic constraint is assumed. This implies no mass flow across the interface, thus, the normal velocities at the interface have to match. Furthermore, a relative tangential movement between the embedded fluid and the structure is prohibited. Therefore, the kinematic condition at the fluid-structure interface

reads as

$$\frac{\partial \mathbf{d}_{\Gamma^{\text{FSI}}}^s}{\partial t} = \mathbf{u}_{\Gamma^{\text{FSI}}}^e \quad \text{on} \quad \Gamma^{\text{FSI}} \times (0, T). \quad (2.107)$$

Hereby, $\mathbf{u}_{\Gamma^{\text{FSI}}}^e$ denotes the velocity field of the embedded fluid subdomain at Γ^{FSI} and $\mathbf{d}_{\Gamma^{\text{FSI}}}^s$ the displacement of the structure at Γ^{FSI} . This condition couples the physical fields, i.e. the velocity of embedded fluid subdomain with the displacement of the structure field. On the other hand, as a non-physical condition, the embedded fluid velocity and the embedded grid velocity at the fluid-structure interface have to be the same

$$\mathbf{u}_{\Gamma^{\text{FSI}}}^e = \mathbf{u}_{\Gamma^{\text{FSI}}}^g \quad \text{on} \quad \Gamma^{\text{FSI}} \times (0, T). \quad (2.108)$$

Considering (2.107), this condition can be expressed by

$$\frac{\partial \mathbf{d}_{\Gamma^{\text{FSI}}}^s}{\partial t} = \frac{\partial \mathbf{d}_{\Gamma^{\text{FSI}}}^g}{\partial t} \quad \text{on} \quad \Gamma^{\text{FSI}} \times (0, T), \quad (2.109)$$

which is equivalent to the following equation after integration with respect to time

$$\mathbf{d}_{\Gamma^{\text{FSI}}}^s = \mathbf{d}_{\Gamma^{\text{FSI}}}^g \quad \text{on} \quad \Gamma^{\text{FSI}} \times (0, T). \quad (2.110)$$

Hereby, $\mathbf{d}_{\Gamma^{\text{FSI}}}^g$ denotes the grid displacement of the embedded fluid at the fluid-structure interface Γ^{FSI} . The dynamic equilibrium at the fluid-structure interface Γ^{FSI} is given as

$$\boldsymbol{\sigma}^e \cdot \mathbf{n}^e = -\boldsymbol{\sigma}^s \cdot \mathbf{n}^s \quad \text{on} \quad \Gamma^{\text{FSI}} \times (0, T), \quad (2.111)$$

which implies that the surface traction of the embedded fluid and the structure have to be equal. Hereby, \mathbf{n}^e is the normal vector with respect to Ω^e and \mathbf{n}^s the normal vector with respect to Ω^s at the shared interface, as shown in Figure 2.1a. It holds $\mathbf{n}^e = -\mathbf{n}^s$ at Γ^{FSI} .

Coupling conditions at the fluid-fluid interface

Also at the internal fluid-fluid interface Γ^{FF} the kinematic and dynamic continuities have to be assured. The velocities of the background fluid subdomain Ω^b and the embedded fluid subdomain Ω^e have to be equal at the common interface Γ^{FF} . This condition can be expressed by

$$\mathbf{u}_{\Gamma^{\text{FF}}}^b = \mathbf{u}_{\Gamma^{\text{FF}}}^e, \quad \text{on} \quad \Gamma^{\text{FF}} \times (0, T). \quad (2.112)$$

In (2.112), $\mathbf{u}_{\Gamma^{\text{FF}}}^b$ and $\mathbf{u}_{\Gamma^{\text{FF}}}^e$ denote the velocity of the background fluid subdomain and embedded fluid subdomain, respectively. Furthermore, the momentum balance requires the surface tensions to be equal

$$\boldsymbol{\sigma}^b \cdot \mathbf{n}^b = -\boldsymbol{\sigma}^e \cdot \mathbf{n}^e, \quad \text{on} \quad \Gamma^{\text{FF}} \times (0, T), \quad (2.113)$$

where \mathbf{n}^b is the normal vector with respect to Ω^b and \mathbf{n}^e the normal vector with respect to Ω^e at Γ^{FF} , and it holds $\mathbf{n}^b = -\mathbf{n}^e$, as depicted in Figure 2.1a.

3 An XFEM-based embedded fluid formulation

As it has been discussed in the previous chapter, a stabilized embedded fluid formulation, which is the focus of this chapter, is an important step towards developing the hybrid ALE-fixed-grid FSI approach. In the first part of this chapter, a stabilized embedded fluid formulation based on the extended finite element method (XFEM) for transient problems with stationary interfaces, having regard to applying it to moving interfaces, is developed step-by-step. For this purpose, the standard finite element formulation for incompressible flow, given in Section 2.3, is extended to a coupled formulation of embedded and background fluid subdomains. First, an XFEM-based formulation for fixed-grid background fluid subdomain using cut elements, is presented. Afterwards, the focus is shifted to the main challenge of the embedded fluid formulation: finding a stable formulation for weak enforcement of coupling conditions at the embedded fluid interface. In this context, different coupling methods and various stabilization terms are discussed. This coupling needs to be robust, stable and accurate independent of fluid-fluid interface position or the complexity of the form of the embedded fluid subdomain. For an evaluation of different coupling methods a study of convergence behavior is carried out. In the end, a stabilized XFEM-based embedded fluid formulation for stationary interfaces is presented. In the second part of this chapter, the proposed formulation is extended to handle moving interfaces by introducing a new approach to deal with XFEM time-integration issue in Eulerian background fluid formulation. Finally, the proposed method is validated numerically for two- and three-dimensional flow simulations involving stationary and moving interfaces.

3.1 Problem definition

As a first step towards the embedded fluid formulation, a fluid domain Ω^f is considered. For the purpose of using different discrete function spaces for the spatial approximation of the solution at different parts of the fluid domain, the domain Ω^f is separated into an embedded fluid subdomain Ω^e and a background fluid subdomain Ω^b . Now, the problem consists of two fluid subdomains and the internal fluid-fluid interface. This is a simplified version of the problem definition given in Section 2.5.1, where the structure and subsequently the fluid-structure interface, which is the shared interface between embedded fluid subdomain and the structure, are omitted.

The general setup of the embedded fluid formulation is shown in Figure 3.1a. Let $\Omega^f = \Omega^b \cup \Omega^e$ be the whole fluid domain. The interface between the embedded fluid domain Ω^e and the fixed-grid background fluid domain Ω^b is denoted as Γ^{FF} . The fluid subdomain Ω^e is discretized with the classical Finite Element mesh \mathcal{T}^e , where the elements are aligned with the fluid-fluid boundary Γ^{FF} . For the background fluid subdomain Ω^b the fixed-grid mesh \mathcal{T}^b using cut elements is applied, which is independent of the interface position, see Figure 3.1b. As a result of this,

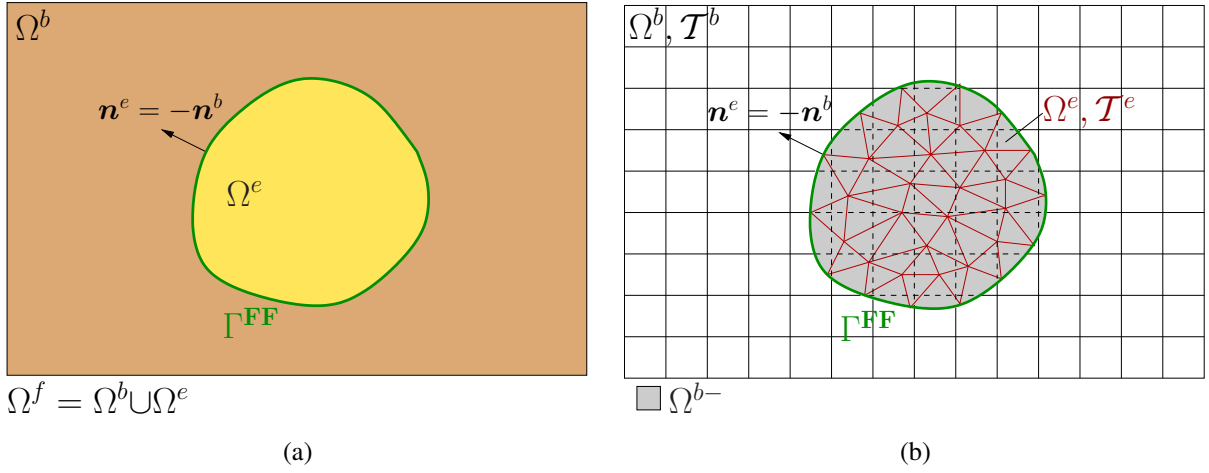


Figure 3.1: **(a)** The domain Ω^f is separated into an embedded fluid subdomain Ω^e and a background fluid subdomain Ω^b by the fluid-fluid interface Γ^{FF} . **(b)** The interface Γ^{FF} also divides the entire background fluid subdomain in a physical fluid subdomain Ω^b and an inactive void/fictitious fluid subdomain Ω^{b-} , which is covered by Ω^e . The subdomain Ω^e is discretized with the classical finite element mesh \mathcal{T}^e , aligned with the fluid-fluid interface Γ^{FF} . For the approximation of background fluid subdomain a fixed-grid mesh \mathcal{T}^b using cut elements is applied, which is independent of the interface position.

the interface Γ^{FF} subdivides the background fluid mesh into an active physical part aligned with Ω^b and an inactive void/fictitious domain part Ω^{b-} , which is covered by Ω^e , see Figure 3.1b. Therefore, the physical part of background fluid subdomain Ω^b , depends on the position of Γ^{FF} . The coupling of the flow fields in Ω^b and Ω^e only takes place at the shared interface Γ^{FF} , where the coupling conditions (2.112) and (2.113), defined in Section 2.5.2, are enforced weakly. In Figure 3.1a, \mathbf{n}^b and \mathbf{n}^e denote the outward pointing normal vectors with respect to subdomains Ω^b and Ω^e , respectively.

In Figure 3.2, the spatial discretizations of the embedded fluid subdomain and background fluid subdomain are depicted. The entire physical fluid domain is divided into background fluid subdomain and embedded fluid subdomain by the fluid-fluid interface. For the embedded mesh \mathcal{T}^e , the classical continuous finite element approximation

$$V_h^e := \{v \in C^0(\Omega^e) : v|_K \in Q^1(K) \forall K \in \mathcal{T}^e\}$$

is used for the spatial discretization of the solution fields u_i^e , ($i = 1, 2, 3$) and p^e on Ω^e , see Figures 3.2a and 3.2b. Hereby, $Q^1(K)$ defines polynomial of order at most 1 on a hexahedral element K , which is used in this work. However, it has to be pointed out that any other element types with different polynomial orders can also be used. As it can be seen in Figures 3.2a and 3.2c, for the approximation of background fluid subdomain cut elements, which are not aligned with the fluid-fluid interface, are used. The physical and void/fictitious parts of background fluid are depicted in Figure 3.2c. A close up view of the cut elements are shown in Figure 3.2d.

In the next section, an XFEM-based spatial discretization using cut elements, which is used for background fluid subdomain, is presented.

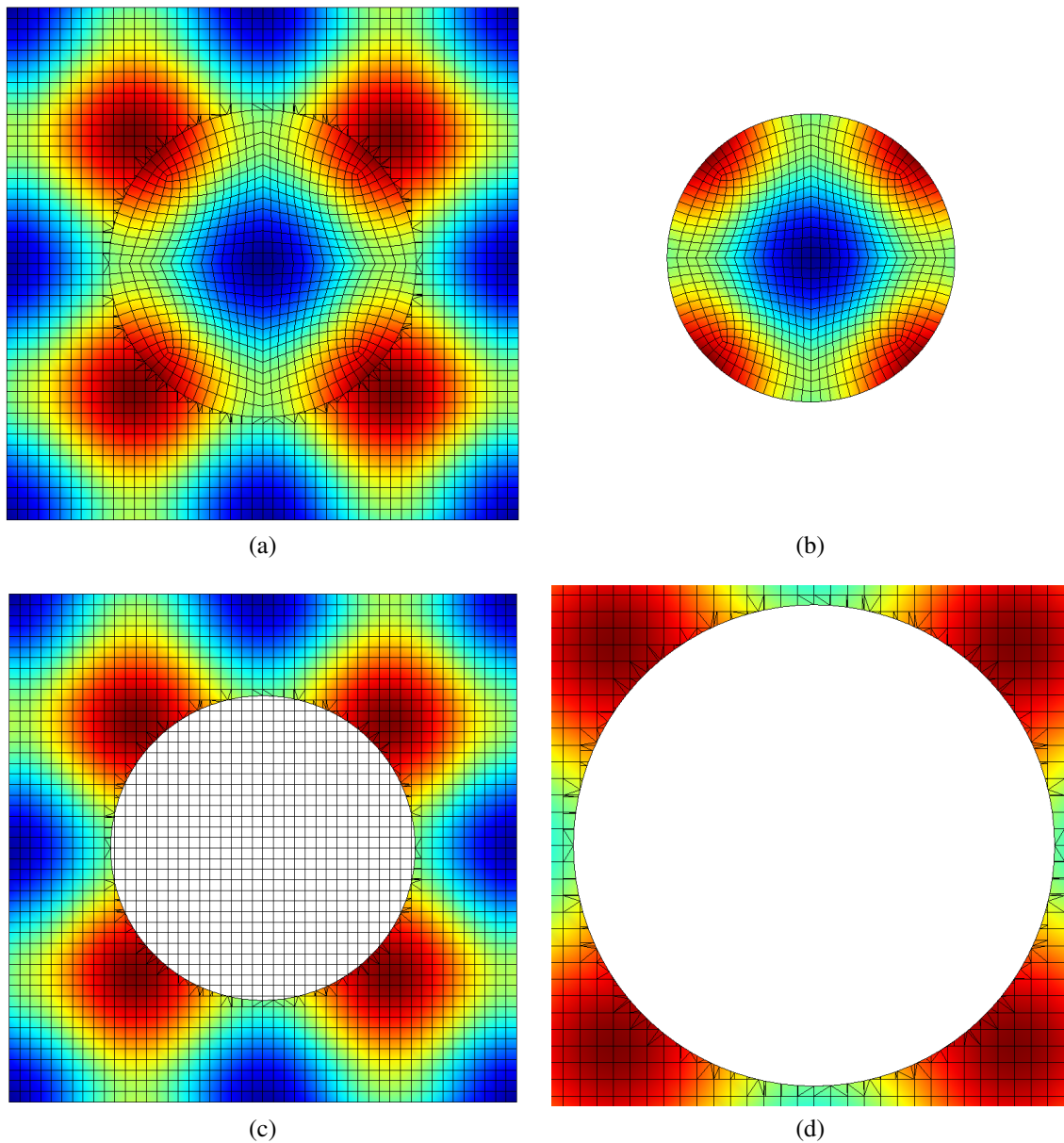


Figure 3.2: **(a)** Different discrete function spaces for the spatial approximation of the solution at different parts of the fluid domain are applied. For the approximation of background fluid subdomain cut elements, which are not aligned with the fluid-fluid interface are used. For the embedded fluid subdomain classical finite elements aligned with the fluid-fluid interface are applied. **(b)** Embedded fluid subdomain approximated with classical finite elements aligned with fluid-fluid interface. **(c)** The physical and void/fictitious parts of background fluid subdomain. **(d)** Close up view of the cut elements of background fluid subdomain in the interface zone.

3.2 An XFEM-based formulation for background fluid field

The motivation of the extended finite element method (XFEM) comes from the requirement of describing a discontinuity sharply in the physical fields, e.g. the velocity and pressure field. As already shown in Figure 3.1, the internal fluid-fluid interface Γ^{FF} divides the background fluid in a physical part Ω^b and an inactive void/fictitious subdomain Ω^{b-} . Regarding to the coupling of the physical background fluid subdomain Ω^b with the embedded fluid subdomain Ω^e at the shared interface Γ^{FF} , it is necessary to decouple the physical background fluid subdomain Ω^b from the non-physical void/fictitious subdomain Ω^{b-} and describe the discontinuity sharply. Therefore, a jump along the interface Γ^{FF} from the physical values in Ω^b to zero in Ω^{b-} need to be specified. In this manner, fluid unknowns of the void/fictitious subdomain, which are not associated with the cut elements, are removed and the coupling between background fluid subdomain Ω^b and the embedded fluid subdomain Ω^e takes place at the interface without defining overlapping solutions.

In this section, first an introduction to the extended finite element method is given. Then, a volume-cell representation of the background fluid subdomain, which is an alternative technique to the classical extended finite element method, will be described. Afterwards, a DOF-management algorithm to handle several degrees of freedom (DOFs) for nodes of cut elements, which are necessary for a precise representation of solutions on complex cut topologies will be provided.

3.2.1 Introduction to Extended Finite Element Method (XFEM)

In real-world applications there are a number of examples, where the resulting solutions involve non-smooth characteristics like discontinuities and singularities, which need to be described sharply. Common examples of non-smooth solutions in solid mechanics are for instance modeling of cracks or dislocations. In fluid mechanics the non-smooth solutions can be found in modeling of shocks, boundary layers or multi-phase flows. Standard finite element approximations do not allow such behavior of the physical fields within one element. A straightforward approach is to use the polynomial approximation spaces and align the mesh to the discontinuity. However, for large deformations, as the discontinuity moves, such an approach requires remeshing. A much more sophisticated approach is to enrich the polynomial approximation space to be able to describe the non-smooth properties of the problem. In this way, the discontinuity can be represented independent of the mesh for example often in a cartesian grid. In the review article of Fries and Belytschko [77] these methods are referred to *enriched methods*. The enriched methods can be achieved by replacing the shape functions in the polynomial approximation space by special shape functions or by extending/adding special shape functions to the polynomial approximations. Some of the enriched methods, which are able to describe a sharp discontinuity arbitrarily within the domain, are the partition of unity methods (PUFEM), see e.g. Griebel and Schweitzer [90], Melenk and Babuška [137] and Babuška and Melenk [8], the generalized finite element method (GFEM), see e.g. Strouboulis et al. [160] and Strouboulis et al. [161], and extended finite element methods (XFEM), which are basically classified as similar methods by Belytschko et al. [24] and Fries and Belytschko [77]. All these methods are based on the partition of unity (PU) concept, which has been proposed by Babuška et al. [9]. For a description of

PU concept in framework of XFEM the reader is referred to the overview article of Belytschko et al. [24].

Originally, the XFEM was developed by Belytschko and Black [22] and Moës et al. [139] for crack problems. It has then been applied to other problems like modeling of holes and inclusions by Sukumar et al. [165], solidification problems for example by Chessa et al. [48], two-phase-flow problems for example by Chessa and Belytschko [45], Groß and Reusken [91], Rasthofer et al. [147], Sauerland and Fries [151] and Schott et al. [155], fluid-structure interaction problems by Gerstenberger and Wall [83, 84], Legay et al. [128] and Zilian and Legay [185] and to combustion problems by Van der Bos and Gravemeier [169] and Henke [101]. In the concept of XFEM, the enrichment strategies considered, are mesh-based, i.e. constructed by standard FE shape functions, and local, i.e. the enrichment is applied locally to some nodes, and based on PU concept. The basic idea is to locally add enrichment functions to the FE space to extend the approximation properties. Depending on the type of discontinuity different enrichment functions in the concept of XFEM are available. An overview of different enrichments is given by Fries and Belytschko [77].

As mentioned above, the aim of the present work is to describe a jump from the physical values to zero in the primary variables of the background fluid domain, i.e. the velocity and pressure fields, across the interface. This kind of discontinuity, where the variables and their gradients at both sides of the interface are fully decoupled, is referred to as *strong discontinuity*, see Fries and Belytschko [77]. In contrast to this, solutions with *weak discontinuities* have kinks across the interface, i.e. they are continuous and just the gradients are discontinuous across the interface. An example for these weak discontinuities is the velocity field of two-phase flow problem by Rasthofer et al. [147].

A typical choice for describing the strong discontinuity is the Heaviside function, which has been proposed in the early works of XFEM, for example by Belytschko and Black [22], Moës et al. [139] and Dolbow et al. [60]. The Heaviside function, which is also known as void or step function, is defined as

$$\hat{\psi}(\mathbf{x}) = \begin{cases} 1 & \text{in } \Omega^b \\ 0 & \text{in } \Omega^{b-} \end{cases} \quad (3.1)$$

for the background fluid subdomain. It has to be pointed out that for the stationary interfaces considered in this section, the Heaviside function is independent of time. The finite element shape functions are then extended by using additional degrees of freedom combined with the Heaviside function. The resulting velocity and pressure fields are

$$\mathbf{u}_h^b(\mathbf{x}, t) = \sum_I (N_I(\mathbf{x})\check{\mathbf{u}}_I^b(t) + N_I(\mathbf{x})\hat{\psi}(\mathbf{x})\hat{\mathbf{u}}_I^b(t)), \quad (3.2)$$

$$p_h^b(\mathbf{x}, t) = \sum_I (N_I(\mathbf{x})\check{p}_I^b(t) + N_I(\mathbf{x})\hat{\psi}(\mathbf{x})\hat{p}_I^b(t)), \quad (3.3)$$

where $\check{\mathbf{u}}_I^b$ and \check{p}_I^b represent the standard nodal degrees of freedom at a node I . Additional degrees of freedom $\hat{\mathbf{u}}_I^b$ and \hat{p}_I^b multiplied with the Heaviside function $\hat{\psi}(\mathbf{x})$ are used to enhance the solution.

Modeling of voids can also be treated without using any enrichments. For this purpose, the areas of the elements inside the fictitious domains are simply neglected in the integration of the

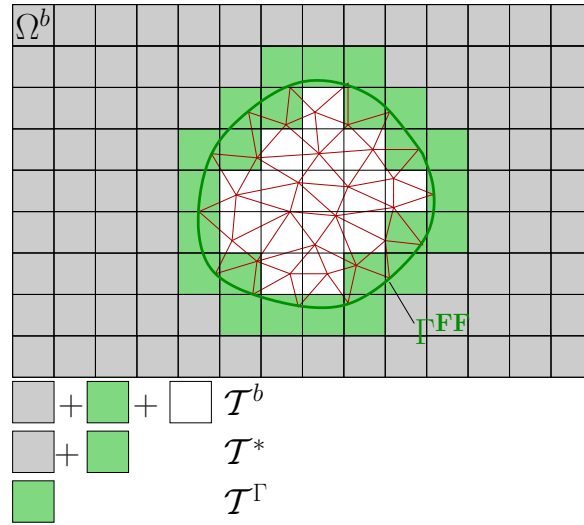


Figure 3.3: The fluid-fluid interface Γ^{FF} intersects the background fluid domain Ω^b . The entire background fluid mesh is denoted as \mathcal{T}^b . The set of elements which are intersected by Γ^{FF} are signified as \mathcal{T}^Γ . \mathcal{T}^* denotes the set of elements which lies in the physical background fluid domain unified with the set of cut elements.

weak form and the integration is just performed in the physical part of the domain. As an example, for the modeling of holes in Daux et al. [56] the degrees of freedom associated with the nodes inside the void domain are removed from the system of equations. Treating the voids without any enrichment functions provides a much more efficient and flexible implementation framework. In Schott and Wall [154] a fixed-grid volume-cell spatial discretization of the fluid domain based on a standard FEM framework is introduced. Furthermore, a general DOF-management algorithm has been given to handle multiple sets of degrees of freedom, which are important for fixed-grid fluid-structure interaction or multiphase-flow problems, like two-phase flow or combustion. For these kinds of applications it is crucial to approximate independent solutions on two sides of the interface within one fluid element, since they could be very different. In the present work, the DOF-management algorithm of Schott and Wall [154] is applied to the spatial approximation of the background fluid subdomain. However, as for embedding fluid patches the same physical properties of the fluid subdomains are assumed, the solution across the interface within one fluid element does not vary considerably. Therefore, multiple sets of degrees of freedom are not as essential as for example for fixed-grid FSI approach. In Sections 3.2.2 and 3.2.2, the volume-cell representation of the background fluid subdomain and the DOF-management algorithm for relevant cases of embedded fluid formulation, will be presented. The formulations and notations are closely related to Schott and Wall [154], where the volume-cell representation and the DOF-management algorithm is formulated for a pure fixed-grid FSI approach. For representation of complex fluid topologies, which appears in modeling of thin structures in the context of fixed-grid FSI, the interested reader is referred to Schott and Wall [154].

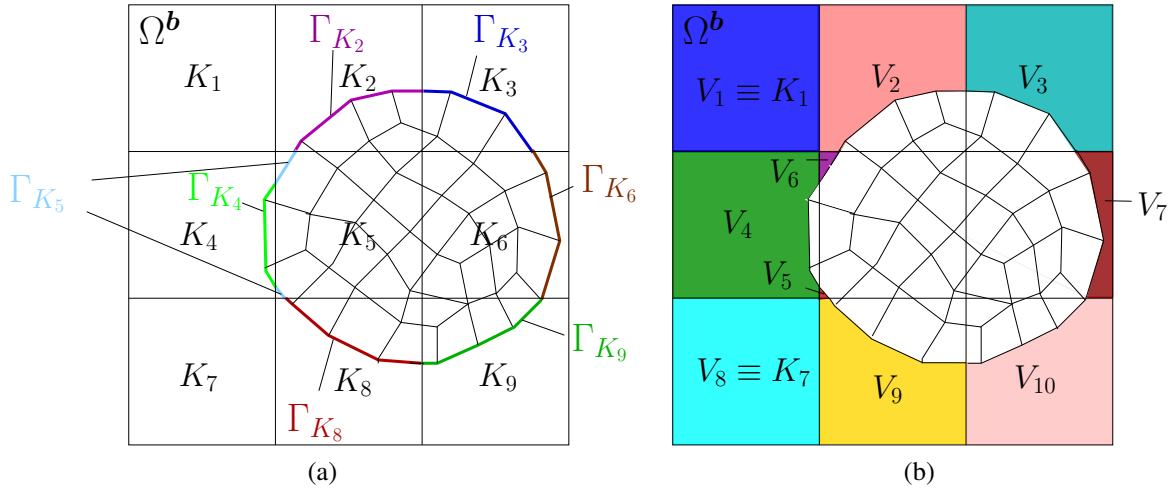


Figure 3.4: An example for a cut situation: **(a)** Cut elements and boundary segments. **(b)** Resulting volume-cells.

3.2.2 Volume-cell representation of background fluid domain

For the volume-cell representation of the background fluid subdomain, introduced by Schott and Wall [154], some more notations have to be introduced. The entire background fluid, i.e. the physical part Ω^b and the void/fictitious part of background fluid Ω^{b^-} , is discretized with a fixed-grid finite element mesh \mathcal{T}^b , which is not aligned with the interface Γ^{FF} (see Figure 3.3). The set of the finite elements K intersected by Γ^{FF} is given by $\mathcal{T}^\Gamma := \{K \in \mathcal{T} \mid K \cap \Gamma^{\text{FF}} \neq \emptyset\}$. Elements in \mathcal{T}^Γ are called cut elements. Furthermore, \mathcal{T}^* denotes the set of all finite elements which lie in the physical background fluid domain unified with the set of cut elements, $\mathcal{T}^* := \{K \in \mathcal{T} \mid K \cap \Omega^b \neq \emptyset\}$. The introduced element sets, \mathcal{T}^* and \mathcal{T}^Γ , are depicted in the Figure 3.3.

As is can be seen in Figure 3.3, the fluid-fluid interface Γ^{FF} , which is represented explicitly by the boundary of the embedded fluid mesh, intersects the elements of background fluid mesh. This intersection subdivides a cut background fluid element $K \in \mathcal{T}^\Gamma$ into several arbitrary complex formed polyhedra, the so called *volume-cells* denoted as V_i , which are located in the physical part as well as in the inactive/fictitious parts of the background fluid subdomain. A volume-cell which is located in the physical part of background fluid Ω^b , is denoted as an *active fluid volume-cell*. The volume-cells which do not lie in the physical fluid domain Ω^b are not required and will not be considered anymore. Hence, the physical background fluid domain Ω^b consists of its active fluid volume-cells. The number of active fluid volume-cells for a cut element depends on the position of the interface; there can be one fluid volume-cell, or more. Therefore, the physical fluid volume for a cut element K consists of active volume-cells, which are not connected within an element

$$\Omega_K^b = \{V \subseteq K \cap \Omega^b \text{ polyhedra} \mid V_i \cap V_j = 0 \text{ for } i \neq j\}. \quad (3.4)$$

For elements, which are uncut ($K \notin \mathcal{T}^\Gamma$) the element itself is equal to the volume-cell, $K \equiv V_i$. Furthermore, the interface Γ^{FF} is subdivided into small parts, which are associated with the underlying background fluid element. These element boundary parts are denoted as $\Gamma_{K_i} = \Gamma^{\text{FF}} \cap K_i$.

In Figure 3.4, an example for a cut situation is depicted. The underlying cut elements are denoted as $K_2, K_3, K_4, K_5, K_6, K_8, K_9 \in \mathcal{T}^\Gamma$. The interface Γ^{FF} is subdivided into small element parts $\Gamma_{K_2}, \Gamma_{K_3}, \Gamma_{K_4}, \Gamma_{K_5}, \Gamma_{K_6}, \Gamma_{K_8}$ and Γ_{K_9} associated with the cut elements $K_2, K_3, K_4, K_5, K_6, K_8$ and K_9 , see Figure 3.4a. The cut elements consist of their active fluid volume-cells

$$\begin{aligned} \Omega_{K_2}^b &= \{V_2\}, & \Omega_{K_3}^b &= \{V_3\}, & \Omega_{K_4}^b &= \{V_4\}, \\ \Omega_{K_5}^b &= \{V_5, V_6\}, & \Omega_{K_6}^b &= \{V_7\}, & \Omega_{K_8}^b &= \{V_9\}, \\ \Omega_{K_9}^b &= \{V_{10}\}. \end{aligned} \quad (3.5)$$

All cut elements with the exception of K_5 consist of one active fluid volume-cell, while K_5 is divided into two non-connected active fluid volume-cells. For elements, which are not interested with Γ^{FF} , i.e. K_1 and K_7 , the fluid volume-cell is the element itself, see Figure 3.4b, and it can be expressed by

$$\Omega_{K_1}^b = \{V_1 \equiv K_1\}, \quad \Omega_{K_7}^b = \{V_8 \equiv K_7\}. \quad (3.6)$$

Consequently, based on the volume-cell representation, the background fluid subdomain can be described as

$$\Omega^b = \bigcup_{K \in \mathcal{T}^*} \Omega_K^b = \bigcup_{K \in \mathcal{T}^*} \bigcup_{V \in \Omega_K^b} V. \quad (3.7)$$

Furthermore, based on the subdivision of the interface Γ^{FF} into boundary element parts associated with the volume cell, as depicted in Figure 3.4a, the Γ^{FF} can be expressed as

$$\Gamma^{\text{FF}} = \bigcup_{K \in \mathcal{T}^\Gamma} \bigcup_{V \in \Omega_K^b} (\Gamma_K \cap \bar{V}), \quad (3.8)$$

with \bar{V} denoting the boundary of the volume-cell V . Considering the volume-cell information, the volume-cell based standard finite element space of continuous approximations can be reformulated as

$$V_h^b := \{v \in C^0(\Omega^b) : v|_V \in Q^1(K) \forall V \in \Omega_K^b, \forall K \in \mathcal{T}^*\}, \quad (3.9)$$

where Q^1 defines the polynomial of order at most 1. The element's volume-cell approximation is based on the standard polynomial shape functions N_i^b of the underlying background fluid element K and can be written as

$$v|_V = \sum_{i=1}^{n_{en}} N_i^b(x) \cdot v^i, \quad (3.10)$$

where n_{en} denotes the number of nodes in element K . As it can be seen in Figure 3.4b, some elements involve more than one non-connected active fluid volume-cells, such as element K_5 . In order to approximate independent solutions at different sides of the interface within one fluid element more than one set of degrees of freedom (DOF-set) have to be used. The number of DOF-sets of a node depends on the connection between the volume-cells, which will be described in detail in the following section. Hence, in (3.10) the degrees of freedom v^i are assigned to the respective volume-cell V . Again, in the following section, the formulation is adopted from Schott and Wall [154].

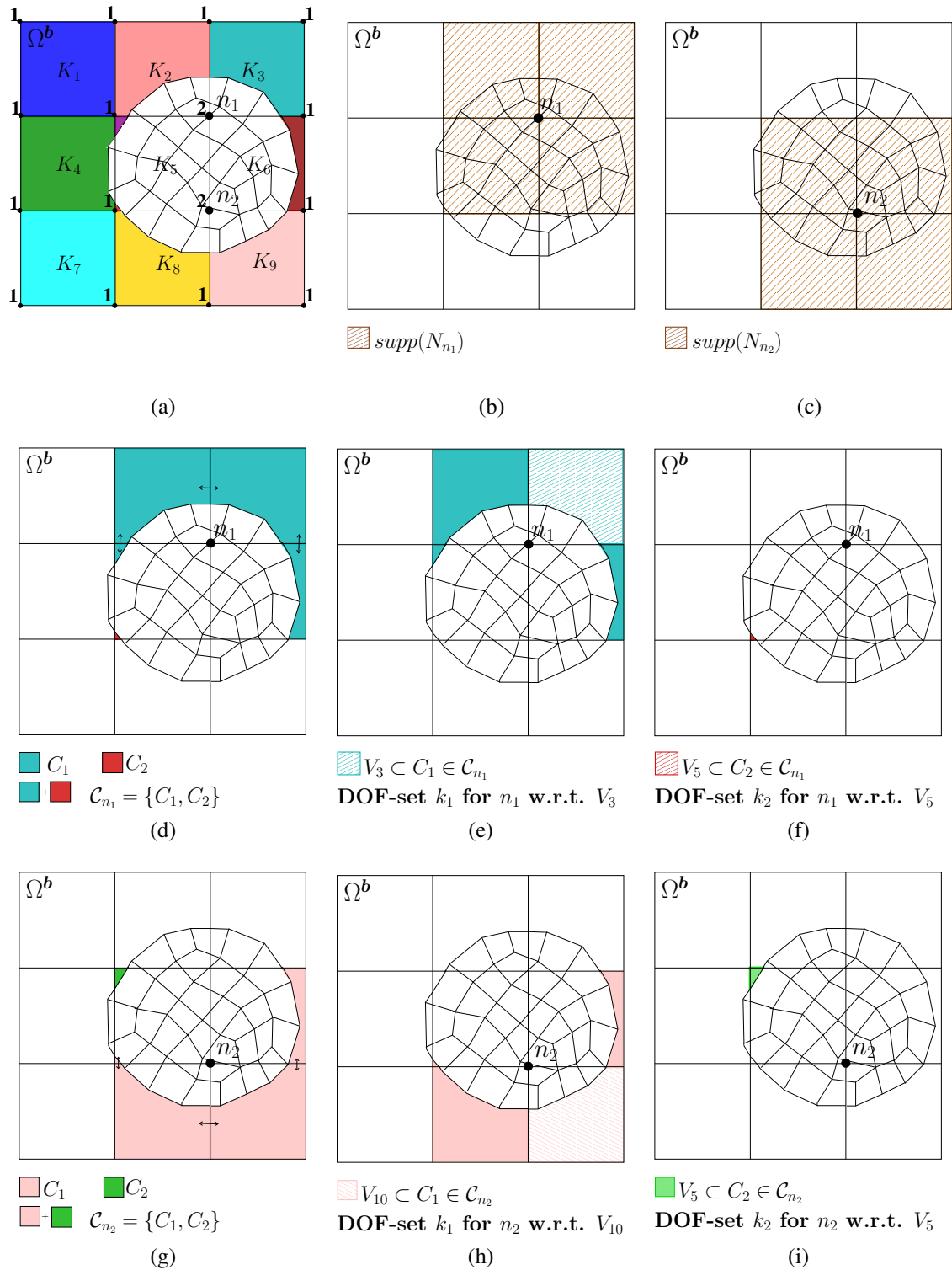


Figure 3.5: Illustration of DOF-management algorithm.

3.2.3 A DOF-management algorithm for complex topologies

In this section, a DOF-management algorithm, introduced by Schott and Wall [154], will be reviewed for background fluid mesh. To approximate the solution accurately for finite elements with more than one non-connected volume-cells, multiple DOF-sets are used. The DOF-management algorithm is based on two phases.

In the phase I, the number of DOFs for each node is determined. Afterwards, in phase II, for each volume-cell, the respective DOF-numbers of all nodes of its underlying element are assigned. This volume-cell based DOF-set information is then used for the assembly procedure of discrete weak formulation.

The number of required DOFs for a node n is influenced by the support of the shape functions of the node N_n , which is denoted as $\text{supp}\{N_n\}$. The $\text{supp}\{N_n\}$ is defined by the patch of elements which surround the node. Therefore, all the active fluid volume-cells, which are located in $\text{supp}\{N_n\}$ influence the DOFs of the node n . For the purpose of determining the number of DOFs required for a node, the number of connected active fluid volume-cells within $\text{supp}\{N_n\}$ of node has to be found. The connected active volume-cells are identified by the facets between the elements. In a 2D case, the facets are reduced to a 1D line, while in a 3D case they become arbitrary shaped polygons between two volume-cells. Mathematically, as introduced in Schott and Wall [154], the connections between the active fluid volume-cells are expressed by

$$C := \{V \subset \text{supp}\{N^n\} \cup \Omega^b | \tilde{V} \in C : \exists \text{PATH}_C(V, \tilde{V})\} \quad (3.11)$$

with

$$\begin{aligned} \text{PATH}_C(V, \tilde{V}) &:= (V = V_0, V_1, \dots, V_{k-1}, V_k = \tilde{V}) \\ &\text{with } V_j \cap V_{j+1} = f \text{ facet}, V_i \in C, i = 0, \dots, k. \end{aligned} \quad (3.12)$$

PATH_C denotes the connection between the volume-cells via facets. The set of the connections with respect to the shape-function support of the node n is then referred to as \mathcal{C}_n , i.e. $\mathcal{C}_n = \{C_1, C_2, \dots\}$. For every connection of volume-cells $C \subset \mathcal{C}_n$, the respective node obtains a DOF-set, which can be either a physical or ghost DOF-set. However, a node can have at most one physical DOF-set. The number of DOF-sets for a node is then equal to $|\mathcal{C}_n|$, which denotes the number of elements of \mathcal{C}_n .

In the next phase of the algorithm, every volume-cell obtains the respective DOF index for all nodes of its underlying element. In the phase I, every DOF of a node has been assigned to a connection of volume-cells $C_k \in \mathcal{C}_n$. Therefore, every node in combination of a volume-cell is already connected to one connection of volume-cells C_k . In this step, each volume-cell obtains the index k of volume-cell connections C_k as its DOF-set index for each node n of the element K . The volume-cell based DOF-set information $(k_1, k_2, \dots, k_{n_{en}})$ is then used in assembly procedure of the weak formulation.

In Figure 3.5, the DOF-management algorithm is demonstrated for two nodes n_1 and n_2 using bilinear elements in a 2D case. The same numbering of elements and volume-cells as in Figure 3.4 is chosen. Figure 3.5a shows the number of DOF-sets related to all nodes of elements K_1, \dots, K_9 . The nodes n_1 and n_2 have two DOF-sets. All other nodes carry one DOF-set. The $\text{supp}\{N_n\}$ of the nodes n_1 and n_2 are shown in Figures 3.5b and 3.5c, respectively. Figures 3.5d, 3.5e and 3.5f refer to DOF-management procedure of the node n_1 . First, the connected volume-cells in $\text{supp}\{N_n\}$ of the the node n_1 have to be determined. As depicted in Figure 3.5d, two

non-connected volume-cell connections, C_1 and C_2 , exist in $\text{supp}\{N_{n_1}\}$. The arrows show the connections of the volume-cells through the facets. As there are two connections of volume-cells for the node n_1 , i.e. $|\mathcal{C}_{n_1}| = 2$, the node n_1 obtains two DOF-sets. In Figures 3.5e and 3.5f, the phase II of the algorithm for Node n_1 concerning the volume-cells $V_3 \subset C_1$ and $V_5 \subset C_2$ is shown. As the volume-cell V_3 belongs to the connection C_1 , the DOF-set key k_1 is assigned to n_1 in combination of V_3 (Figure 3.5e). For n_1 in combination of V_5 , for which holds $V_5 \subset C_2$, the DOF-set key k_2 is assigned (Figure 3.5f).

The DOF-management algorithm for the Node n_2 is depicted in Figures 3.5g, 3.5h and 3.5i. In the first phase, the number of DOF-sets according to the amount of volume-cells connections is determined, which is 2, as two volume-cell connections in $\text{supp}\{N_{n_2}\}$ exist, i.e. $|\mathcal{C}_{n_2}| = 2$ (see Figure 3.5g). Afterwards, DOF-set keys for n_2 regarding volume-cells V_{10} and V_5 based on the associated connections are assigned (Figures 3.5h and 3.5i).

3.2.4 Numerical integration

As already shown in Section 3.2.2, the cut algorithm decomposes the elements in the physical background fluid subdomain into volume-cells (3.7), and the interface Γ^{FF} into boundary segments, which are associated to the volume-cells (3.8). In order to perform integration of the weak form, i.e. evaluating the stiffness matrix for the cut elements, the shape functions and their derivatives have to be integrated over the resulting irregularly shaped volume-cells. The usual Gaussian quadrature rule, which is used for regular elements can not be used in cut elements and, thus, the numerical integration in XFEM needs special care.

The straightforward and mostly used approach for integration over the irregular shaped volume-cells is the tessellation method, as for example in Gerstenberger and Wall [85], Sukumar et al. [164] and Massing et al. [131]. In this approach, the volume-cells V_i are decomposed into regular shaped sub-volume-cells, which are generally tetrahedra or hexahedra. These sub-volume-cells, which are aligned along the interface, are called *integration-cells*. The integration-cells are then transformed to the parameter space of the cell, and then the Gaussian rules are applied in the parameter space of the cell. As the quadrature points are defined within the parameter space of the cells, they have to be transformed to the element parameter space using appropriate interpolations. Finally, the integration over the volume-cell is performed by collecting the integration points of all integration-cells. The integration over the boundary segments performs in a similar way. First, the boundary interface Γ_{K_i} associated to a volume-cell is subdivided into regular shaped geometries, the so called *boundary integration-cells*. The boundary integration-cells are then transformed into a two-dimensional cell parameter space. Also here, the standard Gaussian integration rules are applied in the parameter space of the boundary integration-cell and some transformations from the boundary integration-cell parameter space to element parameter space and finally to physical space are required. The visualization of the coordinate systems and the complete overview of all required transformations is given in Henke [101] and Schott [153]. Although tessellation delivers accurate results, its applicability to complex problems is difficult. The division of volume-cells into integration and boundary integration-cells is a time-consuming process. Moreover, the decomposition procedure in 3D is complicated to implement and challenging in terms of robustness. Particularly when dealing with problems including moving interfaces like FSI problems, where the decomposition of complex volume-cells has to be performed at every time step. Another drawback of the tessellation approach is the high number

of Gauss point, required in integration-cells. The reason is that the integration-cells are usually arbitrarily oriented in the background element parameter space and not necessarily oriented to the mesh, where higher order polynomials occur. In Gerstenberger [82], an investigation for the required number of Gauss points is given.

Another class of integration methods in XFEM are the adaptive quadrature methods. Unlike the tessellation method, the integration-cells are not aligned to the interface, see for example Strouboulis et al. [161] and Xiao and Karihaloo [180]. To keep the error small, the size of the integration-cells has to be very small, Sudhakar and Wall [162]. The number of the required Gauss points is therefore higher and in many cases accurate results are not achieved.

Another class of methods is based on using moment fitting equations. In these methods, the moment fitting equations are used to construct quadrature rules for complex 2D and 3D shapes. To obtain a quadrature rule for such complex shapes of order n , all the monomials $\phi = \{x^i y^j z^k, i+j+k \leq n\}$ have to be integrated over the volume-cell. Afterwards a quadrature is fit to integrate these monomials exactly. Different methods are used to integrate ϕ . Mousavi and Sukumar [143] uses the Lasserre's method to integrate the base functions. The use of Lasserre's method restricts the applicability of method to convex volumes. Sudhakar and Wall [162] applied the divergence theorem to integrate ϕ . The divergence theorem enables the integration over convex and concave volume cells. However, as investigated in Sudhakar and Wall [162], it is difficult to obtain the location of the quadrature points in 3D problems and the achieved results are not as accurate as the tessellation approach.

Another class of methods use divergence theorem for numerical integration of polynomials over complex polyhedra. Using the divergence theorem, the domain integral is transformed into boundary integrals, i.e. integrals over the boundaries of the domain, which are the facets of the polyhedra. The facet integrals are easily computed with the help of quadratures available for regular shaped boundary integration-cells as triangles and quadrilaterals. Most of the available methods of this kind assume that the integrand is predefined, or symbolic computations are used during the integration process, see Sudhakar et al. [163] for more detail. In the recent work of Sudhakar et al. [163], the divergence theorem is applied to FEM problems, without using symbolic computation packages, since using symbolic computation packages would reduce the efficiency and is not desirable in the context of FEM. Hereby, the need of symbolic computation in the transformation procedure is eliminated by using the one-dimensional Gauss quadrature rule. In the following a short overview of this procedure is given. The application of divergence theorem converts the domain integral into integrals over the facets of the volume-cell

$$\int_{\mathcal{R}} \nabla \cdot \mathbf{F} d\mathcal{R} = \int_{\mathcal{S}} \mathbf{F} \cdot \mathbf{n} d\mathcal{S}. \quad (3.13)$$

Hereby, \mathcal{R} denotes the region in \mathbb{R}^3 bounded by the surface \mathcal{S} and \mathbf{n} denotes the outward pointing normal of \mathcal{R} on \mathcal{S} . Since the integrand of interest (\mathcal{F}) is a scalar, in order to use the divergence theorem, it should be expressed as the divergence of a vector as

$$\nabla \cdot \mathbf{F} = \mathcal{F}. \quad (3.14)$$

Using

$$\mathbf{F} = \mathcal{G}(x)\mathbf{i} + 0\mathbf{j} + 0\mathbf{k}, \quad (3.15)$$

with i, j and k denoting unit normal vectors along x -, y - and z -directions, respectively, results in the line integration

$$\mathcal{G}(x) = \int_{\kappa}^x \mathcal{F} dx. \quad (3.16)$$

Hereby, κ is a reference point, which is needed to compute $\mathcal{G}(x)$. Using the equations (3.14) and (3.15) converts the expression (3.13) to

$$\int_{\mathcal{R}} \mathcal{F} d\mathcal{R} = \int_S \mathcal{G}(x) n_x d\mathcal{S}, \quad (3.17)$$

with n_x the component of \mathbf{n} along x -direction. The equation (3.17) can be written as

$$\int_{\mathcal{R}} \mathcal{F} d\mathcal{R} = \sum_{i=1}^{N_f} \int_{F_i} \mathcal{G}(x) n_x dF_i, \quad (3.18)$$

where N_f is the total number of the facets and F_i denotes the i^{th} facet of the polyhedra. If $\mathcal{G}(x)$ is available, the equation (3.18) can be directly evaluated. In order to avoid symbolic computations, the one-dimensional Gauss quadrature rule is applied to compute $\mathcal{G}(x)$.

The integration procedure for 2D polygons and 3D polyhedra is described in Sudhakar et al. [163] in detail. The results demonstrated in Sudhakar et al. [163] show the accuracy and efficiency of the proposed method, which is comparable to tessellation method. Moreover, in contrast to tessellation technique the method is easy-to-implement and robust. In the present work, along with tessellation technique, this recently developed technique has been applied.

3.3 Enforcement of fluid-fluid interface conditions

In this section, the weak enforcement of coupling conditions at the embedded fluid interface Γ^{FF} , which is the main challenge of the embedded fluid formulation, will be discussed. For applicability of such fluid patches in complex FSI problems it is crucial to satisfy high demands on the coupling between background fluid and embedded fluid subdomains. This coupling needs to be accurate, robust and independent of the interface position or the complexity of the shape of embedded fluid subdomain. Furthermore, it has to be applicable to complex three-dimensional problems. Taking into account the weak form of the transient incompressible Navier-Stokes equations, given in Section 2.3.7, the weak formulation of embedded fluid formulation after partial integration on both fluid subdomains, Ω^b and Ω^e , reads as

$$\begin{aligned} & (\mathbf{v}^b, \rho^f \frac{\partial \mathbf{u}^b}{\partial t} \Big|_x)_{\Omega^b} + (\mathbf{v}^b, \rho^f \mathbf{u}^b \cdot \nabla \mathbf{u}^b)_{\Omega^b} \\ & + (q^b, \nabla \cdot \mathbf{u}^b)_{\Omega^b} - (\nabla \cdot \mathbf{v}^b, p^b)_{\Omega^b} + (\boldsymbol{\epsilon}(\mathbf{v}^b), 2\mu \boldsymbol{\epsilon}(\mathbf{u}^b))_{\Omega^b} \\ & \quad + \langle \mathbf{v}^b, p^b \cdot \mathbf{n}^b - 2\mu \boldsymbol{\epsilon}(\mathbf{u}^b) \cdot \mathbf{n}^b \rangle_{\Gamma^{\text{FF}}} \\ & + (\mathbf{v}^e, \rho^f \frac{\partial \mathbf{u}^e}{\partial t} \Big|_x)_{\Omega^e} + (\mathbf{v}^e, \rho^f \mathbf{c} \cdot \nabla \mathbf{u}^e)_{\Omega^e} \\ & + (q^e, \nabla \cdot \mathbf{u}^e)_{\Omega^e} - (\nabla \cdot \mathbf{v}^e, p^e)_{\Omega^e} + (\boldsymbol{\epsilon}(\mathbf{v}^e), 2\mu \boldsymbol{\epsilon}(\mathbf{u}^e))_{\Omega^e} \\ & \quad + \langle \mathbf{v}^e, p^e \cdot \mathbf{n}^e - 2\mu \boldsymbol{\epsilon}(\mathbf{u}^e) \cdot \mathbf{n}^e \rangle_{\Gamma^{\text{FF}}} \\ & = \langle \mathbf{v}^b, \bar{\mathbf{h}}^b \rangle_{\partial \Omega_N^b} + (\mathbf{v}^b, \rho^f \mathbf{b}^b)_{\Omega^b} + (\mathbf{v}^e, \rho^f \mathbf{b}^e)_{\Omega^e}. \end{aligned} \quad (3.19)$$

The terms at Γ^{FF} result from the fact that the test functions \mathbf{v}^b and \mathbf{v}^e do not vanish at the fluid-fluid interface Γ^{FF} . Defining $\mathbf{n} := \mathbf{n}^b = -\mathbf{n}^e$ and the jump operator $\llbracket f \rrbracket := f^b - f^e$ at the shared interface, the weak form (3.19) becomes

$$\begin{aligned}
& (\mathbf{v}^b, \rho^f \frac{\partial \mathbf{u}^b}{\partial t} \Big|_x)_{\Omega^b} + (\mathbf{v}^b, \rho^f \mathbf{u}^b \cdot \nabla \mathbf{u}^b)_{\Omega^b} \\
& + (q^b, \nabla \cdot \mathbf{u}^b)_{\Omega^b} - (\nabla \cdot \mathbf{v}^b, p^b)_{\Omega^b} + (\boldsymbol{\epsilon}(\mathbf{v}^b), 2\mu \boldsymbol{\epsilon}(\mathbf{u}^b))_{\Omega^b} \\
& + (\mathbf{v}^e, \rho^f \frac{\partial \mathbf{u}^e}{\partial t} \Big|_x)_{\Omega^e} + (\mathbf{v}^e, \rho^f \mathbf{c} \cdot \nabla \mathbf{u}^e)_{\Omega^e} \\
& + (q^e, \nabla \cdot \mathbf{u}^e)_{\Omega^e} - (\nabla \cdot \mathbf{v}^e, p^e)_{\Omega^e} + (\boldsymbol{\epsilon}(\mathbf{v}^e), 2\mu \boldsymbol{\epsilon}(\mathbf{u}^e))_{\Omega^e} \\
& \quad \langle \llbracket \mathbf{v}, p \cdot \mathbf{n} - 2\mu \boldsymbol{\epsilon}(\mathbf{u}) \cdot \mathbf{n} \rrbracket \rangle_{\Gamma^{\text{FF}}} \\
& = \langle \mathbf{v}^b, \bar{\mathbf{h}}^b \rangle_{\partial \Omega_N^b} + (\mathbf{v}^b, \rho^f \mathbf{b}^b)_{\Omega^b} + (\mathbf{v}^e, \rho^f \mathbf{b}^e)_{\Omega^e}.
\end{aligned} \tag{3.20}$$

It should be noted that in (3.19) and (3.20) the coupling conditions

$$\mathbf{u}_{\Gamma^{\text{FF}}}^b = \mathbf{u}_{\Gamma^{\text{FF}}}^e \quad \forall x \in \Gamma^{\text{FF}} \tag{3.21}$$

and

$$\boldsymbol{\sigma}^b \cdot \mathbf{n}^b = -\boldsymbol{\sigma}^e \cdot \mathbf{n}^e \quad \forall x \in \Gamma^{\text{FF}} \tag{3.22}$$

have not been included yet. In this work, we will make use of the following weighted interface average operators

$$\{a\} := \kappa^b a^b + \kappa^e a^e, \quad \langle a \rangle := \kappa^e a^b + \kappa^b a^e, \tag{3.23}$$

where the weights $\kappa^e, \kappa^b \geq 0$ are real numbers satisfying $\kappa^e + \kappa^b = 1$. Then, for two sufficiently smooth functions x and y the following relationship holds

$$\llbracket xy \rrbracket = \langle x \rangle \llbracket y \rrbracket + \llbracket x \rrbracket \{y\}. \tag{3.24}$$

Applying relation (3.24), the flux coupling condition in the fifth line of (3.20) is transformed to

$$\langle \llbracket \mathbf{v}, p \cdot \mathbf{n} - 2\mu \boldsymbol{\epsilon}(\mathbf{u}) \cdot \mathbf{n} \rrbracket \rangle_{\Gamma^{\text{FF}}} = \langle \llbracket \mathbf{v} \rrbracket, \{p \cdot \mathbf{n} - 2\mu \boldsymbol{\epsilon}(\mathbf{u}) \cdot \mathbf{n}\} \rangle_{\Gamma^{\text{FF}}}. \tag{3.25}$$

Considering the special discretizations of embedded fluid and the background fluid subdomains, using classical and cut finite elements, respectively, as shown in Section 3.2, the semi-discrete formulation of embedded fluid formulation without any coupling terms becomes:

Find $(\mathbf{u}_h^e, p_h^e) \in V_h^e \times Q_h^e$ and $(\mathbf{u}_h^b, p_h^b) \in V_h^b \times Q_h^b$ such that $\forall (\mathbf{v}_h^e, q_h^e) \in V_h^e \times Q_h^e$ and $\forall (\mathbf{v}_h^b, q_h^b) \in V_h^b \times Q_h^b$ holds

$$\begin{aligned}
& (\mathbf{v}_h^b, \rho^f \frac{\partial \mathbf{u}_h^b}{\partial t} \Big|_x)_{\Omega^b} + (\mathbf{v}_h^b, \rho^f \mathbf{u}_h^b \cdot \nabla \mathbf{u}_h^b)_{\Omega^b} \\
& + (q_h^b, \nabla \cdot \mathbf{u}_h^b)_{\Omega^b} - (\nabla \cdot \mathbf{v}_h^b, p_h^b)_{\Omega^b} + (\boldsymbol{\epsilon}(\mathbf{v}_h^b), 2\mu \boldsymbol{\epsilon}(\mathbf{u}_h^b))_{\Omega^b} \\
& + (\mathbf{v}_h^e, \rho^f \frac{\partial \mathbf{u}_h^e}{\partial t} \Big|_x)_{\Omega^e} + (\mathbf{v}_h^e, \rho^f \mathbf{c} \cdot \nabla \mathbf{u}_h^e)_{\Omega^e} \\
& + (q_h^e, \nabla \cdot \mathbf{u}_h^e)_{\Omega^e} - (\nabla \cdot \mathbf{v}_h^e, p_h^e)_{\Omega^e} + (\boldsymbol{\epsilon}(\mathbf{v}_h^e), 2\mu \boldsymbol{\epsilon}(\mathbf{u}_h^e))_{\Omega^e} \\
& \quad + \langle \llbracket \mathbf{v}_h \rrbracket, \{p_h \cdot \mathbf{n} - 2\mu \boldsymbol{\epsilon}(\mathbf{u}_h) \cdot \mathbf{n}\} \rangle_{\Gamma^{\text{FF}}} \\
& = \langle \mathbf{v}_h^b, \bar{\mathbf{h}}^b \rangle_{\partial \Omega_N^b} + (\mathbf{v}_h^b, \rho^f \mathbf{b}^b)_{\Omega^b} + (\mathbf{v}_h^e, \rho^f \mathbf{b}^e)_{\Omega^e}.
\end{aligned} \tag{3.26}$$

Hereby, equal-order continuous approximations on 3D linear hexahedral elements for all velocity components, u_h^i, v_h^i , ($i = 1, 2, 3$) and the pressure fields of both fluid subdomains, p_h, q_h , are used such that

$$\mathbf{v}_h^b, \mathbf{u}_h^b \in V_h^b := \{\mathbf{v} \in [C^0(\Omega^b)]^3 : \mathbf{v}|_V \in [Q^1(K)]^3 \forall V \in \Omega_K^b, \forall K \in \mathcal{T}^*\}, \quad (3.27)$$

$$q_h^b, p_h^b \in Q_h^b := \{q \in C^0(\Omega^b) : q|_V \in Q^1(K) \forall V \in \Omega_K^b, \forall K \in \mathcal{T}^*\}, \quad (3.28)$$

$$\mathbf{v}_h^e, \mathbf{u}_h^e \in V_h^e := \{\mathbf{v} \in [C^0(\Omega^e)]^3 : \mathbf{v}|_K \in [Q^1(K)]^3 \forall K \in \mathcal{T}^e\}, \quad (3.29)$$

$$q_h^e, p_h^e \in Q_h^e := \{q \in C^0(\Omega^e) : q|_K \in Q^1(K) \forall K \in \mathcal{T}^e\}. \quad (3.30)$$

Hereby, $Q^1(K)$ defines polynomial of order at most 1 on a hexahedral element K , which is used in this work.

The focus of following part of the work is the weak imposition of the coupling conditions (3.21) and (3.22), which have not been included in (3.26) yet. In the following, first, an overview of different coupling methods, including the classical as well as the relevant methods for 3D-incompressible Navier-Stokes equations, are given. Next, the main methods, which can be used for the weak coupling of both fluid subdomains, are explained in detail.

3.3.1 Overview of different methods

The weak enforcement of the coupling conditions, has been an active research topic in the last years. The imposition of boundary conditions in a weak sense occurs in different contexts. For instance, between element boundaries of neighboring elements in discontinuous Galerkin approaches, where the constraint is aligned to the mesh, imposing Dirichlet boundary conditions in a mesh that does not match the boundary of the computational domain, as in the context of fictitious domain methods or immersed boundary methods, see e.g. Codina and Baiges [51], or mesh tying of two non-conforming discretizations, see e.g. Ehrl et al. [66]. The coupling of background and embedded fluid subdomains belongs to the wide class of interface problems, where the constraints have to be enforced along an embedded interface, which is not aligned to the element boundaries. Other examples for such problems are premixed combustion problems, see e.g. Henke [101] or two-phase flow problems, see e.g. Schott et al. [155].

A classical method for imposing constraints weakly is the Lagrange multiplier method introduced by Babuška [6]. Lagrange multiplier approach has been applied to XFEM problems, for example, in the early works of Ji and Dolbow [112]. The constraint is enforced by adding an additional parameter, the Lagrange multiplier, to the system. However, the Lagrange multiplier method has shown several difficulties when dealing with interface problems. It has been shown by Ji and Dolbow [112], Simone [158] and Moës et al. [140] that a most convenient choice of the Lagrange multiplier space results in instabilities at the interface and decreases the overall convergence rate. The reason is that the Lagrange multiplier space needs to satisfy the 'inf-sup' condition, or known as Ladyzhenskaya-Babuška-Brezzi (LBB) condition, see Brezzi [28] and Babuška [5]. Stable Lagrange multiplier spaces have been developed by Moës et al. [140] and Béchet et al. [16]. These approaches are based on coarsening the discretization of the multiplier with respect to bulk mesh. Another remedy is to stabilize the Lagrange multiplier method, which has been discussed in Mourad et al. [142], and Dolbow and Franca [61]. Nitsche's method, Nitsche [144], which will be discussed in detail in the following, can be considered as a stabilized Lagrange multiplier method by adding a stabilization term. However, all these studies

are limited to two-dimensional problems. The Lagrange multiplier method requires additionally a surface mesh, which is difficult to generate robustly for three-dimensional problems. The Lagrange multiplier method has been applied to two-dimensional fixed-grid FSI problems and embedded fluid patches by Gerstenberger and Wall [83, 84].

Another class of methods are the penalty methods. In contrast to Lagrange multiplier method, the penalty method does not introduce any new primary variable to the system and penalize the constraint by adding a penalty parameter, see e.g. Hautefeuille et al. [98]. This makes the method easy to implement. Furthermore, no special care regarding stability issues has to be taken. The main drawback of this method is that the method is variationally inconsistent, i.e. the exact solution of the differential equation does not satisfy the weak formulation. The desired problem is only solved if the penalty parameter goes to infinity, Hautefeuille et al. [98], Sanders et al. [150]. This leads to a further difficulty, which is the choice of the penalty parameter. A too large penalty parameter leads to ill-conditioning of the system, whereas choosing a small parameter results in a bad approximation of the solution. An overview of penalty methods for flow problems is given by Reddy [148].

Nitsche's method was introduced to enforce Dirichlet boundary conditions weakly, by Nitsche [144]. It can be said to be an intermediate between the both mentioned methods, as it combines the advantages of them. The formulation is variationally consistent, it is a stabilized method, no primary variable, as in Lagrange multiplier method, is added, and, thus, it can be easily extended to three-dimensional problems. Hence, Nitsche's method can be considered as a consistent penalty formulation or a stabilized Lagrange multiplier method. The idea behind it is to replace the Lagrange multipliers through their physical representation, the fluxes at the interface. Nitsche's method has been first applied to elliptic interface problems on intersected meshes by Hansbo and Hansbo [92]. Later, Becker et al. [19] studied Nitsche's method for incompressible elasticity problems. In Hansbo et al. [93] an approximation of second order elliptic problems on composite grids based on Nitsche's method has been proposed. Further studies have been done by Dolbow and Harari [59]. An overview of Nitsche's method for interface problems is given by Hansbo [94]. Nitsche's method has been also used for discontinuous Galerkin methods, e.g. by Hansbo and Larson [95] for incompressible elasticity. For Nitsche's method, as for penalty methods, a user-defined stabilization parameter is required. However, in contrast to penalty method, the Nitsche parameter is viewed rather as a stabilization parameter than a penalty parameter and it does not need to be chosen large in order to asymptotically enforce the constraint, see Hautefeuille et al. [98]. The Nitsche parameter can be estimated for arbitrary shape, form and polynomial order of elements through a series of local eigenvalue problems.

Another approach applied to fluid-structure interaction based on a mixed/hybrid formulation was proposed by Gerstenberger and Wall [85], where an additional discontinuous element stress field is defined on cut background mesh to enforce the boundary/coupling condition. In contrast to the classical Lagrange multiplier method, the additional stress unknown is introduced as a field in the domain, which acts as a traction force at the interface. Furthermore, the method involves an implicit stabilization in the formulation, which is automatically incorporated in the formulation independent of the polynomial order or the spatial discretization. This implicit stabilization corresponds to the estimation of the Nitsche parameter via solving local eigenvalue problems, however, in contrast to Nitsche's method, it is included automatically in the formulation and evolves from the weak formulation itself. Moreover, the method allows for complete

condensation of additional stress unknowns on the element level. In Shahmiri et al. [157], this method has been applied to embed fluid patch meshes into background fluid mesh.

Baiges et al. [11] introduced a symmetric variant of mixed/hybrid stress-based method of Gerstenberger and Wall [85] and showed the similarity of the symmetric stress-based method to Nitsche's method. Similar to the mixed/hybrid stress-based method of Gerstenberger and Wall [85], this method makes use of an additional discontinuous stress field based on viscous stresses to enforce the boundary/coupling conditions. Also for this method, the extra stress field can then be condensed from the linear system on the element level.

In the following, the focus is on the three last methods mentioned above, Nitsche's method, mixed/hybrid Cauchy stress-based method (MHCS) of Gerstenberger and Wall [85] and symmetric variant of it introduced by Baiges et al. [11], stated as a mixed/hybrid viscous stress-based formulation (MHVS) in this work, which are all applicable to three-dimensional embedded fluid formulation. The differences and similarities in the formulations and solution behaviors will be discussed in the context of embedded fluid formulation. The formulations and notations of MHCS method are closely related to the formulation used in Shahmiri et al. [157]. The formulation of classical Lagrange multiplier method and penalty method for Poisson interface problems can be found for example in Henke [101]. For the formulation of MHVS method applied to Poisson and Stokes problems in context of embedded patches the interested reader is referred to Kruse [119].

3.3.2 Nitsche's method

In this section, Nitsche's method is applied for the weak coupling of background fluid subdomain Ω^b and embedded fluid subdomain Ω^e . In (3.26), the discrete weak formulation of embedded fluid formulation without applying any coupling conditions is given. The semi-discrete embedded fluid formulation of (3.26) including the coupling conditions on the shared interface Γ^{FF} using Nitsche's method becomes:

Find $(\mathbf{u}_h^e, p_h^e) \in V_h^e \times Q_h^e$ and $(\mathbf{u}_h^b, p_h^b) \in V_h^b \times Q_h^b$ such that $\forall (\mathbf{v}_h^e, q_h^e) \in V_h^e \times Q_h^e$ and $\forall (\mathbf{v}_h^b, q_h^b) \in V_h^b \times Q_h^b$ holds

$$\begin{aligned}
 & \boxed{1} \quad \left(\mathbf{v}_h^b, \rho^f \frac{\partial \mathbf{u}_h^b}{\partial t} \Big|_x \right)_{\Omega^b} + \left(\mathbf{v}_h^b, \rho^f \mathbf{u}_h^b \cdot \nabla \mathbf{u}_h^b \right)_{\Omega^b} \\
 & \boxed{2} \quad + \left(q_h^b, \nabla \cdot \mathbf{u}_h^b \right)_{\Omega^b} - \left(\nabla \cdot \mathbf{v}_h^b, p_h^b \right)_{\Omega^b} + \left(\boldsymbol{\epsilon}(\mathbf{v}_h^b), 2\mu \boldsymbol{\epsilon}(\mathbf{u}_h^b) \right)_{\Omega^b} \\
 & \boxed{3} \quad + \left(\mathbf{v}_h^e, \rho^f \frac{\partial \mathbf{u}_h^e}{\partial t} \Big|_x \right)_{\Omega^e} + \left(\mathbf{v}_h^e, \rho^f \mathbf{u}_h^e \cdot \nabla \mathbf{u}_h^e \right)_{\Omega^e} \\
 & \boxed{4} \quad + \left(q_h^e, \nabla \cdot \mathbf{u}_h^e \right)_{\Omega^e} - \left(\nabla \cdot \mathbf{v}_h^e, p_h^e \right)_{\Omega^e} + \left(\boldsymbol{\epsilon}(\mathbf{v}_h^e), 2\mu \boldsymbol{\epsilon}(\mathbf{u}_h^e) \right)_{\Omega^e} \\
 & \boxed{5} \quad + \langle \llbracket \mathbf{v}_h \rrbracket, \{p_h \cdot \mathbf{n}\} \rangle_{\Gamma^{\text{FF}}} - \langle \llbracket \mathbf{v}_h \rrbracket, \{2\mu \boldsymbol{\epsilon}(\mathbf{u}_h) \cdot \mathbf{n}\} \rangle_{\Gamma^{\text{FF}}} \\
 & \boxed{6} \quad - \langle \{q_h \cdot \mathbf{n}\}, \llbracket \mathbf{u}_h \rrbracket \rangle_{\Gamma^{\text{FF}}} - \beta_n \langle \{2\mu \boldsymbol{\epsilon}(\mathbf{v}_h) \cdot \mathbf{n}\}, \llbracket \mathbf{u}_h \rrbracket \rangle_{\Gamma^{\text{FF}}} \\
 & \boxed{7} \quad + \langle \alpha' \llbracket \mathbf{v}_h \rrbracket, \llbracket \mathbf{u}_h \rrbracket \rangle_{\Gamma^{\text{FF}}} \\
 & \boxed{8} \quad = \langle \mathbf{v}_h^b, \bar{\mathbf{h}}^b \rangle_{\partial \Omega_N^b} + \left(\mathbf{v}_h^b, \rho^f \mathbf{b}^b \right)_{\Omega^b} + \left(\mathbf{v}_h^e, \rho^f \mathbf{b}^e \right)_{\Omega^e}.
 \end{aligned} \tag{3.31}$$

The first four lines of (3.31) refer to the weak form of the Navier-Stokes equations of the two fluid subdomains. The terms on the fifth line result from partial integration of the standard Galerkin terms, which remains at Γ^{FF} due to not vanishing test functions and correspond to the fifth line of

(3.26). These viscous and pressure interface terms are called the *consistency terms*. The terms at line six are required for a consistent weak imposition of coupling conditions, i.e. all the coupling terms vanish for an exact solution. It is possible to choose $\beta_n = 1$ or $\beta_n = -1$, which results in a symmetric or non-symmetric viscous part of Nitsche's formulation. The formulation introduced by Nitsche [144] was symmetric to reflect the symmetry of the underlying Poisson problem. The non-symmetric version of Nitsche's method was proposed later by Freund and Stenberg [76]. Choosing $\beta_n = -1$ leads to out-canceling of the viscous interface terms for $(\mathbf{v}_h, q_h) = (\mathbf{u}_h, p_h)$ and results in a better stability behavior. However, it has been shown in Arnold et al. [3] that it can lead to suboptimal convergence behavior. In the recent work of Burman [33], it has been proven for weak imposition of boundary conditions of a Poisson problem that the non-symmetric Nitsche's formulation is stable and results in an optimal convergence behavior in the H^1 -norm for polynomial orders $k \geq 1$. The convergence rate of the error in the L^2 -norm is though sub-optimal with half a power of h . In this work, a symmetric variant of the viscous interface term $\beta_n = 1$ is chosen. Corresponding to the anti-symmetric formulation of standard Galerkin pressure term, a negative sign to the pressure Lagrange multiplier term, $-\langle \{q_h \cdot \mathbf{n}\}, \llbracket \mathbf{u}_h \rrbracket \rangle_{\Gamma^{\text{FF}}}$, has been applied. The terms in the sixth line of (3.31) are referred to as so-called *adjoint consistency terms*. The term in the seventh line is known as *coercivity term*, *Nitsche stabilization term* or *Nitsche penalty term* since it needs to balance the lack of coercivity introduced by the viscous consistency and viscous adjoint consistency terms of symmetric version of Nitsche's formulation. As shown in Burman [33], the non-symmetric version of Nitsche's formulation is stable without the penalty term for uncut elements. The Nitsche stabilization term, again introduces the coupling condition (3.21) consistently with a stabilization parameter α' . In the following the meaning and the choice of the stabilization parameter α' will be discussed.

The stability/coercivity of Nitsche's method

As mentioned above, Nitsche stabilization term, $\langle \alpha' \llbracket \mathbf{v}_h \rrbracket, \llbracket \mathbf{u}_h \rrbracket \rangle_{\Gamma^{\text{FF}}}$, has to balance the negative amount of coercivity due to the viscous consistency and adjoint consistency terms of symmetric version of Nitsche's formulation. The Nitsche stabilization parameter α' has to be sufficient large to ensure coercivity but not too large, to prevent ill-conditioning of the system matrix. Furthermore, a too large penalty parameter α' can cause spurious kinks in the pressure field at the interface region, which results from the over-penalization of the coupling condition (3.21) in a weak sense. An appropriate choice of the stabilization parameter α' is essential to have a stable and accurate solution. It has been shown by Dolbow and Harari [59] and Hautefeuille et al. [98] for Poisson embedded interface problems that the smallest choice of α' depends on a positive constant C_1 , such that the following inequality holds

$$\|\nabla v_h \cdot \mathbf{n}\|_{L_2(\Gamma_K)} \leq C_1 \cdot \|\nabla v_h\|_{L_2(\Omega_K)}. \quad (3.32)$$

This inequality relates the L_2 -norm of the normal fluxes at the interface segments to the L_2 -norm of the gradient on the element domain with a mesh dependent constant C_1 . It holds for the whole domain but also for each of the elements adjacent to the interface. As shown, e.g. by Hautefeuille et al. [98], applying the Cauchy-Schwarz inequality to the viscous standard consistency term and using (3.32) lead to a lower bound of the stabilization parameter α' . Considering the case of linear tetrahedral elements, where $\nabla v_h = \text{const}$, the constant C_1 can be defined by a simple

geometric relation between the surface area and the physical volume as

$$C_1^2 := \frac{\text{meas}(\Gamma_K)}{\text{meas}(\Omega_K)}. \quad (3.33)$$

An optimal choice for the Nitsche stabilization parameter is then given by $\alpha' \gtrsim C_1^2$.

Dependent on the choice of the weights in the average operators in (3.31), κ_b and κ_e , the definition of the consistency terms and adjoint consistency terms alters. Thus, the definition of the stabilization parameter α' depends on the choice of κ_b and κ_e . In Annavarapu et al. [2], the dependency of the stabilization parameter on the weighting of Nitsche's formulation for cut elements is studied and it is shown that an arbitrary choice of Nitsche's weights such that they sum to unity, could lead to a large value of the stabilization parameter. In this work, for simplicity only two cases are considered: the background element weighting for $\kappa_b = 1 = 1 - \kappa_e$ and embedded element weighting for $\kappa_e = 1 = 1 - \kappa_b$. In the following, first, the choice of the stabilization parameter for background element weighting and then for embedded element weighting will be discussed.

For the background element weighting with $\kappa_b = 1$ and $\kappa_e = 0$, the consistency and adjoint consistency terms become

$$\begin{aligned} & + \langle \llbracket \mathbf{v}_h \rrbracket, p_h^b \cdot \mathbf{n} \rangle_{\Gamma^{\text{FF}}} - \langle \llbracket \mathbf{v}_h \rrbracket, 2\mu \boldsymbol{\epsilon}(\mathbf{u}_h^b) \cdot \mathbf{n} \rangle_{\Gamma^{\text{FF}}} \\ & - \langle q_h^b \cdot \mathbf{n}, \llbracket \mathbf{u}_h \rrbracket \rangle_{\Gamma^{\text{FF}}} - \beta_n \langle 2\mu \boldsymbol{\epsilon}(\mathbf{v}_h^b) \cdot \mathbf{n}, \llbracket \mathbf{u}_h \rrbracket \rangle_{\Gamma^{\text{FF}}}. \end{aligned} \quad (3.34)$$

Similar to the work of Dolbow and Harari [59], Hautefeuille et al. [98] and Griebel and Schweitzer [90], and the process described above, a lower bound of Nitsche stabilization parameter α' can be derived from the mesh dependent element-wise constant C_K^b for which the following inverse inequality holds

$$\|\boldsymbol{\epsilon}(\mathbf{v}_h^b) \cdot \mathbf{n}\|_{\Gamma^{\text{FF}} \cap K}^2 \leq C_K^b \cdot \|\boldsymbol{\epsilon}(\mathbf{v}_h^b)\|_{K \cap \Omega^b}^2, \quad (3.35)$$

where $K \in \mathcal{T}^{\text{I}}$ denotes a cut element. The inequality (3.35) shows the relation between the L^2 -norm of viscous fluxes at the interface segment of a cut element K and the L^2 -norm of the strain rate tensor at the physical part of the background fluid element. It can be shown, that the formulation is coercive for an element-wise Nitsche stabilization parameter

$$\alpha'_K := \delta \mu C_K^b, \quad (3.36)$$

with a sufficiently large δ , where δ is independent of h , the position of Γ^{FF} and material properties. However, since the background element weighting is considered, C_K^b in (3.35) depends on the position of the interface Γ^{FF} and, therefore, also on the mesh size h . As mentioned above, for linear tetrahedral elements the parameter C_K^b can be defined by a relation between coupling surface area of the background fluid element and physical background fluid element volume as

$$C_K^b = \frac{\text{meas}(\Gamma^{\text{FF}} \cap K)}{\text{meas}(\Omega^b \cap K)}. \quad (3.37)$$

Equation (3.37) makes the interface position dependency of C_K^b clear, which leads to further difficulties regarding critical cut situations. An example for a critical cut is a sliver cut, as depicted in Figure 3.6a. As it can be seen, for a sliver cut, the physical background fluid element

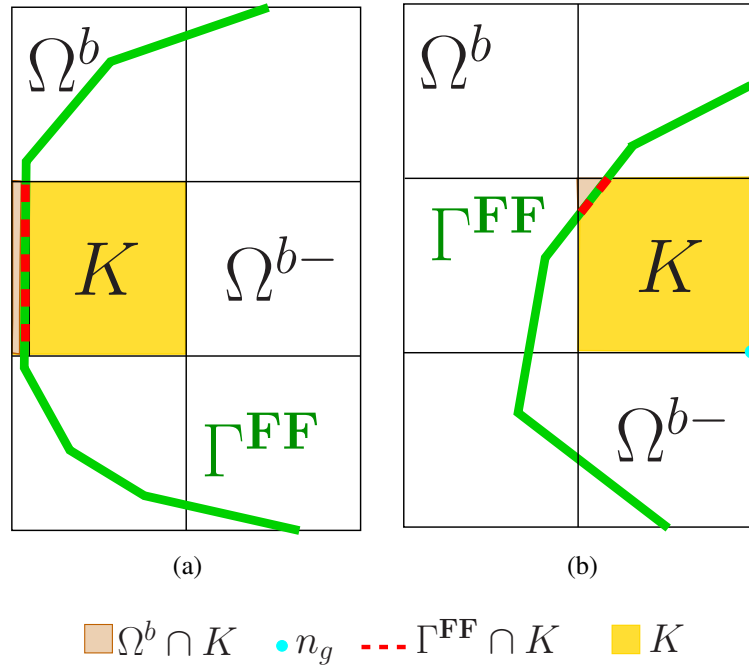


Figure 3.6: Examples of critical cut situations: **(a)** The fluid-fluid interface Γ^{FF} intersects the background fluid domain. The result of the intersection is a critical sliver cut, where the physical volume of the element K tends to zero and surface area remains constant. This results in unboundedness of stabilization parameter α'_K and overweighting of the weak imposition of the coupling conditions and, moreover, in unbounded condition numbers. **(b)** Another example for a critical cut. The physical part of background fluid element is small, thus, the support of the nodal shape functions of ghost-node n_g becomes small. This leads to non-physical values at ghost-node n_g and unbounded condition numbers.

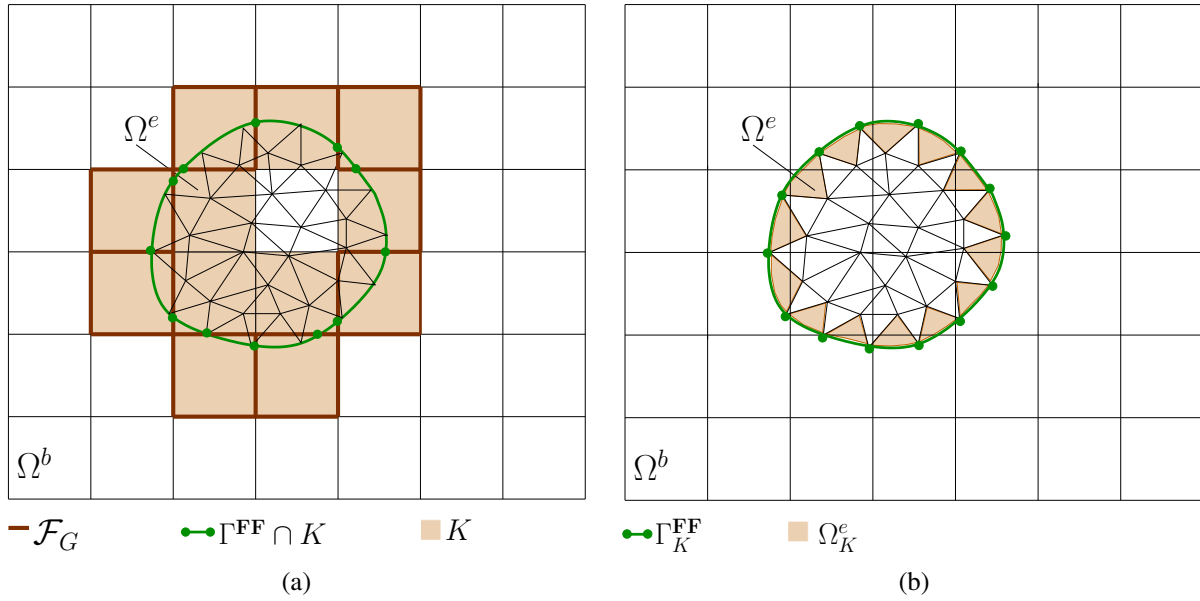


Figure 3.7: **(a)** In the case of background element weighting, the cut elements of background fluid domain and their contribution on shared interface Γ^{FF} affect the mesh dependent element-wise constant C_K^b . To balance the missing coercivity the viscous ghost-penalty operator is applied to \mathcal{F}_G . **(b)** In the case of embedded element weighting, the constant C_K^e and the stabilization parameter α' depend on whole embedded fluid elements which share one side with Γ^{FF} .

$\Omega^b \cap K$ tends to zero, while the coupling surface area $\Gamma^{\text{FF}} \cap K$ stays constant, which result in unboundedness of stabilization parameter α'_K and unbounded condition numbers, as discussed in Burman and Hansbo [39]. Furthermore, as shown in Schott and Wall [154], such a choice of stabilization parameter could lead to a over-weighting of the weak imposition of the coupling condition compared to other domain terms and result in a non-physical solution at the interface region. Another example for a critical cut is depicted in Figure 3.6b, where the physical part of background fluid element, $\Omega^b \cap K$, is small. In this case, the support of the nodal shape functions of ghost-node n_g becomes small, such that not enough information for the node n_g is available to determine its value. This results in unbounded condition numbers, and moreover, in a non-physical ghost-values at n_g if using standard residual-based stabilizations at cut elements, since they are performed only on the small physical background fluid of element K , depicted as $\Omega^b \cap K$ in Figure 3.6b. The fluid instabilities at cut elements will be discussed in Section 3.5. It has to be pointed out that problems with fluid instabilities also appear in the case of the sliver cut, since also there, the physical part of the background element is small, see Figure 3.6a.

To overcome the problems with critical cuts different remedies have been proposed in the context of XFEM. Reusken [149] uses the strategy of blocking the ghost degrees of freedom, when the critical cut situations occur. This strategy is based on removing the volume-cell, when the relative ratio between the physical volume of an element and the element volume becomes smaller than a tolerance. Thus, the elements with small ratio will be considered as uncut elements. This strategy has the main drawback that a tolerance is necessary, which is hard to determine for every cut situation. Moreover, it would only bound the conditioning of the system and would not

overcome the stability issues. Stable-XFEM introduced by Babuška and Banerjee [7], modifies the enrichment functions in order to improve the condition of the system. However, the method is not able to produce independent gradients at the both sides of the interface. To overcome the ill-conditioning and the problem with stability issues, in Burman and Hansbo [38, 39], a viscous *ghost-penalty* operator has been proposed, which has been extended to the Navier-Stokes equations by Schott and Wall [154]. To obtain a stable formulation in the case of background element weighting of Nitsche's formulation, also in this work the ghost-penalty operator

$$j_{\text{GP}}(\mathbf{v}_h^b, \mathbf{u}_h^b) := \sum_{F \in \mathcal{F}_G} \sum_{i=1}^k \int_F \alpha_{\text{GP}} \cdot \mu h_F^{2(i-1)+1} \llbracket D^i \mathbf{v}_h^b \rrbracket : \llbracket D^i \mathbf{u}_h^b \rrbracket ds, \quad (3.38)$$

has been applied. In (3.38), \mathcal{F}_G denotes the set of faces F between active fluid volume-cells around the interface (see Figure 3.7a), k is the highest polynomial order in \mathbf{u}_h^b , and α_{GP} a user-defined parameter. Further, D^i denotes the normal derivative on the faces with the order i . For linear approximations $k = 1$ the ghost-penalty term becomes

$$j_{\text{GP}}(\mathbf{v}_h^b, \mathbf{u}_h^b) := \sum_{F \in \mathcal{F}_G} \int_F \alpha_{\text{GP}} \cdot \mu h_F \llbracket \nabla \mathbf{v}_h^b \rrbracket : \llbracket \nabla \mathbf{u}_h^b \rrbracket ds. \quad (3.39)$$

In (3.38) and (3.39), h_F is the maximal distance from the face F to the opposite faces of the both adjacent elements, i.e. $h_F = \max\{h_{K_1}, h_{K_2}\}$, where K_1 and K_2 are the two neighboring background mesh elements, which share the face F , and h_{K_1} and h_{K_2} the distances of K_1 and K_2 to face F , respectively. The operator $\llbracket \nabla \mathbf{u}_h^b \rrbracket$ denotes the jump in the velocity gradients across the adjacent elements $\llbracket \nabla \mathbf{u}_h^b \rrbracket := \nabla \mathbf{u}_h^b|_{K_1} - \nabla \mathbf{u}_h^b|_{K_2}$. Since we are using continuous shape functions, the jump in the velocity gradients across the adjacent elements can be reduced to $\llbracket \nabla \mathbf{u}_h^b \rrbracket := \nabla \mathbf{u}_h^b \cdot \mathbf{n}^F|_{K_1} - \nabla \mathbf{u}_h^b \cdot \mathbf{n}^F|_{K_2}$, where \mathbf{n}^F denotes a unit normal to the face F . The idea of ghost-penalty operator is a smooth continuation of the available polynomial approximation in the neighboring elements. It transfers the physical information from the physical part of the domain to the ghost domain and, thus, takes control over the non-physical values of the ghost degrees of freedom. It has been shown in Burman and Hansbo [39], and Schott and Wall [154] that if the definition of element-wise Nitsche stabilization parameter α'_K , a measure of coupling surface area to physical domain (3.36), is replaced by a uniform scaling with the element length

$$\alpha'_K := \alpha \frac{\mu}{h}, \quad (3.40)$$

the ghost-penalty operator balances the missing coercivity and leads to a stable formulation. Furthermore, it overcomes the problems with ill-conditioning and over-penalization of the coupling conditions. In (3.40), α is a positive constant independent of the element length, the material parameter or the interface position, and h denotes the volume-equivalent diameter characteristic element length.

The embedded element weighting $\kappa_e = 1 = 1 - \kappa_b$, which has been already introduced in the early work of Hansbo et al. [93] and is the preferred method in the present work, will be discussed in the following.

The consistency and adjoint consistency terms for embedded element weighting read as

$$\begin{aligned} & + \langle \llbracket \mathbf{v}_h \rrbracket, p_h^e \cdot \mathbf{n} \rangle_{\Gamma^{\text{FF}}} - \langle \llbracket \mathbf{v}_h \rrbracket, 2\mu \boldsymbol{\epsilon}(\mathbf{u}_h^e) \cdot \mathbf{n} \rangle_{\Gamma^{\text{FF}}} \\ & - \langle q_h^e \cdot \mathbf{n}, \llbracket \mathbf{u}_h \rrbracket \rangle_{\Gamma^{\text{FF}}} - \beta_n \langle 2\mu \boldsymbol{\epsilon}(\mathbf{v}_h^e) \cdot \mathbf{n}, \llbracket \mathbf{u}_h \rrbracket \rangle_{\Gamma^{\text{FF}}}, \end{aligned} \quad (3.41)$$

with $\beta_n = 1$ for a symmetric Nitsche's formulation. Choosing embedded element weighting circumvents the problems with ill-conditioning of the system and over-penalization as discussed above. In this case, similar to (3.37), the Nitsche stabilization parameter for linear tetrahedral elements can be stated as

$$C_K^e = \frac{\text{meas}(\Gamma^{\text{FF}} \cap K)}{\text{meas}(\Omega^e \cap K)}. \quad (3.42)$$

However, for embedded element weighting of Nitsche's formulation the value of C_K^e is always bounded, since $\text{meas}(\Omega^e \cap K)$ is the entire volume of the embedded element K . Thus, in this case, the element-wise Nitsche stabilization parameter α'_K depends on a constant C_K^e , which is independent of interface position, for which the following inverse inequality holds

$$\|\boldsymbol{\epsilon}(\mathbf{u}_h^e) \cdot \mathbf{n}\|_{\Gamma^{\text{FF}}}^2 \leq C_K^e \|\boldsymbol{\epsilon}(\mathbf{u}_h^e)\|_{\Omega_K^e}^2, \quad (3.43)$$

where $\Omega_K^e := \Omega^e \cap K$ is the entire embedded fluid element K adjacent to the interface and $\Gamma_K^{\text{FF}} := \Gamma^{\text{FF}} \cap K$ denotes the boundary of K at Γ^{FF} . The elements of background and embedded fluid mesh, boundary segments and faces, which are relevant for inverse inequalities (3.35) and (3.43) and for the ghost-penalty operator (3.39), are depicted in Figure 3.7. The element-wise Nitsche stabilization parameter α'_K can then be determined by

$$\alpha'_K := \delta \mu C_K^e, \quad (3.44)$$

with a user-defined constant δ . In Appendix A.1, the derivation of the Nitsche stabilization parameter (3.44) for Stokes problem is given. Griebel and Schweitzer [90] proposed to solve a global eigenvalue problem to find a lower bound for the global parameter C . The value of constant C can be estimated as the maximum eigenvalue of the problem. However, for problems with moving interfaces this global eigenvalue problem has to be solved in every time step and adds significance computational cost to the problem. Therefore, Embar et al. [67] and Hautefeuille et al. [98] proposed to solve a local eigenvalue problem for each element to estimate the element specific parameter C_K . This method is applied to the embedded fluid formulation; for every embedded fluid element adjacent to Γ^{FF} a local eigenvalue problem is solved to estimate the value of C_K^e . This approach provides a reliable and an automatic computation of C_K^e and, consequently, the Nitsche stabilization parameter α'_K . In this way, Nitsche stabilization parameter can be estimated automatically for arbitrary element shapes and forms, and polynomial orders. The maximum eigenvalue of the following eigenvalue problem

$$Av = \lambda Bv, \quad (3.45)$$

with

$$A = \int_{\Gamma_K^{\text{FF}}} (\boldsymbol{\epsilon}(\mathbf{v}_h^e) \cdot \mathbf{n}) \cdot (\boldsymbol{\epsilon}(\mathbf{u}_h^e) \cdot \mathbf{n}) \, ds \quad (3.46)$$

and

$$B = \int_{\Omega_K^e} \boldsymbol{\epsilon}(\mathbf{v}_h^e) : \boldsymbol{\epsilon}(\mathbf{u}_h^e) \, d\Omega, \quad (3.47)$$

gives an estimation of the constant C_K^e . The user-defined constant δ has been chosen at least 2 to ensure stability, see e.g. Embar et al. [67] and Appendix A.1.

Remark: 3.3.1. When using the embedded element weighting, due to balancing the coercivity of the Nitsche's formulation, the ghost-penalty operator (3.39) is not required. However, it is beneficial to also apply the ghost-penalty operator in combination of embedded element weighting, since the ghost-penalty operator takes control over the ghost DOFs of the background fluid mesh in case of critical cuts. Furthermore, using ghost-penalty terms improve the system conditioning, see Burman and Hansbo [38, 39] and Schott and Wall [154].

Remark: 3.3.2. In the case of background element weighting, applying ghost-penalty operator in combination of uniform scaling with the element length of Nitsche parameter (3.40) results in a stable formulation and an appropriate estimation of stabilization parameter, see Burman and Hansbo [38], such that applying a measure of coupling surface area to physical domain of Nitsche stabilization parameter (3.36), is not necessary anymore. Furthermore, as already discussed in this section, with the measure of coupling surface area to physical domain the Nitsche parameter depends on the position of the interface, which, in this case, would vary a lot between elements.

Remark: 3.3.3. Particularly, it is recommended to solve the eigenvalue problem (3.45) for stretched embedded fluid elements, which are the objective of this work in terms of applying an appropriate boundary layer mesh around the structure for FSI problems. As mentioned above, solving local eigenvalue problems provide good estimations for elements with arbitrary shapes and forms. Considering the two definitions of the Nitsche stabilization parameter α' , the definition with unified scaling of the element length (3.40) and measure of coupling surface area to volume (3.44), for an uniform element, it holds $\frac{\text{meas}(\Gamma^{\text{FF}} \cap K)}{\text{meas}(\Omega^e \cap K)} \simeq \frac{1}{h}$. Thus, applying the two different definitions would not lead to significant difference in the value of α' . However, applying (3.40) to stretched embedded elements, would result in an inappropriate estimation of it. Furthermore, as discussed in Embar et al. [67] and mentioned above, solving the eigenvalue problem (3.45) provides a good estimation of Nitsche stabilization parameter for higher order elements.

Matrix formulation

In the following, the matrix formulation of the embedded fluid formulation with Nitsche's method will be accomplished. For this purpose, first, a time discretization of the semi-discrete embedded fluid formulation (3.31) is given. It has to be noted that the fluid stabilization terms are not included yet, i.e. besides the standard Galerkin terms only the Nitsche coupling terms are added to the formulation. As given in Section 2.3.8, for the time discretization the one-step- θ scheme, is used. The matrix formulation in the following is given for to the background element weighting of Nitsche's formulation. The matrix formulation of embedded element weighting of Nitsche's method, can be derived in the same way, which is omitted here. The discrete formulation of nonlinear embedded fluid formulation (3.31), omitting the index $n + 1$ for the current time step, reads as:

Find $(\mathbf{u}_h^e, p_h^e) \in V_h^e \times Q_h^e$ and $(\mathbf{u}_h^b, p_h^b) \in V_h^b \times Q_h^b$ such that $\forall (\mathbf{v}_h^e, q_h^e) \in V_h^e \times Q_h^e$ and $\forall (\mathbf{v}_h^b, q_h^b) \in V_h^b \times Q_h^b$ holds

$$\begin{aligned}
 & (\mathbf{u}_h^b, \frac{\rho^f}{\Theta} \mathbf{u}_h^b)_{\Omega^b} + (\mathbf{v}_h^b, \rho^f \mathbf{u}_h^b \cdot \nabla \mathbf{u}_h^b)_{\Omega^b} \\
 & + (q_h^b, \nabla \cdot \mathbf{u}_h^b)_{\Omega^b} - (\nabla \cdot \mathbf{v}_h^b, p_h^b)_{\Omega^b} + (\boldsymbol{\epsilon}(\mathbf{v}_h^b), 2\mu \boldsymbol{\epsilon}(\mathbf{u}_h^b))_{\Omega^b} \\
 & + (\mathbf{u}_h^e, \frac{\rho^f}{\Theta} \mathbf{u}_h^e)_{\Omega^e} + (\mathbf{v}_h^e, \rho^f \mathbf{c}_h^e \cdot \nabla \mathbf{u}_h^e)_{\Omega^e} \\
 & + (q_h^e, \nabla \cdot \mathbf{u}_h^e)_{\Omega^e} - (\nabla \cdot \mathbf{v}_h^e, p_h^e)_{\Omega^e} + (\boldsymbol{\epsilon}(\mathbf{v}_h^e), 2\mu \boldsymbol{\epsilon}(\mathbf{u}_h^e))_{\Omega^e} \\
 & - \langle \mathbf{v}_h^b, \bar{\mathbf{h}}^b \rangle_{\partial \Omega_N^b} - (\mathbf{v}_h^b, \rho^f \mathbf{b}^b)_{\Omega^b} - (\mathbf{v}_h^e, \rho^f \mathbf{b}^e)_{\Omega^e} \\
 & + \langle \llbracket \mathbf{v}_h \rrbracket, p_h^b \cdot \mathbf{n} \rangle_{\Gamma^{\text{FF}}} - \langle \llbracket \mathbf{v}_h \rrbracket, 2\mu \boldsymbol{\epsilon}(\mathbf{u}_h^b) \cdot \mathbf{n} \rangle_{\Gamma^{\text{FF}}} \\
 & - \langle q_h^b \cdot \mathbf{n}, \llbracket \mathbf{u}_h \rrbracket \rangle_{\Gamma^{\text{FF}}} - \beta_n \langle 2\mu \boldsymbol{\epsilon}(\mathbf{v}_h^b) \cdot \mathbf{n}, \llbracket \mathbf{u}_h \rrbracket \rangle_{\Gamma^{\text{FF}}} \\
 & \quad + \langle \alpha' \llbracket \mathbf{v}_h \rrbracket, \llbracket \mathbf{u}_h \rrbracket \rangle_{\Gamma^{\text{FF}}} \\
 & = (\mathbf{v}_h^b, \frac{\rho^f}{\Theta} \mathbf{u}_h^{b, \text{hist}})_{\Omega^b} + (\mathbf{v}_h^e, \frac{\rho^f}{\Theta} \mathbf{u}_h^{e, \text{hist}})_{\Omega^e}.
 \end{aligned} \tag{3.48}$$

In (3.48), the history values $\mathbf{u}_h^{b, \text{hist}}$ and $\mathbf{u}_h^{e, \text{hist}}$ are defined as

$$\mathbf{u}_h^{i, \text{hist}} = \mathbf{u}_h^{i, n} + \Delta t(1 - \theta) \dot{\mathbf{u}}_h^{i, n}, \quad \text{for } i \in \{b, e\}. \tag{3.49}$$

Furthermore, $\Theta = \Delta t \theta$, denotes the one-step- θ time factor. As the solution of the (3.48) is based on the Newton-Raphson scheme, the equations have to be linearized with respect to unknown qualities. For this purpose, the following contributions of discrete weak residuals are introduced

$$\begin{aligned}
 R_{u^b}(\mathbf{u}_h^b, p_h^b, \mathbf{u}_h^e, p_h^e) & = R_{u^b}^{\text{std}}(p_h^b, \mathbf{u}_h^b) \\
 & + \langle \mathbf{v}_h^b, p_h^b \cdot \mathbf{n} \rangle_{\Gamma^{\text{FF}}} - \langle \mathbf{v}_h^b, 2\mu \boldsymbol{\epsilon}(\mathbf{u}_h^b) \cdot \mathbf{n} \rangle_{\Gamma^{\text{FF}}} \\
 & - \beta_n \langle 2\mu \boldsymbol{\epsilon}(\mathbf{v}_h^b) \cdot \mathbf{n}, \mathbf{u}_h^b \rangle_{\Gamma^{\text{FF}}} + \beta_n \langle 2\mu \boldsymbol{\epsilon}(\mathbf{v}_h^b) \cdot \mathbf{n}, \mathbf{u}_h^e \rangle_{\Gamma^{\text{FF}}} \\
 & + \langle \alpha' \mathbf{v}_h^b, \mathbf{u}_h^b \rangle_{\Gamma^{\text{FF}}} - \langle \alpha' \mathbf{v}_h^b, \mathbf{u}_h^e \rangle_{\Gamma^{\text{FF}}},
 \end{aligned} \tag{3.50}$$

$$R_{p^b}(\mathbf{u}_h^b, p_h^b, \mathbf{u}_h^e) = R_{p^b}^{\text{std}}(\mathbf{u}_h^b, p_h^b) - \langle q_h^b \cdot \mathbf{n}, \mathbf{u}_h^b \rangle_{\Gamma^{\text{FF}}} + \langle q_h^b \cdot \mathbf{n}, \mathbf{u}_h^e \rangle_{\Gamma^{\text{FF}}}, \tag{3.51}$$

$$\begin{aligned}
 R_{u^e}(\mathbf{u}_h^b, p_h^b, \mathbf{u}_h^e, p_h^e) & = R_{u^e}^{\text{std}}(\mathbf{u}_h^e, p_h^e) \\
 & - \langle \mathbf{v}_h^e, p_h^b \cdot \mathbf{n} \rangle_{\Gamma^{\text{FF}}} + \langle \mathbf{v}_h^e, 2\mu \boldsymbol{\epsilon}(\mathbf{u}_h^b) \cdot \mathbf{n} \rangle_{\Gamma^{\text{FF}}} \\
 & - \langle \alpha' \mathbf{v}_h^e, \mathbf{u}_h^b \rangle_{\Gamma^{\text{FF}}} + \langle \alpha' \mathbf{v}_h^e, \mathbf{u}_h^e \rangle_{\Gamma^{\text{FF}}},
 \end{aligned} \tag{3.52}$$

$$R_{p^e}(\mathbf{u}_h^b, p_h^b) = R_{p^e}^{\text{std}}(\mathbf{u}_h^e, p_h^e). \tag{3.53}$$

The terms $R_{u^b}^{\text{std}}$, $R_{p^b}^{\text{std}}$, $R_{u^e}^{\text{std}}$ and $R_{p^e}^{\text{std}}$ denote the contributions of the standard Galerkin for background and embedded fluid subdomains as defined in (2.72), (2.73), (2.77) and (2.78). The linearization of the contributions of the weighted residual terms R_{u^b} , R_{p^b} , R_{u^e} and R_{p^e} with respect to \mathbf{u}_h^b , p_h^b , \mathbf{u}_h^e and p_h^e , result in the rows of the linearized system. The resulting global linearized system, which has to be solved in every Newton step i is then given as

$$\begin{aligned}
 & \left[\begin{array}{cc|cc}
 F_{u^b u^b} + G_{u^b u^b}^c + G_{u^b u^b}^a + G_{u^b u^b}^\alpha & F_{u^b p^b} + G_{u^b p^b}^c & G_{u^b u^e}^a + G_{u^b u^e}^\alpha & 0 \\
 \hline
 F_{p^b u^b} + G_{p^b u^b}^a & 0 & G_{p^b u^e}^a & 0 \\
 G_{u^e u^b}^c + G_{u^e u^b}^\alpha & G_{u^e p^b}^c & F_{u^e u^e} + G_{u^e u^e}^\alpha & F_{u^e p^e} \\
 0 & 0 & F_{p^e u^e} & 0
 \end{array} \right]^{n+1}_i \cdot \begin{bmatrix} \Delta u^b \\ \Delta p^b \\ \Delta u^e \\ \Delta p^e \end{bmatrix}^{n+1}_{i+1} \\
 & = - \begin{bmatrix} r_u^b \\ r_p^b \\ r_u^e \\ r_p^e \end{bmatrix}^{n+1}_i.
 \end{aligned} \tag{3.54}$$

In the linear system (3.54) the elements far from the interface Γ^{FF} , which are not affected by the interface coupling terms, are omitted. The unknown nodal velocity and pressure increments are identified as Δu^b , Δp^b , Δu^e and Δp^e . The submatrices $F_{u^i u^i}$, $F_{u^i p^i}$ and $F_{p^i u^i}$, for $i \in \{b, e\}$, denote the discrete standard Galerkin fluid systems for background and embedded fluid subdomains as in (2.96). Since the fluid stabilization terms are not added into the formulation yet, the block matrices at $p^b p^b$ and $p^e p^e$ are zero. Adding the PSPG stabilization term (2.85) or face-oriented pressure stabilization operator, which will be explained in Section 3.5, adds two more submatrices, $F_{p^b p^b}$ and $F_{p^e p^e}$, into the linear system (3.54). Furthermore, the submatrices with superscript $(\cdot)^c$, G_{**}^c , denote the Nitsche standard consistency terms, and the submatrices with superscript $(\cdot)^a$, G_{**}^a , the Nitsche adjoint consistency terms. The Nitsche stabilization matrices are indicated as G_{**}^α . The residual terms, r_j^i for $i \in \{b, e\}$ and $j \in \{u, p\}$, include the contributions of the standard Galerkin and Nitsche terms. It has to be noted that the signs of the coupling matrices are included in each term. The linear system (3.54) is anti-symmetric regarding the terms $G_{u^e p^b}^c$ and $G_{p^b u^e}^a$, and $G_{u^b p^b}^c$ and $G_{p^b u^b}^a$. Accordingly, the linear system (3.54) is symmetric or anti-symmetric in the viscous part depending on the parameter β_n . The coupling submatrices, which are obtained from linearization of the weighted residual of Nitsche's coupling terms, are given in Table 3.1. To shorten the notation the index $n + 1$ is omitted.

3.3.3 Mixed/hybrid Cauchy stress-based method (MHCS)

The mixed/hybrid Cauchy stress-based method (MHCS) introduces an additional discontinuous element stress field to enforce the coupling conditions. In the original publication by Gerstenberger and Wall [85], the additional discontinuous element stress field is introduced on the background mesh, i.e. a background element weighting is performed. In the present work, as in Shahmiri et al. [157], following the original publication by Gerstenberger and Wall [85], also a background element weighting is performed, i.e. an additional discontinuous element stress field $\bar{\sigma}^b$ is defined on background fluid elements. However, as in Nitsche's method, an embedded element weighting of MHCS is possible, with the additional discontinuous stress field introduced on the embedded mesh, and would avoid the problems with over-weighting of the weak imposition of the coupling conditions for critical cuts, as discussed in Section 3.3.2. In contrast to classical Lagrange multiplier method, this additional stress unknown is introduced as a field in the domain. As mentioned in Section 3.3.1, the Lagrange multiplier methods have shown

Submatrix	Linearized term
$G_{u^b p^b}^c$	$\frac{\partial \langle \mathbf{v}_h^b, p_h^b \cdot \mathbf{n} \rangle_{\Gamma^{\text{FF}}}}{\partial p^b}$
$G_{u^e p^b}^c$	$\frac{\partial \langle \mathbf{v}_h^e, p_h^b \cdot \mathbf{n} \rangle_{\Gamma^{\text{FF}}}}{\partial p^b}$
$G_{u^b u^b}^c$	$\frac{\partial \langle \mathbf{v}_h^b, 2\mu\epsilon(\mathbf{u}_h^b) \cdot \mathbf{n} \rangle_{\Gamma^{\text{FF}}}}{\partial \mathbf{u}^b}$
$G_{u^e u^b}^c$	$\frac{\partial \langle \mathbf{v}_h^e, 2\mu\epsilon(\mathbf{u}_h^b) \cdot \mathbf{n} \rangle_{\Gamma^{\text{FF}}}}{\partial \mathbf{u}^b}$
$G_{p^b u^b}^a$	$\frac{\partial \langle q_h^b \cdot \mathbf{n}, \mathbf{u}_h^b \rangle_{\Gamma^{\text{FF}}}}{\partial \mathbf{u}^b}$
$G_{p^b u^e}^a$	$\frac{\partial \langle q_h^b \cdot \mathbf{n}, \mathbf{u}_h^e \rangle_{\Gamma^{\text{FF}}}}{\partial \mathbf{u}^e}$
$G_{u^b u^b}^a$	$\frac{\partial \beta_n \langle 2\mu\epsilon(\mathbf{v}_h^b) \cdot \mathbf{n}, \mathbf{u}_h^b \rangle_{\Gamma^{\text{FF}}}}{\partial \mathbf{u}^b}$
$G_{u^b u^e}^a$	$\frac{\partial \beta_n \langle 2\mu\epsilon(\mathbf{v}_h^b) \cdot \mathbf{n}, \mathbf{u}_h^e \rangle_{\Gamma^{\text{FF}}}}{\partial \mathbf{u}^e}$
$G_{u^b u^b}^\alpha$	$\frac{\partial \langle \alpha' \mathbf{v}_h^b, \mathbf{u}_h^b \rangle_{\Gamma^{\text{FF}}}}{\partial \mathbf{u}^b}$
$G_{u^b u^e}^\alpha$	$\frac{\partial \langle \alpha' \mathbf{v}_h^b, \mathbf{u}_h^e \rangle_{\Gamma^{\text{FF}}}}{\partial \mathbf{u}^e}$
$G_{u^e u^b}^\alpha$	$\frac{\partial \langle \alpha' \mathbf{v}_h^e, \mathbf{u}_h^b \rangle_{\Gamma^{\text{FF}}}}{\partial \mathbf{u}^b}$
$G_{u^e u^e}^\alpha$	$\frac{\partial \langle \alpha' \mathbf{v}_h^e, \mathbf{u}_h^e \rangle_{\Gamma^{\text{FF}}}}{\partial \mathbf{u}^e}$

Table 3.1: Submatrices of Nitsche's method

instabilities when dealing with interface problems since the most convenient choice of the Lagrange multiplier space results in instabilities at the interface, see Ji and Dolbow [112], Simone [158] and Moës et al. [140]. In contrast, the MHCS method can be considered as a stabilized Lagrange multiplier method, as its formulation involves an implicit stabilization, corresponding to Nitsche's stabilization term, independent of the polynomial order or the spatial discretization. However, in contrast to Nitsche's formulation, where additionally an eigenvalue problem has to be solved to estimate the stabilization parameter, the stabilizing term of MHCS is automatically included in the formulation. Furthermore, because of the discontinuity of the additional stress field between elements, it will be condensed out on element level. The substitution of standard consistency terms at Γ^{FF} in (3.26), which are obtained from the partial integration, with the new traction $\bar{\boldsymbol{\sigma}}^b \cdot \mathbf{n}$, results in

$$- \langle \llbracket \mathbf{v} \rrbracket, \bar{\boldsymbol{\sigma}}^b \cdot \mathbf{n} \rangle_{\Gamma^{\text{FF}}} . \quad (3.55)$$

Similar to the classical Lagrange multiplier method, the stress test function $\bar{\boldsymbol{\tau}}^b$ is employed to enforce the kinematic condition $\llbracket \mathbf{u} \rrbracket = \mathbf{0}$ on Γ^{FF} in a weak sense

$$- \langle \bar{\boldsymbol{\tau}}^b \cdot \mathbf{n}, \llbracket \mathbf{u} \rrbracket \rangle_{\Gamma^{\text{FF}}} = 0. \quad (3.56)$$

Hence, $\bar{\boldsymbol{\tau}}^b \cdot \mathbf{n}$ can be considered as the virtual traction force along the interface.

The additional stress field $\bar{\boldsymbol{\sigma}}^b$ is a symmetric tensor with six components. To close the system of equations, a strain rate balance

$$\frac{1}{2\mu}(\bar{\boldsymbol{\sigma}}^b + p^b \mathbf{I}) = \boldsymbol{\epsilon}(\mathbf{u}^b), \quad \text{on } \Omega^b. \quad (3.57)$$

is added with $\boldsymbol{\epsilon}(\mathbf{u}^b) = \frac{1}{2}(\nabla \mathbf{u}^b + (\nabla \mathbf{u}^b)^\top)$. It claims that the strain rate $\boldsymbol{\epsilon}(\mathbf{u}^b)$ derived from the background velocity should be equal to the strain rate derived from the additional Cauchy stress field $\bar{\boldsymbol{\sigma}}^b$. The strain rate balance (3.57) results in the extra stabilization term, which does not exist in the classical Lagrange multiplier method. Equation (3.57) is tested with the stress test functions $\bar{\boldsymbol{\tau}}^b$, leading to

$$(\bar{\boldsymbol{\tau}}^b, \boldsymbol{\epsilon}(\mathbf{u}^b))_{\Omega^b} - (\bar{\boldsymbol{\tau}}^b, \frac{1}{2\mu} \bar{\boldsymbol{\sigma}}^b)_{\Omega^b} - (\bar{\boldsymbol{\tau}}^b, \frac{1}{2\mu} p^b \mathbf{I})_{\Omega^b} = 0. \quad (3.58)$$

The resulting semi-discrete weak formulation becomes:

Find $(\mathbf{u}_h^e, p_h^e) \in V_h^e \times Q_h^e$, $(\mathbf{u}_h^b, p_h^b) \in V_h^b \times Q_h^b$ and $\bar{\boldsymbol{\sigma}}_h^b \in S_h^b$, such that $\forall (\mathbf{v}_h^e, q_h^e) \in V_h^e \times Q_h^e$, $\forall (\mathbf{v}_h^b, q_h^b) \in V_h^b \times Q_h^b$ and $\forall \bar{\boldsymbol{\tau}}_h^b \in S_h^b$ holds

$$\begin{aligned} \boxed{1} & \quad (\mathbf{v}_h^b, \rho^f \frac{\partial \mathbf{u}_h^b}{\partial t} \Big|_x)_{\Omega^b} + (\mathbf{v}_h^b, \rho^f \mathbf{u}_h^b \cdot \nabla \mathbf{u}_h^b)_{\Omega^b} \\ \boxed{2} & \quad + (q_h^b, \nabla \cdot \mathbf{u}_h^b)_{\Omega^b} - (\nabla \cdot \mathbf{v}_h^b, p_h^b)_{\Omega^b} + (\boldsymbol{\epsilon}(\mathbf{v}_h^b), 2\mu \boldsymbol{\epsilon}(\mathbf{u}_h^b))_{\Omega^b} \\ \boxed{3} & \quad + (\mathbf{v}_h^e, \rho^f \frac{\partial \mathbf{u}_h^e}{\partial t} \Big|_x)_{\Omega^e} + (\mathbf{v}_h^e, \rho^f \mathbf{c}_h^e \cdot \nabla \mathbf{u}_h^e)_{\Omega^e} \\ \boxed{4} & \quad + (q_h^e, \nabla \cdot \mathbf{u}_h^e)_{\Omega^e} - (\nabla \cdot \mathbf{v}_h^e, p_h^e)_{\Omega^e} + (\boldsymbol{\epsilon}(\mathbf{v}_h^e), 2\mu \boldsymbol{\epsilon}(\mathbf{u}_h^e))_{\Omega^e} \\ \boxed{5} & \quad - \langle \llbracket \mathbf{v}_h \rrbracket, \bar{\boldsymbol{\sigma}}_h^b \cdot \mathbf{n} \rangle_{\Gamma^{\text{FF}}} \\ \boxed{6} & \quad - \langle \bar{\boldsymbol{\tau}}_h^b \cdot \mathbf{n}, \llbracket \mathbf{u}_h \rrbracket \rangle_{\Gamma^{\text{FF}}} \\ \boxed{7} & \quad + (\bar{\boldsymbol{\tau}}_h^b, \boldsymbol{\epsilon}(\mathbf{u}_h^b))_{\Omega^b} - (\bar{\boldsymbol{\tau}}_h^b, \frac{1}{2\mu} \bar{\boldsymbol{\sigma}}_h^b)_{\Omega^b} - (\bar{\boldsymbol{\tau}}_h^b, \frac{1}{2\mu} p_h^b \mathbf{I})_{\Omega^b} \\ \boxed{8} & \quad = \langle \mathbf{v}_h^b, \bar{\mathbf{h}}^b \rangle_{\partial \Omega_N^b} + (\mathbf{v}_h^b, \rho^f \mathbf{b}^b)_{\Omega^b} + (\mathbf{v}_h^e, \rho^f \mathbf{b}^e)_{\Omega^e}. \end{aligned} \quad (3.59)$$

The finite element space S_h^b is defined as

$$S_h^b := \{v \in [C^{-1}(\Omega^b)]^6 : v|_V \in [Q^1(K)]^6 \forall V \in \Omega_K^b, \forall K \in \mathcal{T}^*\}. \quad (3.60)$$

It can be seen that the standard weak form of the Navier-Stokes equations for both background and embedded subdomains remains unchanged and the extra stress terms are simply added to the weak fluid formulation.

Furthermore, as it can be seen in (3.60), the added discontinuous stress field $\bar{\boldsymbol{\sigma}}_h^b \in S_h^b$ is defined on the mesh \mathcal{T}^* , which is the set of elements located in the physical background fluid subdomain unified with the set of cut elements (see Figure 3.3). However, since $\bar{\boldsymbol{\sigma}}_h^b$ is discontinuous between element boundaries, the discrete strain rate balance, which corresponds to the seventh line of the semi-discrete formulation (3.59), is satisfied elementwise for every element of \mathcal{T}^* . Hence, in the implementation of MHCS, the additional stress-field is just added to cut elements of background fluid \mathcal{T}^Γ and can be omitted on uncut elements, which are not affected by the coupling terms.

Matrix formulation

In the following, the matrix formulation of the embedded fluid formulation with mixed/hybrid Cauchy stress-based method is accomplished. The time discretization of semi-discrete embedded fluid formulation (3.59), omitting the index $n + 1$ for the current time step, using one-step- θ scheme reads as:

Find $(\mathbf{u}_h^e, p_h^e) \in V_h^e \times Q_h^e$, $(\mathbf{u}_h^b, p_h^b) \in V_h^b \times Q_h^b$ and $\bar{\boldsymbol{\sigma}}_h^b \in S_h^b$, such that $\forall (\mathbf{v}_h^e, q_h^e) \in V_h^e \times Q_h^e$, $\forall (\mathbf{v}_h^b, q_h^b) \in V_h^b \times Q_h^b$ and $\forall \bar{\boldsymbol{\tau}}_h^b \in S_h^b$ holds

$$\begin{aligned}
 & (\mathbf{u}_h^b, \frac{\rho^f}{\Theta} \mathbf{u}_h^b)_{\Omega^b} + (\mathbf{v}_h^b, \rho^f \mathbf{u}_h^b \cdot \nabla \mathbf{u}_h^b)_{\Omega^b} \\
 & + (q_h^b, \nabla \cdot \mathbf{u}_h^b)_{\Omega^b} - (\nabla \cdot \mathbf{v}_h^b, p_h^b)_{\Omega^b} + (\boldsymbol{\epsilon}(\mathbf{v}_h^b), 2\mu \boldsymbol{\epsilon}(\mathbf{u}_h^b))_{\Omega^b} \\
 & + (\mathbf{u}_h^e, \frac{\rho^f}{\Theta} \mathbf{u}_h^e)_{\Omega^e} + (\mathbf{v}_h^e, \rho^f \mathbf{c}_h^e \cdot \nabla \mathbf{u}_h^e)_{\Omega^e} \\
 & + (q_h^e, \nabla \cdot \mathbf{u}_h^e)_{\Omega^e} - (\nabla \cdot \mathbf{v}_h^e, p_h^e)_{\Omega^e} + (\boldsymbol{\epsilon}(\mathbf{v}_h^e), 2\mu \boldsymbol{\epsilon}(\mathbf{u}_h^e))_{\Omega^e} \\
 & - \langle \mathbf{v}_h^b, \bar{\mathbf{h}}^b \rangle_{\partial \Omega_N^b} - (\mathbf{v}_h^b, \rho^f \mathbf{b}^b)_{\Omega^b} - (\mathbf{v}_h^e, \rho^f \mathbf{b}^e)_{\Omega^e} \\
 & - \langle \llbracket \mathbf{v}_h \rrbracket, \bar{\boldsymbol{\sigma}}_h^b \cdot \mathbf{n} \rangle_{\Gamma^{\text{FF}}} - \langle \bar{\boldsymbol{\tau}}_h^b \cdot \mathbf{n}, \llbracket \mathbf{u}_h \rrbracket \rangle_{\Gamma^{\text{FF}}} \\
 & + (\bar{\boldsymbol{\tau}}_h^b, \boldsymbol{\epsilon}(\mathbf{u}_h^b))_{\Omega^b} - (\bar{\boldsymbol{\tau}}_h^b, \frac{1}{2\mu} \bar{\boldsymbol{\sigma}}_h^b)_{\Omega^b} - (\bar{\boldsymbol{\tau}}_h^b, \frac{1}{2\mu} p_h^b \mathbf{I})_{\Omega^b} \\
 & = (\mathbf{v}_h^b, \frac{\rho^f}{\Theta} \mathbf{u}_h^{b,\text{hist}})_{\Omega^b} + (\mathbf{v}_h^e, \frac{\rho^f}{\Theta} \mathbf{u}_h^{e,\text{hist}})_{\Omega^e}.
 \end{aligned} \tag{3.61}$$

In (3.61), the history values $\mathbf{u}_h^{b,\text{hist}}$ and $\mathbf{u}_h^{e,\text{hist}}$ are defined as in (3.49). As before, the parameter $\Theta = \Delta t \theta$, denotes the one-step- θ time factor. In order to linearize (3.61) with respect to the unknown qualities, the following contributions of the weak residuals are introduced

$$R_{u^b}(\mathbf{u}_h^b, p_h^b, \bar{\boldsymbol{\sigma}}_h^b) = R_{u^b}^{\text{std}}(\mathbf{u}_h^b, p_h^b) - \langle \mathbf{v}_h^b, \bar{\boldsymbol{\sigma}}_h^b \cdot \mathbf{n} \rangle_{\Gamma^{\text{FF}}}, \tag{3.62}$$

$$R_{p^b}(\mathbf{u}_h^b, p_h^b) = R_{p^b}^{\text{std}}(\mathbf{u}_h^b, p_h^b), \tag{3.63}$$

$$R_{u^e}(\mathbf{u}_h^e, p_h^e, \bar{\boldsymbol{\sigma}}_h^b) = R_{u^e}^{\text{std}}(\mathbf{u}_h^e, p_h^e) + \langle \mathbf{v}_h^e, \bar{\boldsymbol{\sigma}}_h^b \cdot \mathbf{n} \rangle_{\Gamma^{\text{FF}}}, \tag{3.64}$$

$$R_{p^e}(\mathbf{u}_h^e, p_h^e) = R_{p^e}^{\text{std}}(\mathbf{u}_h^e, p_h^e), \tag{3.65}$$

$$\begin{aligned}
 R_{\bar{\boldsymbol{\sigma}}^b}(\mathbf{u}_h^b, \mathbf{u}_h^e, p_h^b, \bar{\boldsymbol{\sigma}}_h^b) &= (\bar{\boldsymbol{\tau}}_h^b, \boldsymbol{\epsilon}(\mathbf{u}_h^b))_{\Omega^b} - (\bar{\boldsymbol{\tau}}_h^b, \frac{1}{2\mu} \bar{\boldsymbol{\sigma}}_h^b)_{\Omega^b} - (\bar{\boldsymbol{\tau}}_h^b, \frac{1}{2\mu} p_h^b \mathbf{I})_{\Omega^b} \\
 &- \langle \bar{\boldsymbol{\tau}}_h^b \cdot \mathbf{n}, \mathbf{u}_h^b \rangle_{\Gamma^{\text{FF}}} + \langle \bar{\boldsymbol{\tau}}_h^b \cdot \mathbf{n}, \mathbf{u}_h^e \rangle_{\Gamma^{\text{FF}}}.
 \end{aligned} \tag{3.66}$$

Hereby, $R_{u^b}^{\text{std}}$, $R_{p^b}^{\text{std}}$, $R_{u^e}^{\text{std}}$ and $R_{p^e}^{\text{std}}$ denote the contributions of the standard Galerkin terms for background and embedded fluid subdomains defined in (2.72), (2.73), (2.77) and (2.78). Linearization of the contributions in (3.62), (3.63), (3.64), (3.65) and (3.66) with respect to the unknowns $\mathbf{u}_h^b, p_h^b, \bar{\boldsymbol{\sigma}}_h^b, \mathbf{u}_h^e$ and p_h^e , results in the rows of the linearized system. However, it needs to be pointed out that only nonlinear terms in (3.61) are the standard Galerkin convective terms of background and embedded fluid subdomains. As discussed in Section 2.3.10, in order to solve the nonlinear system with Newton-Raphson method a full linearization of terms is required, which leads to an incremental formulation of the linear system in context of Newton-Raphson

scheme. Omitting the elements far from interface, the global linearized discrete system including the additional stress unknowns is given as

$$\begin{bmatrix} F_{u^b u^b} & F_{u^b p^b} & G_{u^b \bar{\sigma}^b} & 0 & 0 \\ F_{p^b u^b} & 0 & 0 & 0 & 0 \\ \hline K_{\bar{\sigma}^b u^b} + G_{\bar{\sigma}^b u^b} & K_{\bar{\sigma}^b p^b} & K_{\bar{\sigma}^b \bar{\sigma}^b} & G_{\bar{\sigma}^b u^e} & 0 \\ 0 & 0 & G_{u^e \bar{\sigma}^b} & F_{u^e u^e} & F_{u^e p^e} \\ 0 & 0 & 0 & F_{p^e u^e} & 0 \end{bmatrix}_i^{n+1} \cdot \begin{bmatrix} \Delta u^b \\ \Delta p^b \\ \Delta \bar{\sigma}^b \\ \Delta u^e \\ \Delta p^e \end{bmatrix}_{i+1}^{n+1} = - \begin{bmatrix} r_u^b \\ r_p^b \\ r_{\bar{\sigma}}^b \\ r_u^e \\ r_p^e \end{bmatrix}_i^{n+1}, \quad (3.67)$$

which has to be solved in every Newton step i . The unknown nodal velocity and pressure increments are as before identified as Δu^b , Δp^b , Δu^e and Δp^e , while $\Delta \bar{\sigma}^b$ denotes the element stress increments. The submatrices $F_{u^b u^b}$, $F_{u^b p^b}$ and $F_{p^b u^b}$ and $F_{u^e u^e}$, $F_{u^e p^e}$ and $F_{p^e u^e}$ are the background and embedded standard Galerkin submatrices, respectively, as given in (2.95). As mentioned above, since the fluid stabilizations are not added yet, the matrix blocks at $p^b p^b$ and $p^e p^e$ are zero. The remaining submatrices result from the linearization of the boundary integral terms, denotes as G_{**} , and from the linearization of the volume integral terms, denotes as K_{**} . The matrix block $K_{\bar{\sigma}^b \bar{\sigma}^b}$ refers to the stabilization included in MHCS method, which is 0 for classical Lagrange multiplier method. The assignment of coupling submatrices, G_{**} and K_{**} , to the weighted residual contributions, omitting the index $n + 1$, is given in Table 3.2. The residual terms, r_u^b , r_p^b , $r_{\bar{\sigma}}^b$, r_u^e , and r_p^e include the contributions of the standard Galerkin and the coupling terms. As already described above, the stress increments are discontinuous between elements,

Submatrix	Linearized term
$G_{u^b \bar{\sigma}^b}$	$-\frac{\partial \langle \mathbf{v}_h^b, \bar{\boldsymbol{\sigma}}_h^b \cdot \mathbf{n} \rangle_{\Gamma^{\text{FF}}}}{\partial \bar{\boldsymbol{\sigma}}^b}$
$G_{\bar{\sigma}^b u^b}$	$-\frac{\partial \langle \bar{\boldsymbol{\tau}}_h^b \cdot \mathbf{n}, \mathbf{u}_h^b \rangle_{\Gamma^{\text{FF}}}}{\partial \mathbf{u}^b}$
$G_{\bar{\sigma}^b u^e}$	$\frac{\partial \langle \bar{\boldsymbol{\tau}}_h^b \cdot \mathbf{n}, \mathbf{u}_h^e \rangle_{\Gamma^{\text{FF}}}}{\partial \mathbf{u}^e}$
$G_{u^e \bar{\sigma}^b}$	$\frac{\partial \langle \mathbf{v}_h^e, \bar{\boldsymbol{\sigma}}_h^b \cdot \mathbf{n} \rangle_{\Gamma^{\text{FF}}}}{\partial \bar{\boldsymbol{\sigma}}^b}$
$K_{\bar{\sigma}^b u^b}$	$\frac{\partial (\bar{\boldsymbol{\tau}}_h^b, \boldsymbol{\epsilon}(\mathbf{u}_h^b))_{\Omega^b}}{\partial \mathbf{u}^b}$
$K_{\bar{\sigma}^b p^b}$	$-\frac{\partial (\bar{\boldsymbol{\tau}}_h^b, \frac{1}{2\mu} p_h^b \mathbf{I})_{\Omega^b}}{\partial p^b}$
$K_{\bar{\sigma}^b \bar{\sigma}^b}$	$-\frac{\partial (\bar{\boldsymbol{\tau}}_h^b, \frac{1}{2\mu} \bar{\boldsymbol{\sigma}}_h^b)_{\Omega^b}}{\partial \bar{\boldsymbol{\sigma}}^b}$

Table 3.2: Submatrices of MHCS

see the equation (3.60), and influence the velocity and pressure solutions only in cut elements via boundary integrals G_{**} . Thus, for non-intersected background fluid elements, where no boundary integrals exist, the stress increments can be omitted. Because of the C^{-1} -continuity of stress increments with neighboring elements, in the cut elements they can be condensed separately for each element. The stress increments for a cut element $K \in \mathcal{T}^\Gamma$ can be expressed as

$$\Delta \bar{\sigma}^{b,K} = (K_{\bar{\sigma}^b \bar{\sigma}^b}^K)^{-1} (-r_{\bar{\sigma}}^{b,K} - (K_{\bar{\sigma}^b u^b}^K + G_{\bar{\sigma}^b u^b}^K) \Delta u^{b,K} - K_{\bar{\sigma}^b p^b}^K \Delta p^{b,K} - G_{\bar{\sigma}^b u^e}^K \Delta u^{e,K}). \quad (3.68)$$

In (3.68), $\Delta \mathbf{u}^{b,K}$ and $\Delta \mathbf{p}^{b,K}$ denote the velocity and pressure nodal unknowns belonging to the element K , and $\Delta \bar{\sigma}^{b,K}$ the element unknowns for the stress approximation. The vector $\Delta \mathbf{u}^{e,K}$ contains all velocities belonging to embedded fluid elements, which intersects the background fluid K . To condense the stress unknowns, the following element coupling matrices are defined

$$\mathbf{C}_{u^b u^b}^K = -\mathbf{G}_{u^b \bar{\sigma}^b}^K (\mathbf{K}_{\bar{\sigma}^b \bar{\sigma}^b}^K)^{-1} (\mathbf{K}_{\bar{\sigma}^b u^b}^K + \mathbf{G}_{\bar{\sigma}^b u^b}^K), \quad (3.69)$$

$$\mathbf{C}_{u^b p^b}^K = -\mathbf{G}_{u^b \bar{\sigma}^b}^K (\mathbf{K}_{\bar{\sigma}^b \bar{\sigma}^b}^K)^{-1} \mathbf{K}_{\bar{\sigma}^b p^b}^K, \quad (3.70)$$

$$\mathbf{C}_{u^b u^e}^K = -\mathbf{G}_{u^b \bar{\sigma}^b}^K (\mathbf{K}_{\bar{\sigma}^b \bar{\sigma}^b}^K)^{-1} \mathbf{G}_{\bar{\sigma}^b u^e}^K, \quad (3.71)$$

and for the embedded fluid velocity unknowns

$$\mathbf{C}_{u^e u^b}^K = -\mathbf{G}_{u^e \bar{\sigma}^b}^K (\mathbf{K}_{\bar{\sigma}^b \bar{\sigma}^b}^K)^{-1} (\mathbf{K}_{\bar{\sigma}^b u^b}^K + \mathbf{G}_{\bar{\sigma}^b u^b}^K), \quad (3.72)$$

$$\mathbf{C}_{u^e p^b}^K = -\mathbf{G}_{u^e \bar{\sigma}^b}^K (\mathbf{K}_{\bar{\sigma}^b \bar{\sigma}^b}^K)^{-1} \mathbf{K}_{\bar{\sigma}^b p^b}^K, \quad (3.73)$$

$$\mathbf{C}_{u^e u^e}^K = -\mathbf{G}_{u^e \bar{\sigma}^b}^K (\mathbf{K}_{\bar{\sigma}^b \bar{\sigma}^b}^K)^{-1} \mathbf{G}_{\bar{\sigma}^b u^e}^K. \quad (3.74)$$

The residual terms are defined as

$$\mathbf{c}_u^{b,K} = -\mathbf{G}_{u^b \bar{\sigma}^b}^K (\mathbf{K}_{\bar{\sigma}^b \bar{\sigma}^b}^K)^{-1} \mathbf{r}_{\bar{\sigma}^b}^{b,K}, \quad (3.75)$$

$$\mathbf{c}_u^{e,K} = -\mathbf{G}_{u^e \bar{\sigma}^b}^K (\mathbf{K}_{\bar{\sigma}^b \bar{\sigma}^b}^K)^{-1} \mathbf{r}_{\bar{\sigma}^b}^{b,K}. \quad (3.76)$$

$$(3.77)$$

With these definitions, the condensed global system can be assembled from element entries in every Newton step i of the time step $n+1$ as

$$\mathbf{A}_K \begin{bmatrix} \mathbf{F}_{u^b u^b}^K + \mathbf{C}_{u^b u^b}^K & \mathbf{F}_{u^b p^b}^K + \mathbf{C}_{u^b p^b}^K & \mathbf{C}_{u^b u^e}^K & 0 \\ \mathbf{F}_{p^b u^b}^K & 0 & 0 & 0 \\ \mathbf{C}_{u^e u^b}^K & \mathbf{C}_{u^e p^b}^K & \mathbf{F}_{u^e u^e}^K + \mathbf{C}_{u^e u^e}^K & \mathbf{F}_{u^e p^e}^K \\ 0 & 0 & \mathbf{F}_{p^e u^e}^K & 0 \end{bmatrix}^{n+1} \begin{bmatrix} \Delta \mathbf{u}^{b,K} \\ \Delta \mathbf{p}^{b,K} \\ \Delta \mathbf{u}^{e,K} \\ \Delta \mathbf{p}^{e,K} \end{bmatrix}^{n+1} = -\mathbf{A}_K \begin{bmatrix} \mathbf{r}_u^{b,K} + \mathbf{c}_u^{b,K} \\ \mathbf{r}_p^{b,K} \\ \mathbf{r}_u^{e,K} + \mathbf{c}_u^{e,K} \\ \mathbf{r}_p^{e,K} \end{bmatrix}^{n+1}. \quad (3.78)$$

Considering only the cut background elements and the embedded elements, which share a side with the fluid-fluid interface Γ^{FF} , i.e. omitting the elements far from interface, the condensed global system reads as

$$\begin{bmatrix} \mathbf{F}_{u^b u^b} + \mathbf{C}_{u^b u^b} & \mathbf{F}_{u^b p^b} + \mathbf{C}_{u^b p^b} & \mathbf{C}_{u^b u^e} & 0 \\ \mathbf{F}_{p^b u^b} & 0 & 0 & 0 \\ \mathbf{C}_{u^e u^b} & \mathbf{C}_{u^e p^b} & \mathbf{F}_{u^e u^e} + \mathbf{C}_{u^e u^e} & \mathbf{F}_{u^e p^e} \\ 0 & 0 & \mathbf{F}_{p^e u^e} & 0 \end{bmatrix}^{n+1} \begin{bmatrix} \Delta \mathbf{u}^b \\ \Delta \mathbf{p}^b \\ \Delta \mathbf{u}^e \\ \Delta \mathbf{p}^e \end{bmatrix}^{n+1} = - \begin{bmatrix} \mathbf{r}_u^b + \mathbf{c}_u^b \\ \mathbf{r}_p^b \\ \mathbf{r}_u^e + \mathbf{c}_u^e \\ \mathbf{r}_p^e \end{bmatrix}^{n+1}. \quad (3.79)$$

3.3.4 Mixed/hybrid viscous stress-based method (MHVS)

Similar to MHCS discussed in Section 3.3.3, the mixed/hybrid viscous stress-based method (MHVS), introduced by Baiges et al. [11], makes use of an additional discontinuous Lagrange multiplier field based on viscous stresses to enforce the coupling conditions. Thus, the idea of introducing an additional Lagrange multiplier field on the background fluid subdomain Ω^b , remains the same, however, in contrast to MHCS instead of an additional Cauchy stress field, a viscous stress field is introduced. As shown for MHCS method in Section 3.3.3, the additional stress field substitutes the whole interface traction, while in the MHVS method only the viscous part of the traction is replaced by the additional stress field. Since, again, the additional stress-based field is discontinuous across element boundaries, it can be condensed from the linear system. Furthermore, as for MHCS, a strain rate balance, similar to strain rate balance from MHCS (3.57), is added. However, in contrast to MHCS, an additional equation to strain rate balance is included to the formulation, which makes the method symmetric in its form for symmetric problems. It has to be remarked that MHCS is a non-symmetric method even for symmetric problems. This is the only difference between the both methods, when the stress-based methods are applied to Poisson's problem, due to the lack of the pressure variable. However, considering Stokes or Navier-Stokes problems, the pressure field in MHVS method is treated in the same way as Nitsche's method, which is the second main difference to MHCS. In the following, again, a background element weighting is considered. However, the formulation can easily be accomplished for embedded element weighting, where the discontinuous additional stress field is defined on the embedded fluid elements. Furthermore, the method holds a stabilization parameter n to ensure stability, which can be fixed a priori, see Baiges et al. [11]. According to Baiges et al. [11], the parameter n should be chosen greater than one ($n > 1$).

As already mentioned, in both mixed hybrid methods an additional discontinuous Lagrange multiplier field $\bar{\sigma}^b$ is introduced on the background fluid subdomain Ω^b . In MHCS method, the additional stress field is used to substitute the whole interface traction, i.e. the standard consistency terms, as shown in (3.55). In contrast, in MHVS method only the viscous traction on Γ^{FF} is substituted by $\bar{\sigma}^b \cdot \mathbf{n}$ and the pressure terms remain unchanged, as

$$\langle \llbracket \mathbf{v}_h \rrbracket, p_h^b \cdot \mathbf{n} \rangle_{\Gamma^{\text{FF}}} - \langle \llbracket \mathbf{v} \rrbracket, \bar{\sigma}^b \cdot \mathbf{n} \rangle_{\Gamma^{\text{FF}}} = 0. \quad (3.80)$$

Furthermore, the weak enforcement of the kinematic coupling $\llbracket \mathbf{u} \rrbracket = \mathbf{0}$ is added as

$$- \langle q^b \cdot \mathbf{n}, \llbracket \mathbf{u} \rrbracket \rangle_{\Gamma^{\text{FF}}} - \langle \bar{\tau}^b \cdot \mathbf{n}, \llbracket \mathbf{u} \rrbracket \rangle_{\Gamma^{\text{FF}}} = 0. \quad (3.81)$$

As for Nitsche's method (3.34), according to the anti-symmetric formulation of standard Galerkin pressure term, an anti-symmetric formulation for the pressure terms is chosen. Similar to the strain rate balance of MHCS (3.57), a strain rate balance is introduced to close the system

$$\frac{1}{2\mu} \bar{\sigma}^b - \epsilon(\mathbf{u}^b) = \mathbf{0}, \quad \text{on } \Omega^b. \quad (3.82)$$

Additionally, a further stress equality from rearranging (3.82), the so called viscous stress balance, is introduced as

$$\bar{\sigma}^b - 2\mu\epsilon(\mathbf{u}^b) = \mathbf{0}, \quad \text{on } \Omega^b, \quad (3.83)$$

which leads to the symmetric structure of the method. The strain rate balance (3.82) is tested with stress test functions $\bar{\boldsymbol{\tau}}^b$ multiplied by $\frac{1}{n}$ as

$$-\frac{1}{n}(\bar{\boldsymbol{\tau}}^b, \frac{1}{2\mu}\bar{\boldsymbol{\sigma}}^b)_{\Omega^b} + \frac{1}{n}(\bar{\boldsymbol{\tau}}^b, \boldsymbol{\epsilon}(\mathbf{u}^b))_{\Omega^b} = 0. \quad (3.84)$$

Furthermore, the viscous stress balance (3.83) is weighted by test strains as

$$\beta_v \frac{1}{n}(\boldsymbol{\epsilon}(\mathbf{v}^b), \bar{\boldsymbol{\sigma}}^b)_{\Omega^b} - \beta_v \frac{1}{n}(\boldsymbol{\epsilon}(\mathbf{v}^b), 2\mu\boldsymbol{\epsilon}(\mathbf{u}^b))_{\Omega^b} = 0, \quad (3.85)$$

with the parameter n mentioned above. Similar to the parameter β_n of Nitsche's method, the parameter β_v indicates, whether the method is symmetric or non-symmetric in the viscous part, $\beta_v = 1$ or $\beta_v = -1$, respectively. After the weak form has been stated, the resulting semi-discrete weak embedded fluid formulation without adding the fluid stabilization terms becomes:

Find $(\mathbf{u}_h^e, p_h^e) \in V_h^e \times Q_h^e$, $(\mathbf{u}_h^b, p_h^b) \in V_h^b \times Q_h^b$ and $\bar{\boldsymbol{\sigma}}_h^b \in S_h^b$, such that $\forall (\mathbf{v}_h^e, q_h^e) \in V_h^e \times Q_h^e$, $\forall (\mathbf{v}_h^b, q_h^b) \in V_h^b \times Q_h^b$ and $\forall \bar{\boldsymbol{\tau}}_h^b \in S_h^b$, holds

$$\begin{aligned} & \boxed{1} \quad (\mathbf{v}_h^b, \rho^f \frac{\partial \mathbf{u}_h^b}{\partial t} \Big|_x)_{\Omega^b} + (\mathbf{v}_h^b, \rho^f \mathbf{u}_h^b \cdot \nabla \mathbf{u}_h^b)_{\Omega^b} \\ & \boxed{2} \quad + (q_h^b, \nabla \cdot \mathbf{u}_h^b)_{\Omega^b} - (\nabla \cdot \mathbf{v}_h^b, p_h^b)_{\Omega^b} + (\boldsymbol{\epsilon}(\mathbf{v}_h^b), 2\mu\boldsymbol{\epsilon}(\mathbf{u}_h^b))_{\Omega^b} \\ & \boxed{3} \quad + (\mathbf{v}_h^e, \rho^f \frac{\partial \mathbf{u}_h^e}{\partial t} \Big|_x)_{\Omega^e} + (\mathbf{v}_h^e, \rho^f \mathbf{u}_h^e \cdot \nabla \mathbf{u}_h^e)_{\Omega^e} \\ & \boxed{4} \quad + (q_h^e, \nabla \cdot \mathbf{u}_h^e)_{\Omega^e} - (\nabla \cdot \mathbf{v}_h^e, p_h^e)_{\Omega^e} + (\boldsymbol{\epsilon}(\mathbf{v}_h^e), 2\mu\boldsymbol{\epsilon}(\mathbf{u}_h^e))_{\Omega^e} \\ & \boxed{5} \quad + \langle [\mathbf{v}_h], p_h^b \cdot \mathbf{n} \rangle_{\Gamma^{\text{FF}}} - \langle [\mathbf{v}_h], \bar{\boldsymbol{\sigma}}_h^b \cdot \mathbf{n} \rangle_{\Gamma^{\text{FF}}} \\ & \boxed{6} \quad - \langle q_h^b \cdot \mathbf{n}, [\mathbf{u}_h] \rangle_{\Gamma^{\text{FF}}} - \langle \bar{\boldsymbol{\tau}}_h^b \cdot \mathbf{n}, [\mathbf{u}_h] \rangle_{\Gamma^{\text{FF}}} \\ & \boxed{7} \quad - \frac{1}{n}(\bar{\boldsymbol{\tau}}_h^b, \frac{1}{2\mu}\bar{\boldsymbol{\sigma}}_h^b)_{\Omega^b} + \frac{1}{n}(\bar{\boldsymbol{\tau}}_h^b, \boldsymbol{\epsilon}(\mathbf{u}_h^b))_{\Omega^b} \\ & \boxed{8} \quad + \beta_v \frac{1}{n}(\boldsymbol{\epsilon}(\mathbf{v}_h^b), \bar{\boldsymbol{\sigma}}_h^b)_{\Omega^b} - \beta_v \frac{1}{n}(\boldsymbol{\epsilon}(\mathbf{v}_h^b), 2\mu\boldsymbol{\epsilon}(\mathbf{u}_h^b))_{\Omega^b} \\ & \boxed{9} \quad = \langle \mathbf{v}_h^b, \bar{\mathbf{h}}^b \rangle_{\partial\Omega_N^b} + (\mathbf{v}_h^b, \rho^f \mathbf{b}^b)_{\Omega^b} + (\mathbf{v}_h^e, \rho^f \mathbf{b}^e)_{\Omega^e}, \end{aligned} \quad (3.86)$$

with the finite element space S_h^b defined as (3.60). As it can be seen, the standard weak form of the Navier-Stokes equations remains unchanged and the extra stress terms are simply added to the fluid weak formulation. In the following, the matrix formulation of the embedded fluid formulation with mixed/hybrid viscous stress-based method will be presented.

Matrix formulation

The time discretization of (3.86) applying an one-step- θ scheme is given as

$$\begin{aligned}
& (\mathbf{u}_h^b, \frac{\rho^f}{\Theta} \mathbf{u}_h^b)_{\Omega^b} + (\mathbf{v}_h^b, \rho^f \mathbf{u}_h^b \cdot \nabla \mathbf{u}_h^b)_{\Omega^b} \\
& + (q_h^b, \nabla \cdot \mathbf{u}_h^b)_{\Omega^b} - (\nabla \cdot \mathbf{v}_h^b, p_h^b)_{\Omega^b} + (\boldsymbol{\epsilon}(\mathbf{v}_h^b), 2\mu \boldsymbol{\epsilon}(\mathbf{u}_h^b))_{\Omega^b} \\
& + (\mathbf{u}_h^e, \frac{\rho^f}{\Theta} \mathbf{u}_h^e)_{\Omega^e} + (\mathbf{v}_h^e, \rho^f \mathbf{c}_h^e \cdot \nabla \mathbf{u}_h^e)_{\Omega^e} \\
& + (q_h^e, \nabla \cdot \mathbf{u}_h^e)_{\Omega^e} - (\nabla \cdot \mathbf{v}_h^e, p_h^e)_{\Omega^e} + (\boldsymbol{\epsilon}(\mathbf{v}_h^e), 2\mu \boldsymbol{\epsilon}(\mathbf{u}_h^e))_{\Omega^e} \\
& - \langle \mathbf{v}_h^b, \bar{\mathbf{h}}^b \rangle_{\partial \Omega_N^b} - (\mathbf{v}_h^b, \rho^f \mathbf{b}^b)_{\Omega^b} - (\mathbf{v}_h^e, \rho^f \mathbf{b}^e)_{\Omega^e} \\
& + \langle \llbracket \mathbf{v}_h \rrbracket, p_h^b \cdot \mathbf{n} \rangle_{\Gamma^{\text{FF}}} - \langle \llbracket \mathbf{v}_h \rrbracket, \bar{\boldsymbol{\sigma}}_h^b \cdot \mathbf{n} \rangle_{\Gamma^{\text{FF}}} \\
& - \langle q_h^b \cdot \mathbf{n}, \llbracket \mathbf{u}_h \rrbracket \rangle_{\Gamma^{\text{FF}}} - \langle \bar{\boldsymbol{\tau}}_h^b \cdot \mathbf{n}, \llbracket \mathbf{u}_h \rrbracket \rangle_{\Gamma^{\text{FF}}} \\
& - \frac{1}{n} (\bar{\boldsymbol{\tau}}_h^b, \frac{1}{2\mu} \bar{\boldsymbol{\sigma}}_h^b)_{\Omega^b} + \frac{1}{n} (\bar{\boldsymbol{\tau}}_h^b, \boldsymbol{\epsilon}(\mathbf{u}_h^b))_{\Omega^b} \\
& + \beta_v \frac{1}{n} (\boldsymbol{\epsilon}(\mathbf{v}_h^b), \bar{\boldsymbol{\sigma}}_h^b)_{\Omega^b} - \beta_v \frac{1}{n} (\boldsymbol{\epsilon}(\mathbf{v}_h^b), 2\mu \boldsymbol{\epsilon}(\mathbf{u}_h^b))_{\Omega^b} \\
& = (\mathbf{v}_h^b, \frac{\rho^f}{\Theta} \mathbf{u}_h^{b,\text{hist}})_{\Omega^b} + (\mathbf{v}_h^e, \frac{\rho^f}{\Theta} \mathbf{u}_h^{e,\text{hist}})_{\Omega^e},
\end{aligned} \tag{3.87}$$

with the history values $\mathbf{u}_h^{b,\text{hist}}$ and $\mathbf{u}_h^{e,\text{hist}}$ defined as

$$\mathbf{u}_h^{i,\text{hist}} = \mathbf{u}_h^{i,n} + \Delta t(1 - \theta) \dot{\mathbf{u}}_h^{i,n}, \quad \text{for } i \in \{b, e\} \tag{3.88}$$

and $\Theta = \theta \Delta t$. In order to obtain the linear system, the following contributions of the discrete weak residuals need to be linearized by the primary unknowns

$$\begin{aligned}
R_{u^b}(\mathbf{u}_h^b, p_h^b, \bar{\boldsymbol{\sigma}}_h^b) &= R_{u^b}^{\text{std}}(\mathbf{u}_h^b, p_h^b) - \langle \mathbf{v}_h^b, \bar{\boldsymbol{\sigma}}_h^b \cdot \mathbf{n} \rangle_{\Gamma^{\text{FF}}} + \langle \mathbf{v}_h^b, p_h^b \cdot \mathbf{n} \rangle_{\Gamma^{\text{FF}}} \\
& + \beta_v \frac{1}{n} (\boldsymbol{\epsilon}(\mathbf{v}_h^b), \bar{\boldsymbol{\sigma}}_h^b)_{\Omega^b} - \beta_v \frac{1}{n} (\boldsymbol{\epsilon}(\mathbf{v}_h^b), 2\mu \boldsymbol{\epsilon}(\mathbf{u}_h^b))_{\Omega^b},
\end{aligned} \tag{3.89}$$

$$R_{p^b}(\mathbf{u}_h^b, p_h^b) = R_{p^b}^{\text{std}}(\mathbf{u}_h^b, p_h^b) - \langle q_h^b \cdot \mathbf{n}, \mathbf{u}_h^b \rangle_{\Gamma^{\text{FF}}} + \langle q_h^b \cdot \mathbf{n}, \mathbf{u}_h^e \rangle_{\Gamma^{\text{FF}}}, \tag{3.90}$$

$$R_{u^e}(p_h^e, \bar{\boldsymbol{\sigma}}_h^e) = R_{u^e}^{\text{std}}(\mathbf{u}_h^e, p_h^e) + \langle \mathbf{v}_h^e, \bar{\boldsymbol{\sigma}}_h^e \cdot \mathbf{n} \rangle_{\Gamma^{\text{FF}}} - \langle \mathbf{v}_h^e, p_h^e \cdot \mathbf{n} \rangle_{\Gamma^{\text{FF}}}, \tag{3.91}$$

$$R_{p^e}(\mathbf{u}_h^e, p_h^e) = R_{p^e}^{\text{std}}(\mathbf{u}_h^e, p_h^e), \tag{3.92}$$

$$\begin{aligned}
R_{\bar{\boldsymbol{\sigma}}^b}(\mathbf{u}_h^b, p_h^b, \bar{\boldsymbol{\sigma}}_h^b) &= -\frac{1}{n} (\bar{\boldsymbol{\tau}}_h^b, \frac{1}{2\mu} \bar{\boldsymbol{\sigma}}_h^b)_{\Omega^b} + \frac{1}{n} (\bar{\boldsymbol{\tau}}_h^b, \boldsymbol{\epsilon}(\mathbf{u}_h^b))_{\Omega^b} \\
& - \langle \bar{\boldsymbol{\tau}}_h^b \cdot \mathbf{n}, \mathbf{u}_h^b \rangle_{\Gamma^{\text{FF}}} + \langle \bar{\boldsymbol{\tau}}_h^b \cdot \mathbf{n}, \mathbf{u}_h^e \rangle_{\Gamma^{\text{FF}}}.
\end{aligned} \tag{3.93}$$

As before, $R_{u^b}^{\text{std}}$, $R_{p^b}^{\text{std}}$, $R_{u^e}^{\text{std}}$ and $R_{p^e}^{\text{std}}$ denote the contributions of the standard Galerkin terms for background and embedded fluid subdomains. The global linear system including the additional

stress unknowns is given as

$$\begin{aligned}
 & \left[\begin{array}{cc|cc}
 F_{u^b u^b} + K_{u^b u^b} & F_{u^b p^b} + G_{u^b p^b} & G_{u^b \bar{\sigma}^b} + K_{u^b \bar{\sigma}^b} & 0 & 0 \\
 F_{p^b u^b} + G_{p^b u^b} & 0 & 0 & G_{p^b u^e} & 0 \\
 K_{\bar{\sigma}^b u^b} + G_{\bar{\sigma}^b u^b} & 0 & K_{\bar{\sigma}^b \bar{\sigma}^b} & G_{\bar{\sigma}^b u^e} & 0 \\
 \hline
 0 & G_{u^e p^b} & G_{u^e \bar{\sigma}^b} & F_{u^e u^e} & F_{u^e p^e} \\
 0 & 0 & 0 & F_{p^e u^e} & 0
 \end{array} \right]^{n+1}_i \cdot \begin{bmatrix} \Delta u^b \\ \Delta p^b \\ \Delta \bar{\sigma}^b \\ \Delta u^e \\ \Delta p^e \end{bmatrix}^{n+1}_{i+1} \\
 & = - \begin{bmatrix} r_u^b \\ r_p^b \\ r_{\bar{\sigma}}^b \\ r_u^e \\ r_p^e \end{bmatrix}_i. \tag{3.94}
 \end{aligned}$$

It can be seen in (3.94) that in contrast to MHCS method, see (3.67), also coupling terms are added to the standard Galerkin submatrices. As previously mentioned, the reason is that only the viscous traction on Γ^{FF} is substituted by the addition stress field and the pressure field remains unchanged, see equations (3.80) and (3.81). Table (3.3) assigns the submatrices G_{**} and K_{**} to the corresponding weighted residual contributions. The residual terms are denoted by $r_u^b, r_p^b, r_{\bar{\sigma}}^b, r_u^e,$ and r_p^e including the contributions of the standard Galerkin and the viscous stress-based method. As in MHCS, the stress increments $\Delta \bar{\sigma}^b$ are discontinuous between elements and

Submatrix	Linearized term
$G_{u^b p^b}$	$\frac{\partial \langle \mathbf{v}_h^b, p_h^b \cdot \mathbf{n} \rangle_{\Gamma^{\text{FF}}}}{\partial p^b}$
$G_{u^b \bar{\sigma}^b}$	$\frac{\partial \langle \mathbf{v}_h^b, \bar{\boldsymbol{\sigma}}_h^b \cdot \mathbf{n} \rangle_{\Gamma^{\text{FF}}}}{\partial \bar{\boldsymbol{\sigma}}^b}$
$G_{p^b u^b}$	$\frac{\partial \langle q_h^b \cdot \mathbf{n}, \mathbf{u}_h^b \rangle_{\Gamma^{\text{FF}}}}{\partial \mathbf{u}^b}$
$G_{p^b u^e}$	$\frac{\partial \langle q_h^b \cdot \mathbf{n}, \mathbf{u}_h^e \rangle_{\Gamma^{\text{FF}}}}{\partial \mathbf{u}^e}$
$G_{\bar{\sigma}^b u^b}$	$\frac{\partial \langle \bar{\boldsymbol{\tau}}_h^b \cdot \mathbf{n}, \mathbf{u}_h^b \rangle_{\Gamma^{\text{FF}}}}{\partial \mathbf{u}^b}$
$G_{\bar{\sigma}^b u^e}$	$\frac{\partial \langle \bar{\boldsymbol{\tau}}_h^b \cdot \mathbf{n}, \mathbf{u}_h^e \rangle_{\Gamma^{\text{FF}}}}{\partial \mathbf{u}^e}$
$G_{u^e p^b}$	$\frac{\partial \langle \mathbf{v}_h^e, p_h^b \cdot \mathbf{n} \rangle_{\Gamma^{\text{FF}}}}{\partial p^b}$
$G_{u^e \bar{\sigma}^b}$	$\frac{\partial \langle \mathbf{v}_h^e, \bar{\boldsymbol{\sigma}}^b \cdot \mathbf{n} \rangle_{\Gamma^{\text{FF}}}}{\partial \bar{\boldsymbol{\sigma}}^b}$
$K_{u^b u^b}$	$-\frac{\partial \beta_v \frac{1}{n} (\boldsymbol{\epsilon}(\mathbf{v}_h^b), 2\mu \boldsymbol{\epsilon}(\mathbf{u}_h^b))_{\Omega^b}}{\partial \boldsymbol{\epsilon}(\mathbf{u}_h^b)}$
$K_{u^b \bar{\sigma}^b}$	$\frac{\partial \beta_v \frac{1}{n} (\boldsymbol{\epsilon}(\mathbf{v}_h^b), \bar{\boldsymbol{\sigma}}^b)_{\Omega^b}}{\partial \bar{\boldsymbol{\sigma}}^b}$
$K_{\bar{\sigma}^b u^b}$	$\frac{\partial \frac{1}{n} (\bar{\boldsymbol{\tau}}_h^b, \boldsymbol{\epsilon}(\mathbf{u}_h^b))_{\Omega^b}}{\partial \boldsymbol{\epsilon}(\mathbf{u}_h^b)}$
$K_{\bar{\sigma}^b \bar{\sigma}^b}$	$-\frac{\partial \frac{1}{n} (\bar{\boldsymbol{\tau}}_h^b, \frac{1}{2\mu} \bar{\boldsymbol{\sigma}}^b)_{\Omega^b}}{\partial \bar{\boldsymbol{\sigma}}^b}$

Table 3.3: Submatrices of MHVS

influence the velocity and pressure solutions only in cut elements via boundary integrals G_{**} . Furthermore, due to the discontinuity of $\bar{\sigma}_h^b$, the discrete strain rate balance and discrete viscous strain rate balance, lines seven and eighth of (3.86), are always satisfied for uncut elements, thus, they can be omitted for uncut elements. For cut elements, the stress increments can be condensed element-wise because of their C^{-1} -continuity. Employing the third row of (3.94), the stress increments for an element $K \in \mathcal{T}^\Gamma$ reads as

$$\Delta \bar{\sigma}^{b,K} = (\mathbf{K}_{\bar{\sigma}^b \bar{\sigma}^b}^K)^{-1} (-r_{\bar{\sigma}}^{b,K} - (\mathbf{K}_{\bar{\sigma}^b u^b}^K + \mathbf{G}_{\bar{\sigma}^b u^b}^K) \Delta u^{b,K} - \mathbf{G}_{\bar{\sigma}^b u^e}^K \Delta u^{e,K}). \quad (3.95)$$

Hereby, $\Delta u^{b,K}$ denotes the velocity nodal unknowns belonging to the cut element K and $\Delta \bar{\sigma}^{b,K}$ the element unknowns for the viscous stress approximation. Furthermore, $\Delta u^{e,K}$ contains the velocities of embedded fluid elements, which intersect the background fluid K . For the condensed linear system the following element coupling matrices has to be defined

$$\mathbf{C}_{u^b u^b}^K = \mathbf{K}_{u^b u^b}^K - (\mathbf{G}_{u^b \bar{\sigma}^b}^K + \mathbf{K}_{u^b \bar{\sigma}^b}^K) (\mathbf{K}_{\bar{\sigma}^b \bar{\sigma}^b}^K)^{-1} (\mathbf{K}_{\bar{\sigma}^b u^b}^K + \mathbf{G}_{\bar{\sigma}^b u^b}^K), \quad (3.96)$$

$$\mathbf{C}_{u^b u^e}^K = -(\mathbf{G}_{u^b \bar{\sigma}^b}^K + \mathbf{K}_{u^b \bar{\sigma}^b}^K) (\mathbf{K}_{\bar{\sigma}^b \bar{\sigma}^b}^K)^{-1} \mathbf{G}_{\bar{\sigma}^b u^e}^K, \quad (3.97)$$

and for the embedded fluid velocity unknowns

$$\mathbf{C}_{u^e u^b}^K = -\mathbf{G}_{u^e \bar{\sigma}^b}^K (\mathbf{K}_{\bar{\sigma}^b \bar{\sigma}^b}^K)^{-1} (\mathbf{K}_{\bar{\sigma}^b u^b}^K + \mathbf{G}_{\bar{\sigma}^b u^b}^K), \quad (3.98)$$

$$\mathbf{C}_{u^e u^e}^K = -\mathbf{G}_{u^e \bar{\sigma}^b}^K (\mathbf{K}_{\bar{\sigma}^b \bar{\sigma}^b}^K)^{-1} \mathbf{G}_{\bar{\sigma}^b u^e}^K. \quad (3.99)$$

The additional residual terms are defined as

$$\mathbf{c}_u^{b,K} = -(\mathbf{G}_{u^b \bar{\sigma}^b}^K + \mathbf{K}_{u^b \bar{\sigma}^b}^K) (\mathbf{K}_{\bar{\sigma}^b \bar{\sigma}^b}^K)^{-1} r_{\bar{\sigma}}^{b,K}, \quad (3.100)$$

$$\mathbf{c}_u^{e,K} = -\mathbf{G}_{u^e \bar{\sigma}^b}^K (\mathbf{K}_{\bar{\sigma}^b \bar{\sigma}^b}^K)^{-1} r_{\bar{\sigma}}^{b,K}. \quad (3.101)$$

Considering these definitions, the condensed global system can be assembled from element entries in every Newton step i of the time step $n + 1$

$$\mathbf{A}_K \begin{bmatrix} \mathbf{F}_{u^b u^b}^K + \mathbf{C}_{u^b u^b}^K & \mathbf{F}_{u^b p^b}^K + \mathbf{G}_{u^b p^b}^K & \mathbf{C}_{u^b u^e}^K & 0 \\ \mathbf{F}_{p^b u^b}^K + \mathbf{G}_{p^b u^b}^K & 0 & \mathbf{G}_{p^b u^e}^K & 0 \\ \mathbf{C}_{u^e u^b}^K & \mathbf{G}_{u^e p^b}^K & \mathbf{F}_{u^e u^e}^K + \mathbf{C}_{u^e u^e}^K & \mathbf{F}_{u^e p^e}^K \\ 0 & 0 & \mathbf{F}_{p^e u^e}^K & 0 \end{bmatrix}^{n+1}_i \quad (3.102)$$

$$\cdot \mathbf{A}_K \begin{bmatrix} \Delta u^{b,K} \\ \Delta p^{b,K} \\ \Delta u^{e,K} \\ \Delta p^{e,K} \end{bmatrix}^{n+1}_{i+1} = - \mathbf{A}_K \begin{bmatrix} r_u^{b,K} + \mathbf{c}_u^{b,K} \\ r_p^{b,K} \\ r_u^{e,K} + \mathbf{c}_u^{e,K} \\ r_p^{e,K} \end{bmatrix}_i.$$

Omitting the elements far from interface of both fluid subdomains, i.e. considering only the cut background elements and the embedded elements, which share a side with Γ^{FF} , the condensed

global system reads as

$$\begin{aligned}
 & \left[\begin{array}{cc|cc} F_{u^b u^b} + C_{u^b u^b} & F_{u^b p^b} + G_{u^b p^b} & C_{u^b u^e} & 0 \\ F_{p^b u^b} + G_{p^b u^b} & 0 & G_{p^b u^e} & 0 \\ \hline C_{u^e u^b} & G_{u^e p^b} & F_{u^e u^e} + C_{u^e u^e} & F_{u^e p^e} \\ 0 & 0 & F_{p^e u^e} & 0 \end{array} \right]_{i}^{n+1} \cdot \begin{bmatrix} \Delta u^b \\ \Delta p^b \\ \Delta u^e \\ \Delta p^e \end{bmatrix}_{i+1}^{n+1} \\
 & = - \begin{bmatrix} r_u^b + c_u^b \\ r_p^b \\ r_u^e + c_u^e \\ r_p^e \end{bmatrix}_{i}^{n+1} .
 \end{aligned} \tag{3.103}$$

3.3.5 Comparison of different methods

In Sections 3.3.2, 3.3.3 and 3.3.4, three methods for weak imposition of coupling conditions on embedded fluid interface Γ^{FF} , Nitsche's method, mixed/hybrid Cauchy stress-based method (MHCS) and mixed/hybrid viscous stress-based method (MHVS), have been introduced. In the following, the similarities and differences among them will be highlighted. A comparison of the MHVS method and Nitsche's method for Poisson's Problem is given in the original publication by Baiges et al. [11]. Furthermore, Kruse [119] compared the three methods for Poisson's problem, Stokes and Navier-Stokes problems. Since Nitsche's method is the most known and established method among them, it will be considered as a reference formulation for the purpose of comparison. Thus, each of the stress-based methods will be compared to Nitsche's formulation. Again, in this part, the formulation is restricted to background fluid element weighting, which could be derived for the embedded fluid element weighting in the same way. First, the MHVS method will be compared to Nitsche's approach, since it is the more similar method to Nitsche's formulation.

Nitsche's method compared to MHVS method

In the following, the mixed/hybrid viscous stress-based method (MHVS) will be compared to Nitsche's method in terms of signs and scaling of the terms. Considering MHVS method, after partial integration, the viscous part of the interface traction is replaced by the introduced Lagrange multiplier at the interface $\bar{\sigma}_h^b \cdot \mathbf{n}$, and the pressure consistency term remains unchanged. Thus, the consistency terms read as

$$\langle \llbracket \mathbf{v}_h \rrbracket, p_h^b \cdot \mathbf{n} \rangle_{\Gamma^{\text{FF}}} - \langle \llbracket \mathbf{v}_h \rrbracket, \bar{\sigma}_h^b \cdot \mathbf{n} \rangle_{\Gamma^{\text{FF}}} . \tag{3.104}$$

Furthermore, due to discontinuity of $\bar{\sigma}_h^b$ the strain rate balance is element-wise satisfied. Considering the Nitsche's standard consistency terms, obtained from partial integration

$$\langle \llbracket \mathbf{v}_h \rrbracket, p_h^b \cdot \mathbf{n} \rangle_{\Gamma^{\text{FF}}} - \langle \llbracket \mathbf{v}_h \rrbracket, 2\mu\epsilon(\mathbf{u}_h^b) \cdot \mathbf{n} \rangle_{\Gamma^{\text{FF}}} , \tag{3.105}$$

it can be easily seen that the pressure consistency terms of the both methods are equal. Nitsche's weighted interface kinematic condition leads to the so-called velocity and pressure adjoint consistency terms as

$$-\beta_n \langle 2\mu\epsilon(\mathbf{v}_h^b) \cdot \mathbf{n}, \llbracket \mathbf{u}_h \rrbracket \rangle_{\Gamma^{\text{FF}}} - \langle q_h^b \cdot \mathbf{n}, \llbracket \mathbf{u}_h \rrbracket \rangle_{\Gamma^{\text{FF}}} , \tag{3.106}$$

where $\beta_n \in \{-1, 1\}$ indicates a non-symmetric or a symmetric viscous part of Nitsche's formulation. On the other hand, in the case of MHVS method the weighted kinematic continuity can be stated as

$$-\langle \bar{\boldsymbol{\tau}}_h^b \cdot \boldsymbol{n}, \llbracket \boldsymbol{u}_h \rrbracket \rangle_{\Gamma^{\text{FF}}} - \langle q_h^b \cdot \boldsymbol{n}, \llbracket \boldsymbol{u}_h \rrbracket \rangle_{\Gamma^{\text{FF}}}, \quad (3.107)$$

with the discontinuous test stress field $\bar{\boldsymbol{\tau}}_h^b$. It is also obvious from (3.106) and (3.107) that the pressure adjoint consistency term of Nitsche's method corresponds to the pressure term of weighted kinematic continuity of MHVS method. Hence, all pressure terms of MHVS method fully correspond to the one obtained for Nitsche's method. For the further similarities to Nitsche's method, the condensed system has to be considered. It will be shown that after eliminating the discontinuous stress field some of the terms cancel out and the final expression shows further similarities to Nitsche's method. Baiges et al. [11] showed for Poisson's problem that the MHVS method, except for penalty terms, is identical to Nitsche's formulation.

The resulting linear system after element-wise condensation of added discontinuous stress field was shown in (3.103). The coupling matrices C_{**} consist of volumetric terms K_{**} , which scale with the physical part of the element volume, $\text{meas}(\Omega^b \cap K)$, and of interface terms G_{**} , which scale with the coupling surface area, $\text{meas}(\Gamma^{\text{FF}} \cap K)$, i.e. an element's contribution to the interface. On the other hand, the Nitsche stabilization parameter, $\alpha' := \delta \mu C_K^b$, scales with $\frac{\text{meas}(\Gamma^{\text{FF}} \cap K)}{\text{meas}(\Omega^b \cap K)}$ as shown in Section 3.3.2. With these statements, the corresponding Nitsche terms to the MHVS can be composed. The associations of Nitsche's stabilization terms with the MHVS are given in Table 3.4. The user-defined parameter n of MHVS method, acts in the same way as the parameter δ of Nitsche's formulation. As it can be seen in Table 3.4, the signs of the penalty terms for Nitsche's formulation and the MHVS are the same. Thus, it can be concluded that MHVS method involves an implicit stabilization term in its formulation, corresponding to Nitsche's penalty term, which is automatically incorporated in the formulation independent of the polynomial order or the spatial discretization.

In Table 3.5, the standard consistency and adjoint consistency terms of Nitsche's method and the corresponding terms of the MHVS method are shown. As mentioned above, the pressure standard consistency and adjoint consistency terms are the same. Considering the velocity standard consistency terms of MHVS, the volumetric scaling $\text{meas}(\Omega^b \cap K)$ cancels out and the remaining part has the same scale and sign as Nitsche's velocity standard consistency term. Also the volumetric scaling vanishes in the case of velocity adjoint consistency terms and the remaining terms correspond to Nitsche's velocity adjoint consistency terms. Furthermore, the parameter β_v corresponds to the parameter β_n of Nitsche's formulation, which leads to a symmetric or non-symmetric formulation of the viscous part of the MHVS method.

Nitsche's method compared to MHCS method

In the following, MHCS method will be compared to Nitsche's method in terms of signs and scaling of the terms. The Cauchy stress-based Lagrange multiplier field can be directly identified as real forces at the shared interface Γ^{FF} . As a consequence of this, in contrast to Nitsche's method or the viscous stress-based method, which are very similar, the additional stress-based field of MHCS method also includes the pressure field. This leads to significant differences in the formulation of MHCS method. As for the comparison between MHVS method and Nitsche's

Penalty terms			
Nitsche's method		MHVS method	
Matrix	Scaling	Matrix	Scaling
$G_{u^b u^b}^\alpha$	$+\mu\delta \frac{\text{meas}(\Gamma^{\text{FF}} \cap K)}{\text{meas}(\Omega^b \cap K)} \cdot \text{meas}(\Gamma^{\text{FF}} \cap K)$	$-G_{u^b \bar{\sigma}^b} K_{\bar{\sigma}^b \bar{\sigma}^b}^{-1} G_{\bar{\sigma}^b u^b}$	$+2\mu n \frac{\text{meas}(\Gamma^{\text{FF}} \cap K)}{\text{meas}(\Omega^b \cap K)} \cdot \text{meas}(\Gamma^{\text{FF}} \cap K)$
$G_{u^b u^e}^\alpha$	$-\mu\delta \frac{\text{meas}(\Gamma^{\text{FF}} \cap K)}{\text{meas}(\Omega^b \cap K)} \cdot \text{meas}(\Gamma^{\text{FF}} \cap K)$	$-G_{u^b \bar{\sigma}^b} K_{\bar{\sigma}^b \bar{\sigma}^b}^{-1} G_{\bar{\sigma}^b u^e}$	$-2\mu n \frac{\text{meas}(\Gamma^{\text{FF}} \cap K)}{\text{meas}(\Omega^b \cap K)} \cdot \text{meas}(\Gamma^{\text{FF}} \cap K)$
$G_{u^e u^b}^\alpha$	$-\mu\delta \frac{\text{meas}(\Gamma^{\text{FF}} \cap K)}{\text{meas}(\Omega^b \cap K)} \cdot \text{meas}(\Gamma^{\text{FF}} \cap K)$	$-G_{u^e \bar{\sigma}^b} K_{\bar{\sigma}^b \bar{\sigma}^b}^{-1} G_{\bar{\sigma}^b u^b}$	$-2\mu n \frac{\text{meas}(\Gamma^{\text{FF}} \cap K)}{\text{meas}(\Omega^b \cap K)} \cdot \text{meas}(\Gamma^{\text{FF}} \cap K)$
$G_{u^e u^e}^\alpha$	$+\mu\delta \frac{\text{meas}(\Gamma^{\text{FF}} \cap K)}{\text{meas}(\Omega^b \cap K)} \cdot \text{meas}(\Gamma^{\text{FF}} \cap K)$	$-G_{u^e \bar{\sigma}^b} K_{\bar{\sigma}^b \bar{\sigma}^b}^{-1} G_{\bar{\sigma}^b u^e}$	$+2\mu n \frac{\text{meas}(\Gamma^{\text{FF}} \cap K)}{\text{meas}(\Omega^b \cap K)} \cdot \text{meas}(\Gamma^{\text{FF}} \cap K)$

Table 3.4: Association of Nitsche's method with MHVS method

method given above, the formulation after condensation of the additional stress field is considered.

The association of the penalty terms for Nitsche's method and MHCS are given in Table 3.6. As it can be seen, considering the volumetric and boundary terms, the scale of the Nitsche parameter $\alpha' \simeq \frac{\text{meas}(\Gamma^{\text{FF}} \cap K)}{\text{meas}(\Omega^b \cap K)}$, is implicitly contained in penalty terms of the MHCS. In contrast to the penalty terms of the MHVS method, the user-defined parameter corresponding to δ of Nitsche's stabilization parameter is not included. However, comparing again the penalty terms of both methods, it can be asserted that the penalty term of MHCS method corresponds to Nitsche's penalty term $\delta = 2$.

The standard consistency and adjoint consistency terms are shown in Table 3.7. Again the volumetric scaling of $K_{\bar{\sigma}^b \bar{\sigma}^b}^{-1}$ with $G_{\bar{\sigma}^b u^b}$ and $G_{\bar{\sigma}^b p^b}$ cancels out, leading to the similar terms as Nitsche's velocity and pressure consistency terms. While all the consistency terms of Nitsche's method can be identified, all adjoint consistency terms for the MHCS method are missing. In the numerical examples, the influence of missing adjoint consistency will be shown.

Discussion

In this section, each of the stress-based methods have been compared to Nitsche's formulation in detail. In the following, a summary of the similarities and differences of the discussed methods is given.

The MHVS method is very similar to Nitsche's method. After the condensation of the additional stress field, it contains all the velocity and pressure standard and adjoint consistency terms corresponding to Nitsche's formulation. As for Nitsche's method, it also contains the parameter β_v , a switch for a symmetric and non-symmetric viscous part, and the parameter n , which corresponds the δ -parameter of Nitsche stabilization parameter in (3.36) and (3.44). Due to an additional equation besides the strain rate balance (3.82), which is stated as viscous stress balance (3.83), like Nitsche's method the formulation is symmetric in its form, i.e. if the signs of the terms are not considered. The MHVS method treats also the pressure terms in an equal manner like Nitsche's method, since the additional stress field is a viscous stress and does not contain the pressure field. Hence, as also shown by Baiges et al. [11], the MHVS method is a very similar method to Nitsche's method.

Standard consistency terms			
Nitsche's method		MHVS method	
Matrix	Scaling	Matrix	Scaling
$G_{u^b p^b}^c$	$+\text{meas}(\Gamma^{\text{FF}} \cap K)$	$G_{u^b p^b}$	$+\text{meas}(\Gamma^{\text{FF}} \cap K)$
$G_{u^e p^b}^c$	$-\text{meas}(\Gamma^{\text{FF}} \cap K)$	$G_{u^e p^b}$	$-\text{meas}(\Gamma^{\text{FF}} \cap K)$
$G_{u^b u^b}^c$	$-2\mu \text{meas}(\Gamma^{\text{FF}} \cap K)$	$-G_{u^b \bar{\sigma}^b} K_{\bar{\sigma}^b \bar{\sigma}^b}^{-1} K_{\bar{\sigma}^b u^b}$	$-2\mu \text{meas}(\Gamma^{\text{FF}} \cap K) \cdot \frac{1}{\text{meas}(\Omega^b \cap K)} \cdot \text{meas}(\Omega^b \cap K)$
$G_{u^e u^b}^c$	$+2\mu \text{meas}(\Gamma^{\text{FF}} \cap K)$	$-G_{u^e \bar{\sigma}^b} K_{\bar{\sigma}^b \bar{\sigma}^b}^{-1} K_{\bar{\sigma}^b u^b}$	$+2\mu \text{meas}(\Gamma^{\text{FF}} \cap K) \cdot \frac{1}{\text{meas}(\Omega^b \cap K)} \cdot \text{meas}(\Omega^b \cap K)$
Adjoint consistency terms			
Nitsche's method		MHVS method	
Matrix	Scaling	Matrix	Scaling
$G_{p^b u^b}^a$	$-\text{meas}(\Gamma^{\text{FF}} \cap K)$	$G_{p^b u^b}$	$-\text{meas}(\Gamma^{\text{FF}} \cap K)$
$G_{p^b u^e}^a$	$+\text{meas}(\Gamma^{\text{FF}} \cap K)$	$G_{p^b u^e}$	$+\text{meas}(\Gamma^{\text{FF}} \cap K)$
$G_{u^b u^b}^a$	$-2\mu\beta_n \text{meas}(\Gamma^{\text{FF}} \cap K)$	$-K_{u^b \bar{\sigma}^b} K_{\bar{\sigma}^b \bar{\sigma}^b}^{-1} G_{\bar{\sigma}^b u^b}$	$-2\mu\beta_n \text{meas}(\Omega^b \cap K) \cdot \frac{1}{\text{meas}(\Omega^b \cap K)} \cdot \text{meas}(\Gamma^{\text{FF}} \cap K)$
$G_{u^b u^e}^a$	$+2\mu\beta_n \text{meas}(\Gamma^{\text{FF}} \cap K)$	$-K_{u^b \bar{\sigma}^b} K_{\bar{\sigma}^b \bar{\sigma}^b}^{-1} G_{\bar{\sigma}^b u^e}$	$+2\mu\beta_n \text{meas}(\Omega^b \cap K) \cdot \frac{1}{\text{meas}(\Omega^b \cap K)} \cdot \text{meas}(\Gamma^{\text{FF}} \cap K)$

Table 3.5: Association of Nitsche's method with MHVS method

Furthermore, the characteristic of the method provides a automatic calculation of the penalty term for arbitrary element shapes or forms and polynomial orders, which can be compared to Nitsche's penalty term including an eigenvalue problem to estimate Nitsche's stabilization parameter as shown in (3.45).

On the other hand, the MHCS method holds a physical motivation, i.e. Lagrange multiplier at the interface can be identified as a true interface traction. This leads to some differences in the formulation between the MHCS method and Nitsche's method or the MHVS method. The strain rate balance is added to the formulation to close the equation. However, the strain rate balance is the only additional equation in the formulation, leading to a non-symmetric form of the approach even for symmetric problems. Moreover, in the final formulation after the condensation of the stress field, it comes out that the Cauchy stress-based is free of any adjoint consistency terms for both velocity and pressure fields. The MHVS method develops these terms from the additional equation to the strain rate balance, the viscous stress balance, which also ensures the symmetrical form of the approach. The missing adjoint consistency terms could be a reason for uncontrolled pressure behavior, as it will be shown in the Section 3.7. Furthermore, no other stabilization parameter like n of MHVS method is included, thus, it can be stated that the formulation involves an implicit stabilization parameter with the value of 2, see Table 3.6. To sum up, the mentioned characteristic of MHCS method leads to an unstable behavior of the method, as it will be shown in Section 3.7. It has to be pointed out that a mathematical proof for the stability of the MHCS method is still missing.

As a similarity between both stress-based methods and the main difference to Nitsche's formulation, it needs to be noted that in both stress-based methods, the estimation of a penalty

Penalty terms			
Nitsche's method		MHCS method	
Matrix	Scaling	Matrix	Scaling
$\mathbf{G}_{u^b u^b}^\alpha$	$+\mu\delta \frac{\text{meas}(\Gamma^{\text{FF}} \cap K)}{\text{meas}(\Omega^b \cap K)} \cdot \text{meas}(\Gamma^{\text{FF}} \cap K)$	$-\mathbf{G}_{u^b \bar{\sigma}^b} \mathbf{K}_{\bar{\sigma}^b \bar{\sigma}^b}^{-1} \mathbf{G}_{\bar{\sigma}^b u^b}$	$+2\mu \cdot \frac{\text{meas}(\Gamma^{\text{FF}} \cap K)}{\text{meas}(\Omega^b \cap K)} \cdot \text{meas}(\Gamma^{\text{FF}} \cap K)$
$\mathbf{G}_{u^b u^e}^\alpha$	$-\mu\delta \frac{\text{meas}(\Gamma^{\text{FF}} \cap K)}{\text{meas}(\Omega^b \cap K)} \cdot \text{meas}(\Gamma^{\text{FF}} \cap K)$	$-\mathbf{G}_{u^b \bar{\sigma}^b} \mathbf{K}_{\bar{\sigma}^b \bar{\sigma}^b}^{-1} \mathbf{G}_{\bar{\sigma}^b u^e}$	$-2\mu \cdot \frac{\text{meas}(\Gamma^{\text{FF}} \cap K)}{\text{meas}(\Omega^b \cap K)} \cdot \text{meas}(\Gamma^{\text{FF}} \cap K)$
$\mathbf{G}_{u^e u^b}^\alpha$	$-\mu\delta \frac{\text{meas}(\Gamma^{\text{FF}} \cap K)}{\text{meas}(\Omega^b \cap K)} \cdot \text{meas}(\Gamma^{\text{FF}} \cap K)$	$-\mathbf{G}_{u^e \bar{\sigma}^b} \mathbf{K}_{\bar{\sigma}^b \bar{\sigma}^b}^{-1} \mathbf{G}_{\bar{\sigma}^b u^b}$	$-2\mu \cdot \frac{\text{meas}(\Gamma^{\text{FF}} \cap K)}{\text{meas}(\Omega^b \cap K)} \cdot \text{meas}(\Gamma^{\text{FF}} \cap K)$
$\mathbf{G}_{u^e u^e}^\alpha$	$+\mu\delta \frac{\text{meas}(\Gamma^{\text{FF}} \cap K)}{\text{meas}(\Omega^b \cap K)} \cdot \text{meas}(\Gamma^{\text{FF}} \cap K)$	$-\mathbf{G}_{u^e \bar{\sigma}^b} \mathbf{K}_{\bar{\sigma}^b \bar{\sigma}^b}^{-1} \mathbf{G}_{\bar{\sigma}^b u^e}$	$+2\mu \cdot \frac{\text{meas}(\Gamma^{\text{FF}} \cap K)}{\text{meas}(\Omega^b \cap K)} \cdot \text{meas}(\Gamma^{\text{FF}} \cap K)$

Table 3.6: Association of Nitsche's method with MHCS method

parameter is included in the formulation in a natural way, i.e. the Nitsche parameter α' - or the relation $\frac{\text{meas}(\Gamma^{\text{FF}} \cap K)}{\text{meas}(\Omega^e \cap K)}$ - evolves from the formulation itself. This characteristic of the methods provides an automatic calculation of the penalty term independent of the discretization or polynomial order. Thus, the stress-based methods are comparable with a Nitsche's formulation, which involves solving an eigenvalue problem, where the estimation of Nitsche's parameter is done implicitly. Depending on the weighting side, this feature could be considered as a benefit or a drawback of the stress-based methods. In case of embedded element weighting, where the additional stress fields are introduced on the uncut embedded elements adjacent to the interface, the relation $\frac{\text{meas}(\Gamma^{\text{FF}} \cap K)}{\text{meas}(\Omega^e \cap K)}$ depends on the shape and form of the element. Therefore, using the MHVS method is similar with applying a Nitsche's formulation without any additional cost for solving the eigenvalue problem to estimate Nitsche stabilization parameter. In contrast, applying the background element weighting of MHVS method corresponds to background element weighting of Nitsche's formulation in combination of solving an eigenvalue problem, which results in a penalty parameter dependent on the position of the interface. Thus, in the case of critical cuts (see Figure 3.6a), same problems as for background element weighting of Nitsche's formulation in combination of solving an eigenvalue problem, as discussed in Section 3.3.2, are expected. The analysis in Section 3.7 confirms the dependency of background element weighting of stress-based methods on the interface position.

3.4 Extension to convection-dominated flow

For convection dominated flow, the embedded fluid formulation needs further attention, since the convection terms,

$$(\mathbf{v}_h^b, \rho^f \mathbf{u}_h^b \cdot \nabla \mathbf{u}_h^b)_{\Omega^b} \quad (3.108)$$

and

$$(\mathbf{v}_h^e, \rho^f \mathbf{c}_h^e \cdot \nabla \mathbf{u}_h^e)_{\Omega^e}, \quad (3.109)$$

introduce a further instability at the interface Γ^{FF} , due to the convective mass transport across the interface. In other words the mass conservation needs to be ensured, whenever there is a flow crossing the interface. Mathematically, it can be shown that this instability refers to a lack of coercivity at the interface. To examine the stability, a continuous advective velocity β_h for both

Standard consistency terms			
Nitsche's method		MHCS method	
Matrix	Scaling	Matrix	Scaling
$G_{u^b p^b}^c$	$+\text{meas}(\Gamma^{\text{FF}} \cap K)$	$-G_{u^b \bar{\sigma}^b} K_{\bar{\sigma}^b \bar{\sigma}^b}^{-1} K_{\bar{\sigma}^b p^b}$	$+\text{meas}(\Gamma^{\text{FF}} \cap K) \cdot \frac{1}{\text{meas}(\Omega^b \cap K)} \cdot \text{meas}(\Omega^b \cap K)$
$G_{u^e p^b}^c$	$-\text{meas}(\Gamma^{\text{FF}} \cap K)$	$-G_{u^e \bar{\sigma}^b} K_{\bar{\sigma}^b \bar{\sigma}^b}^{-1} K_{\bar{\sigma}^b p^b}$	$-\text{meas}(\Gamma^{\text{FF}} \cap K) \cdot \frac{1}{\text{meas}(\Omega^b \cap K)} \cdot \text{meas}(\Omega^b \cap K)$
$G_{u^b u^b}^c$	$-2\mu \text{meas}(\Gamma^{\text{FF}} \cap K)$	$-G_{u^b \bar{\sigma}^b} K_{\bar{\sigma}^b \bar{\sigma}^b}^{-1} K_{\bar{\sigma}^b u^b}$	$-2\mu \text{meas}(\Gamma^{\text{FF}} \cap K) \cdot \frac{1}{\text{meas}(\Omega^b \cap K)} \cdot \text{meas}(\Omega^b \cap K)$
$G_{u^e u^b}^c$	$+2\mu \text{meas}(\Gamma^{\text{FF}} \cap K)$	$-G_{u^e \bar{\sigma}^b} K_{\bar{\sigma}^b \bar{\sigma}^b}^{-1} K_{\bar{\sigma}^b u^b}$	$+2\mu \text{meas}(\Gamma^{\text{FF}} \cap K) \cdot \frac{1}{\text{meas}(\Omega^b \cap K)} \cdot \text{meas}(\Omega^b \cap K)$
Adjoint consistency terms			
Nitsche's method		MHCS method	
Matrix	Scaling	Matrix	Scaling
$G_{p^b u^b}^a$	$-\text{meas}(\Gamma^{\text{FF}} \cap K)$	-	-
$G_{p^b u^e}^a$	$+\text{meas}(\Gamma^{\text{FF}} \cap K)$	-	-
$G_{u^b u^b}^a$	$-2\mu \beta_n \text{meas}(\Gamma^{\text{FF}} \cap K)$	-	-
$G_{u^b u^e}^a$	$+2\mu \beta_n \text{meas}(\Gamma^{\text{FF}} \cap K)$	-	-

Table 3.7: Association of Nitsche's method with MHCS method

fluid subdomains is assumed, which is ensured regarding to the continuity of the velocity at the interface. Furthermore, it is assumed that $\mathbf{v}_h^b = \mathbf{u}_h^b$ and $\mathbf{v}_h^e = \mathbf{u}_h^e$. Using the identity

$$\nabla \cdot (\mathbf{v}_h \otimes \boldsymbol{\beta}_h) = \boldsymbol{\beta}_h \cdot \nabla \mathbf{v}_h + \mathbf{v}_h (\nabla \cdot \boldsymbol{\beta}_h) \quad (3.110)$$

to transform the conservative and convective forms of the Navier-Stokes equations, and applying partial integration yields for both fluid subdomains $i \in \{b, e\}$

$$\begin{aligned} (\mathbf{v}_h^i, \rho^f \boldsymbol{\beta}_h \cdot \nabla \mathbf{v}_h^i)_{\Omega^i} &= - (\mathbf{v}_h^i, \rho^f (\nabla \cdot \boldsymbol{\beta}_h) \cdot \mathbf{v}_h^i)_{\Omega^i} \\ &\quad - (\boldsymbol{\beta}_h \nabla \mathbf{v}_h^i, \rho^f \mathbf{v}_h^i)_{\Omega^i} + \langle \mathbf{v}_h^i, \rho^f (\boldsymbol{\beta}_h \cdot \mathbf{n}^i) \mathbf{v}_h^i \rangle_{\Gamma^{\text{FF}}} . \end{aligned} \quad (3.111)$$

Summing both fluid subdomains, Ω^b and Ω^e , and using $\mathbf{n} := \mathbf{n}^b = -\mathbf{n}^e$ results in

$$\begin{aligned} 2(\mathbf{v}_h^b, \rho^f \boldsymbol{\beta}_h \cdot \nabla \mathbf{v}_h^b)_{\Omega^b} + 2(\mathbf{v}_h^e, \rho^f \boldsymbol{\beta}_h \cdot \nabla \mathbf{v}_h^e)_{\Omega^e} &= \\ - (\mathbf{v}_h^b, \rho^f (\nabla \cdot \boldsymbol{\beta}_h) \cdot \mathbf{v}_h^b)_{\Omega^b} - (\mathbf{v}_h^e, \rho^f (\nabla \cdot \boldsymbol{\beta}_h) \cdot \mathbf{v}_h^e)_{\Omega^e} & \\ + \langle \mathbf{v}_h^b, \rho^f (\boldsymbol{\beta}_h \cdot \mathbf{n}) \mathbf{v}_h^b \rangle_{\Gamma^{\text{FF}}} - \langle \mathbf{v}_h^e, \rho^f (\boldsymbol{\beta}_h \cdot \mathbf{n}) \mathbf{v}_h^e \rangle_{\Gamma^{\text{FF}}} . & \end{aligned} \quad (3.112)$$

Using $\llbracket xy \rrbracket = 2\llbracket x \rrbracket \{y\}_m$ with $\{y\}_m = \frac{1}{2}(y^b + y^e)$, the standard mean value, leads to

$$\begin{aligned} (\mathbf{v}_h^b, \rho^f \boldsymbol{\beta}_h \cdot \nabla \mathbf{v}_h^b)_{\Omega^b} + (\mathbf{v}_h^e, \rho^f \boldsymbol{\beta}_h \cdot \nabla \mathbf{v}_h^e)_{\Omega^e} &= \\ - \frac{1}{2} (\mathbf{v}_h^b, \rho^f (\nabla \cdot \boldsymbol{\beta}_h) \cdot \mathbf{v}_h^b)_{\Omega^b} - \frac{1}{2} (\mathbf{v}_h^e, \rho^f (\nabla \cdot \boldsymbol{\beta}_h) \cdot \mathbf{v}_h^e)_{\Omega^e} & \\ + \langle \rho^f (\boldsymbol{\beta}_h \cdot \mathbf{n}) \{ \mathbf{v}_h \}_m, \llbracket \mathbf{v}_h \rrbracket \rangle_{\Gamma^{\text{FF}}} . & \end{aligned} \quad (3.113)$$

Assuming that the field $\boldsymbol{\beta}_h$ is divergence-free for the solution of Navier-Stokes equations, i.e. $\nabla \cdot \boldsymbol{\beta}_h = 0$, the only term in (3.113) which causes a lack of coercivity at Γ^{FF} is

$$\langle \rho^f(\boldsymbol{\beta}_h \cdot \mathbf{n})\{\mathbf{v}_h\}_m, \llbracket \mathbf{v}_h \rrbracket \rangle_{\Gamma^{\text{FF}}} . \quad (3.114)$$

To ensure the coercivity of the formulation, one has to make sure that (3.113) is positive. For this purpose, the following expression can be added to the formulation

$$- \langle \rho^f(\boldsymbol{\beta}_h \cdot \mathbf{n})\{\mathbf{v}_h\}_m, \llbracket \mathbf{u}_h \rrbracket \rangle_{\Gamma^{\text{FF}}} + \gamma_{adv} \langle \rho^f |\boldsymbol{\beta}_h \cdot \mathbf{n}| \llbracket \mathbf{v}_h \rrbracket, \llbracket \mathbf{u}_h \rrbracket \rangle_{\Gamma^{\text{FF}}} , \quad (3.115)$$

which consistently ensures the kinematic coupling condition at the interface, $\llbracket \mathbf{u} \rrbracket = 0$. The first term in (3.115), which is referred to as *averaged term*, is sufficient to balance the missing coercivity from (3.113), as it has the opposite sign to (3.114). The second term is of the same type as the Nitsche penalty term, however, with a scaling $\gamma_{adv} \rho^f |\boldsymbol{\beta}_h \cdot \mathbf{n}|$. For any parameter $\gamma_{adv} \geq 0$, the coercivity of the formulation is ensured. In the case of convection dominated flows, where the viscosity is small, the advective scaling penalty term, the second term in (3.115), dominates Nitsche viscous stabilization term. Using $\gamma_{adv} = \frac{1}{2}$, leads to

$$\begin{aligned} & - \langle \rho^f(\boldsymbol{\beta}_h \cdot \mathbf{n})\{\mathbf{v}_h\}_m, \llbracket \mathbf{u}_h \rrbracket \rangle_{\Gamma^{\text{FF}}} + \frac{1}{2} \langle \rho^f |\boldsymbol{\beta}_h \cdot \mathbf{n}| \llbracket \mathbf{v}_h \rrbracket, \llbracket \mathbf{u}_h \rrbracket \rangle_{\Gamma^{\text{FF}}} \\ & = \begin{cases} \langle \rho^f(\boldsymbol{\beta}_h \cdot \mathbf{n}) \mathbf{v}_h^e, \mathbf{u}_h^e - \mathbf{u}_h^b \rangle_{\Gamma^{\text{FF}}} , & \text{if } (\boldsymbol{\beta}_h \cdot \mathbf{n}) > 0 \\ \langle \rho^f |\boldsymbol{\beta}_h \cdot \mathbf{n}| \mathbf{v}_h^b, \mathbf{u}_h^b - \mathbf{u}_h^e \rangle_{\Gamma^{\text{FF}}} , & \text{if } (\boldsymbol{\beta}_h \cdot \mathbf{n}) < 0 \end{cases} \end{aligned} \quad (3.116)$$

which is the well-known classical upwinding scheme, see e.g. Donea and Huerta [62]. For the classical upwinding scheme, the fluid-fluid interface is considered as two separate inflow boundaries with respect to the two fluid subdomains. The differentiation between the two inflow boundaries happens automatically dependent on the normal component of the advective velocity such that only one of both terms is active, as shown in Figure 3.8.

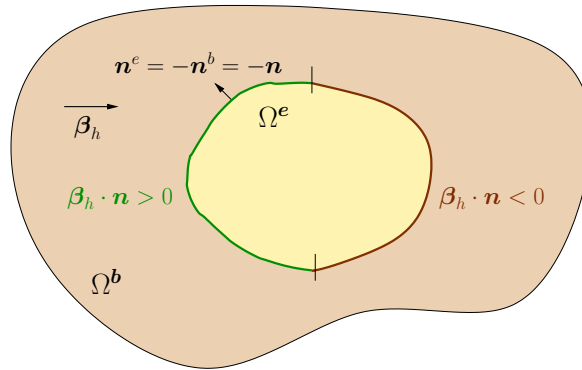


Figure 3.8: Upwinding interface stabilization terms: (3.116) is active on the inflow part of the respective subdomain Ω^i for $i \in \{b, e\}$. In case of $\boldsymbol{\beta}_h \cdot \mathbf{n} > 0$ an upwinding with respect to Ω^e is used, in case of $\boldsymbol{\beta}_h \cdot \mathbf{n} < 0$ an upwinding with respect to Ω^b .

Upwinding stabilization terms can be found in the literature in different contexts. Hughes and Wells [110] examined the conservation properties of the convective form of the Navier-Stokes equations. The total fluxes, i.e. the convective and diffusive fluxes, are considered at the inflow

part of the boundary, while at the outflow part of the boundary only diffusive flux boundary condition are applied. After partial integration and assuming that the convective velocity is divergence free, an upwinding inflow term remains at the left side. Bazilevs and Hughes [14] also distinguished between the treatment of inflow and outflow parts of the boundary in case of the imposition of weak Dirichlet boundary conditions and added convective consistency terms to the formulation. In context of the stabilization of discontinuous Galerkin finite element methods by Arnold et al. [3], also an upwinding term is included in the formulation. Furthermore, the same upwinding inflow term has been also described by Burman and Zunino [40] in context of weighted interior penalties for advection-diffusion-reaction problems and by Becker [17] in terms of treatment of inhomogeneous Dirichlet boundary conditions for Navier-Stokes equations with Nitsche's method. Moreover, in context of discontinuous Galerkin method, in Burman [31] besides the upwinding stabilization term at the inflow boundary, the averaged term (the first term of (3.115)) is included as an interior penalty term between element edges. Baiges et al. [11] showed the stability of mixed/hybrid viscous stress-based method by adding an upwinding term with a factor of $\frac{1}{2}$.

Since Nitsche's stabilization term scales with the viscosity, its value gets small for high Reynolds number. Furthermore, for flow in tangential direction the value of $|\boldsymbol{\beta} \cdot \boldsymbol{n}|$ could become small as well. Therefore, it is useful to redefine the Nitsche stabilization parameter in order to preserve the penalty effect of the Nitsche stabilization term and to ensure the mass conservation across the interface. The redefinition of the Nitsche stabilization parameter reads as

$$\alpha' := \max(\rho^f \|\boldsymbol{\beta}_h\|_\infty, \delta \mu C_k). \quad (3.117)$$

The additional penalty factor strengthens the coupling condition in the convective limit. Similar penalty factors have been also introduced by Burman [32] and Schott and Wall [154]. The effects of (3.117) will be shown in Section 3.7. In the context of two-face flow, in the recent paper by Schott et al. [155], an additional transient factor $\frac{h}{\theta \Delta t}$ has also been included in the redefinition of the stabilization parameter α' . This factor is useful, when the time step is very small, or if the velocity as well as the viscosity hold very small values, e.g. in the initial phase of transient problems starting from a zero field. However, in the present work this additional transient factor has not been considered.

3.5 Face-oriented fluid stabilizations

As already mentioned, the standard (Bubnov-)Galerkin scheme for incompressible flow suffers from two major instabilities: instability of convection-dominated flow and the inf-sup instability in the case of equal order interpolations for velocity and pressure field. Different methods have been proposed to overcome these instabilities, see e.g. Braack et al. [27]. In Section 2.3.9, the well-known residual-based stabilization methods, i.e. the Streamline-Upwind/Petrov-Galerkin (SUPG) and Pressure-Stabilizing/Petrov-Galerkin (PSPG) methods have been introduced. However, the residual-based methods also have some undesirable features as: the strong coupling between the velocity and pressure, non-symmetry of residual-based stabilizations, artificial pressure boundary conditions and artificial effects at interior boundaries of elements with different sizes. Specially, applying residual-based stabilizations in combination of fictitious domain problems using cut elements leads to under-stabilization of the cut elements and to non-physical

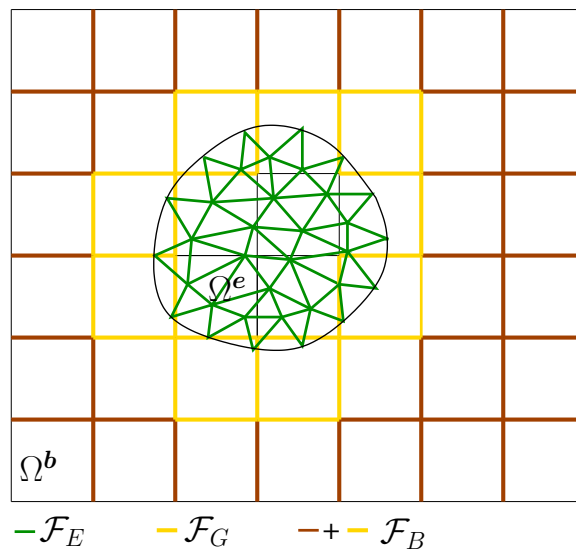


Figure 3.9: Sets of faces: \mathcal{F}_E denotes the interior faces of embedded fluid mesh and \mathcal{F}_B all cut faces and interior faces of background fluid mesh. \mathcal{F}_G indicates the set of cut faces of the background fluid mesh.

values of the void/ghost nodes of background fluid subdomain in the case of critical cuts, as shown in Burman and Hansbo [39], Schott and Wall [154] and Shadmiri et al. [156]. As mentioned in Section 3.3.2, the reason is that residual-based stabilizations are only performed at physical parts of cut elements, hence, in the case of critical cuts (Figure 3.6b), the physical part and subsequently the support of the nodal shape functions of ghost-nodes becomes too small. This leads to non-physical values at ghost-nodes and unbounded condition numbers. Therefore, in the present work, as a solution to this problem, another class of stabilization methods, the *edge-/face-oriented* fluid stabilizations, has been applied to cut problems. The face-oriented fluid stabilizations have been originally proposed by Douglas and Dupont [65] on interior penalty procedures for elliptic and parabolic problems. These methods are also well-known as continuous interior penalty stabilizations as discussed for example in Burman [32], Burman and Fernández [34], Burman and Zunino [40] and Burman and Hansbo [37]. Face-oriented stabilizations have been successfully applied to Stokes problem involving cut elements in Burman and Hansbo [38]. Schott and Wall [154] extended the face-oriented stabilizations to stabilize the three-dimensional Navier-Stokes equations in a fictitious domain framework using cut elements. The face-oriented stabilizations are based on penalty terms of the jumps over the gradients at element faces. Applying face-oriented stabilizations to cut elements gives control over the gradient jumps at all interior element faces but also at cut faces. In this way, the stabilization is extended from the physical domain into the ghost domain. Therefore, similar to viscous ghost-penalty stabilizations (3.39), physical values for ghost nodes and improved condition numbers are achieved. Some other advantages of face-oriented stabilizations can be itemized as: decoupled fluid and pressure stabilizations, symmetric stabilization terms and less artificial effects at the boundaries. For more details about different fluid stabilizations the reader is referred to Becker and Braack [18].

In the present work, in order to make the formulation inf-sup stable, the following face-oriented pressure stabilization operator

$$j_p(q_h^i, p_h^i) := \sum_{F \in \mathcal{F}_j} \int_F \gamma_p \cdot \llbracket \nabla q_h^i \rrbracket \llbracket \nabla p_h^i \rrbracket ds, \quad (3.118)$$

with $i \in \{b, e\}$ and $j \in \{B, E, G\}$, which indicates different sets of faces of the fluid domain is used. The sets of different faces of fluid domain is shown in Figure 3.9. The pressure face-oriented stabilization has been introduced by Burman and Hansbo [37] and applied to cut elements by Burman and Hansbo [38] and Schott and Wall [154]. It gives control over the pressure gradient jumps of all cut faces and/or interior faces. For $j = B$, the pressure face-oriented stabilization is applied to physical background fluid mesh \mathcal{T}^* , i.e. all cut faces and interior faces of the physical background fluid mesh, and for $j = E$, to all interior faces of embedded fluid mesh \mathcal{T}^e . For the embedded mesh also any other class of stabilizations, e.g. residual-based stabilizations, can be used. As for the embedded fluid mesh, far from the interface zone, it is also possible to use other type of stabilizations for background fluid mesh and apply pressure face-oriented stabilization only along the faces of cut elements \mathcal{T}^Γ , i.e. $j = G$ in (3.118). Along faces of the background mesh which are cut by the interface \mathcal{F}_G , the stabilization operators act as ghost-penalties (3.39), since the whole faces of cut elements, i.e. not only the physical part of the faces, are integrated and take thereby control over the ghost values in the inactive part of the cut elements of the background fluid mesh. The definition of the stabilization parameter γ_p , as given in Schott and Wall [154], accounts for viscous dominated as well as convection dominated regimes and is defined as

$$\gamma_p := \gamma_\alpha \frac{h_F^2}{\rho^f} \cdot \left(1 + \frac{\nu}{h_F}\right)^{-1} = \begin{cases} \gamma_\alpha \frac{h_F^3}{\rho^f \nu} & \text{if } h_F \ll \nu \quad (\text{viscous-dominated}) \\ \gamma_\alpha \frac{h_F^2}{\rho^f} & \text{if } h_F \gg \nu \quad (\text{convection-dominated}) \end{cases} \quad (3.119)$$

In the recent paper of Schott et al. [155], the stabilization parameter γ_p additionally includes a reactive stabilization term, which becomes useful when using small time step sizes. However, in this work it will not be considered further. Furthermore, γ_α is a constant, which is set to 0.05 as in Schott and Wall [154] and Shahmiri et al. [156].

To overcome the convective instability, a velocity gradient-based streamline stabilization operator as proposed in Burman and Fernández [35], Burman and Hansbo [36] and Schott and Wall [154] is added

$$j_{\text{stream}}(\mathbf{v}_h^i, \mathbf{u}_h^i) := \sum_{F \in \mathcal{F}_j} \int_F \gamma_s h_F^2 \rho^f \cdot |\mathbf{u}_h^i \cdot \mathbf{n}^F| \llbracket \nabla \mathbf{v}_h^i \rrbracket : \llbracket \nabla \mathbf{u}_h^i \rrbracket ds, \quad (3.120)$$

for $i \in \{b, e\}$, $j \in \{B, E, G\}$, denoting different sets of faces, and $\gamma_s = 0.02$. In this term, the normal component of the velocity $|\mathbf{u}_h^i \cdot \mathbf{n}^F|$ with respect to the face F is contained, which indicates the streamline character of this term. Again, it has to be emphasized that also for velocity face-oriented stabilization the faces in the interface zone are stabilized along the entire cut face. In the convection dominated regime, the streamline face-oriented terms takes over the role of the ghost-penalty operator (equations (3.38) and (3.39)) to improve the system conditioning. In

contrast to ghost-penalty, which is only active at faces of the interface zone \mathcal{F}_G , the convective stabilization operator with $j = B$ takes control over the velocity gradient jumps of all the interior and cut faces of background fluid mesh \mathcal{F}_B . As for the pressure face-oriented stabilization (3.118), it is possible to penalize only the gradient jumps across the faces of cut element \mathcal{F}_G and use other types of stabilizations for non-intersected elements. Similar to ghost-penalty operators, (3.38) and (3.39), also in (3.118) and (3.120), h_F is the maximal distance of the face F to the opposite faces of both adjacent elements, i.e. $h_F = \max\{h_{K_1}, h_{K_2}\}$, where K_1 and K_2 are the two neighboring elements, which share the face F . Both stabilization operators, (3.118) and (3.120), together lead to reasonable pressure and velocity values at the ghost nodes of the background fluid domain, independent of the cut position for low and high Reynolds number flows, as it will be shown in Section 3.9.

However, it needs to be mentioned that the face-oriented stabilizations have also some drawbacks, see Burman et al. [42]. They increase the bandwidth of the matrix since information from the neighboring elements is needed. Furthermore, from the implementation point of view further additional data structures are required, which hold the information about faces and adjacent elements. However, in combination with cut elements, the advantage of having a robust and stable formulation independent of interface position prevails.

In the present work, both variants, the face-oriented stabilizations on the whole background and embedded fluid faces, and the combination of residual-based with face-oriented fluid stabilizations, are used. In the latter case, the face-oriented stabilization terms are evaluated at the background fluid elements in the interface zone \mathcal{T}^Γ , i.e. the cut faces \mathcal{F}_G , and residual-based fluid stabilizations are applied additionally to all physical background fluid elements \mathcal{T}^* and the embedded fluid elements \mathcal{T}^e . The combination of residual-based with face-oriented fluid stabilizations has also been considered by Massing et al. [132, 134] or in context of two-phase flow for Stokes equations by Cattaneo et al. [43].

Remark: 3.5.1. Similar to ghost-penalty stabilization operator (3.38), for higher order elements in the interface zone, the velocity and pressure face-oriented stabilization terms also need to take control over the jumps of all the higher order normal derivatives of the faces, i.e. $[[D^i \mathbf{u}_h^b]]$ and $[[D^i p_h^b]]$ for $i = 1 \dots k$, where k denotes the highest polynomial order of \mathbf{u}_h^b and p_h^b .

Remark: 3.5.2. Similar to pressure and convection face-oriented stabilizations, a gradient-based incompressibility constraint can also be used at the element faces as given in Burman et al. [41]. In the present work, the classical least-square incompressibility constraint term (2.87) is used. As mentioned in Section 2.3.9, this term provides a better control of the incompressibility condition in convection dominated flow. Using a face-oriented incompressibility stabilization on cut elements would have some advantages due to the additional penalty effect at the interface zone, but would additionally increase the bandwidth of the matrix.

3.6 Fluid stabilization at the interface

In this section, two other fluid stabilizations will be introduced, which additionally to face-oriented stabilizations, given in Section 3.5, provide a smooth transition of velocity and pressure field across the interface Γ^{FF} . Considering the continuity of the fluxes at the interface $[[\boldsymbol{\sigma} \cdot \mathbf{n}]] = 0$, the interface stabilizations are based on the penalization of the jump in the velocity gradients and

the pressure fields across the interface. For this purpose, a velocity gradient-based stabilization similar to ghost-penalty operator (3.39) is introduced as

$$j_{\text{intv}}(\mathbf{v}_h, \mathbf{u}_h) := \int_{\Gamma^{\text{FF}}} \alpha_{\text{intv}} \cdot \mu h_F \llbracket \nabla \mathbf{v}_h \rrbracket : \llbracket \nabla \mathbf{u}_h \rrbracket ds, \quad (3.121)$$

with $\alpha_{\text{intv}} = \alpha_{\text{GP}}$. It has to be noted that in contrast to ghost-penalty operator, the operator (3.121) penalizes the jump in the velocity gradients of both fluid subdomains across the interface and is not evaluated at the element faces. Furthermore, a pressure stabilization term evaluated at the interface, which penalizes the jump in the pressure fields across the interface, is defined as

$$j_{\text{intp}}(q_h, p_h) := \int_{\Gamma^{\text{FF}}} \gamma_{\text{intp}} \cdot \llbracket q_h \rrbracket \llbracket p_h \rrbracket ds. \quad (3.122)$$

Similar to (3.119), the stabilization parameter γ_{intp} reads as

$$\gamma_{\text{intp}} := \alpha_{\text{pc}} \frac{1}{\rho^f} \cdot \left(1 + \frac{\nu}{h^b}\right)^{-1}, \quad (3.123)$$

with h^b denoting the characteristic background fluid element length and α_{pc} a user-defined parameter. Becker et al. [19] uses a similar stabilization term as (3.122), penalizing the jumps of discontinuous element-wise P^0 pressure field across the element edges, in context of incompressible elasticity. In Section 3.7, it will be shown that these additional stabilization terms result in a smoother solution at the interface, but they do not improve the convergence behavior and, thus, they are not considered as essential terms in the present work.

3.7 Convergence study with two-dimensional Kim-Moin flow

In the following, the convergence behavior of the embedded fluid formulation for different methods of weak enforcement of coupling conditions at the interface, discussed in Section 3.3, and different stabilization operators, introduced in Sections 3.4, 3.5 and 3.6, will be studied. A similar study is given in Shahmiri et al. [156]. For this purpose, the stationary 2D-Kim-Moin flow for viscous dominated flow and, the instationary 2D-Kim-Moin flow for convection dominated flow, proposed by Kim and Moin [114], are used. In all cases, the behavior of the error in both fluid subdomains and the coupling errors at the shared interface Γ^{FF} are shown. The analytical solution to the Kim-Moin flow, also known as Taylor-Problem, is given as

$$u_x(x, y, t) = -\cos(a\pi x) \sin(a\pi y) \cdot \exp(-2a^2\pi^2 t\nu), \quad (3.124)$$

$$u_y(x, y, t) = \sin(a\pi y) \cos(a\pi y) \cdot \exp(-2a^2\pi^2 t\nu), \quad (3.125)$$

$$p(x, y, t) = -\frac{1}{4}(\cos(2a\pi x) + \cos(2a\pi y)) \cdot \exp(-4a^2\pi^2 t\nu). \quad (3.126)$$

The problem is solved on a fluid domain $\Omega^f = [0, 1] \times [0, 1]$, where a fluid patch $\Omega^e = [0.5, 0.5] \times [0.5, 0.5]$ rotated by 45° is embedded into it, see Figure 3.10. The background fluid mesh, which is aligned with the whole fluid domain Ω^f , is meshed regularly with $h^b = 1/(2n)$. For the

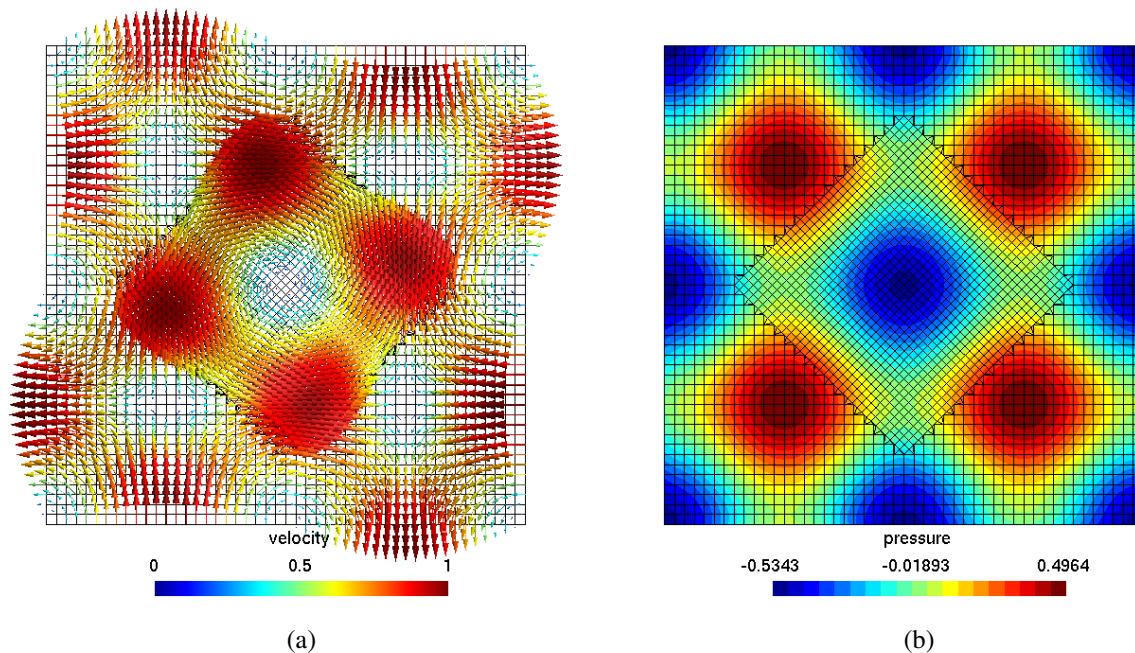


Figure 3.10: 2D-Kim-Moin: Velocity field **(a)** and pressure field **(b)** with $n = 24$.

embedded squared mesh also a regular mesh with $h^e = 1/(3n)$ is used. For both meshes a refinement by varying n is applied. At the outer boundary of the background fluid subdomain, the analytic solution for the velocity, (3.124) and (3.125), is prescribed as Dirichlet boundary condition. The pressure is prescribed at one point $x = 0.5, y = 0.5$ using (3.126) to fix the pressure level. For the viscous dominated flow we solve a stationary flow at $t = 0$. In this case, the right-hand side \mathbf{b}^f is adapted such that the equations (3.124) to (3.126) evaluated at $t = 0$ are the solutions of the stationary Navier-Stokes equations. For the error analysis, the following domain error norms, for $i \in \{b, e\}$, and interface error norms, in analogy to Schott and Wall [154] and Shahmiri et al. [156], are used

$$\|\mathbf{u} - \mathbf{u}_h^i\|_{L^2(\Omega^i)} = \left(\int_{\Omega^i} (\mathbf{u} - \mathbf{u}_h^i) \cdot (\mathbf{u} - \mathbf{u}_h^i) \right)^{1/2}, \quad (3.127)$$

$$\|\nabla(\mathbf{u} - \mathbf{u}_h^i)\|_{L^2(\Omega^i)} = \left(\int_{\Omega^i} \nabla(\mathbf{u} - \mathbf{u}_h^i) : \nabla(\mathbf{u} - \mathbf{u}_h^i) \right)^{1/2}, \quad (3.128)$$

$$\|p - p_h^i\|_{L^2(\Omega^i)} = \left(\int_{\Omega^i} (p - p_h^i) \cdot (p - p_h^i) \right)^{1/2}, \quad (3.129)$$

$$\|\nu^{-1/2}(p_h^b - p_h^e)\|_{H^{-1/2}(\Gamma^{\text{FF}})} = \left(\sum_K h_b \| \nu^{-1/2}(p_h^b - p_h^e) \|_{L^2(\Gamma_K^{\text{FF}})}^2 \right)^{1/2}, \quad (3.130)$$

$$\|\nu^{1/2} \nabla(\mathbf{u}_h^b - \mathbf{u}_h^e) \cdot \mathbf{n}\|_{H^{-1/2}(\Gamma^{\text{FF}})} = \left(\sum_K h_b \| \nu^{1/2} \nabla(\mathbf{u}_h^b - \mathbf{u}_h^e) \cdot \mathbf{n} \|_{L^2(\Gamma_K^{\text{FF}})}^2 \right)^{1/2}, \quad (3.131)$$

$$\|\nu^{1/2}(\mathbf{u}_h^b - \mathbf{u}_h^e)\|_{H^{1/2}(\Gamma^{\text{FF}})} = \left(\sum_K \frac{1}{h_b} \| \nu^{1/2}(\mathbf{u}_h^b - \mathbf{u}_h^e) \|_{L^2(\Gamma_K^{\text{FF}})}^2 \right)^{1/2}. \quad (3.132)$$

The error norms (3.127) to (3.129) measure the L^2 -errors for \mathbf{u} , $\nabla\mathbf{u}$ and p for each fluid subdomain independently. The interface norms, (3.130) to (3.132), measure the enforcement of the coupling conditions in the primal variable (3.21) and the fluxes (3.22) at the interface Γ^{FF} . For the interface norms, (3.130) to (3.132), the characteristic background element length h_b is used. As the mesh size of the both subdomains differ from each other in a constant, taking h_b for the both fluid domains does not influence the order of the convergence. Moreover, the coupling condition for the fluxes is separated into viscous and pressure fluxes. Referring to Burman and Hansbo [38], using linear elements, the optimal convergence error rate expected for the norms (3.128) to (3.132) is $\mathcal{O}(h)$, and $\mathcal{O}(h^2)$ for (3.127). It has to be noted that in this study only the symmetric case of Nitsche's method and hybrid/mixed viscous stress-based method, i.e. $\beta_n = 1$ and $\beta_v = 1$, respectively, are considered.

This example is organized as follows: in the first part, the user-defined parameters will be investigated on stability and accuracy, and optimal parameters, which are required for the following convergence studies, will be chosen. The study is carried out for a Nitsche parameter δ in (3.44) for the case of embedded element weighting of Nitsche's method, a Nitsche parameter α in (3.40) for background element weighting of Nitsche's method, the ghost-penalty parameter α_{GP} in (3.39), the parameter n of mixed/hybrid viscous stress-based method (MHVS), and the interface pressure coupling stabilization parameter α_{pc} as given in (3.123). Then, a convergence study of different methods of weak imposition of coupling conditions at the embedded fluid interface, given in Section 3.3, will be performed. To focus on these different coupling methods for the weak enforcement of the coupling conditions, the same stabilization terms are applied to all configurations. Next, the influence of the different fluid stabilizations, i.e. the face-oriented fluid stabilizations, (3.118) and (3.120), the classical residual-based stabilizations, the ghost-penalty operator (3.39) and the additional interface stabilization operators, (3.121) and (3.122), will be investigated. Finally, a convergence study of different convective stabilizations, given in Section 3.4, regarding the weak enforcement of the coupling conditions for convection dominated flows is provided. The results of the studies of the hybrid/mixed viscous stress-based method (MHVS) are based on the work of Kruse [119].

All parameter studies, and the spatial convergence studies of weak coupling formulations and stabilizations methods are performed, in viscous dominated case for a stationary dominated flow with $\nu = 0.1 \text{ m}^2/\text{s}$. On the other hand, the convergence study of different convective stabilizations are performed for an instationary convection dominated flow with $\nu = 10^{-4} \text{ m}^2/\text{s}$. Furthermore, all face-oriented stabilizations are applied on the whole faces of background and embedded fluid meshes, i.e. (3.118) and (3.120) with $j \in \{B, E\}$.

3.7.1 Analysis of different parameters

Nitsche parameters

For the embedded element weighting of Nitsche's method the influence of user-defined parameter δ in (3.44) needs to be investigated on the stability and accuracy of the solution. For this purpose, the error norms (3.127) to (3.132) are calculated for different values of $\delta \in \{5, 7, 10, 20, 35, 50, 100, 200, 500, 1000\}$ and four different meshes $n \in \{24, 32, 40, 64\}$. All the simulations are run with face-oriented velocity and pressure stabilizations (3.118) and (3.120) and the additional ghost-penalty stabilization (3.39) using a parameter of $\alpha_{\text{GP}} = 0.003$. A param-

eter study for the ghost-penalty parameter is done in the subsequent paragraph which establishes the choice of $\alpha_{\text{GP}} = 0.003$. As expected, the interface norms react more sensitive to varying δ than the domain errors, see Figures 3.11. For small values of δ , the formulation indicates the expected instability, which is specially obvious in Figure 3.11g for $\delta < 10$. The pressure-flux error increases for larger Nitsche parameters $\delta > 50$ (Figure 3.11i). Hence, in order to find a balance between ensuring stability, minimizing the error for the coupling condition (3.21) and not to deteriorate the flux error, a Nitsche parameter $\delta \approx 35.0$ seems to be an appropriate choice, which is in good agreement with Schott and Wall [154]. It needs to be pointed out that although theoretically a Nitsche parameter of $\delta > 1$ (see e.g. Embar et al. [67] and Appendix A.1) already results in a coercive formulation, better error behavior in some of the norms (3.127) to (3.132) is achieved when the maximal eigenvalue obtained from solving (3.44) is scaled with $\delta \approx 35.0$. The same study is done for the Nitsche parameter α in (3.40) for a background element weighting of Nitsche's method with an additional ghost-penalty operator (3.39) with a ghost-penalty parameter $\alpha_{\text{GP}} = 0.003$ and using face-oriented stabilizations. The results are shown in the Appendix, Figure A.1. The same behavior as the Nitsche parameter δ for embedded element weighting can also be observed for the Nitsche parameter α . Thus, also here, a Nitsche parameter $\alpha \approx 35.0$ seems to be an appropriate choice.

The ghost-penalty parameter

The ghost-penalty operator (3.39) is necessary in order to ensure coercivity when the Nitsche background element weighting ($\kappa_e = 0$ and $\kappa_b = 1$) is applied. However, it can be used to improve the system conditioning, when Nitsche embedded element weighting ($\kappa_e = 1$ and $\kappa_b = 0$) on the whole embedded elements is used. A similar study to above is done to find an optimal range for the ghost-penalty parameter α_{GP} . For different values of ghost-penalty parameter $\alpha_{\text{GP}} \in [0.001, 100]$ and four different meshes $n \in \{24, 32, 40, 64\}$, the error norms, (3.127) to (3.132), are calculated. For all simulations the embedded element weighting of Nitsche's method is used with $\delta = 35.0$, which is motivated by the previous parameter study. Furthermore, additional face-oriented velocity and pressure stabilizations are applied. In Figure 3.12, the resulting errors are shown. As it can be seen, the L^2 -norms of velocity, its gradient and the velocity fluxes are less sensitive to varying values of α_{GP} , see Figures 3.12a, 3.12b, 3.12c, 3.12d and 3.12g. For $\alpha_{\text{GP}} > 0.5$ the L^2 -norms of velocity fields increase slightly, see Figures 3.12a and 3.12b, whereas the L^2 -norms of the pressure fields increase already for $\alpha_{\text{GP}} > 0.1$, see Figures 3.12e and 3.12f. The most sensitive results are obtained for the pressure fluxes. There, the error increases drastically for $\alpha_{\text{GP}} > 0.05$, see Figure 3.12i. Whereas the coupling of the viscous fluxes is positively influenced by the coupling condition (3.21) in the primal variable, any perturbation at the interface can be seen in the pressure fluxes first. Motivated by the fact that in the case of embedded element weighting of Nitsche, the viscous ghost-penalty operator is used only to improve the system conditioning and not to ensure coercivity, a small ghost-penalty parameter of $\alpha_{\text{GP}} = 0.003$ is chosen.

The MHVS parameter

As for Nitsche's method, the user-defined parameter n in the formulation of MHVS method (3.86) has to be investigated. For this purpose, for different values of $n \in [1, 500]$ and three dif-

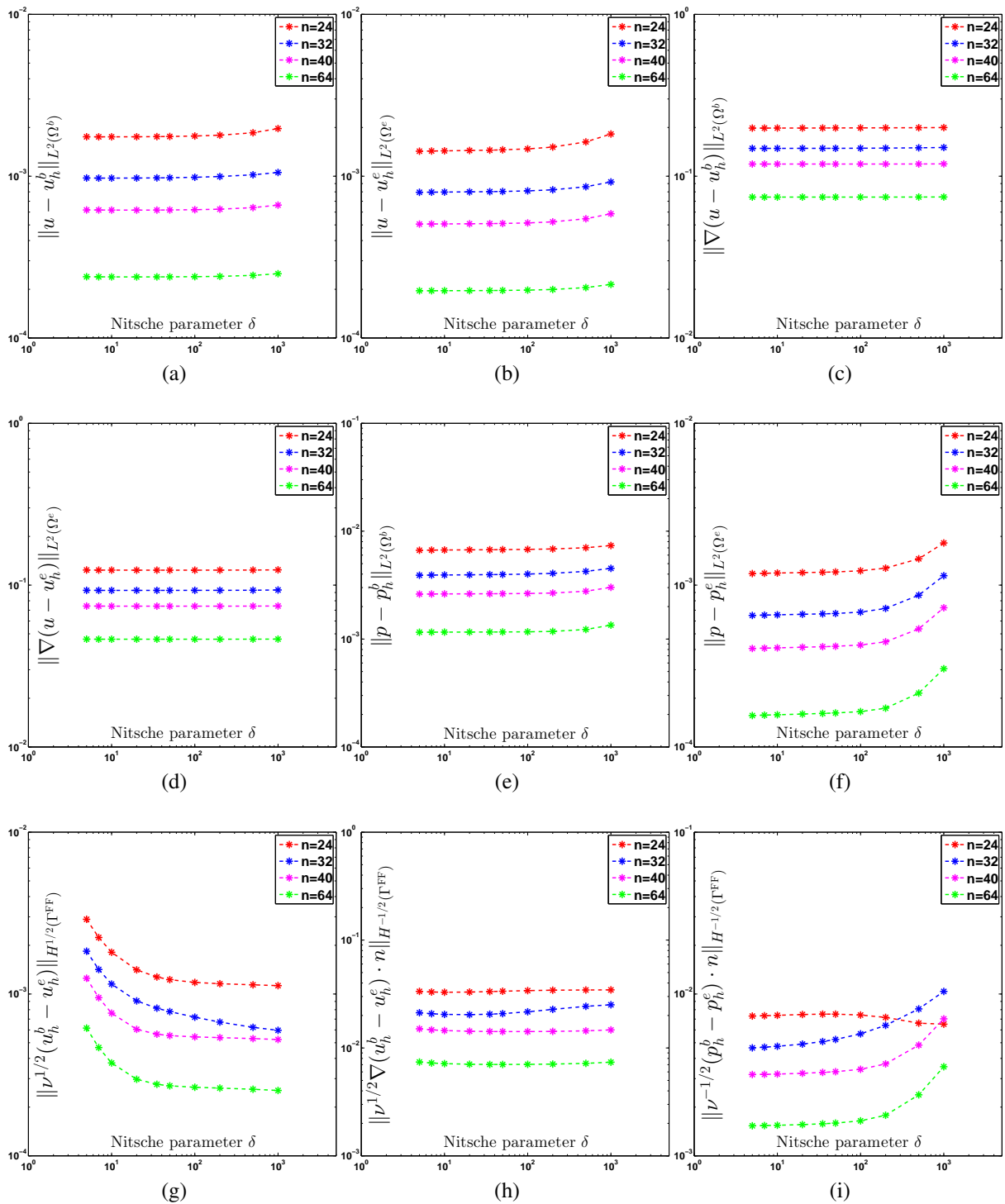
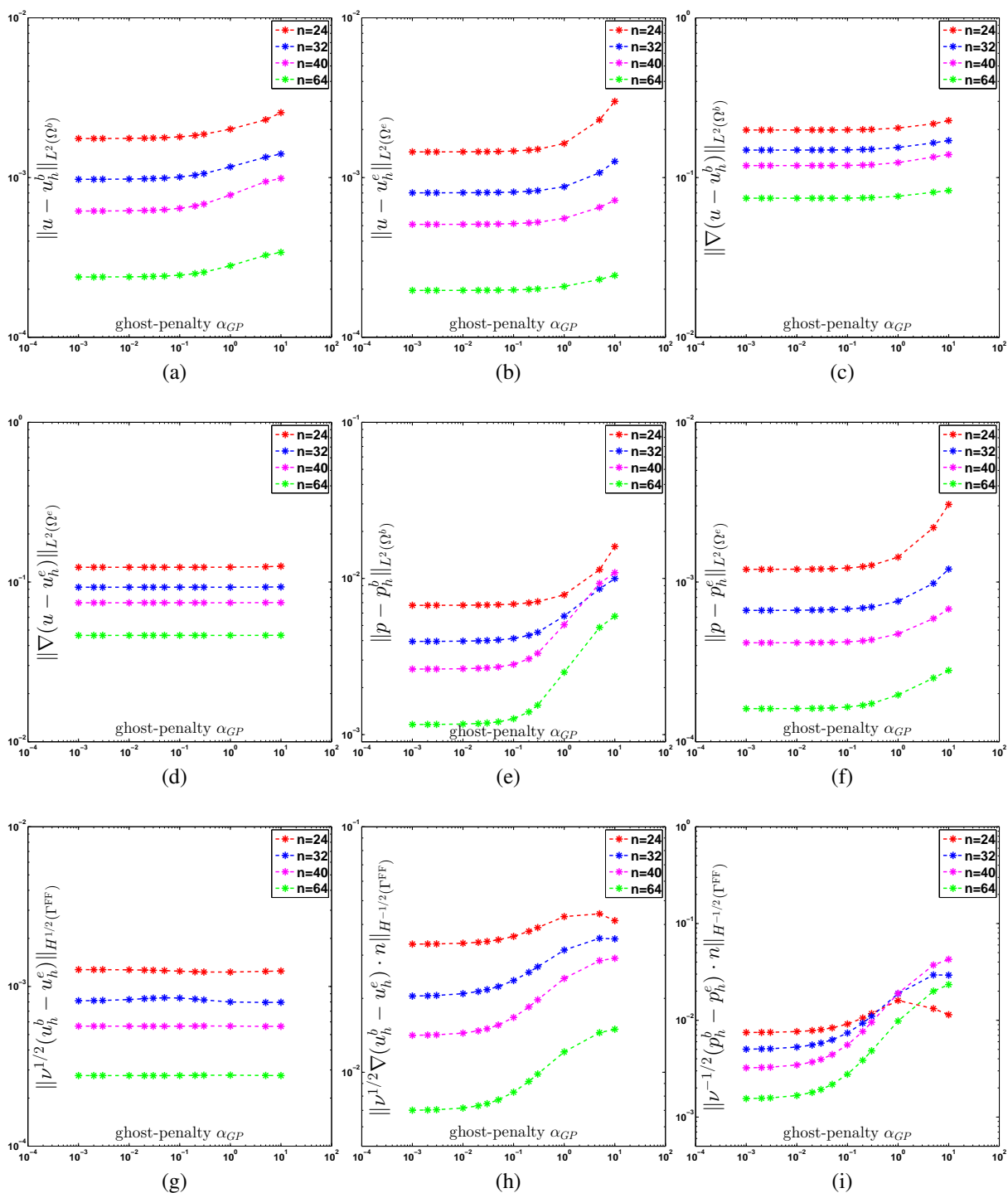


Figure 3.11: Stationary Kim-Moin-flow: error-norms for varying Nitsche parameter δ .


 Figure 3.12: Stationary Kim-Moin flow: Error-norms for varying ghost-penalty parameter α_{GP} .

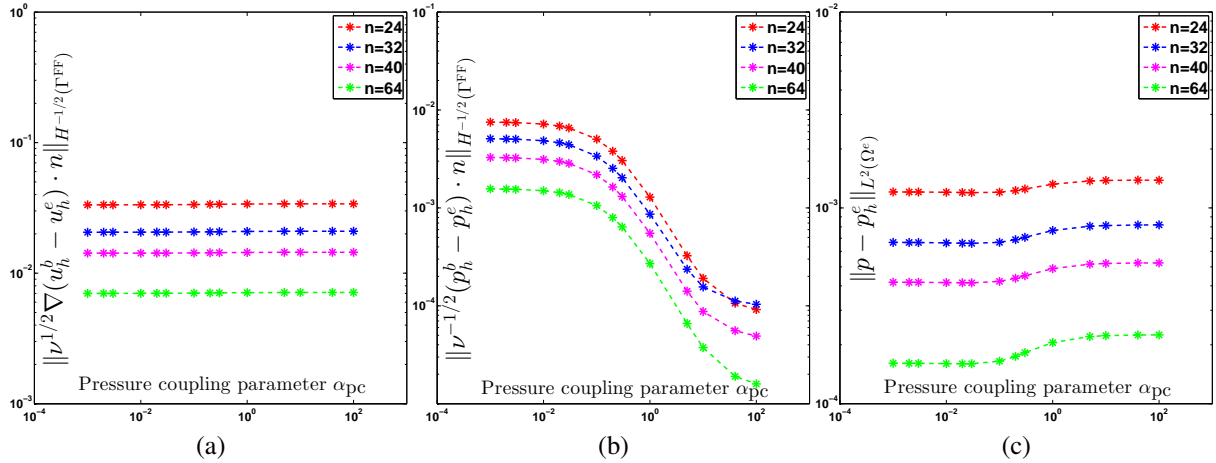


Figure 3.13: Stationary Kim-Moin flow: Error-norms for varying interface pressure coupling parameter α_{pc} .

ferent meshes $n \in \{24, 48, 64\}$, the error norms, (3.127) to (3.132), are calculated. Again, all the simulations are run with a ghost-penalty operator ($\alpha_{GP} = 0.003$) and face-oriented velocity and pressure stabilizations. Furthermore, an embedded element weighting for MHVS is chosen. The behavior of the parameter n is similar to the Nitsche parameter δ , which confirms the similarity of both stabilization parameters as discussed in Section 3.3. In Appendix, Figure A.2, the domain and interface errors are shown. As for Nitsche's method, the domain errors stay unchanged to varying n and the interface norms react much more sensitive. For too small values of n , the error in viscous fluxes gets bigger. On the other hand, for larger values of n , the pressure-flux error increases. Thus, in order to find a balance between minimizing the error for the coupling condition and fluxes, a parameter of $n = 35.0$ is chosen, which is in a good agreement with the values of Nitsche parameters δ and α . The results of parameter study of Nitsche's method and MHVS method confirm the similarity of them, as already discussed in Section 3.3.5.

The interface pressure coupling stabilization parameter

The influence of the user-defined parameter α_{pc} in (3.123) of the interface pressure coupling term (3.122) needs to be investigated on different error norms. For this purpose, for different values of $\alpha_{pc} \in [0.001, 100]$ and four different meshes $n \in \{24, 32, 40, 64\}$, the error norms (3.127) to (3.132) are calculated. All the simulations are run for embedded element weighting of Nitsche's method with $\delta = 35.0$ and a ghost-penalty operator with $\alpha_{GP} = 0.003$. As expected, the pressure flux error is mostly affected by the interface pressure coupling term. The pressure flux error decreases with increasing α_{pc} , see Figure 3.13b. A slightly increase of the error can be seen in the L^2 -error for p^e , as shown in Figure 3.13c. On the other hand, the error in the velocity fluxes remains unchanged for varying parameter α_{pc} (Figure 3.13a). Other error norms stay unchanged for different parameter α_{pc} as well (see Appendix Figure A.3). In order to find a balance between minimum error in pressure fluxes and L^2 -error for embedded pressure field, the parameter $\alpha_{pc} = 0.3$ is chosen.

In the next section, a convergence study for the different coupling methods is performed. Hereby, the optimal parameters chosen in this section, i.e. Nitsche parameters $\delta = 35.0$ and $\alpha = 35.0$, ghost-penalty parameter $\alpha_{\text{GP}} = 0.003$ and the MHVS parameter $n = 35.0$, are used.

3.7.2 Analysis of different methods for weak enforcement of coupling conditions

In the following, a spatial convergence analysis for a stationary viscous dominated flow with $\nu = 0.1 \text{ m}^2/\text{s}$ and mesh sizes $n \in \{4, 8, 16, 32, 64, 128\}$ for different methods of weak imposition of coupling conditions at the fluid-fluid interface presented in Section 3.3, is performed. The methods of weak imposition of coupling conditions, which will be investigated are: embedded element weighting of Nitsche's formulation ($\kappa_b = 0$ and $\kappa_e = 1$) with $\delta = 35.0$, background element weighting of Nitsche's formulation ($\kappa_b = 1$ and $\kappa_e = 0$) with $\alpha = 35.0$, background element weighting of mixed/hybrid Cauchy stress-based method (MHCS), and embedded and background element weighting of mixed/hybrid viscous stress-based method (MHVS), both with $n = 35.0$. In order to focus on the named coupling methods and to exclude the effects of different stabilization operators, for all coupling strategies the face-oriented fluid stabilizations are used. This leads to a balanced inf-sup condition of the pressure field for both subdomains and particularly on cut elements. Furthermore, for all configurations, an additional ghost-penalty operator with $\alpha_{\text{GP}} = 0.003$ is used. In order to estimate the Nitsche stabilization parameter α' , for embedded element weighting formulation the eigenvalue problem (3.45) is solved (with $\delta = 35.0$). In contrast, for background element weighting of Nitsche's formulation the uniform scaling with the element length (3.40) with $\alpha = 35.0$ is applied, which results in a stable formulation in combination of ghost-penalty stabilization. The results of domain and interface error norms, (3.127) to (3.132), are given in Figure 3.14 in the same order of the coupling strategies listed above. In Figure 3.14 the following abbreviations are used: Nitsche embedded element weighting (Nite), Nitsche background element weighting (Nitb), mixed/hybrid Cauchy stress-based background element weighting (Mhcsb), mixed/hybrid viscous stress-based embedded element weighting (Mhvse), and mixed/hybrid viscous stress-based background element weighting (Mhvsb), all with face-oriented and ghost-penalty stabilizations (Fos-Gp).

Both, embedded and background element weighting of Nitsche's formulation are stable with respect to satisfying the inverse inequality and the issue with lack of coercivity, since for the embedded element weighting of Nitsche's formulation the imposition of coupling condition on uncut elements is performed and for the background element weighting a ghost-penalty operator is added to balance the missing coercivity on cut elements. This is also clear from the results shown in Figure 3.14, as both Nitsche's formulations show the optimal convergence behavior in all domain and interface norms, (3.127) to (3.132). Considering the MHVS method, it can be seen that the method shows different behavior for background and embedded element weighting. While the embedded element weighting delivers optimal behavior for all domain and interface norms, the background element weighting variant of MHVS shows unstable behavior in almost all error norms specially in the interface norms, see Figures 3.14g to 3.14i. Dependent on the interface-location, flux-errors vary over a large range even in the presence of the ghost-penalty operator. As already discussed in Section 3.3.5, MHVS includes an implicit scaling with $\frac{\text{meas}(\Gamma^{\text{FF}} \cap K)}{\text{meas}(\Omega^b \cap K)}$, which results in a dependency of the interface position of the formulation and consequently a variation

of the error for different meshes. Kruse [119] showed that for a non-symmetric formulation of the MHVS ($\beta_v = -1$), which corresponds to the non-symmetric Nitsche formulation, the errors remain stable even though the formulation holds the same interface-dependent scaling and the same interface positions. Burman [33] showed that the non-symmetric version of Nitsche's formulation is stable for uncut elements without the penalty term. The error behavior for the velocity fluxes of MHCS shows a dependency on the interface positions as well, see Figure 3.14e. However, compared to MHVS, the error varies over a lower range. It needs to be pointed out that also MHCS includes the scaling $\frac{\text{meas}(\Gamma^{\text{FF}} \cap K)}{\text{meas}(\Omega^b \cap K)}$ in its formulation, as discussed in Section 3.3.5. In contrast to Nitsche's method and MHVS, MHCS shows no converged behavior in the errors of background and embedded pressure fields (Figures 3.14e and 3.14f). However, a good pressure flux error behavior of the method can be observed, see Figure 3.14i. As already discussed in Section 3.3.5, the MHCS method treats the pressure field in a different way as in MHVS and Nitsche's method, which leads to a method free of any adjoint consistency terms. This characteristic of MHCS can be mentioned as a possible reason of the instability in the pressure fields.

3.7.3 Analysis of different stabilization techniques

In the following, effects of different stabilization techniques: pressure and velocity face-oriented stabilizations, (3.118) and (3.120), classical residual-based stabilizations, ghost-penalty operator (3.39) and the interface velocity gradient and pressure coupling stabilizations, (3.121) and (3.122), will be investigated. The parameters $\alpha_{\text{gp}} = 0.003$ and $\gamma_{\text{pc}} = 0.3$ are chosen from the studies above. For this purpose, also here a spatial convergence analysis for stationary viscous dominated Kim-Moin flow with $\nu = 0.1 \text{ m}^2/\text{s}$ and mesh sizes $n \in \{4, 8, 16, 32, 64, 128\}$ is performed for following configurations and the corresponding abbreviations: Nitsche embedded element weighting with face-oriented stabilizations (Nite-Fos), Nitsche background element weighting with face-oriented stabilizations (Nitb-Fos), Nitsche embedded element weighting with face-oriented stabilizations and ghost-penalty operator (Nite-Fos-Gp), Nitsche embedded element weighting with face-oriented stabilizations, ghost-penalty operator, and additional interface velocity gradient and pressure stabilizations (Nite-Fos-Gp-vp), the embedded element weighting of Nitsche's method with residual-based pressure and streamline stabilizations, PSPG and SUPG, (Nite-Rbs) and finally the mixed/hybrid Cauchy stress-based method with PSPG and SUPG stabilizations (Mhcs-Rbs). It has to be noted that almost all stabilization techniques are combined with the Nitsche's method to exclude the effects of different coupling methods for weak imposition of coupling conditions, as shown in previous section. The resulting domain and error norms are given in Figure 3.15.

In this study, the importance of face-oriented stabilizations when using cut elements is highlighted. Whereas the velocity-norms are not influenced, the pressure solution clearly shows the non-balanced inf-sup instability for the PSPG-stabilized formulations without pressure face-oriented stabilization around the interface. Observing the L^2 -norms of the pressure field and pressure fluxes at the interface, a clear improvement is obtained using the face-oriented pressure and velocity stabilizations. This is mostly obvious for pressure fluxes at the interface (Figure 3.15i) and for the L^2 -norms of the pressure field in embedded domain (Figure 3.15f), where the optimal convergence gets lost with residual-based stabilizations. This behavior is observed independent of the coupling method, i.e. for embedded element weighting of Nitsche's method and also

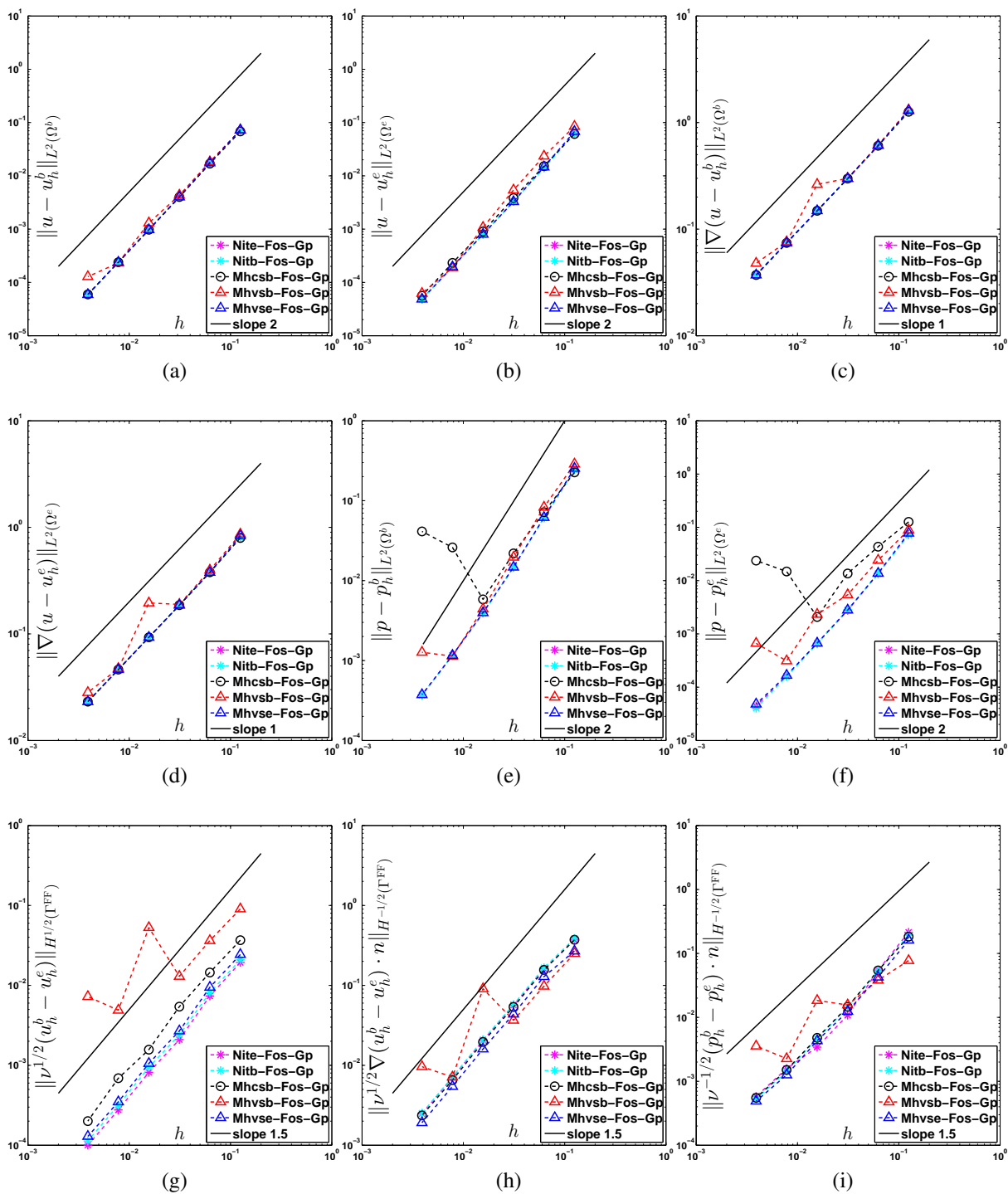


Figure 3.14: Stationary Kim-Moin flow: Error-norms for different methods of weak enforcement of coupling conditions.

for mixed/hybrid Cauchy stress-based method. However, as discussed above, the mixed/hybrid Cauchy stress-based method shows also a loss of convergence of the L^2 -norm of background and embedded pressure fields due to its formulation, see Figures 3.15e and 3.15f.

Furthermore, it can be seen that using an additional ghost-penalty operator with $\alpha_{GP} = 0.003$ provides the same convergence behavior as the results of face-oriented stabilizations without it, for both embedded and background weighting of Nitsche's method. This confirms the fact that an additional ghost-penalty operator does not deteriorate the convergence behavior. Moreover, for flows with small normal velocities along the interface, in the case of background element weighting of Nitsche's method, adding a viscous ghost-penalty operator can be necessary. This is due to the fact that for such examples the face-oriented convective operator (3.120), which scales with normal velocities, can not give a sufficient control over the ghost values and take control over the system conditioning anymore.

As expected, with the additional pressure and velocity gradient stabilizations at the interface, an improvement in the level of the pressure flux errors at the interface, Figure 3.15i, can be seen. However, with the additional interface stabilization terms the convergence rates for all error norms remain unchanged and the optimal convergence and stability is already achieved without adding these interface stabilizations. Thus, the additional pressure and velocity gradient stabilizations, (3.121) and (3.122), are not considered in the final formulation, which will be presented in Section 3.8.

Moreover, a clear improvement of the system conditioning can be observed using face-oriented stabilizations in the interface zone. In Figure 3.16 an estimate of the condition number for Nitsche embedded weighting with face-oriented stabilizations and the ghost-penalty operator compared with pure residual-based stabilizations, i.e. without any face-oriented stabilizations at the interface region is given. It can be observed that in contrast to the configuration with residual-based stabilizations, the conditioning of the system remains bounded for all different cut situations using face-oriented stabilizations and ghost-penalty operator.

Thus, to sum up, in these examples the importance of using face-oriented stabilizations and ghost-penalty operators for cut elements is demonstrated. In contrast to pure residual-based stabilizations, optimal convergence rates independent of the fluid-fluid interface position are achieved. Furthermore, face-oriented stabilizations give an sufficient control over the ghost values and an improvement of system conditioning, which is an important issue when using iterative solvers.

3.7.4 Analysis of inflow stabilizations for convection dominated flow

In the following, the influence of the different convective stabilizations, introduced in Section 3.4, regarding the weak enforcement of coupling conditions for convection dominated flows will be investigated. For the convection dominated case with $\nu = 10^{-4} m^2/s$, the instationary incompressible Navier-Stokes equations are solved for the total time $T = 0.3 s$ and time step $\Delta t = 0.003 s$. For the time discretization scheme, a one-step- θ scheme with $\theta = 1$ is used. The embedded element weighting of the Nitsche's method is used for the weak imposition of the coupling conditions. The results of instationary computations for different convective stabilization terms are shown in Figure 3.17. As in the viscous dominated stationary case, the error

3.7 Convergence study with two-dimensional Kim-Moin flow

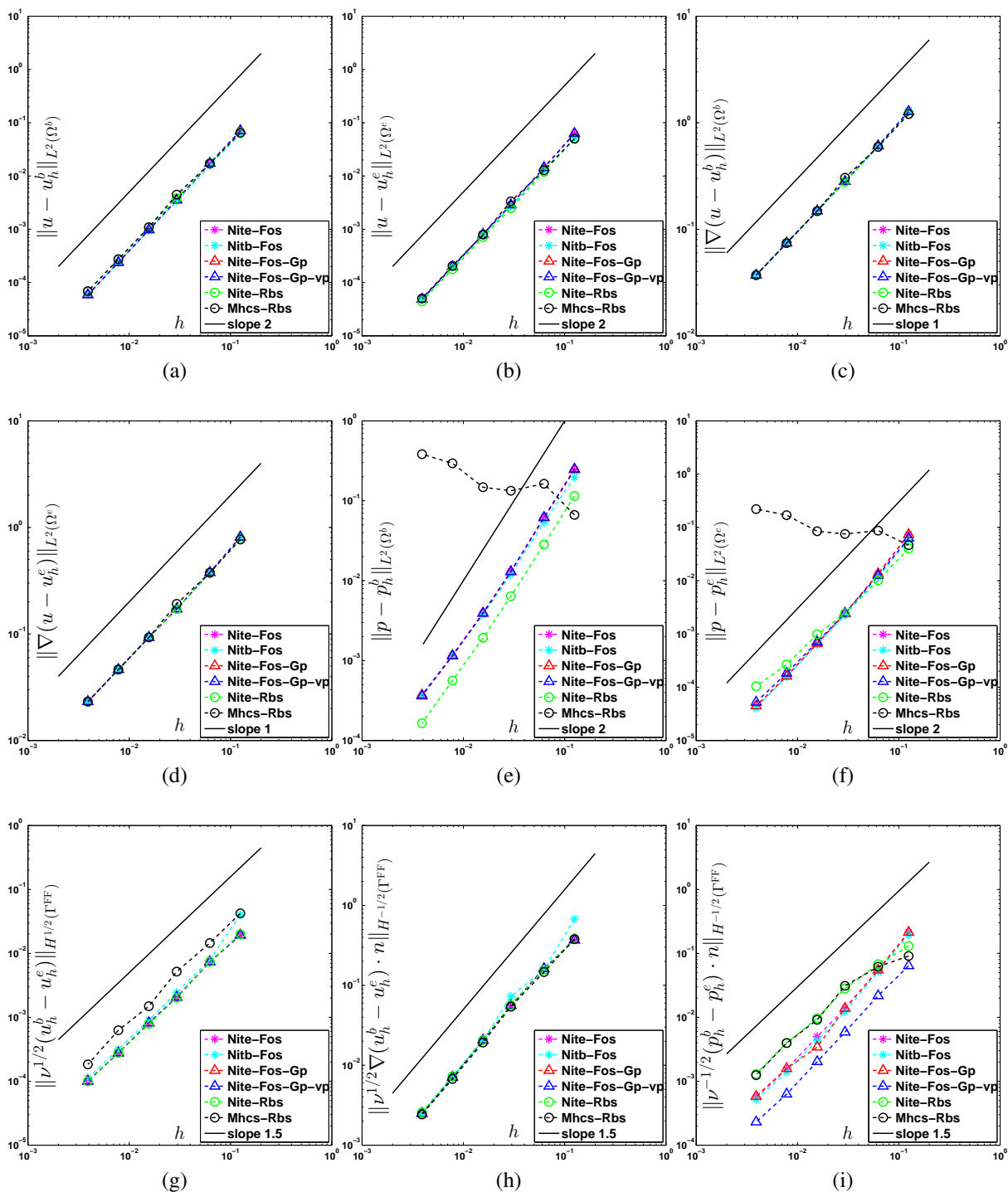


Figure 3.15: Stationary Kim-Moin flow: Error-norms for different stabilization methods.

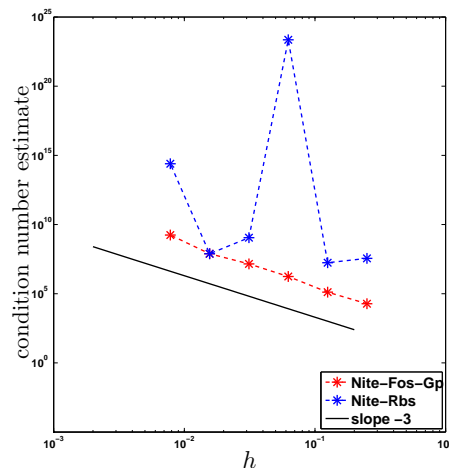


Figure 3.16: Stationary Kim-Moin flow $\nu = 10^{-1} \text{ m}^2/\text{s}$: Condition numbers for viscous dominated flow.

is plotted against element length h . Figure 3.17 depicts the L^2 -norms of both subdomains and the error at the interface. The computation is done for four different configurations on six different meshes with $n \in \{4, 8, 16, 32, 64, 128\}$. The first curve shows the error behavior of the averaged-inflow stabilization formulation, (3.115) with $\gamma_{adv} = 0$. For the second curve, the one-sided upwinding inflow stabilization terms ((3.115) with $\gamma_{adv} = 1/2$, or (3.116)) are applied. The third and fourth curves are the combination of the averaged and the one-sided upwinding inflow stabilization terms with the additional penalty formulation (3.117) controlling the mass conservation for convection dominated problems. In the same order, the following abbreviations for different inflow stabilizations are used in Figure 3.17: Nite-Fos-Gp-Av, Nite-Fos-Gp-Up, Nite-Fos-Gp-AvP, Nite-Fos-Gp-UpP. For all variants, the embedded element weighting of Nitsche's methods ($\delta = 35.0$), face-oriented fluid stabilizations, and viscous ghost-penalty stabilization operator ($\alpha_{GP} = 0.003$) are used. In order to estimate the Nitsche stabilization parameter α' , the eigenvalue problem (3.45) is solved.

Optimal error convergence rates for domain errors can be seen for all four methods. As expected, different configurations do not have much effect on the bulk errors. The influence of the penalty term (3.117) is obvious in the enforcement of the coupling condition at the interface (Figure 3.17g). Here, the error for the coarser mesh, which represents the convection dominated regime, is larger for the first and second configurations, whereas with the additional penalty term (3.117) a clear improvement can be observed (third and fourth curve). Furthermore, the additional penalty factor does not deteriorate any other convergence behavior. It can also be observed that the one-sided upwinding inflow stabilization terms provide better convergence behavior than averaged-inflow stabilization, due to stronger enforcement of coupling condition caused by $\gamma_{adv} > 0$. As expected, applying residual-based stabilizations (PSPG, SUPG) without additional face-oriented interface stabilizations, results in no or poor convergence of the Newton scheme, which indicates an unstable formulation and, thus, it is not depicted here.

To summarize, both inflow stabilization formulations, averaged and one-sided upwinding stabilizations, behave the same for domain errors, and pressure and viscous fluxes. For all the

considered norms, optimal convergence results, similar to the study of Schott and Wall [154], are obtained. However, for the enforcement of the boundary condition best results are obtained with a classical upwinding stabilization combined with the scaling (3.117).

3.7.5 Summary

In this section, first, the user-defined parameters, Nitsche parameters (δ and α), ghost-penalty parameter α_{GP} , mixed/hybrid viscous stress-based method (MHVS) parameter n , and finally interface pressure coupling stabilization parameter α_{pc} , were investigated in terms of stability and accuracy, and optimal values were chosen ($\delta = \alpha = n = 35.0$, $\alpha_{\text{GP}} = 0.003$, $\alpha_{\text{pc}} = 0.3$). Afterwards, using these optimal parameters, the convergence behavior of the embedded fluid formulation for different methods of weak imposition of coupling conditions at the interface, Nitsche's method, MHCS method and MHVS method, introduced in Section 3.3, was studied. To estimate the Nitsche stabilization parameter α' for embedded element weighting, the eigenvalue problem (3.45) is solved. In contrast, for background element weighting of Nitsche's formulation the uniform scaling with the element length (3.40) is applied, which results in a stable formulation, regarding imposition of coupling condition at the interface, in combination of an additional ghost-penalty operator. To focus on the coupling methods, same stabilization terms were applied to all configurations. Subsequently, to investigate the effect of appropriate stabilizations, a convergence study for different stabilization operators, given in Sections 3.4, 3.5 and 3.6, for viscous dominated flow was carried out. Finally, the effect of different inflow stabilization terms in a convective dominated regime was investigated.

It was shown that with appropriate Nitsche and ghost-penalty parameters, and face-oriented stabilizations, the embedded and background element weighting of Nitsche's method and the embedded element weighting of MHVS method result in optimal convergence error rates. On the other hand, even with the same ghost-penalty parameter and use of face-oriented stabilizations, for the background element weighting of MHVS and MHCS methods, optimal convergence behavior was not achieved. As discussed in Section 3.3.5, MHVS and MHCS methods include an implicit scaling with $\frac{\text{meas}(\Gamma^{\text{FF}} \cap K)}{\text{meas}(\Omega^b \cap K)}$, which results in a dependency of the interface position of the formulation and, consequently, a variation of the error for different meshes, when the background element weighting is chosen. Furthermore, in contrast to Nitsche's method and MHVS method, MHCS method showed no converged behavior in the errors of background and embedded pressure fields, however, a good behavior of the pressure flux error was observed. As already discussed in Section 3.3.5, the additional stress field in MHCS method is a Cauchy stress field, and, therefore, the method treats the pressure field in a different way as for MHVS and Nitsche's method. This characteristic of MHCS leads to a method free of any adjoint consistency terms, which results in instabilities in the pressure fields.

As already mentioned, additional to face-oriented stabilizations, a ghost-penalty operator along the faces of the cut elements was added to the formulation. The same results were obtained with the ghost-penalty operator, such as the results of face-oriented stabilization without the ghost-penalty operator. However, due to the fact that for small normal velocities at the interface the face-oriented convective operator, can not give a sufficient control over the ghost values, in order to obtain physical values at ghost nodes and take control over the system conditioning, using a ghost-penalty operator is advisable. Hence, even for the embedded element weighting, which is a stable method regarding interface coupling, a ghost-penalty operator is added to the

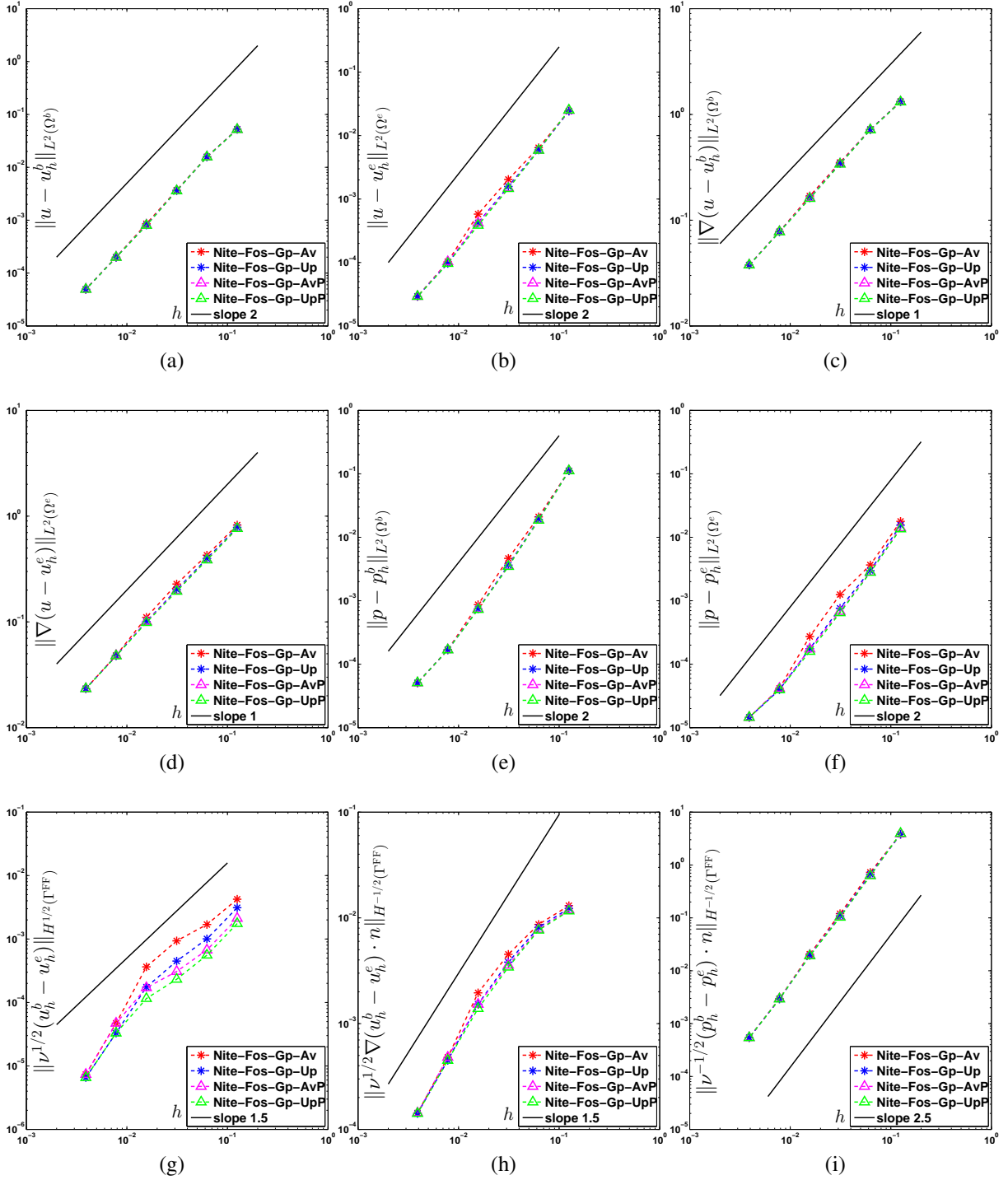


Figure 3.17: Instationary Kim-Moin flow: Error-norms for different inflow stabilization variants.

formulation. However, it needs to be pointed out that from the parameter study the value of ghost-penalty parameter was chosen small ($\alpha_{GP} = 0.003$).

It was also shown that additional interface velocity gradient and interface pressure stabilization terms, improve the level of error for the pressure fluxes at the interface, but stability and optimal convergence rates are already achieved without these additional stabilization operators. Thus, the additional pressure and velocity gradient stabilizations, are not considered in the final formulation, which will be presented in Section 3.8.

Furthermore, in order to demonstrate the necessity and importance of using face-oriented stabilizations, to overcome the fluid instabilities at cut elements, and improve system conditioning, a comparison with classical residual-based stabilizations without any additional face-oriented stabilizations at the faces of cut elements, was given. In contrast to pure residual-based stabilizations, with face-oriented stabilizations optimal convergence rates independent of the fluid-fluid interface position were achieved. Furthermore, it was shown that face-oriented stabilizations give a sufficient control over the ghost values and an improved system conditioning, which is an important issue when using iterative solvers.

Moreover, as mentioned above, the effect of different inflow stabilization terms in convective dominated case was investigated. It was shown that one-sided upwinding inflow stabilization terms provide a better convergence behavior than averaged-inflow stabilization. However, best results were obtained with one-sided upwinding stabilizations combined with the penalty term controlling the mass conservation.

For further studies of the present work, regarding to weak imposition of coupling conditions, the embedded element weighting of the well-established Nitsche's method, which is performed on uncut embedded fluid elements adjacent to the interface is used. As already mentioned, the formulation is stable due to weak imposition of coupling conditions for every position of the interface without adding an additional ghost-penalty operator. Besides face-oriented stabilizations to overcome the fluid instabilities on cut elements, an additional ghost-penalty operator is used to take control over the system conditioning and to achieve physically reasonable values at ghost nodes. Furthermore, convective interface stabilizations are applied to stabilize the weak enforcement of the coupling conditions for convective dominated flow. In the following section, the transient stabilized embedded fluid formulation will be extended to moving interfaces and the final discrete stabilized embedded fluid formulation for moving interfaces will be presented.

3.8 Moving embedded fluid

In this section, the moving embedded fluid will be introduced into the framework. In terms of fluid-structure interaction, which is the focus of the next chapter, an accurate and stable time-integration strategy for the moving embedded fluid mesh is essential. When the embedded mesh moves, both fluid domains, $\Omega^b(t)$ and $\Omega^e(t)$, become time-dependent. The movement of the embedded subdomain, is described using the classical Arbitrary-Lagrangian-Eulerian (ALE) concept as presented for example in Donea and Huerta [62]. In doing so, a consistent time-discretization of the equations on the embedded fluid subdomain is given, since the ALE concept provides an appropriate description of moving domains. The reason is that in the methods based on the classical ALE approach, the grid of the fluid domain is deformed due to the motion of the boundary and the flow field is solved on the deformed mesh.

As already mentioned, the equations on the time-dependent background fluid subdomain are discretized using a fixed-grid Eulerian formulation. In contrast to ALE formulation, where the grid of the fluid domain is deformed with the moving boundary and provides an appropriate description for it, the Eulerian formulation is naturally inappropriate for moving interfaces, since it is generally not aligned with the interface. This leads to an inconsistency, since integrals on the time-dependent background subdomain $\Omega^b(t)$ involve values from the last time step, which change their number of degrees of freedom over time. In the context of extended finite element methods (XFEM), the space-time methods proposed in Chessa and Belytschko [46, 47] and Zilian and Legay [185] are the most consistent methods. However, these methods are expensive and challenging to implement, since a four-dimensional cut algorithm has to be implemented and, moreover, the number of degrees of freedoms are usually doubled for space-time approaches. In order to handle the time-integration with finite difference schemes in the context of XFEM, several approaches, based on the reconstructing the missing values, have been proposed. Codina et al. [52] suggest a combined fixed-grid/ALE approach, to deal with the difficulties arise due to discretizing an Eulerian formulation in moving domains. In this approach, the fluid elements around the interface deform to follow the moving interface using the ALE formulation. A projection step is then necessary to obtain the values from the deformed mesh into the undeformed background fixed-grid mesh. In order to estimate the history values, in Gerstenberger [82] an extrapolation into the fictitious domain is performed, which is followed by a projection step to ensure the incompressibility condition in the sense of Ghost-fluid method by Hong et al. [105] and Kang et al. [113]. In Fries and Zilian [78] the XFEM time-integration for weak discontinuities is addressed. However, Henke et al. [102] showed that this approach is not applicable to strong discontinuities. In context of premixed combustion, Henke et al. [102] proposed a semi-Lagrangian time-integration approach to handle the XFEM time-integration issue. This approach is based on adapting the previous numerical solutions to the current interface position by tracking back virtual Lagrangian particles to their previous positions, where an appropriate solution can be extrapolated.

Considering embedded fluid formulation, as the embedded fluid Ω^e moves and deforms from time step t^n to t^{n+1} , integrals on the time-dependent background subdomain $\Omega^b(t)$ have to be evaluated with values from the last time step, like $\mathbf{u}_h^{b,n}$ and $\dot{\mathbf{u}}_h^{b,n}$, which are not available and need to be guessed. In Figure 3.18, the problem is depicted. As the embedded fluid subdomain Ω^e moves and deforms from time step t^n to t^{n+1} , the red node, which was located at the inactive part of background fluid subdomain Ω^{b-} is now with respect to the interface position $\Gamma^{\text{FF}}(t^{n+1})$ located at the physical background fluid subdomain Ω^b . For this node, the needed values $\mathbf{u}_h^{b,n}$ and $\dot{\mathbf{u}}_h^{b,n}$ from the time step t^n are not available and have to be reconstructed.

Since at the time step t^n the embedded fluid subdomain provides the same flow field with the same physical properties, it can be used to estimate the missing values of background fluid mesh. For this purpose, the missing values of the node on the background fluid subdomain can be reconstructed from the values of embedded fluid subdomain at the time step t^n . This approach is the most appropriate method in order to reconstruct the missing values of the background fluid subdomain, since a physical field with the same physical parameters is available in time step t^n , which delivers more reasonable values than any other estimations.

In this approach, first the underlying embedded element, where the background fluid node with missing values was located, has to be found. Running a “brute force” algorithm over all

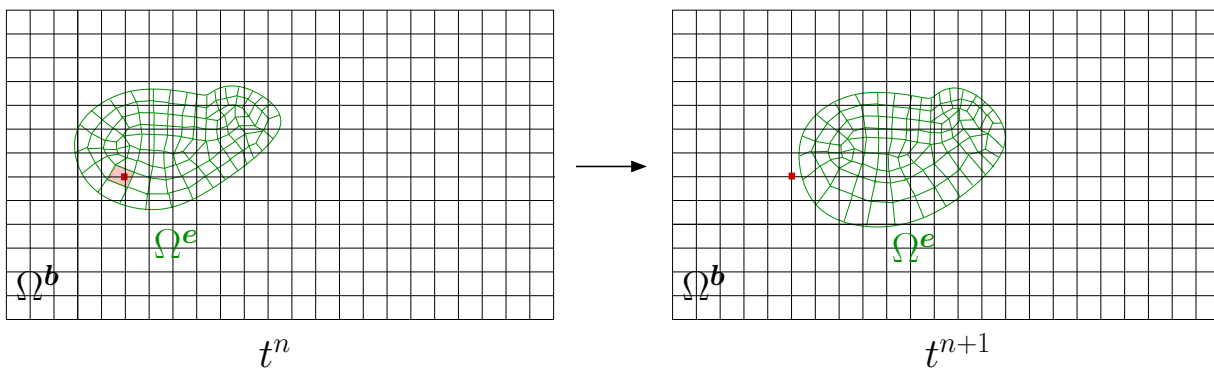


Figure 3.18: Time integration issue of moving embedded fluid: As the embedded fluid Ω^e moves and deforms from time step t^n to t^{n+1} , the red node, which was located at the inactive part of background fluid subdomain is now with respect to the interface position $\Gamma^{\text{FF}}(t^{n+1})$ located at the physical background fluid subdomain. For this node, the needed values $\mathbf{u}_h^{b,n}$ and $\dot{\mathbf{u}}_h^{b,n}$ from the time step t^n are not available and need to be reconstructed. The missing values are then interpolated from the underlying embedded element.

embedded elements and testing whether the background nodes lied in the element in the last time step is too expensive and inefficient. Therefore, finding the underlying background element proceeds in two parts. The first part of algorithm provides the node, a collection of embedded elements, the background node could possibly been covered by. This is done with a parallel octree-based search. After a small amount of possibly elements are provided, each embedded element in this set is checked accurately to find the underlying embedded element.

Now, that the underlying embedded element is found the missing values of the background node are interpolated from the values of the embedded element at the time step t^n as

$$\tilde{\mathbf{u}}_h^{b,n} = \sum_{i=1}^{n_{en}} N_i^e \cdot \mathbf{u}_{i,h}^{e,n}. \quad (3.133)$$

Hereby, n_{en} denotes the number of nodes in the embedded fluid element. In parallel computing, the background node with missing values and the embedded element are not necessarily located on the same processor. To find the correct embedded element the processors need to communicate with each other, which is done by a Round-Robin scheduling scheme.

In order to ensure the discrete incompressibility, an additional step based on the idea of Houzeaux and Codina [106] and Wall et al. [175] is added to the approach. In this step the values of cut elements, which are reconstructed from the values of embedded fluid mesh with classical Lagrangian interpolation functions, $\tilde{\mathbf{u}}_h^{b,n}$, are substituted by the solution of the following least squares problem:

Find $\mathbf{u}_h^{*b,n}$ such that

$$\begin{aligned} \min_{\mathbf{u}_h^{*b,n}} & \|\tilde{\mathbf{u}}_h^{b,n} - \mathbf{u}_h^{*b,n}\|^2 \\ & \int_{\mathcal{T}^\Gamma(t^n)} \nabla \cdot \mathbf{u}_h^{*b,n} = 0. \end{aligned} \quad (3.134)$$

Hereby, $\mathcal{T}^\Gamma(t^n)$ denotes the set of cut elements at time step t^n . In this way, the constructed values of the background fluid mesh ensure the incompressibility constraint on $\mathcal{T}^\Gamma(t^n)$. However, it has to be noted that the numerical examples shown in Section 3.9 are solved without this additional step, which still result in a smooth transition of velocity and pressure field across the interface and a stable solution during the simulation.

Finally, the discrete form of the stabilized embedded fluid formulation for moving fluid-fluid interface using one-step- θ scheme reads as follows:

Find $(\mathbf{u}_h^e, p_h^e) \in V_h^e \times Q_h^e$ and $(\mathbf{u}_h^b, p_h^b) \in V_h^b \times Q_h^b$ such that $\forall (\mathbf{v}_h^e, q_h^e) \in V_h^e \times Q_h^e$ and $\forall (\mathbf{v}_h^b, q_h^b) \in V_h^b \times Q_h^b$ holds

$$\begin{aligned}
 & \boxed{1} \quad (\mathbf{v}_h^b, \frac{\rho^f}{\Theta} \mathbf{u}_h^b)_{\Omega^b(t^{n+1})} + (\mathbf{v}_h^b, \rho^f \mathbf{u}^b \cdot \nabla \mathbf{u}_h^b)_{\Omega^b(t^{n+1})} \\
 & \boxed{2} \quad + (q_h^b, \nabla \cdot \mathbf{u}_h^b)_{\Omega^b(t^{n+1})} - (\nabla \cdot \mathbf{v}_h^b, p_h^b)_{\Omega^b(t^{n+1})} + (\boldsymbol{\epsilon}(\mathbf{v}_h^b), 2\mu\boldsymbol{\epsilon}(\mathbf{u}_h^b))_{\Omega^b(t^{n+1})} \\
 & \boxed{3} \quad + (\mathbf{v}_h^e, \frac{\rho^f}{\Theta} \mathbf{u}_h^e)_{\Omega^e(t^{n+1})} + (\mathbf{v}_h^e, \rho^f \mathbf{c}_h^e \cdot \nabla \mathbf{u}_h^e)_{\Omega^e(t^{n+1})} \\
 & \boxed{4} \quad + (q_h^e, \nabla \cdot \mathbf{u}_h^e)_{\Omega^e(t^{n+1})} - (\nabla \cdot \mathbf{v}_h^e, p_h^e)_{\Omega^e(t^{n+1})} + (\boldsymbol{\epsilon}(\mathbf{v}_h^e), 2\mu\boldsymbol{\epsilon}(\mathbf{u}_h^e))_{\Omega^e(t^{n+1})} \\
 & \boxed{5} \quad + \langle \llbracket \mathbf{v}_h \rrbracket, p_h^e \cdot \mathbf{n} \rangle_{\Gamma^{\text{FF}}(t^{n+1})} - \langle \llbracket \mathbf{v}_h \rrbracket, 2\mu\boldsymbol{\epsilon}(\mathbf{u}_h^e) \cdot \mathbf{n} \rangle_{\Gamma^{\text{FF}}(t^{n+1})} \\
 & \boxed{6} \quad - \langle q_h^e \cdot \mathbf{n}, \llbracket \mathbf{u}_h \rrbracket \rangle_{\Gamma^{\text{FF}}(t^{n+1})} - \langle 2\mu\boldsymbol{\epsilon}(\mathbf{v}_h^e) \cdot \mathbf{n}, \llbracket \mathbf{u}_h \rrbracket \rangle_{\Gamma^{\text{FF}}(t^{n+1})} \\
 & \boxed{7} \quad + \langle \alpha' \llbracket \mathbf{v}_h \rrbracket, \llbracket \mathbf{u}_h \rrbracket \rangle_{\Gamma^{\text{FF}}(t^{n+1})} \\
 & \boxed{8} \quad - \langle \rho^f (\boldsymbol{\beta}_h \cdot \mathbf{n}) \{ \mathbf{v}_h \}_m, \llbracket \mathbf{u}_h \rrbracket \rangle_{\Gamma^{\text{FF}}(t^{n+1})} + \gamma_{adv} \langle \rho^f |\boldsymbol{\beta}_h \cdot \mathbf{n}| \llbracket \mathbf{v}_h \rrbracket, \llbracket \mathbf{u}_h \rrbracket \rangle_{\Gamma^{\text{FF}}(t^{n+1})} \\
 & \boxed{9} \quad + \sum_{F \in \mathcal{F}_G} \frac{1}{\theta} \langle \alpha_{\text{GP}} \cdot \mu h_F \llbracket \nabla \mathbf{v}_h^b \rrbracket, \llbracket \nabla \mathbf{u}_h^b \rrbracket \rangle_{\mathcal{F}_G(t^{n+1})} \\
 & \boxed{10} \quad + \sum_{F \in \mathcal{F}_i} \frac{1}{\theta} [\langle \gamma_p \llbracket \nabla q_h^b \rrbracket, \llbracket \nabla p_h^b \rrbracket \rangle_{\mathcal{F}_i(t^{n+1})} + \langle \gamma_s h_F^2 \rho^f \cdot |\mathbf{u}_h^b \cdot \mathbf{n}^F| \llbracket \nabla \mathbf{v}_h^b \rrbracket, \llbracket \nabla \mathbf{u}_h^b \rrbracket \rangle_{\mathcal{F}_i(t^{n+1})}] \\
 & \boxed{11} \quad + \delta_{ef} \sum_{F \in \mathcal{F}_E} \frac{1}{\theta} [\langle \gamma_p \llbracket \nabla q_h^e \rrbracket, \llbracket \nabla p_h^e \rrbracket \rangle_{\mathcal{F}_k(t^{n+1})} + \langle \gamma_s h_F^2 \rho^f \cdot |\mathbf{c}_h^e \cdot \mathbf{n}^F| \llbracket \nabla \mathbf{v}_h^e \rrbracket, \llbracket \nabla \mathbf{u}_h^e \rrbracket \rangle_{\mathcal{F}_k(t^{n+1})}] \\
 & \boxed{12} \quad + \delta_{br} \sum_e [(\mathbf{v}_h^b, \tau_b^m \frac{\rho^f}{\Theta} \mathbf{u}_h^b)_{\Omega^b(t^{n+1})} + (\mathbf{u}_h^b \cdot \nabla \mathbf{v}_h^b, \rho^f \tau_b^m \mathbf{r}_h^{m,b})_{\Omega^b(t^{n+1})} \\
 & \boxed{13} \quad + (\nabla q_h^b, \tau_b^m \mathbf{r}_h^{m,b})_{\Omega^b(t^{n+1})} + (\nabla \cdot \mathbf{v}_h^b, \tau_b^c \mathbf{r}_h^{c,b})_{\Omega^b(t^{n+1})}] \\
 & \boxed{14} \quad + \delta_{er} \sum_e [(\mathbf{v}_h^e, \tau_e^m \frac{\rho^f}{\Theta} \mathbf{u}_h^e)_{\Omega^e(t^{n+1})} + (\mathbf{c}_h^e \cdot \nabla \mathbf{v}_h^e, \rho^f \tau_e^m \mathbf{r}_h^{m,e})_{\Omega^e(t^{n+1})} \\
 & \boxed{15} \quad + (\nabla q_h^e, \tau_e^m \mathbf{r}_h^{m,e})_{\Omega^e(t^{n+1})} + (\nabla \cdot \mathbf{v}_h^e, \tau_e^c \mathbf{r}_h^{c,e})_{\Omega^e(t^{n+1})}]
 \end{aligned}$$

$$\begin{aligned}
 \boxed{16} \quad &= \langle \mathbf{v}_h^b, \bar{\mathbf{h}}^b \rangle_{\partial\Omega_N^b(t^{n+1})} + (\mathbf{v}_h^b, \rho^f \mathbf{b}^b)_{\Omega^b(t^{n+1})} + (\mathbf{v}_h^e, \rho^f \mathbf{b}^e)_{\Omega^e(t^{n+1})} \\
 \boxed{17} \quad &\quad + (\mathbf{v}_h^b, \frac{\rho^f}{\Theta} \tilde{\mathbf{u}}_h^{b,\text{hist}})_{\Omega^b(t^{n+1})} + (\mathbf{v}_h^e, \frac{\rho^f}{\Theta} \mathbf{u}_h^{e,\text{hist}})_{\Omega^e(t^{n+1})} \\
 \boxed{18} \quad &+ \delta_{br} \left[\sum_{\mathbf{e}} (\mathbf{u}_h^b \cdot \nabla \mathbf{v}_h^b, \tau_b^m \rho^f \tilde{\mathbf{u}}_h^{b,\text{hist}})_{\Omega^b(t^{n+1})} + (\nabla q_h^b, \tau_b^m \tilde{\mathbf{u}}_h^{b,\text{hist}})_{\Omega^b(t^{n+1})} \right] \\
 \boxed{19} \quad &+ \delta_{er} \left[\sum_{\mathbf{e}} (\mathbf{c}_h^e \cdot \nabla \mathbf{v}_h^e, \tau_e^m \rho^f \mathbf{u}_h^{e,\text{hist}})_{\Omega^e(t^{n+1})} + (\nabla q_h^e, \tau_e^m \mathbf{u}_h^{e,\text{hist}})_{\Omega^e(t^{n+1})} \right], \quad (3.135)
 \end{aligned}$$

where the stationary residual of the momentum equation and the continuity equation for the both fluid subdomains are defined as

$$\mathbf{r}_h^{m,b} = \rho^f \mathbf{u}_h^b \cdot \nabla \mathbf{u}_h^b + \nabla p_h^b - 2\mu \nabla \cdot \boldsymbol{\epsilon}(\mathbf{u}_h^b) - \rho^f \mathbf{b}^b, \quad (3.136)$$

$$\mathbf{r}_h^{m,e} = \rho^f \mathbf{c}_h^e \cdot \nabla \mathbf{u}_h^e + \nabla p_h^e - 2\mu \nabla \cdot \boldsymbol{\epsilon}(\mathbf{u}_h^e) - \rho^f \mathbf{b}^e, \quad (3.137)$$

and

$$\mathbf{r}_h^{c,b} = \nabla \cdot \mathbf{u}_h^b, \quad (3.138)$$

$$\mathbf{r}_h^{c,e} = \nabla \cdot \mathbf{u}_h^e. \quad (3.139)$$

Furthermore, the history values $\tilde{\mathbf{u}}_h^{b,\text{hist}}$ and $\mathbf{u}_h^{e,\text{hist}}$ are defined as

$$\tilde{\mathbf{u}}_h^{b,\text{hist}} = \tilde{\mathbf{u}}_h^{b,n} + \Delta t(1 - \theta) \tilde{\mathbf{u}}_h^{b,n}, \quad (3.140)$$

$$\mathbf{u}_h^{e,\text{hist}} = \mathbf{u}_h^{e,n} + \Delta t(1 - \theta) \dot{\mathbf{u}}_h^{e,n}. \quad (3.141)$$

Moreover, $\Theta = \Delta t\theta$, denotes the one-step- θ time factor. The values of the background fluid subdomain at the time step t^n are denoted as $\tilde{\mathbf{u}}_h^{b,n}$ and $\tilde{\dot{\mathbf{u}}}_h^{b,n}$, which are not available for the elements in void/fictitious part of background fluid subdomain at time step t^n and need to be reconstructed.

The first four lines of (3.135) correspond to the standard Galerkin terms of the background and embedded fluid subdomains. The next three lines refer to the embedded element weighting of symmetric Nitsche's formulation, i.e. the consistency terms, the adjoint consistency terms and Nitsche's penalty term. To estimate Nitsche's stabilization parameter α' , the eigenvalue problem (3.45) is solved. The line eight refers to the convective inflow stabilization terms at the interface; the classical upwinding term for $\gamma_{adv} = \frac{1}{2}$ and the averaged formulation for $\gamma_{adv} = 0$. The inflow stabilization terms scale with $\boldsymbol{\beta}_h \cdot \mathbf{n}$, which stands for the normal component of the convective velocity of each subdomain across the interface, $\mathbf{u}_h^b \cdot \mathbf{n}$ for stabilizing the inflow into the background fluid subdomain and $\mathbf{c}_h^e \cdot \mathbf{n}$ for stabilizing the inflow into the embedded fluid subdomain. Furthermore, the ghost-penalty and the pressure and velocity face-oriented stabilizations with $i \in \{G, B\}$ and $\delta_{ef} \in \{0, 1\}$ are stated at lines nine to eleven, which are treated in a full-implicit way as in Burman and Fernández [35]. For $i = B$ and $\delta_{ef} = 1$ the face-oriented stabilizations are applied to all faces of the background and embedded fluid subdomains, while with $i = G$ and $\delta_{ef} = 0$, as for the ghost-penalty operator, the face-oriented stabilizations are applied just to the faces of cut elements. In this case, the classical residual-based stabilizations (SUPG, PSPG and grad-div stabilization), which are shown at the lines twelve to fifteen, are used on both fluid subdomains to overcome the convective and inf-sup related fluid instabilities. According to this,

the parameters δ_{br} and δ_{er} switch between face-oriented stabilizations for the whole faces of the fluid subdomains and face-oriented stabilizations just on the cut elements combined with classical residual-based stabilizations for all elements of background and embedded fluids. Thus, it holds

$$\delta_{br} = \begin{cases} 1 & \text{for } i = G \\ 0 & \text{for } i = B \end{cases} \quad (3.142)$$

and

$$\delta_{er} = \begin{cases} 1 & \text{for } \delta_{ef} = 0 \\ 0 & \text{for } \delta_{ef} = 1. \end{cases} \quad (3.143)$$

The definition of the residual-based stabilization parameters τ_i^m, τ_i^c for $i \in \{b, e\}$ is given in (2.81) and (2.89). The embedded fluid formulation (3.135) is used for the numerical examples demonstrated in the following section.

The global linear system of (3.135), which has to be solved in every Newton step i of a time step t^{n+1} , is given in (3.144). The unknowns on the background and embedded grids are split into standard unknowns (\mathcal{S}), referring to nodes far from the interface, and interface unknowns (\mathcal{I}), which include the cut elements of the background fluid mesh and the embedded elements adjacent to the interface. The standard Galerkin terms are denoted with \mathcal{F} , while the fluid stabilization terms are identified as $\underline{\mathcal{S}}$. Furthermore, the interface coupling terms including the Nitsche terms and the convective inflow stabilizations are assigned to $\underline{\mathcal{G}}$. It has to be pointed out that the linear system (3.135) states for an embedded element weighting of Nitsche's method.

$$\begin{aligned}
 & \left[\begin{array}{c}
 FSS_{u^e u^e} + \underline{SSS}_{u^e u^e} \\
 FSS_{p^e u^e} + \underline{SSS}_{p^e u^e} \\
 FIS_{u^e u^e} + \underline{SIS}_{u^e u^e} \\
 FIS_{p^e u^e} + \underline{SIS}_{p^e u^e} \\
 0 \\
 0 \\
 0 \\
 0
 \end{array} \right]_{i+1}
 \begin{array}{c}
 FSS_{u^e p^e} + \underline{SSS}_{u^e p^e} \\
 \underline{SSS}_{p^e p^e} + \underline{SSS}_{u^e p^e} \\
 FIS_{u^e p^e} + \underline{SIS}_{u^e p^e} \\
 \underline{SIS}_{p^e p^e} \\
 0 \\
 0 \\
 0 \\
 0
 \end{array}
 \begin{array}{c}
 FSI_{u^e u^e} + \underline{SSI}_{u^e u^e} \\
 FSI_{p^e u^e} + \underline{SSI}_{p^e u^e} \\
 FII_{u^e u^e} + \underline{SII}_{u^e u^e} + \underline{GII}_{u^e u^e} \\
 FII_{p^e u^e} + \underline{SII}_{p^e u^e} + \underline{GII}_{p^e u^e} \\
 0 \\
 0 \\
 0 \\
 0
 \end{array}
 \begin{array}{c}
 FSI_{u^e p^e} + \underline{SSI}_{u^e p^e} \\
 \underline{SSI}_{p^e p^e} \\
 FII_{u^e p^e} + \underline{SII}_{u^e p^e} + \underline{GII}_{u^e p^e} \\
 \underline{SII}_{p^e p^e} \\
 0 \\
 0 \\
 0 \\
 0
 \end{array}
 \begin{array}{c}
 0 \\
 0 \\
 \underline{GII}_{u^e u^b} \\
 \underline{GII}_{p^e u^b} \\
 FII_{u^b u^b} + \underline{SII}_{u^b u^b} + \underline{GII}_{u^b u^b} \\
 FII_{p^b u^b} + \underline{SII}_{p^b u^b} \\
 FSI_{u^e u^e} + \underline{SSI}_{u^e u^e} \\
 FSI_{p^e u^e} + \underline{SSI}_{p^e u^e}
 \end{array}
 \begin{array}{c}
 0 \\
 0 \\
 0 \\
 0 \\
 FII_{u^b p^b} + \underline{SII}_{u^b p^b} \\
 \underline{SII}_{p^b p^b} \\
 FSI_{u^e p^e} + \underline{SSI}_{u^e p^e} \\
 \underline{SSI}_{p^e p^e}
 \end{array}
 \begin{array}{c}
 0 \\
 0 \\
 0 \\
 0 \\
 FIS_{u^b u^b} + \underline{SIS}_{u^b u^b} \\
 FIS_{p^b u^b} + \underline{SIS}_{p^b u^b} \\
 FSS_{u^e u^e} + \underline{SSS}_{u^e u^e} \\
 FSS_{u^e p^e} + \underline{SSS}_{u^e p^e} \\
 FSS_{u^e u^e} + \underline{SSS}_{u^e u^e}
 \end{array}
 \begin{array}{c}
 0 \\
 0 \\
 0 \\
 0 \\
 FIS_{u^b p^b} + \underline{SIS}_{u^b p^b} \\
 FIS_{p^b p^b} + \underline{SIS}_{p^b p^b} \\
 FSS_{u^e p^e} + \underline{SSS}_{u^e p^e} \\
 FSS_{u^e u^e} + \underline{SSS}_{u^e u^e}
 \end{array}
 \begin{array}{c}
 0 \\
 0 \\
 0 \\
 0 \\
 0 \\
 0 \\
 0 \\
 0
 \end{array}
 \begin{array}{c}
 0 \\
 0 \\
 0 \\
 0 \\
 0 \\
 0 \\
 0 \\
 0
 \end{array}
 \end{array} \Bigg]_{i+1}^{n+1}
 \begin{array}{c}
 \Delta u^{e,S} \\
 \Delta p^{e,S} \\
 \Delta u^{e,I} \\
 \Delta p^{e,I} \\
 \Delta u^{b,I} \\
 \Delta p^{b,I} \\
 \Delta u^{b,S} \\
 \Delta p^{b,S}
 \end{array} \Bigg]_{i+1}^{n+1}
 = - \left[\begin{array}{c}
 r^{e,S}_u \\
 r^{e,S}_p \\
 r^{e,I}_u \\
 r^{e,I}_p \\
 r^{b,I}_u \\
 r^{b,I}_p \\
 r^{b,S}_u \\
 r^{b,S}_p
 \end{array} \right]_{i+1}^{n+1}
 \end{array} \Bigg]_i
 \tag{3.144}$$

3.9 Numerical examples

In this section, the proposed stabilized embedded fluid formulation (3.135) will be validated for the case of stationary embedded fluid as well as moving embedded fluid by applying the XFEM time-integration procedure described in Section 3.8. Stationary benchmark computations are used to demonstrate the importance of face-oriented stabilizations, and the correctness of the formulation in case of the stationary embedded fluid in viscous dominated regime. Further examples are provided to verify the formulation in the convective dominated regime, for stationary as well as moving embedded fluid. The numerical examples are solved with both stabilization variants of the embedded fluid formulation (3.135), i.e. applying face-oriented stabilizations on the whole faces of the background and embedded fluid meshes ($\delta_{ef} = 1$, $\delta_{br} = \delta_{er} = 0$ and $i = B$) and, the second possibility, using face-oriented stabilizations just on the faces of the cut elements combined with residual-based stabilizations on the whole fluid elements ($\delta_{ef} = 0$, $\delta_{br} = \delta_{er} = 1$ and $i = G$), to demonstrate the correctness and applicability of both stabilization possibilities. Trilinear hexahedral elements are used in all examples. The 2D simulations are performed as a pseudo 2D examples with one element in z -direction. The numerical examples presented in this section are closely related to the examples given in Shahmiri et al. [156, 157].

3.9.1 Benchmark computations

In the following, the benchmark computations 2D-1 and 3D-1Z introduced by Schäfer and Turek [152] are used to verify the proposed formulation and to demonstrate the importance of the face-oriented fluid stabilizations on the solution. As defined in Schäfer and Turek [152], the computation is done for a laminar, incompressible, stationary flow over a cylinder with $RE = 20$. The geometry configurations, particular setups, the boundary conditions as well as the reference results are taken unchanged from Schäfer and Turek [152]. For all computations a boundary layer mesh is constructed around the cylinder, which is then embedded into the background mesh. The cylinder is modelled using 'no-slip' boundary condition on the internal boundary of the embedded fluid subdomain.

Two-dimensional cylinder Benchmark

The whole background fluid of the two-dimensional cylinder Benchmark 2D-1 is a channel with $2.2\text{ m} \times 0.41\text{ m}$ and a cylinder with radius 0.05 is located at $(0.2, 0.2)$. A parabolic inflow with a maximum velocity of $u_x^{\max} = 0.3\text{ m/s}$ and 'no-slip' boundary conditions on the upper and lower walls are prescribed to the channel. Furthermore, the density is set to $\rho^f = 1.0\text{ kg/m}^3$ and for the kinematic viscosity holds $\nu = 10^{-3}\text{ m}^2/\text{s}$. The Reynolds number obtained using the definition in Schäfer and Turek [152] is then 20.

Figure 3.19 illustrates the velocity and pressure fields of the cylinder benchmark computation using the stationary stabilized embedded fluid formulation with a Nitsche parameter of $\delta = 35.0$ and a ghost-penalty stabilization parameter of $\alpha_{GP} = 0.003$, from the parameter studies of 2D-Kim-Moin flow in Section 3.7.1. The face-oriented stabilizations are applied to the whole faces of background and embedded fluid subdomains and, therefore, all the residual-based stabilizations are turned off. Computed lift and drag values (C_{lift} , C_{drag}) are compared with the reference

Method	$N_{\mathbf{u},p}^{\text{DOF}}$	c_{drag}	c_{lift}	Δp
Pure FOS and GP	$\simeq 38512$	5.5814	0.0110	0.1173
Ref. lower bound	-	5.5700	0.0104	0.1172
Ref. upper bound	-	5.5900	0.0110	0.1176

Table 3.8: Cylinder benchmark 2D-1: Lift and drag values and the pressure difference.

paper by Schäfer and Turek [152]. In Table 3.8, the lift and drag values (c_{lift} , c_{drag}) and the pressure difference Δp between front and back end of the cylinder are demonstrated. For all values, a good agreement with the given reference values is achieved.

In order to demonstrate the influence of inappropriate stabilizations for cut elements, a second simulation with the same geometry and setup but using classical residual-based stabilization (SUPG and PSPG) without any face-oriented or ghost-penalty stabilizations along cut faces is run. Also for this simulation, the embedded elements weighting of Nitsche's method is used, such that we have a stable interface formulation in both cases.

In Figure 3.20, the pressure and velocity fields on cut elements are shown for both simulations. Figures 3.20a and 3.20b show results of the proposed embedded fluid formulation. As it can be observed, using face-oriented fluid stabilizations and ghost-penalty operator in the interface region, a smooth continuous velocity and pressure solution within the ghost domain for cut elements is achieved. In Figure 3.21, the pressure field is plotted in z -direction, which again demonstrates the quality of the pressure flux coupling between the two subdomains using the proposed stabilized formulation.

In contrast, when neglecting the interface fluid stabilizations, as the case for a pure residual-based stabilized formulation, non-physical velocity and pressure values at ghost nodes occur, specially for regions with small physical background fluid domain, as shown in Figures 3.20c and 3.20d. A close up view of the Figures 3.20c and 3.20d at two different interface positions is depicted in Figure 3.22. Hereby, to show the uncontrolled ghost values along cut elements more clearly, a different scale from Figure 3.20 is applied. Additionally, the non-physical velocity values at ghost nodes are circled. This lack of stability is also apparent in the worse convergence behavior of the Newton-Raphson loop.

Three-dimensional cylinder Benchmark

The setup of stationary three-dimensional benchmark 3D-1Z is similar to the benchmark 2D-1. The whole background fluid is a channel with $0.41\text{ m} \times 0.41\text{ m} \times 2.5\text{ m}$ with 'no-slip' conditions at the four side walls. A cylinder with radius 0.05 is surrounded by an embedded fluid mesh. A parabolic inflow with a maximum velocity of $u_x^{\text{max}} = 0.3\text{ m/s}$ in x -direction is applied at the inflow boundary and traction-free Neumann condition at the outflow. A viscosity of $\nu = 10^{-3}\text{ m}^2/\text{s}$ is prescribed, which results in a Reynolds number $RE = 20$ according to the definition in Schäfer and Turek [152]. Furthermore, the density of the flow is $\rho^f = 1.0\text{ kg/m}^3$. In contrast to cylinder benchmark 2D-1, the face-oriented stabilizations are just applied to the cut elements and residual-based stabilizations are used for all elements of both fluid subdomains. As above, a Nitsche parameter of $\delta = 35.0$ and a ghost-penalty stabilization parameter

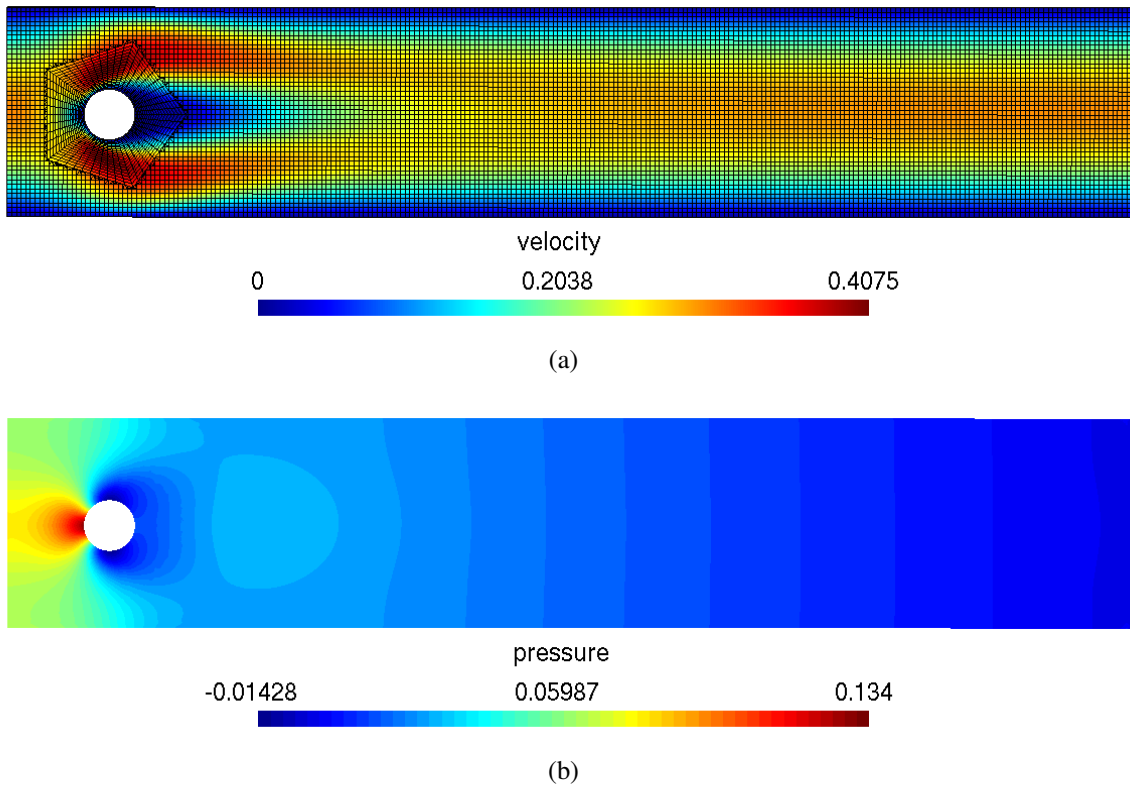


Figure 3.19: Cylinder benchmark 2D-1: Velocity and pressure fields.

Method	$N_{u,p}^{\text{DOF}}$	c_{drag}	c_{lift}	Δp
Res-based and FOS (interface) and GP	$\simeq 35828$	6.1662	0.0109	0.1716
Ref. lower bound	-	6.0500	0.0080	0.1650
Ref. upper bound	-	6.2500	0.0100	0.1750

Table 3.9: Cylinder benchmark 3D-1Z: Lift and drag values and the pressure difference.

of $\alpha_{\text{GP}} = 0.003$ are used. The results of the computed lift and drag values (c_{lift} , c_{drag}) are given in Table 3.9, which match the reference values well. Figure 3.23 illustrates the resulting velocity and pressure field.

3.9.2 Two-dimensional cylinder Benchmark with higher Reynolds number

As introduced in Shahmiri et al. [157], in the following example, a similar setup to the cylinder Benchmark 2D-1, is used to compute an unsteady flow at higher Reynolds number. This example shows that the embedded fluid formulation delivers a smooth and stable solution for velocity and

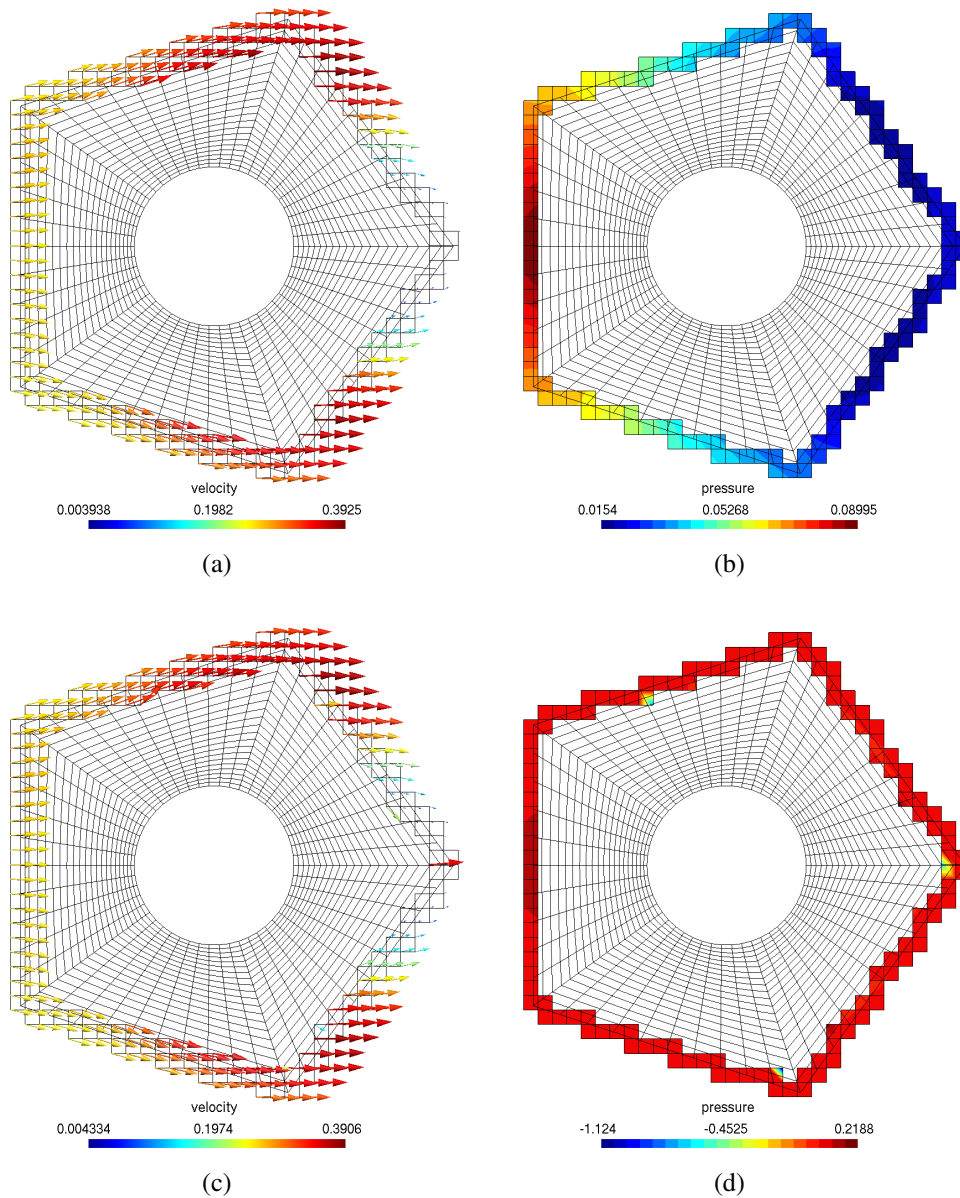


Figure 3.20: Cylinder benchmark 2D-1: Velocity and pressure field for face-oriented fluid and viscous ghost-penalty stabilization ((a) and (b)) versus residual-based stabilization without appropriate interface fluid stabilizations, where non-physical and unreasonable velocity and pressure fields at ghost nodes occur ((c) and (d)).

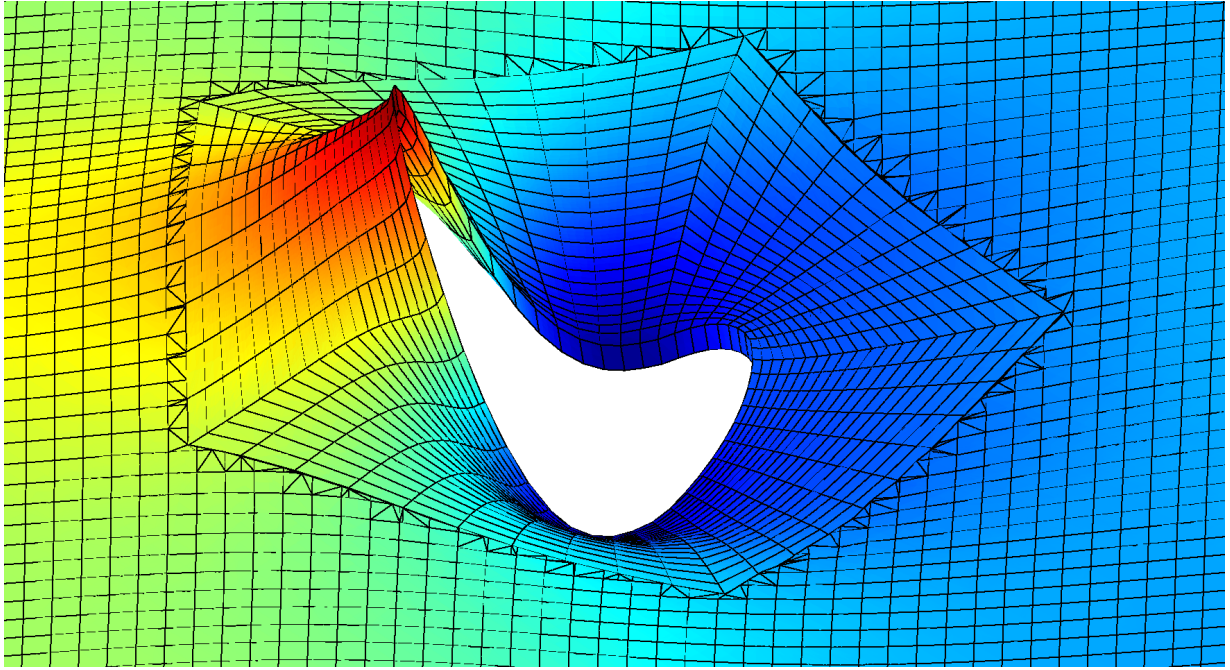


Figure 3.21: Cylinder benchmark 2D-1: Close up view of the pressure field plotted in z -direction. A smooth continued pressure solution within the ghost domain is achieved using face-oriented stabilizations.

pressure in case of higher Reynolds number. A dynamic inflow condition as

$$u_x(x = 0, y, t) = \begin{cases} u_x^{\max} \frac{4y(H - y)}{H^2} \cdot 0.5 \left(1 - \frac{\cos(\pi t)}{T_1}\right) & , t = [0, T_1] \\ u_x^{\max} \frac{4y(H - y)}{H^2} & , t = [T_1, T_{\max}] \end{cases} \quad (3.145)$$

$$u_y = 0 \quad (3.146)$$

is given with $H = 0.41 \text{ m}$, $u_x^{\max} = 1.5 \text{ m/s}$ and $T_1 = 1 \text{ s}$. As in cylinder Benchmark 2D-1, a traction-free Neumann condition at the outflow and 'no-slip' conditions at the upper and lower wall are applied. The kinematic viscosity is $\nu = 0.000128 \text{ m}^2/\text{s}$ and a density of $\rho^f = 1.0 \text{ kg/m}^3$ is chosen. It results in a Reynolds number of $RE = 800$ using the definition in Schäfer and Turek [152]. Also for this example, the embedded fluid formulation (3.135) with a Nitsche parameter of $\delta = 35.0$ and a ghost-penalty stabilization parameter of $\alpha_{GP} = 0.003$ is used, with residual-based stabilizations applied to both fluid subdomain and additional face-oriented stabilizations on the cut faces. Furthermore, a convective inflow stabilization with $\gamma_{adv} = \frac{1}{2}$ is applied. The simulation is run for $T_{\max} = 8 \text{ s}$ with $\theta = 0.66$ and $\Delta t = 0.01 \text{ s}$. A close up view of pressure field around the cylinder for three arbitrary time steps is given in Figure 3.24. In order to demonstrate the smoothness of the solution, additional pressure contour lines are presented. The velocity field for different time steps is shown in Figure 3.25. As it can be seen in Figures 3.24 and 3.25, over the whole simulation time no perturbation of the solution at the fluid-fluid interface is observed and a smooth solution is achieved.

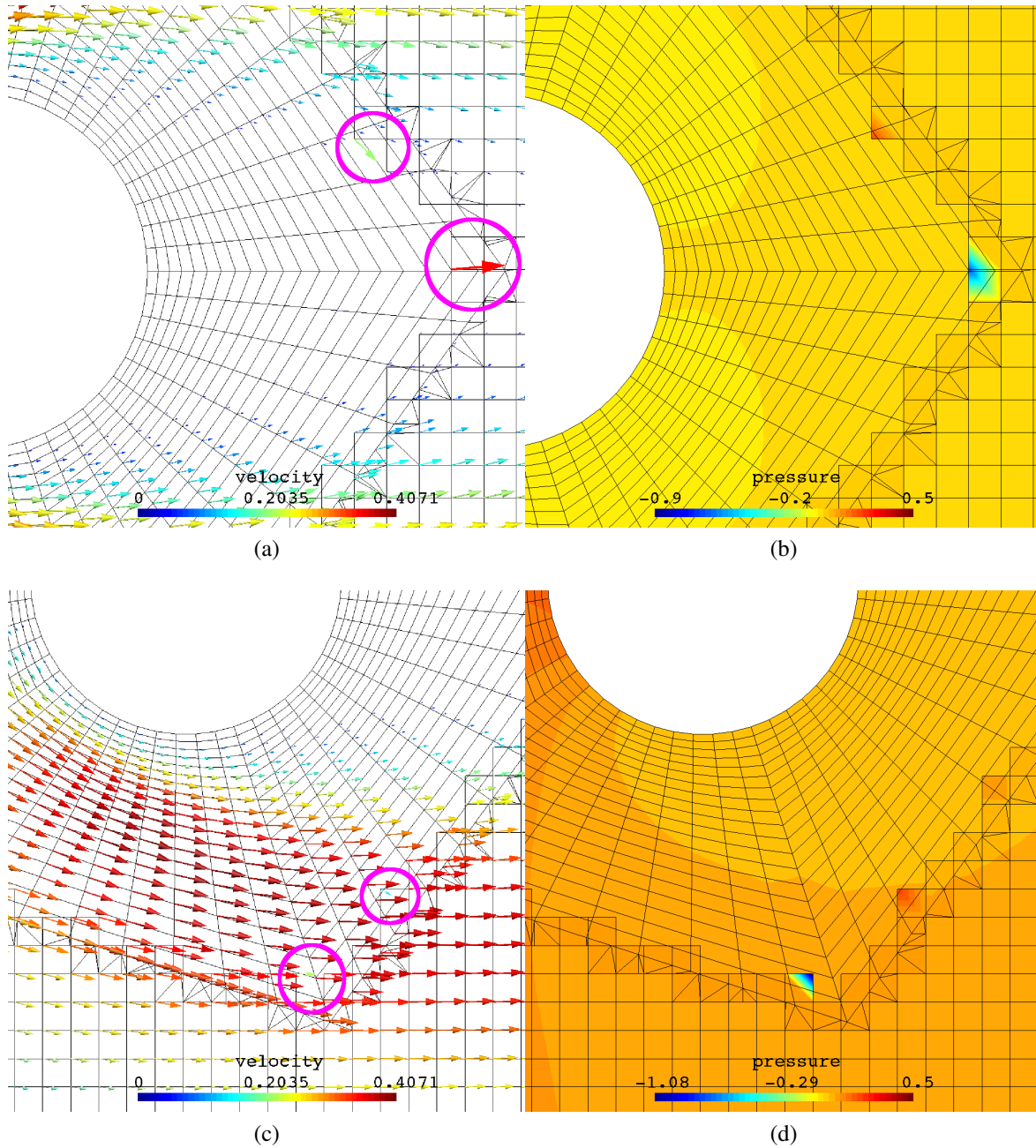


Figure 3.22: Cylinder benchmark 2D-1: Close up view of velocity and pressure field with residual-based stabilization without appropriate interface fluid stabilizations at two different positions at the interface. Non-physical and unreasonable velocity and pressure values occur at ghost nodes with small physical background fluid domain.

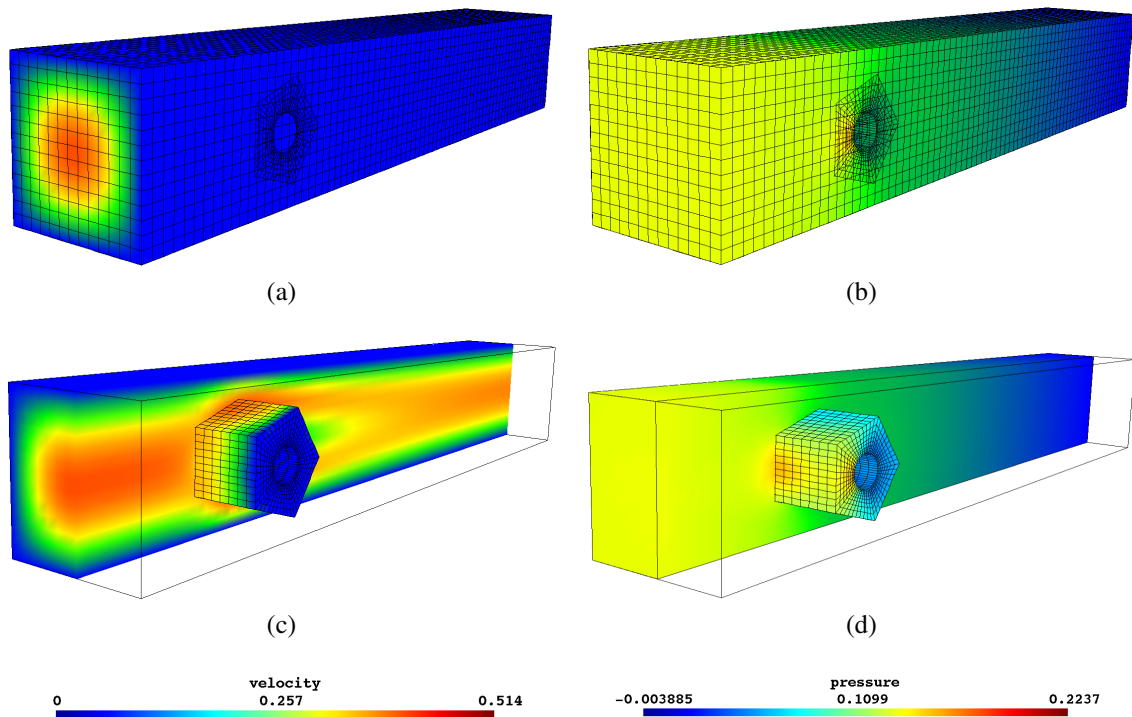


Figure 3.23: Benchmark 3D-1Z: (a) Velocity field, (b) Pressure field, (c) Velocity field in the cross-section, (d) Pressure field in the cross-section

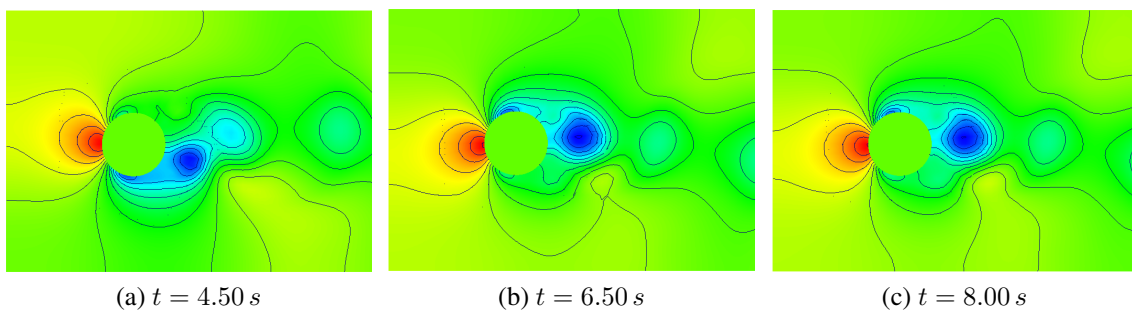


Figure 3.24: Two-dimensional cylinder Benchmark with $RE = 800$: Close up view of the pressure field at different time steps.

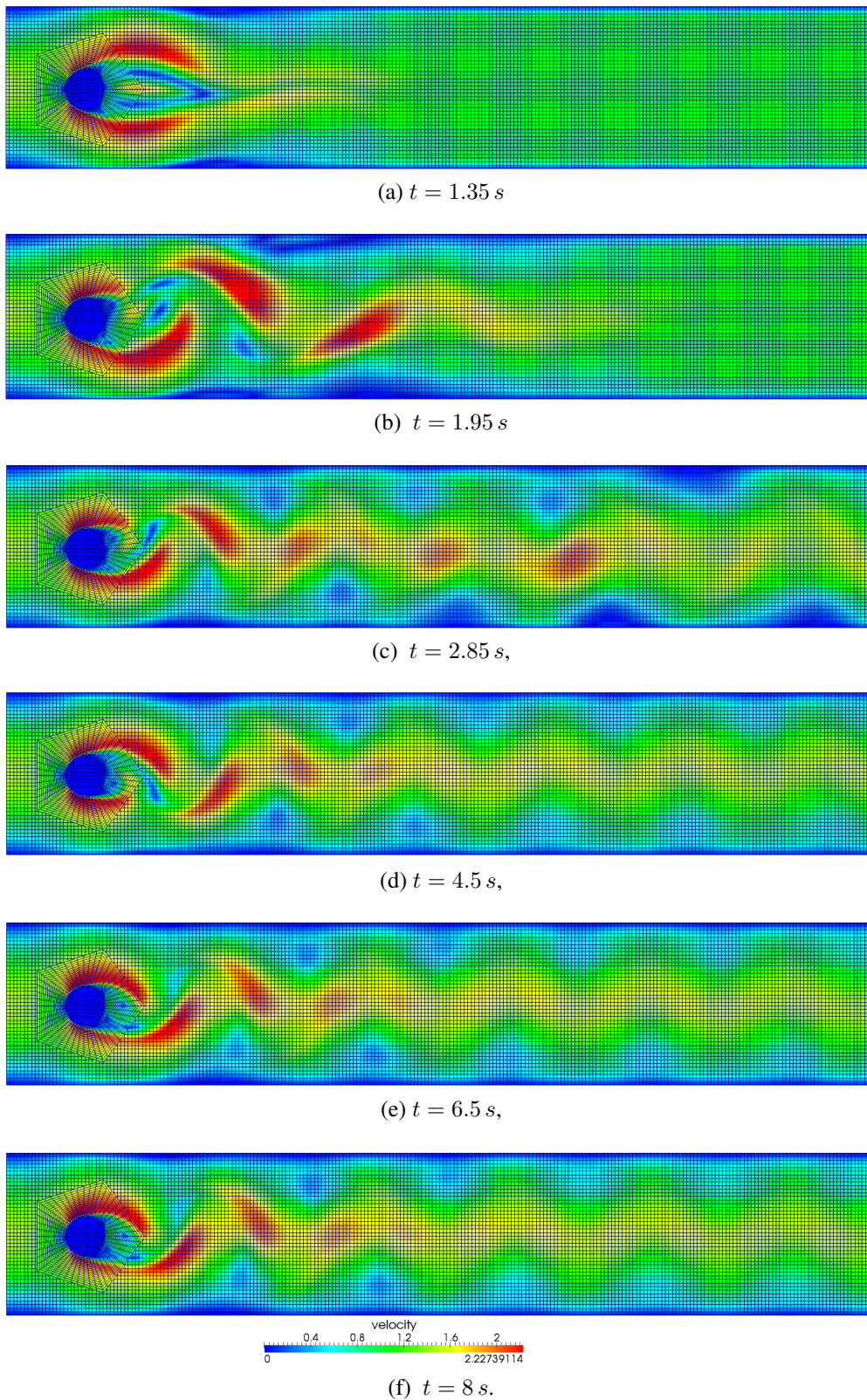


Figure 3.25: Two-dimensional cylinder Benchmark with $RE = 800$: Velocity field at different time steps.

3.9.3 Two-dimensional flow over a moving cylinder

In the following, a flow over a moving cylinder, which is motivated from Codina et al. [52], with the proposed stabilized embedded fluid formulation (3.135) together with the XFEM time-integration procedure described in Section 3.8 is solved. This example shows that the proposed embedded fluid formulation delivers a smooth and stable solution for velocity and pressure over the time for moving interfaces. It also demonstrates that the formulation is applicable for higher Reynolds number in combination with moving interfaces.

The background fluid domain is a rectangular domain $2.2\text{ m} \times 0.44\text{ m}$, where a cylinder with a diameter of $D = 0.2\text{ m}$ is located at the position $(x_c(t=0), 0.22)$, which is surrounded by a fine layer of stretched embedded fluid elements, see Figure 3.26. The movement of the cylinder is prescribed as

$$x_c(t) = 1.1 + 0.8 \sin\left(\frac{2\pi}{3}(t - 0.75)\right).$$

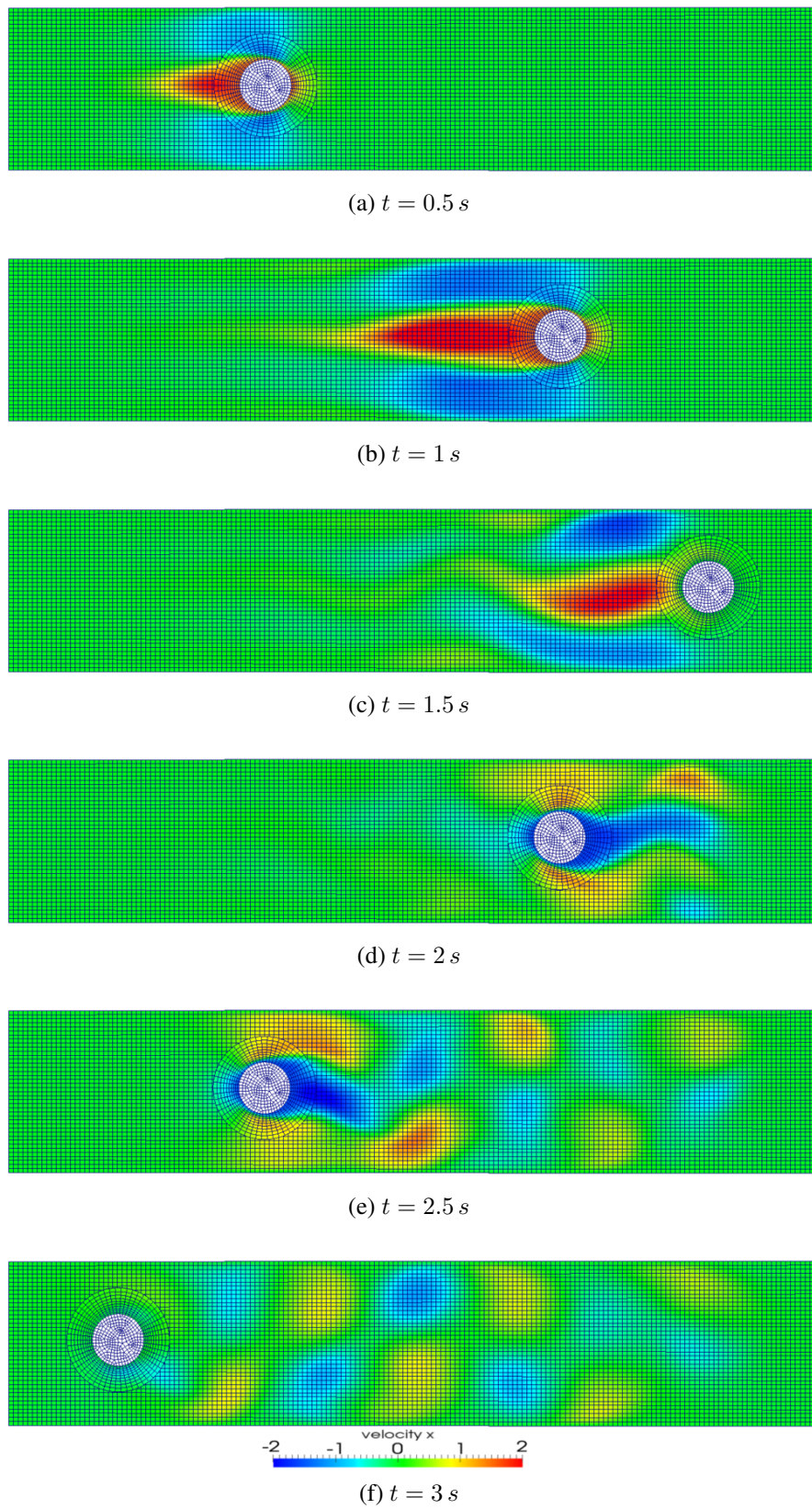
The velocity is set to zero on the left, top and bottom walls of the background fluid subdomain, thus, the flow is only due to the cylinder movement. With a viscosity of $\nu = 0.001\text{ m}^2/\text{s}$, the maximal Reynolds number reached is $\text{RE} \approx 300$. A density of $\rho^f = 1.0\text{ kg}/\text{m}^3$ is chosen. The simulation is done for a full period of $T = 3\text{ s}$. The embedded fluid formulation (3.135) is solved with $\theta = 0.66$ and $\Delta t = 0.00625\text{ s}$, with pure face-oriented stabilizations, i.e. face-oriented stabilizations applied to the whole faces of background and embedded fluid subdomains with an additional ghost-penalty stabilization ($\alpha_{\text{GP}} = 0.003$).

Figures 3.26 and 3.27 show the velocity field in x -direction and the pressure field, respectively, at times 0.5 s , 1 s , 1.5 s , 2 s , 2.5 s and 3 s . Within $T = 3\text{ s}$ the cylinder moves from its initial position to the end of the channel and then changes its direction until it reaches its initial positions again at $t = 3\text{ s}$. The pressure-isolines are depicted in Figure 3.28 to demonstrate the smoothness of the solution at the interface. In Figure 3.28, close up views of the pressure field near to the interface Γ^{FF} are plotted in z -direction for arbitrary times $t = 0.864\text{ s}$, $t = 1.224\text{ s}$ and $t = 1.512\text{ s}$. Figures 3.26, 3.27 and 3.28 indicate the smooth transition of velocity and pressure field across the interface Γ^{FF} during the whole simulation.

3.9.4 Two-dimensional moving snake with prescribed motion

The following example demonstrates the capability of our method to simulate the flow around a deformable structure, which moves over large distances in the fluid domain. It also shows that as the structure moves and deforms, the embedded fluid undergoes the same deformation such that at every time step an appropriate boundary layer mesh surrounds the structure. Furthermore, the proposed embedded fluid formulation delivers again smooth and stable solutions for velocity and pressure fields, over the time, for moving embedded fluid subdomain applying the XFEM time-integration approach.

In this example, which is motivated from Gamnitzer and Wall [80], a thin structure is located at the beginning of a rectangular fluid domain. With a prescribed motion the structure simulates the movement of a snake through the fluid domain. The fluid has a kinematic viscosity of $\nu = 0.1\text{ m}^2/\text{s}$ and a density of $\rho^f = 1.0\text{ kg}/\text{m}^3$. The structure is surrounded by a fine layer of stretched fluid elements (embedded fluid subdomain), which is embedded into the background fluid field. The geometric setup of the example is shown in Figure 3.29. The movement of the

Figure 3.26: Moving cylinder: Velocity field in x -direction at different time steps.

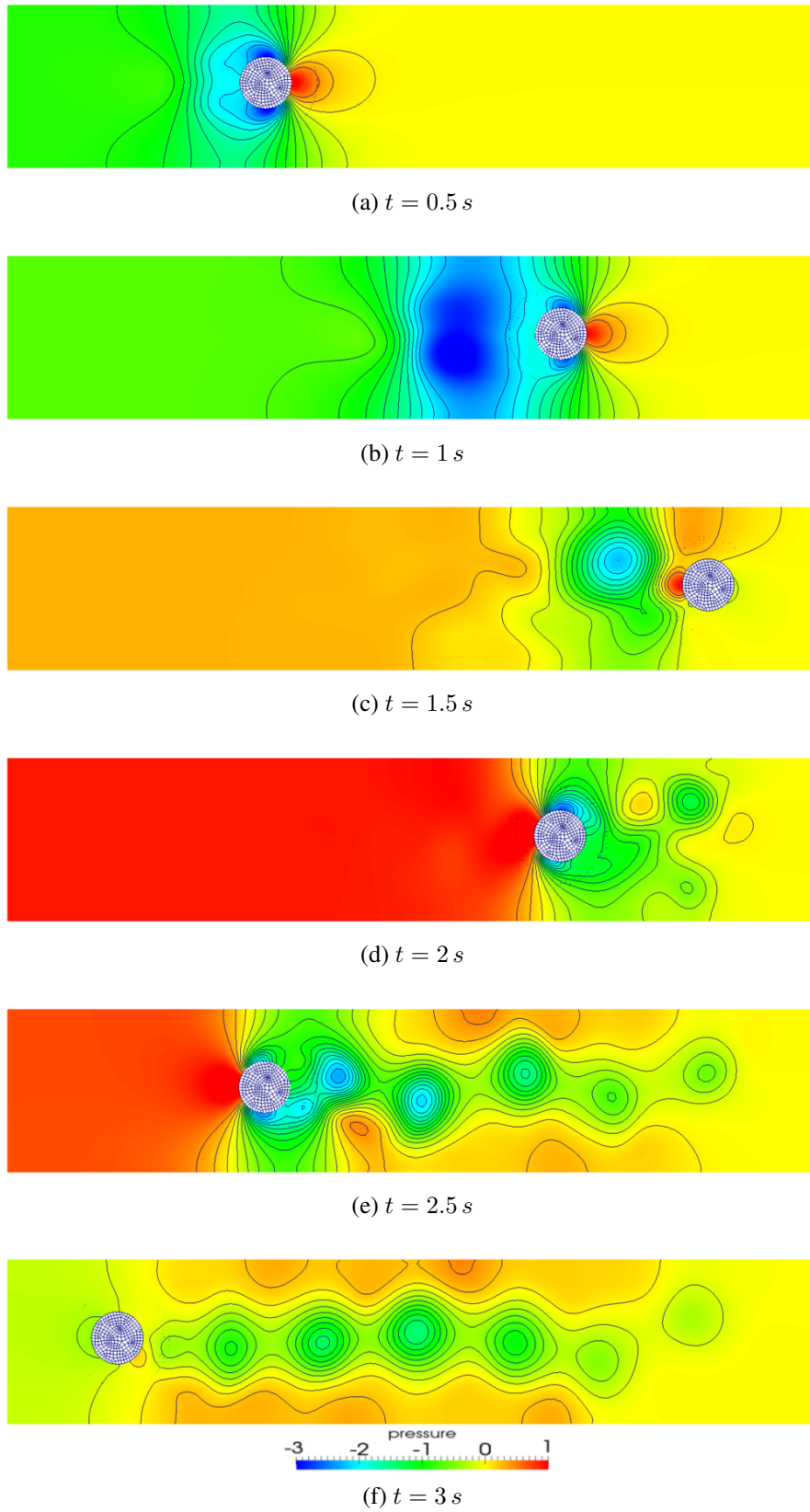


Figure 3.27: Moving cylinder: Pressure field at different time steps.

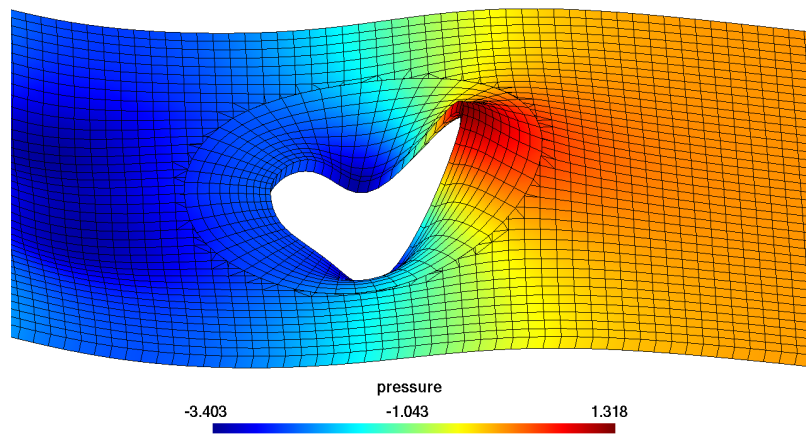
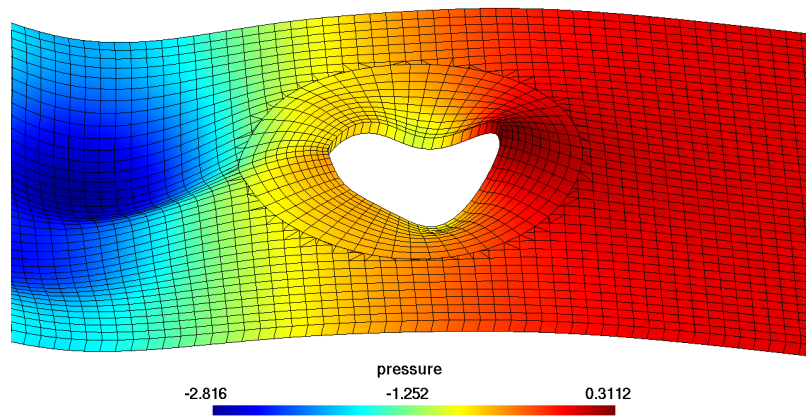
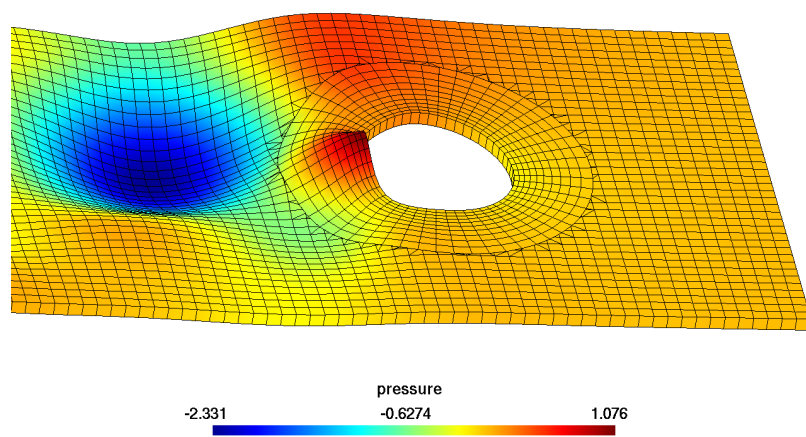
(a) $t = 0.864$ s(b) $t = 1.224$ s(c) $t = 1.512$ s

Figure 3.28: Moving cylinder: Close up view of pressure field plotted in z -direction at different time steps.

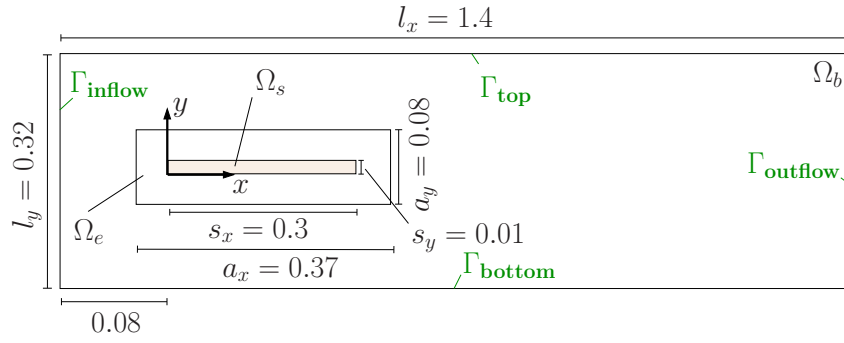


Figure 3.29: Two-dimensional moving snake with prescribed motion: Setup. The unit of lengths is [m]

structure is decomposed in a translation in x -direction and a wave-like deformation, described as

$$d_x(t) = \frac{1}{8}t \quad (3.147)$$

and

$$d_y(t) = \sin(6\pi t) \cdot \cos\left(\frac{2\pi x}{s_x}\right) - 1 \quad (3.148)$$

with s_x denoting the length of the structure. During the simulation time the structure moves from its initial position to the end of the channel. Zero Dirichlet boundary conditions are prescribed at the upper and lower walls (Γ_{top} and Γ_{bottom} in Figure 3.29). At the left wall of the channel (Γ_{inflow}) a parabolic inflow with maximum velocity of $u_x^{\text{max}} = 1.0 \text{ m/s}$ is applied. A zero Neumann boundary condition is applied at the outflow (Γ_{outflow}). The simulation is run for $T = 16 \text{ s}$ with the time step $\Delta t = 0.01 \text{ s}$ and $\theta = 1$. In this example, residual-based stabilizations are applied to both fluid subdomains and additional face-oriented stabilizations on the faces of cut elements. Furthermore, as above, a Nitsche parameter of $\delta = 35.0$ and a ghost-penalty stabilization parameter of $\alpha_{\text{GP}} = 0.003$ are used.

In Figure 3.30, the results of the velocity and pressure fields at two different time steps, $t = 2.51 \text{ s}$ and $t = 6.01 \text{ s}$, are shown. Close up views of the velocity fields near the interface are depicted in Figures 3.31a and 3.31b.

3.9.5 Three-dimensional moving snake with prescribed motion

In this example, a three-dimensional moving snake through the fluid domain is simulated. A similar setup like the two-dimensional moving snake, given in Section 3.9.4, is applied. A flexible structure $0.01 \text{ m} \times 0.01 \text{ m} \times 0.1 \text{ m}$ is located at the beginning of a rectangular channel $0.1 \text{ m} \times 0.1 \text{ m} \times 0.4 \text{ m}$. The structure moves with a prescribed movement to the end of the channel. The fluid has a kinematic viscosity of $\nu = 0.1 \text{ m}^2/\text{s}$ and a density of $\rho^f = 1.0 \text{ kg/m}^3$. The embedded fluid mesh, which surrounds the structure, undergoes the same movement of the

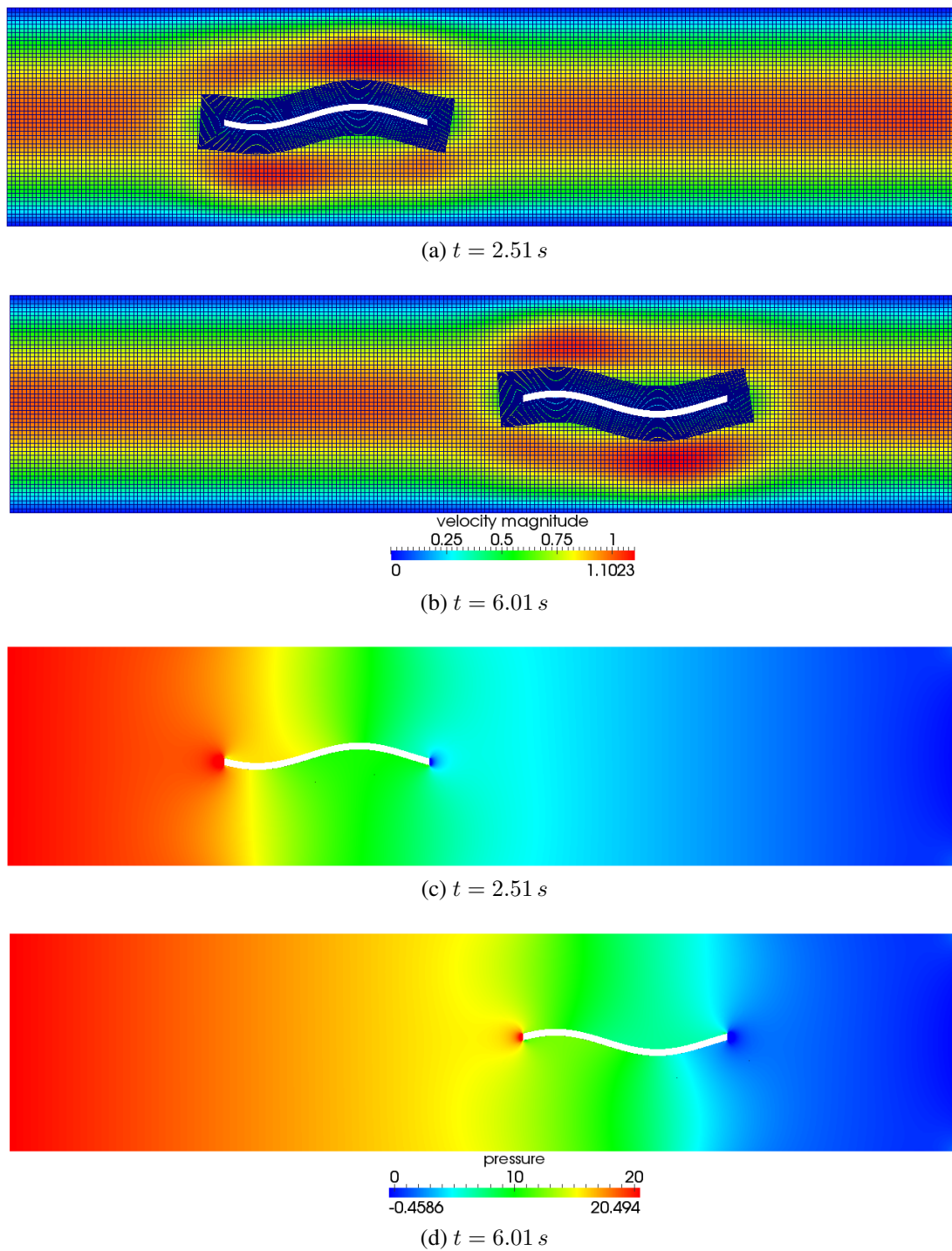


Figure 3.30: Two-dimensional moving snake with prescribed motion: ((a) and (b)) Velocity field at two different time steps, $t = 2.51 \text{ s}$ and $t = 6.01 \text{ s}$. ((c) and (d)) Pressure field at two different time steps, $t = 2.51 \text{ s}$ and $t = 6.01 \text{ s}$.

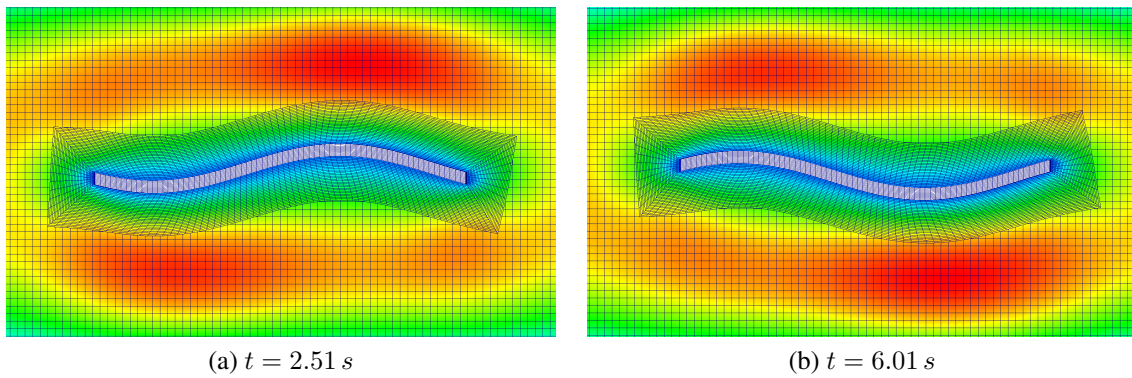


Figure 3.31: Two-dimensional moving snake with prescribed motion: Close up view of the velocity field at two different time steps $t = 2.51 s$ and $t = 6.01 s$.

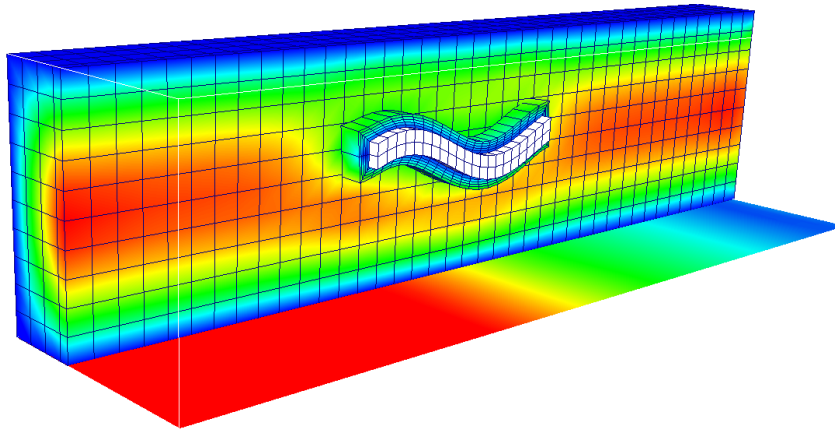


Figure 3.32: Three-dimensional moving snake with prescribed motion: At the cross section the velocity field and at the bottom wall the pressure field at time step $t = 2.83 s$ are illustrated.

structure over the simulation time. The movement of the structure is described as

$$d_x(t) = \frac{1}{8}t, \quad (3.149)$$

$$d_y(t) = \sin(1.2\pi) \cdot \cos\left(\left(\frac{2x}{l_s}\pi\right) - 1\right), \quad (3.150)$$

$$d_z(t) = 0. \quad (3.151)$$

A 'no-slip' boundary condition is prescribed at the four walls of the channel. At the inflow a parabolic profile with maximum velocity of $u_x = 0.5 m/s$ is prescribed and a zero Neumann boundary condition is applied at the outflow. The simulation is run for $T = 6.95 s$ with $\Delta t = 0.01 s$ and $\theta = 1$. Also in this example, residual-based stabilizations are applied to both fluid subdomain and additional face-oriented stabilizations on the faces of cut elements. Figure 3.32 illustrates the velocity magnitude at the cross section and the pressure field at the bottom wall of the channel at time step $t = 2.83 s$.

4 A hybrid ALE-fixed-grid monolithic FSI approach

Up to this point, the fluid domain composed of background fluid and embedded fluid subdomains, separated by the fluid-fluid interface, has been considered. An XFEM-based stabilized embedded fluid formulation has been developed in Chapter 3. This chapter combines the stabilized embedded fluid formulation, proposed in Chapter 3, and the structure field into a coupled hybrid ALE-fixed-grid fluid-structure interaction (FSI) system, which is solved in a monolithic scheme. The challenge of solving the derived monolithic FSI system in combination of moving embedded fluid and fixed-grid background fluid will be explained. In order to deal with this issue, a novel approach stated as *relaxing ALE approach* will be introduced. Numerical examples validate the proposed approach and show the ability and performance of the method.

4.1 Problem definition

A FSI problem consists of the description of fluid and structure fields together with coupling conditions at their common interface. In the classical ALE-based FSI approach, see e.g. Wall [172], a single fluid field, described on a deformable fluid domain, and a structure field interact with each other at the common fluid-structure interface. In the hybrid ALE-fixed-grid FSI approach, the fluid field is subdivided into two subdomains, a background fluid subdomain, described in fixed-grid Eulerian formulation, and a deformable embedded fluid subdomain, described in ALE framework. The two fluid subdomains are separated by an internal fluid-fluid interface. The embedded fluid subdomain interacts with the structure field at the fluid-structure interface. Therefore, the problem consists of two fluid subdomains, a structure field and two interfaces, the internal fluid-fluid interface and the physical fluid-structure interface.

In Figure 4.1a, a general setup of the hybrid ALE-fixed-grid FSI approach is shown. Let $\Omega^f = \Omega^b \cup \Omega^e$ be the whole physical fluid domain. The fluid domain Ω^f is separated into a background fluid subdomain Ω^b and an embedded fluid subdomain Ω^e by the fluid-fluid interface Γ^{FF} . The coupling of the flow fields, Ω^b and Ω^e , takes place at the shared fluid-fluid interface Γ^{FF} . The fluid field interacts with the structure domain Ω^s at the fluid-structure interface Γ^{FSI} via the embedded fluid subdomain Ω^e . In Figure 4.1a, \mathbf{n}^b and \mathbf{n}^e denote the outward pointing normal vectors with respect to the fluid subdomains, Ω^b and Ω^e , respectively. The outward pointing normal vector of the structure domain Ω^s is denoted as \mathbf{n}^s . The embedded fluid subdomain Ω^e is discretized with a classical finite element mesh \mathcal{T}^e as a boundary layer mesh around the structure, see Figure 4.1b. The elements of \mathcal{T}^e are aligned with the fluid-fluid interface Γ^{FF} and the fluid-structure interface Γ^{FSI} . For the background fluid subdomain Ω^b a fixed-grid mesh \mathcal{T}^b using cut elements is used. Thus, the fluid-fluid interface Γ^{FF} subdivides the background fluid into an active physical part identified with Ω^b and an inactive void/fictitious part Ω^{b-} , which is

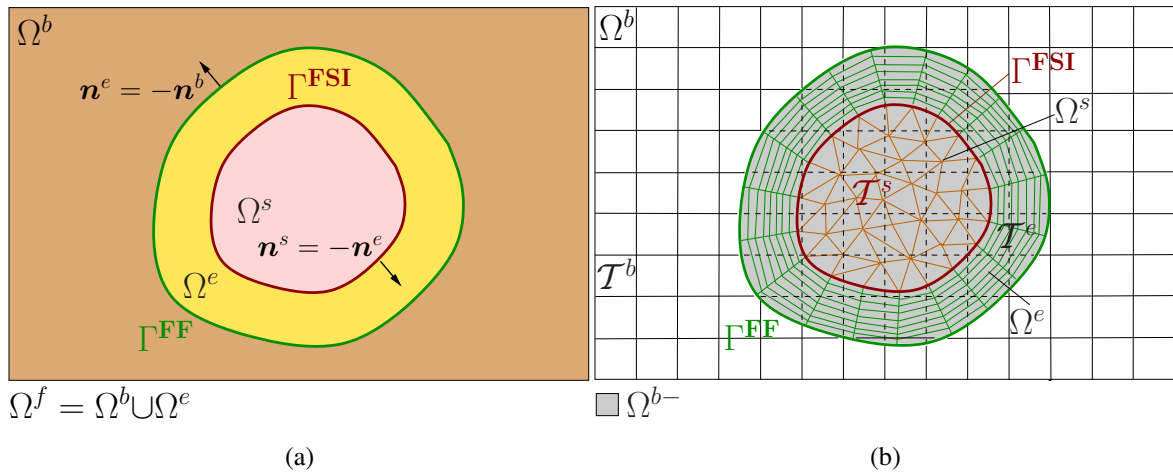


Figure 4.1: **(a)** The fluid domain Ω^f is separated into an embedded fluid subdomain Ω^e and a background fluid subdomain Ω^b by fluid-fluid interface Γ^{FF} . The fluid field interacts with the structure domain Ω^s at the fluid-structure interface Γ^{FSI} via the embedded fluid subdomain Ω^e . **(b)** The background fluid is divided into a physical fluid subdomain Ω^b and an inactive void/fictitious fluid subdomain Ω^{b-} , which is covered by Ω^e and Ω^s , by the fluid-fluid interface Γ^{FF} . The fluid subdomains Ω^b and Ω^e are discretized with finite element meshes \mathcal{T}^b and \mathcal{T}^e , respectively. The structure domain Ω^s is discretized with the finite element mesh \mathcal{T}^s .

covered by Ω^e and Ω^s . The coupling conditions at the fluid-fluid interface are enforced weakly, as discussed in Chapter 3. The structure domain is discretized with a finite element mesh \mathcal{T}^s . In the present work, matching meshes for structure \mathcal{T}^s and embedded fluid subdomain \mathcal{T}^e at the fluid-structure interface Γ^{FSI} are assumed. Thus, the structure shares the same discretization with the embedded fluid at the fluid-structure interface Γ^{FSI} .

An exemplary spatial discretization of the coupled hybrid ALE-fixed-grid FSI problem is depicted in Figure 4.2. The coupled FSI problem is shown in Figure 4.2a. It consists of structure field, embedded fluid subdomain, which surrounds the structure, and background fluid subdomain. The deformable fluid is then embedded into the fixed background fluid mesh, see Figure 4.2a. The structure field and the deformable embedded fluid share the same discretization at their common interface, the fluid-structure interface, see Figure 4.2a. The structure field and the embedded fluid are depicted separately in Figures 4.2b and 4.2d, respectively. The background fluid mesh is shown in Figure 4.2c. For the approximation of the background fluid subdomain cut elements, which are not aligned with the fluid-fluid interface are used. The background fluid subdomain is divided by the fluid-fluid interface into a physical part and a fictitious part, which is covered by the embedded fluid field and the structure.

4.2 Semi-discrete formulation of coupled FSI system

In Section 3.8, the final stabilized embedded fluid formulation based on the Extended Finite Element Method (XFEM) has been proposed. In Sections 2.2 and 2.4, the weak formulations

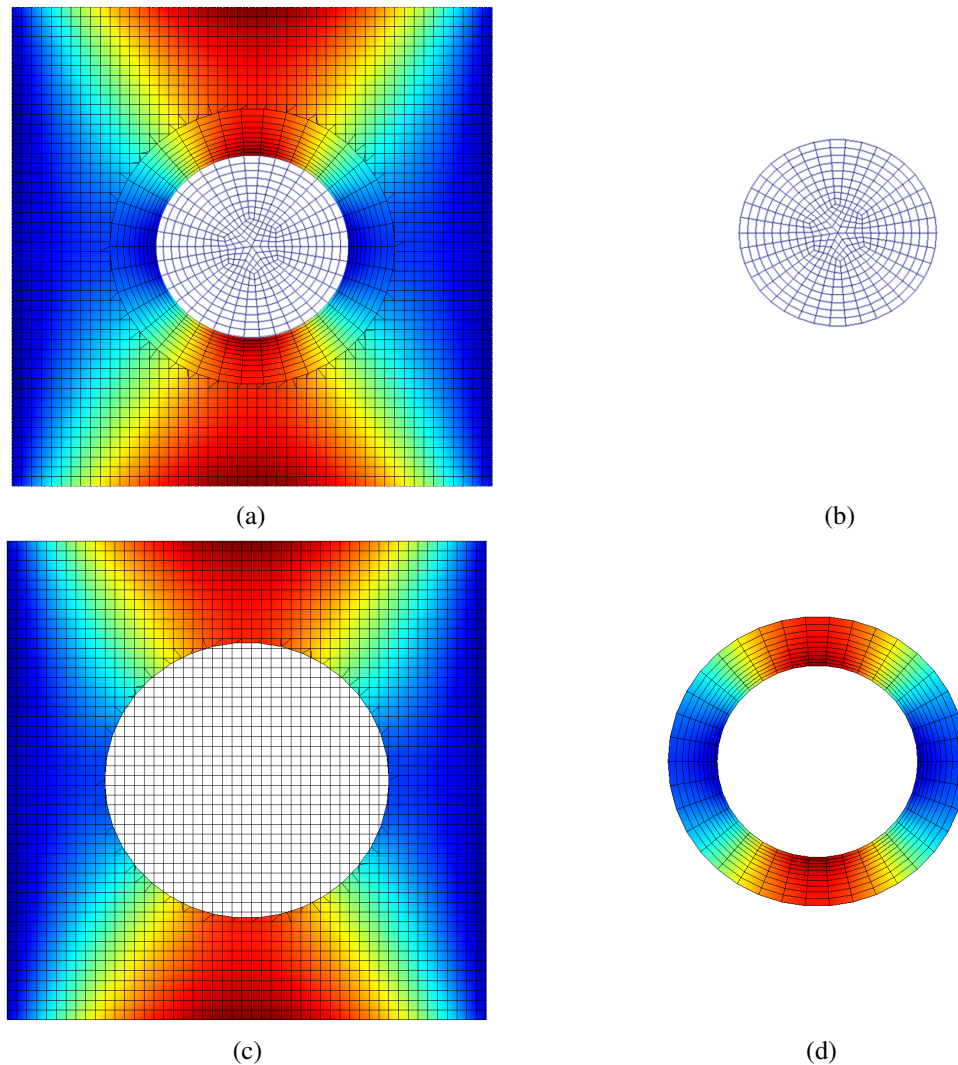


Figure 4.2: **(a)** The coupled problem consists of the structure field, a boundary layer mesh (embedded fluid) and the fixed-grid background fluid. Different spatial approximation of solutions for background fluid subdomain and embedded fluid subdomain are used. For the embedded fluid subdomain classical finite elements aligned with the fluid-fluid interface and fluid-structure interface are applied. For the approximation of background fluid subdomain cut elements, which are not aligned with the fluid-fluid interface are used. The structure field is discretized with classical finite elements. The structure field and the embedded fluid share the same discretization at the fluid-structure interface. **(b)** The structure field is discretized with classical finite elements and shares the same discretization with the embedded fluid at the fluid-structure interface. **(c)** The fixed-grid background fluid subdomain is divided by the fluid-fluid interface into a physical part and a void/fictitious part, which is covered by embedded fluid and the structure field. For the approximation of the background fluid subdomain, cut elements, which are not aligned with the fluid-fluid interface, are used. **(d)** The deformable embedded fluid mesh, which is aligned with the fluid-structure interface and the fluid-fluid interface.

and the discretizations of the structure and ALE field as single fields have been reviewed. In the following, the semi-discrete formulation of the coupled FSI system is presented. The presented derivations are adopted from Mayr et al. [135], where the FSI problem is formulated for a purely ALE-described fluid field. First, the coupling conditions at the fluid-structure interface Γ^{FSI} , which have been introduced briefly in Section 2.5.2, will be described in detail.

At the fluid-structure interface Γ^{FSI} the embedded fluid subdomain and structure field are coupled through kinematic and dynamic coupling constraints. No mass flow across the interface is allowed, therefore, the normal velocities at the interface have to match. Furthermore, a relative tangential movement between the fluid and the structure is prohibited. Thus, a no-slip condition is assumed as the kinematic condition

$$\frac{\partial \mathbf{d}_{\Gamma^{\text{FSI}}}^s}{\partial t} = \mathbf{u}_{\Gamma^{\text{FSI}}}^e \quad \text{on} \quad \Gamma^{\text{FSI}} \times (0, T). \quad (4.1)$$

On the other hand, as a non-physical condition, the embedded fluid velocity and the embedded grid velocity at the fluid-structure interface have to be the same. This condition is expressed by

$$\mathbf{u}_{\Gamma^{\text{FSI}}}^e = \mathbf{u}_{\Gamma^{\text{FSI}}}^g = \frac{\partial \mathbf{d}_{\Gamma^{\text{FSI}}}^g}{\partial t} \quad \text{on} \quad \Gamma^{\text{FSI}} \times (0, T), \quad (4.2)$$

which can be written as

$$\frac{\partial \mathbf{d}_{\Gamma^{\text{FSI}}}^s}{\partial t} = \frac{\partial \mathbf{d}_{\Gamma^{\text{FSI}}}^g}{\partial t} \quad \text{on} \quad \Gamma^{\text{FSI}} \times (0, T). \quad (4.3)$$

Considering (4.1), the equation (4.3) is equivalent to the following equation after integration with respect to time

$$\mathbf{d}_{\Gamma^{\text{FSI}}}^s = \mathbf{d}_{\Gamma^{\text{FSI}}}^g \quad \text{on} \quad \Gamma^{\text{FSI}} \times (0, T). \quad (4.4)$$

The kinematic coupling condition (4.4) is enforced weakly by introducing a Lagrange multiplier field λ and corresponding test function $\delta\lambda$ on the fluid-structure interface Γ^{FSI} as

$$\langle \delta\lambda, \mathbf{d}_{\Gamma^{\text{FSI}}}^s - \mathbf{d}_{\Gamma^{\text{FSI}}}^g \rangle_{\Gamma^{\text{FSI}}} = 0. \quad (4.5)$$

Addition to the kinematic coupling, the embedded fluid field and the structure field have to satisfy the dynamic equilibrium. The additional traction $\mathbf{h}_{\Gamma^{\text{FSI}}}^e$ of the embedded fluid field arising from the fluid-structure coupling acts on the fluid-structure interface Γ^{FSI} , reading

$$\mathbf{h}_{\Gamma^{\text{FSI}}}^e = \boldsymbol{\sigma}^e \cdot \mathbf{n}^e \quad \text{on} \quad \Gamma^{\text{FSI}} \times (0, T). \quad (4.6)$$

Furthermore, the traction $\mathbf{h}_{\Gamma^{\text{FSI}}}^s$ acts on the structural side of the fluid-structure interface Γ^{FSI} , which is defined as

$$\mathbf{h}_{\Gamma^{\text{FSI}}}^s = (\mathbf{F}\mathbf{S}) \cdot \mathbf{N}^s \quad \text{on} \quad \Gamma^{\text{FSI}} \times (0, T). \quad (4.7)$$

In order to satisfy the dynamic equilibrium at the fluid-structure interface it holds

$$\mathbf{h}_{\Gamma^{\text{FSI}}}^s = -\mathbf{h}_{\Gamma^{\text{FSI}}}^e \quad \text{on} \quad \Gamma^{\text{FSI}} \times (0, T). \quad (4.8)$$

Multiplication of the traction acting on the structural side of the fluid-structure interface with the virtual displacements $\delta\mathbf{d}^s$, results in the interface coupling contribution on the structure side

$$\delta W_{\Gamma^{\text{FSI}}}^s = \langle \delta\mathbf{d}^s, \mathbf{h}_{\Gamma^{\text{FSI}}}^s \rangle_{\Gamma^{\text{FSI}}}. \quad (4.9)$$

Moreover, the contribution of the influence of the interface coupling on the fluid field reads as

$$\delta W_{\Gamma^{\text{FSI}}}^{\text{f}} = \langle \mathbf{v}^e, \mathbf{h}_{\Gamma^{\text{FSI}}}^e \rangle_{\Gamma^{\text{FSI}}}. \quad (4.10)$$

By replacing the Lagrange multiplier field $\boldsymbol{\lambda}$ with the interface traction onto the structure field, the interface coupling terms (4.9) and (4.10) can be rewritten as

$$\delta W_{\Gamma^{\text{FSI}}}^{\text{s}} = \langle \delta \mathbf{d}^{\text{s}}, \boldsymbol{\lambda} \rangle_{\Gamma^{\text{FSI}}} \quad (4.11)$$

and

$$\delta W_{\Gamma^{\text{FSI}}}^{\text{f}} = - \langle \mathbf{v}^e, \boldsymbol{\lambda} \rangle_{\Gamma^{\text{FSI}}}. \quad (4.12)$$

The associated solution and test function spaces \mathcal{W}_λ and \mathcal{V}_λ are defined as

$$\mathcal{W}_\lambda := \{ \boldsymbol{\lambda} \in [\mathbf{H}^{-1/2}(\Gamma^{\text{FSI}})]^3 \}, \quad (4.13)$$

$$\mathcal{V}_\lambda := \{ \delta \boldsymbol{\lambda} \in [\mathbf{H}^{-1/2}(\Gamma^{\text{FSI}})]^3 \}. \quad (4.14)$$

Considering the discrete formulation of the stabilized embedded fluid formulation (3.135), the weak formulation of structure field (2.17), and coupling conditions at the fluid-structure interface, the semi-discrete weak formulation of the coupled FSI system reads as:

Find $(\mathbf{u}_h^e, p_h^e) \in V_h^e \times Q_h^e$, $(\mathbf{u}_h^b, p_h^b) \in V_h^b \times Q_h^b$, $\mathbf{d}_h^{\text{s}} \in V_h^{\text{s}}$ and $\boldsymbol{\lambda}_h \in V_h^\lambda$ such that $\forall (\mathbf{v}_h^e, q_h^e) \in V_h^e \times Q_h^e$, $\forall (\mathbf{v}_h^b, q_h^b) \in V_h^b \times Q_h^b$, $\forall (\delta \mathbf{d}_h^{\text{s}}) \in V_h^{\text{s}}$ and $\forall (\delta \boldsymbol{\lambda}_h) \in V_h^\lambda$ holds

$$\begin{aligned}
 & \boxed{1} \quad \left(\mathbf{v}_h^b, \rho^{\text{f}} \frac{\partial \mathbf{u}_h^b}{\partial t} \Big|_x \right)_{\Omega^b} + \left(\mathbf{v}_h^b, \rho^{\text{f}} \mathbf{u}_h^b \cdot \nabla \mathbf{u}_h^b \right)_{\Omega^b} \\
 & \boxed{2} \quad + \left(q_h^b, \nabla \cdot \mathbf{u}_h^b \right)_{\Omega^b} - \left(\nabla \cdot \mathbf{v}_h^b, p_h^b \right)_{\Omega^b} + \left(\boldsymbol{\epsilon}(\mathbf{v}_h^b), 2\mu \boldsymbol{\epsilon}(\mathbf{u}_h^b) \right)_{\Omega^b} \\
 & \boxed{3} \quad + \left(\mathbf{v}_h^e, \rho^{\text{f}} \frac{\partial \mathbf{u}_h^e}{\partial t} \Big|_x \right)_{\Omega^e} + \left(\mathbf{v}_h^e, \rho^{\text{f}} \mathbf{u}_h^e \cdot \nabla \mathbf{u}_h^e \right)_{\Omega^e} \\
 & \boxed{4} \quad + \left(q_h^e, \nabla \cdot \mathbf{u}_h^e \right)_{\Omega^e} - \left(\nabla \cdot \mathbf{v}_h^e, p_h^e \right)_{\Omega^e} + \left(\boldsymbol{\epsilon}(\mathbf{v}_h^e), 2\mu \boldsymbol{\epsilon}(\mathbf{u}_h^e) \right)_{\Omega^e} \\
 & \boxed{5} \quad + \langle \llbracket \mathbf{v}_h \rrbracket, p_h^e \cdot \mathbf{n} \rangle_{\Gamma^{\text{FF}}} - \langle \llbracket \mathbf{v}_h \rrbracket, 2\mu \boldsymbol{\epsilon}(\mathbf{u}_h^e) \cdot \mathbf{n} \rangle_{\Gamma^{\text{FF}}} \\
 & \boxed{6} \quad - \langle q_h^e \cdot \mathbf{n}, \llbracket \mathbf{u}_h \rrbracket \rangle_{\Gamma^{\text{FF}}} - \langle 2\mu \boldsymbol{\epsilon}(\mathbf{v}_h^e) \cdot \mathbf{n}, \llbracket \mathbf{u}_h \rrbracket \rangle_{\Gamma^{\text{FF}}} \\
 & \boxed{7} \quad + \langle \alpha' \llbracket \mathbf{v}_h \rrbracket, \llbracket \mathbf{u}_h \rrbracket \rangle_{\Gamma^{\text{FF}}} \\
 & \boxed{8} \quad - \langle \rho^{\text{f}}(\boldsymbol{\beta}_h \cdot \mathbf{n}) \{ \mathbf{v}_h \}_m, \llbracket \mathbf{u}_h \rrbracket \rangle_{\Gamma^{\text{FF}}} + \gamma_{\text{adv}} \langle \rho^{\text{f}} | \boldsymbol{\beta}_h \cdot \mathbf{n} | \llbracket \mathbf{v}_h \rrbracket, \llbracket \mathbf{u}_h \rrbracket \rangle_{\Gamma^{\text{FF}}} \\
 & \boxed{9} \quad + \sum_{F \in \mathcal{F}_G} \langle \alpha_{\text{GP}} \cdot \mu h_F \llbracket \nabla \mathbf{v}_h^b \rrbracket, \llbracket \nabla \mathbf{u}_h^b \rrbracket \rangle_{\mathcal{F}_G} \\
 & \boxed{10} \quad + \sum_{F \in \mathcal{F}_G} [\langle \gamma_{\text{p}} \llbracket \nabla q_h^b \rrbracket, \llbracket \nabla p_h^b \rrbracket \rangle_{\mathcal{F}_G} + \langle \gamma_{\text{s}} h_F^2 \rho^{\text{f}} \cdot | \mathbf{u}_h^b \cdot \mathbf{n}^F | \llbracket \nabla \mathbf{v}_h^b \rrbracket, \llbracket \nabla \mathbf{u}_h^b \rrbracket \rangle_{\mathcal{F}_G}] \\
 & \boxed{11} \quad + \sum_{\mathbf{e}} [\left(\mathbf{u}_h^b \cdot \nabla \mathbf{v}_h^b, \rho^{\text{f}} \tau_b^m \mathbf{r}_h^{m,b} \right)_{\Omega^b} + \left(\nabla q_h^b, \tau_b^m \mathbf{r}_h^{m,b} \right)_{\Omega^b} + \left(\nabla \cdot \mathbf{v}_h^b, \tau_b^c \mathbf{r}_h^{c,b} \right)_{\Omega^b}] \\
 & \boxed{12} \quad + \sum_{\mathbf{e}} [\left(\mathbf{u}_h^e \cdot \nabla \mathbf{v}_h^e, \rho^{\text{f}} \tau_e^m \mathbf{r}_h^{m,e} \right)_{\Omega^e} + \left(\nabla q_h^e, \tau_e^m \mathbf{r}_h^{m,e} \right)_{\Omega^e} + \left(\nabla \cdot \mathbf{v}_h^e, \tau_e^c \mathbf{r}_h^{c,e} \right)_{\Omega^e}] \\
 & \boxed{13} \quad - \langle \mathbf{v}_h^b, \bar{\mathbf{h}}^b \rangle_{\partial \Omega_N^b} - \left(\mathbf{v}_h^b, \rho^{\text{f}} \mathbf{b}^b \right)_{\Omega^b} - \left(\mathbf{v}_h^e, \rho^{\text{f}} \mathbf{b}^e \right)_{\Omega^e} + \langle \mathbf{v}_h^e, \boldsymbol{\lambda}_h \rangle_{\Gamma^{\text{FSI}}} = 0,
 \end{aligned} \quad (4.15a)$$

$$\begin{aligned}
 (\delta \mathbf{d}_h^s, \rho^s \ddot{\mathbf{d}}_h^s)_{\Omega^s} + (\text{Grad } \delta \mathbf{d}_h^s, \mathbf{F}^s)_{\Omega^s} - (\delta \mathbf{d}_h^s, \rho^s \mathbf{b}^s)_{\Omega^s} - \langle \delta \mathbf{d}_h^s, \bar{\mathbf{h}}^s \rangle_{\partial \Omega_N^s} \\
 - \langle \delta \mathbf{d}_h^s, \boldsymbol{\lambda}_h \rangle_{\Gamma^{\text{FSI}}} = 0,
 \end{aligned} \tag{4.15b}$$

$$\left\langle \delta \boldsymbol{\lambda}_h, \mathbf{d}_{h, \Gamma^{\text{FSI}}}^s - \mathbf{d}_{h, \Gamma^{\text{FSI}}}^g \right\rangle_{\Gamma^{\text{FSI}}} = 0 \tag{4.15c}$$

with

$$\mathbf{r}_h^{m,b} = \rho^f \frac{\partial \mathbf{u}_h^b}{\partial t} \Big|_{\mathbf{x}} + \rho^f \mathbf{u}_h^b \cdot \nabla \mathbf{u}_h^b + \nabla p_h^b - 2\mu \nabla \cdot \boldsymbol{\epsilon}(\mathbf{u}_h^b) - \rho^f \mathbf{b}^b, \tag{4.16}$$

$$\mathbf{r}_h^{m,e} = \rho^f \frac{\partial \mathbf{u}_h^e}{\partial t} \Big|_{\mathbf{x}} + \rho^f \mathbf{c}_h \cdot \nabla \mathbf{u}_h^e + \nabla p_h^e - 2\mu \nabla \cdot \boldsymbol{\epsilon}(\mathbf{u}_h^e) - \rho^f \mathbf{b}^e, \tag{4.17}$$

$$\mathbf{r}_h^{c,b} = \nabla \cdot \mathbf{u}_h^b, \tag{4.18}$$

$$\mathbf{r}_h^{c,e} = \nabla \cdot \mathbf{u}_h^e. \tag{4.19}$$

In (4.15), equal-order continuous approximations on linear hexahedral elements for all velocity components, u_h^i, v_h^i , ($i = 1, 2, 3$), the pressure fields, p_h, q_h , of both fluid subdomains, and all displacement components, $d_h^i, \delta d_h^i$, ($i = 1, 2, 3$), are used such that

$$\mathbf{v}_h^b, \mathbf{u}_h^b \in V_h^b := \{ \mathbf{v} \in [C^0(\Omega^b)]^3 : \mathbf{v}|_V \in [Q^1(K)]^3 \forall V \in \Omega_K^b, \forall K \in \mathcal{T}^* \}, \tag{4.20}$$

$$q_h^b, p_h^b \in Q_h^b := \{ q \in C^0(\Omega^b) : q|_V \in Q^1(K) \forall V \in \Omega_K^b, \forall K \in \mathcal{T}^* \}, \tag{4.21}$$

$$\mathbf{v}_h^e, \mathbf{u}_h^e \in V_h^e := \{ \mathbf{v} \in [C^0(\Omega^e)]^3 : \mathbf{v}|_K \in [Q^1(K)]^3 \forall K \in \mathcal{T}^e \}, \tag{4.22}$$

$$q_h^e, p_h^e \in Q_h^e := \{ q \in C^0(\Omega^e) : q|_K \in Q^1(K) \forall K \in \mathcal{T}^e \}, \tag{4.23}$$

$$\delta \mathbf{d}_h^s, \mathbf{d}_h^s \in V_h^d := \{ \mathbf{v} \in [C^0(\Omega^s)]^3 : \mathbf{v}|_K \in [Q^1(K)]^3 \forall K \in \mathcal{T}^s \}. \tag{4.24}$$

Hereby, \mathcal{T}^* denotes the set of elements which lie in the physical background fluid unified with the set of cut elements, see Figure 3.3, and $Q^1(K)$ defines a polynomial of order at most 1 on a 3D element K , which are used in this work. It has to be emphasized that there are no restrictions regarding the choice of element type or the polynomial order. Thus, any other type of elements with other polynomial order can also be used. For $\delta \boldsymbol{\lambda}_h, \boldsymbol{\lambda}_h$ from the discrete function space V_h^λ it holds

$$\delta \boldsymbol{\lambda}_h, \boldsymbol{\lambda}_h \in V_h^\lambda := \{ \mathbf{v} \in [C^0(\Gamma^{\text{FSI}})]^3 : \mathbf{v}|_{\Gamma_K} \in [Q^1(\Gamma_K)]^3 \forall \Gamma_K \in \Gamma_K^{\text{FSI}} \}, \tag{4.25}$$

where $Q^1(\Gamma_K)$ denotes the polynomial of at most one on the fluid-structure interface segments Γ_K^{FSI} . The semi-discrete embedded fluid formulation, which has been developed step by step in Chapter 3, is given in (4.15a). The first four lines of (4.15a) refer to the standard Galerkin terms of the background and embedded fluid subdomains. The next three lines correspond to the embedded fluid weighting of Nitsche's formulation. The line eight refers to the convective inflow stabilization terms at the fluid-fluid interface Γ^{FF} described in Section 3.4. Furthermore, the ghost-penalty and the pressure and velocity face-oriented stabilizations at the faces of the cut elements of the background fluid mesh are stated at lines nine and ten. The classical residual-based stabilizations (SUPG, PSPG and grad-div stabilizations) at lines eleven and twelve, which have been introduced in Section 2.3.9, are used on both fluid subdomains to overcome the convective and inf-sup fluid instabilities. The last term at the left side of (4.15a) refers to the contribution of

the influence of the interface coupling on the fluid field. It has to be pointed out that in (4.15a) the combination of the residual-based and face-oriented stabilizations are used, i.e. the face-oriented stabilizations are just added at the cut elements of the background fluid subdomain to overcome the fluid instabilities on cut elements.

The structural semi-discrete weak formulation is stated in (4.15b). The last term refers to the traction acting on the structural side of the fluid-structure interface Γ^{FSI} .

Finally, the kinematic coupling is given in (4.15c).

The coupled semi-discrete formulation (4.15) needs to be discretized in time, which can be performed separately for each field. As shown in the previous chapter, the time discretization of the fluid field is performed using one-step- θ scheme. The discretization of the structure field in time is presented in Section 2.2.5 using generalized- α scheme, Chung and Hulbert [49]. In the next section, the linearization of the coupled FSI system will be discussed.

4.3 Linearization of coupled FSI system

The solution of the nonlinear FSI problem can be performed by solving the residual of the nonlinear problem

$$\mathbf{r}^{\text{FSI}} = \begin{bmatrix} \mathbf{r}^{\text{s}} \\ \mathbf{r}^{\text{ff}} \\ \mathbf{r}^{\text{kin}} \end{bmatrix} = 0, \quad (4.26)$$

as introduced by Mayr et al. [135]. The residual \mathbf{r}^{FSI} contains the residuals of the structure field \mathbf{r}^{s} , fluid field \mathbf{r}^{ff} and the residual of the kinematic coupling condition, denoted as \mathbf{r}^{kin} . As shown in Sections 2.2.6 for the structure field, and in Sections 2.3.10 and 3.8, for a single fluid field and the coupled fluid-fluid system, respectively, the Newton-Raphson method is applied to solve the nonlinear systems of equations, which requires the full linearization of the nonlinear equations. After linearization the following linear system has to be solved in every iteration step i of the Newton-Raphson method

$$\begin{bmatrix} \frac{\partial \mathbf{r}_{\text{d}^{\text{s}}}^{\text{s}}}{\partial \mathbf{d}^{\text{s}}} & 0 & \frac{\partial \mathbf{r}_{\lambda}^{\text{s}}}{\partial \lambda} \\ 0 & \frac{\partial \mathbf{r}_{\mathbf{x}^{\text{ff}}}^{\text{ff}}}{\partial \mathbf{x}^{\text{ff}}} & \frac{\partial \mathbf{r}_{\lambda}^{\text{ff}}}{\partial \lambda} \\ \frac{\partial \mathbf{r}^{\text{kin}}}{\partial \mathbf{d}_{\Gamma^{\text{FSI}}}^{\text{s}}} & \frac{\partial \mathbf{r}^{\text{kin}}}{\partial \mathbf{u}_{\Gamma^{\text{FSI}}}^{\text{e}}} & 0 \end{bmatrix}_i^{n+1} \begin{bmatrix} \Delta \mathbf{d}^{\text{s}} \\ \Delta \mathbf{x}^{\text{ff}} \\ \Delta \lambda \end{bmatrix}_{i+1}^{n+1} = - \begin{bmatrix} \mathbf{r}^{\text{s}} \\ \mathbf{r}^{\text{ff}} \\ \mathbf{r}^{\text{kin}} \end{bmatrix}_i^{n+1}, \quad (4.27)$$

at time step t^{n+1} . In (4.27), the matrix contribution $\frac{\partial \mathbf{r}_{\text{d}^{\text{s}}}^{\text{s}}}{\partial \mathbf{d}^{\text{s}}}$ refers to the linearization of the structure equations as shown in Section 2.2.6. The matrix contribution $\frac{\partial \mathbf{r}_{\mathbf{x}^{\text{ff}}}^{\text{ff}}}{\partial \mathbf{x}^{\text{ff}}}$ deals with the linearization of the discrete embedded fluid formulation with \mathbf{x}^{ff} being an abbreviation referring to the discrete fluid quantities $\mathbf{u}^{\text{b}}, \mathbf{u}^{\text{e}}, \mathbf{p}^{\text{b}}, \mathbf{p}^{\text{e}}$ and \mathbf{d}^{g} , representing the nodal velocities and pressure of both fluid subdomains, and the ALE displacements, respectively. Other matrix contributions denote the kinematic and dynamic interface coupling conditions, which will be explained in Section 4.3.3. For sake of shortening the notations, in the following, Γ^{FSI} is replaced with Γ , as the fluid-fluid interface Γ^{FF} is an internal fluid interface hidden in the fluid field and does not affect the FSI coupling directly. Furthermore, to prepare the coupling at the fluid-structure interface, as e.g. in Klöppel et al. [117] and Mayr et al. [135], a split of quantities into degrees of freedom at the fluid-structure interface and the internal degrees of interface, i.e. the quantities far from the

interface, is introduced. Considering this new split of quantities, in the forthcoming sections, the matrix contributions of (4.27) are discussed in detail.

4.3.1 Modified structure field

The structural residuals can be written as

$$\mathbf{r}^s = \mathbf{r}_{d^s}^s + \mathbf{r}_\lambda^s = \begin{bmatrix} \mathbf{r}_I^s \\ \mathbf{r}_\Gamma^s \end{bmatrix} + \begin{bmatrix} \mathbf{0} \\ \mathbf{r}_{\lambda,\Gamma}^s \end{bmatrix}, \quad (4.28)$$

where the first part refers to the standard structure terms and the second term accounts for the fluid-structure coupling. The linearization of the structural residuals, results in the structural matrix \mathbf{S} , as given in (2.34), which is denoted as $\frac{\partial \mathbf{r}_{d^s}^s}{\partial \mathbf{d}^s}$ in (4.27). Considering, the split into interior degrees of freedom far from the fluid-structure interface, denoted by $(\cdot)_I$, and interface degrees of freedom, denoted by $(\cdot)_\Gamma$, the linear system for structure field without considering the FSI-coupling terms reads as

$$\begin{bmatrix} \mathbf{S}_{II} & \mathbf{S}_{I\Gamma} \\ \mathbf{S}_{\Gamma I} & \mathbf{S}_{\Gamma\Gamma} \end{bmatrix}_i^{n+1} \begin{bmatrix} \Delta \mathbf{d}_I^s \\ \Delta \mathbf{d}_\Gamma^s \end{bmatrix}_{i+1}^{n+1} = - \begin{bmatrix} \mathbf{r}_I^s \\ \mathbf{r}_\Gamma^s \end{bmatrix}_i^{n+1}. \quad (4.29)$$

Hereby, \mathbf{S}_{jk} represents the structural stiffness matrix defined as

$$\mathbf{S}_{jk} = \frac{\partial \mathbf{r}_j^s}{\partial \mathbf{d}_k^s} \quad (4.30)$$

with $j, k \in \{I, \Gamma\}$.

4.3.2 Modified fluid field

In the following, the linearization of the fluid residual $\mathbf{r}_{u,p}^{\text{ff}}(\mathbf{u}^b, \mathbf{p}^b, \mathbf{u}^e, \mathbf{p}^e, \mathbf{d}^g)$, identified as $\frac{\partial \mathbf{r}_{u,p}^{\text{ff}}}{\partial \mathbf{x}^{\text{ff}}}$ in (4.27), will be discussed. The nonlinear fluid residual can be written as

$$\mathbf{r}^{\text{ff}} = \mathbf{r}_{u,p}^{\text{ff}} + \mathbf{r}_\lambda^{\text{ff}} = \begin{bmatrix} \mathbf{r}_I^{\text{ff}} \\ \mathbf{r}_\Gamma^{\text{ff}} \\ \mathbf{r}_I^g \\ \mathbf{r}_\Gamma^g \end{bmatrix} + \begin{bmatrix} \mathbf{0} \\ \mathbf{r}_{\lambda,\Gamma}^{\text{ff}} \\ \mathbf{0} \\ \mathbf{0} \end{bmatrix}, \quad (4.31)$$

with $\mathbf{r}_{u,p}^{\text{ff}}$ referring to standard fluid residuals and $\mathbf{r}_{\lambda,\Gamma}^{\text{ff}}$ containing the fluid-structure coupling contributions. As in the previous section, a split of quantities into interior degrees of freedom of the entire fluid domain, i.e. the interior degrees of freedom of embedded fluid subdomain Ω^e and whole degrees of freedom of background fluid subdomain Ω^b (denoted by $(\cdot)_I$), and the degrees of freedom of embedded fluid subdomain Ω^e at the fluid-structure interface (denoted by $(\cdot)_\Gamma$), has been applied. The nodal pressure values of both fluid subdomains are merged into the interior velocities, such that the interface values just contain the fluid velocities. The vector of inner and interface quantities are, thus, defined as

$$\mathbf{u}_I^{\text{ff}} := \begin{bmatrix} \mathbf{u}^b \\ \mathbf{p}^b \\ \mathbf{u}_I^e \\ \mathbf{p}^e \end{bmatrix} \quad (4.32)$$

and

$$\mathbf{u}_\Gamma^{\text{ff}} := \begin{bmatrix} \mathbf{u}_\Gamma^{\text{e}} \end{bmatrix}, \quad (4.33)$$

respectively. Considering the aforementioned split, the linear system for the entire fluid field reads as

$$\begin{bmatrix} \mathbf{F}_{\text{II}}^{\text{ff}} & \mathbf{F}_{\text{I}\Gamma}^{\text{ff}} & \mathbf{F}_{\text{II}}^{\text{g}} & \mathbf{F}_{\text{I}\Gamma}^{\text{g}} \\ \mathbf{F}_{\text{I}\Gamma}^{\text{ff}} & \mathbf{F}_{\text{I}\Gamma}^{\text{ff}} & \mathbf{F}_{\text{I}\Gamma}^{\text{g}} & \mathbf{F}_{\text{I}\Gamma}^{\text{g}} \end{bmatrix}_i^{n+1} \begin{bmatrix} \Delta \mathbf{u}_\text{I}^{\text{ff}} \\ \Delta \mathbf{u}_\text{I}^{\text{ff}} \\ \Delta \mathbf{d}_\text{I}^{\text{g}} \\ \Delta \mathbf{d}_\text{I}^{\text{g}} \end{bmatrix}_{i+1}^{n+1} = - \begin{bmatrix} \mathbf{r}_\text{I}^{\text{ff}} \\ \mathbf{r}_\text{I}^{\text{ff}} \end{bmatrix}_i^{n+1}. \quad (4.34)$$

Hereby, $\mathbf{F}_{jk}^{\text{ff}}$ with $j, k \in \{\text{I}, \Gamma\}$ represents the matrix contributions of the stabilized embedded fluid formulation, given in (3.144). However, the embedded fluid system also depends on embedded fluid grid motion, which is computed based on the fluid grid displacements at the interface, as proposed in Section 2.4. Thus, the fluid system has to be extended by the *shape derivatives*, denoted by $\mathbf{F}_{jk}^{\text{g}}$ with $j, k \in \{\text{I}, \Gamma\}$, which present the derivatives of the fluid residuals \mathbf{r}^{ff} with respect to grid displacements of the embedded fluid \mathbf{d}^{g} . The shape derivatives are discussed in Fernández and Moubachir [71] in detail.

Moreover, considering the split mentioned above, the linear system of the mesh motion of the ALE field, given in (2.106), which is a pure Dirichlet boundary problem, can be rewritten as

$$\begin{bmatrix} \mathbf{A}_{\text{II}} & \mathbf{A}_{\text{I}\Gamma} \end{bmatrix}_i^{n+1} \begin{bmatrix} \Delta \mathbf{d}_\text{I}^{\text{g}} \\ \Delta \mathbf{d}_\text{I}^{\text{g}} \end{bmatrix}_{i+1}^{n+1} = 0. \quad (4.35)$$

The mesh displacements $\mathbf{d}_\Gamma^{\text{g}}$ follow the motion of the embedded fluid field at the fluid-structure interface and the inner displacements of the $\mathbf{d}_\text{I}^{\text{g}}$ are influenced by them. Since the vectors of mesh motion of the embedded fluid field, $\Delta \mathbf{d}_\text{I}^{\text{g}}$ and $\Delta \mathbf{d}_\text{I}^{\text{g}}$, appear in (4.34) as well as in (4.35), both systems can be combined to

$$\begin{bmatrix} \mathbf{F}_{\text{II}}^{\text{ff}} & \mathbf{F}_{\text{I}\Gamma}^{\text{ff}} & \mathbf{F}_{\text{II}}^{\text{g}} & \mathbf{F}_{\text{I}\Gamma}^{\text{g}} \\ \mathbf{F}_{\text{I}\Gamma}^{\text{ff}} & \mathbf{F}_{\text{I}\Gamma}^{\text{ff}} & \mathbf{F}_{\text{I}\Gamma}^{\text{g}} & \mathbf{F}_{\text{I}\Gamma}^{\text{g}} \\ 0 & 0 & \mathbf{A}_{\text{II}} & \mathbf{A}_{\text{I}\Gamma} \end{bmatrix}_i^{n+1} \begin{bmatrix} \Delta \mathbf{u}_\text{I} \\ \Delta \mathbf{u}_\text{I} \\ \Delta \mathbf{d}_\text{I}^{\text{g}} \\ \Delta \mathbf{d}_\text{I}^{\text{g}} \end{bmatrix}_{i+1}^{n+1} = - \begin{bmatrix} \mathbf{r}_\text{I}^{\text{ff}} \\ \mathbf{r}_\text{I}^{\text{ff}} \\ 0 \end{bmatrix}_i^{n+1}. \quad (4.36)$$

In (4.36), the relation between the interface velocity \mathbf{u}_Γ and the ALE displacements at the interface $\mathbf{d}_\Gamma^{\text{g}}$ is still missing, and will be introduced in the following section.

4.3.3 Fluid-structure coupling conditions

In order to complete the coupled system (4.27), the contributions of kinematic and dynamic coupling conditions on the fluid-structure interface, $\frac{\partial \mathbf{r}^{\text{kin}}}{\partial \mathbf{d}_\Gamma^{\text{s}}}$, $\frac{\partial \mathbf{r}^{\text{kin}}}{\partial \mathbf{u}_\Gamma^{\text{e}}}$, and $\frac{\partial \mathbf{r}_\lambda^{\text{s}}}{\partial \lambda}$, $\frac{\partial \mathbf{r}_\lambda^{\text{ff}}}{\partial \lambda}$, respectively, need to be considered. In the following, first, the kinematic coupling conditions and afterwards the dynamic coupling conditions will be discussed.

Fluid-structure coupling - Kinematic

Following Mayr et al. [135], assigning the kinematic coupling conditions at the fluid-structure interface is performed in three steps. The first step refers to the coupling between the embedded

fluid velocities u_{Γ}^e and the ALE displacements d_{Γ}^g . This coupling takes place inside the embedded fluid subdomain and the FSI coupling is not affected by it. The next step is the coupling between structural displacements at the interface d_{Γ}^s and the ALE displacements at the interface d_{Γ}^g . The combination of these two coupling conditions results in the coupling of fluid velocities and the structural displacements at the interface, u_{Γ}^e and d_{Γ}^s , respectively. An illustration of the kinematic coupling condition is given by Mayr et al. [135]. In the following, this process is explained.

Following Förster [73], an accurate conservation of the size of the embedded fluid subdomain Ω^e requires a consistent conversion of the interface fluid velocities and the interface ALE displacements with the fluid time discretization scheme. As mentioned above, the one-step- θ time discretization scheme is applied to the fluid field, which can be considered to have an average acceleration within the time step t^n to t^{n+1} . Following Förster [73], the interface ALE displacements yield from integrating the average acceleration twice, which is a second order accurate transformation of the ALE displacements at the interface, reading

$$d_{\Gamma}^{g,n+1} - d_{\Gamma}^{g,n} = \frac{\Delta t}{2}(u_{\Gamma}^{ff,n+1} + u_{\Gamma}^{ff,n}). \quad (4.37)$$

The relation (4.37) can be interpreted as a trapezoidal rule for the transformation of interface velocities to ALE displacements. As the trapezoidal rule has the property that it tents to oscillations, the backward Euler scheme, which is first order accurate, can also be used alternatively, see Förster [73],

$$d_{\Gamma}^{g,n+1} - d_{\Gamma}^{g,n} = \Delta t u_{\Gamma}^{ff,n+1}. \quad (4.38)$$

Equations (4.37) and (4.38) can be combined to a single equation expressed by solution increments as

$$\Delta d_{\Gamma,i+1}^{g,n+1} = \tau \Delta u_{\Gamma,i+1}^{ff,n+1} + \delta_{i0} \Delta t u_{\Gamma}^{ff,n}, \quad (4.39)$$

where the parameter τ can be chosen as $\frac{\Delta t}{2}$ for trapezoidal rule and as Δt for Backward Euler scheme. The Kronecker delta δ_{i0} indicates that this contribution is just added in the first iteration step of the Newton step, $i = 0$.

The coupling between structural interface displacements d_{Γ}^s and the ALE interface displacements d_{Γ}^g is given in (4.15c). The linearization of it results in the following kinematic coupling constraint in an incremental formulation

$$C_{SF} \Delta d_{\Gamma,i+1}^{s,n+1} - C_{FS} \Delta d_{\Gamma,i+1}^{g,n+1} = 0 \quad (4.40)$$

with the FSI coupling matrices, C_{SF} and C_{FS} , which will be explained in Section 4.4. Following Mayr et al. [135], possible structure predictors are added to (4.40) as

$$C_{SF} \Delta d_{\Gamma,i+1}^{s,n+1} - C_{FS} \Delta d_{\Gamma,i+1}^{g,n+1} = -\delta_{i0} C_{SF} \Delta d_{\Gamma,p}^s. \quad (4.41)$$

Hereby, $\Delta d_{\Gamma,p}^s$ indicates the structure predictor, which can be employed to find a starting guess for the interface displacements in the new time step and, thus, it is just necessary to be considered in first nonlinear iteration.

Combining the two discrete conditions (4.39) and (4.41) leads to the direct conversion of the embedded fluid interface velocities and the displacement of the structure at the fluid-structure interface. By replacing the displacement of the ALE field in (4.39) the final discrete kinematic coupling condition is obtained in the incremental formulation, reading

$$C_{SF} \Delta d_{\Gamma,i+1}^{s,n+1} + \delta_{i0} C_{SF} \Delta d_{\Gamma,p}^s = \tau C_{FS} \Delta u_{\Gamma,i+1}^{ff,n+1} + \delta_{i0} \Delta t C_{FS} u_{\Gamma}^{ff,n}. \quad (4.42)$$

Fluid-structure coupling - Dynamics

In the following, the interface tractions, which are included in the semi-discrete formulations (4.15a) and (4.15b), will be discussed. In the global system (4.27) these terms are denoted as $\frac{\partial r_\lambda^s}{\partial \lambda}$ and $\frac{\partial r_\lambda^{\text{ff}}}{\partial \lambda}$.

As mentioned above, in the present work, different time discretization schemes are applied for fluid and structure fields. For the time discretization of the structure field the generalized- α and for the fluid field the one-step- θ approach are employed. Thus, depending on the time-integration scheme of each field, the dynamic equilibria of fluid and structure field are evaluated at different time points, which in general not coincide. Mayr et al. [135] proposed an approach by keeping the freedom of choosing different time-integration schemes for each field, independently, but achieving a temporal consistency between both fields. Following Mayr et al. [135], to obtain the dynamic equilibrium at the same time level, the time-integration schemes of both fields are evaluated at intermediate time levels indicated by superscript $(\cdot)^m$. Hence, the discrete residual contributions r_λ^s and r_λ^{ff} from the weak forms (4.12) and (4.11) at the intermediate time level can be written as

$$r_\lambda^{s,m} = -C_{\text{SF}}^T(\lambda^{s,m}), \quad (4.43)$$

$$r_\lambda^{\text{ff},m} = C_{\text{FS}}^T(\lambda^{\text{f},m}), \quad (4.44)$$

with the nodal FSI coupling matrices, which will be explained in Section 4.4. Using linear interpolations, the discrete residuals (4.43) and (4.44) can be expressed in terms of known quantities λ^n from the last time step and the unknown nodal quantities λ_i^{n+1} as

$$r_{\lambda,i}^{s,m} = -C_{\text{SF}}^T(a\lambda^n + (1-a)\lambda_i^{n+1}), \quad (4.45)$$

$$r_{\lambda,i}^{\text{ff},m} = C_{\text{FS}}^T(b\lambda^n + (1-b)\lambda_i^{n+1}). \quad (4.46)$$

Hereby, the parameters a and b indicate the time interpolation factors, which depend on the applied time-integration scheme in the single fields. Considering the one-step- θ time-integration schemes (2.64), which is applied to the fluid field, for the time interpolation factor b holds: $b = 1 - \theta$. For generalized- α , applied to structure field, as given in (2.26), the time interpolation factor has to be chosen as $a = \alpha_f$. The discrete residuals (4.45) and (4.46) need to be linearized due to the additional unknown λ_i^{n+1} , resulting in

$$\frac{\partial r_{\lambda,i}^{s,m}}{\partial \lambda_i^{n+1}} = -(1-a)C_{\text{SF}}^T, \quad (4.47)$$

$$\frac{\partial r_{\lambda,i}^{\text{ff},m}}{\partial \lambda_i^{n+1}} = (1-b)C_{\text{FS}}^T, \quad (4.48)$$

which complete the linear system (4.27). In the following section, the final monolithic FSI system is presented.

4.4 Monolithic FSI system

The global monolithic linear system will be assembled from the linearization of the contributions given in the previous section. The global monolithic system, which has to be solved in every

and the corresponding global incremental solution vector and the residual vector,

$$\Delta x_{i+1}^{n+1} = \begin{bmatrix} \Delta d_I^s \\ \Delta d_\Gamma^s \\ \Delta u_I^{ff} \\ \Delta u_\Gamma^{ff} \\ \Delta d_I^g \\ \lambda \end{bmatrix}_{i+1}^{n+1} \quad (4.52b)$$

and

$$r_i^{FSI,n+1} = \begin{bmatrix} r_I^s \\ r_\Gamma^s \\ r_I^{ff} \\ r_\Gamma^{ff} \\ 0 \\ 0 \end{bmatrix}_i^{n+1} + \begin{bmatrix} 0 \\ -a C_{SF}^T \lambda^n \\ 0 \\ b C_{FS}^T \lambda^n \\ 0 \\ 0 \end{bmatrix}_i^{n+1} + \delta_{i0} \begin{bmatrix} 0 \\ 0 \\ \Delta t F_{II}^g u_\Gamma^{ff,n} \\ \Delta t F_{\Gamma\Gamma}^g u_\Gamma^{ff,n} \\ \Delta t A_{II} u_\Gamma^{ff,n} \\ \Delta t C_{FS} u_\Gamma^{ff,n} - C_{SF} \Delta d_{\Gamma,p}^s \end{bmatrix}_i^{n+1}, \quad (4.52c)$$

respectively. Because of the zero block on the main diagonal of the Jacobian matrix (4.52a), the global monolithic linear system (4.52) is of saddle-point type, which is difficult to solve with some iterative solvers. In order to be able to use the available efficient linear solvers for FSI systems, as e.g. given in Gee et al. [81], the saddle-point structure of (4.52) has to be eliminated. For this purpose, the Lagrange multipliers λ_{i+1}^{n+1} have to be condensed from the system. This results in a linear system with only primary variables as unknowns, which is a desirable feature. The unknowns of the condensed system are: structure displacements, velocity and pressure fields of both fluid subdomains, and the grid displacement of the embedded fluid.

Furthermore, the motion of FSI interface can be expressed by degrees of freedom of the embedded fluid field or the structure field. Following Klöppel et al. [117], a fluid-expressed interface motion is referred to as *structure-split*, as a split of structural equations is required. On the other hand, a FSI interface motion expressed by structural degrees of freedom is called a *fluid-split*, since a split of fluid equations is needed. The field which expresses the motion of the FSI interface is called the master field, and the field with split equations the slave field, respectively. In the case of prescribing Dirichlet boundary condition at the fluid-structure interface, the choice of an appropriate split is important, since, for example, to prescribe the velocity field at the interface, a structure-split has to be performed as the interface motion is expressed by the velocity. As it will be shown in the following section, applying the kinematic coupling from Section 4.3.3 leads to condensation of the interface degrees of freedom of the slave field from the global system. Moreover, by applying the balance of linear momentum of the corresponding master field, the Lagrange multiplier unknown λ_{i+1}^{n+1} will be condensed from the FSI system.

Based on the assumption that the nodes of the embedded fluid and the structure match at the fluid-structure interface, the two coupling matrices C_{SF} and C_{FS} are replaced with the identity matrix I , see Küttler [120]. In the case of mortar-based FSI approach for non-matching grids at the interface, where the Lagrange multiplier field is discretized using the dual shape functions, the coupling matrices are the mortar matrices D , belonging to the slave side, and the M , belonging to the master side. The biorthogonality condition of the dual shape functions leads to diagonal form of matrix D . This property is very advantageous, since it allows a cheap inversion

of the matrix D , which is required in the condensation process. For more detail on mortar-based monolithic FSI approach the interested reader is referred to Klöppel [115], Klöppel et al. [117] and Mayr et al. [135].

In the forthcoming sections, the final FSI systems for the structure-split, i.e. the fluid-expressed interface motion, and the fluid-split, i.e. the structure-expressed interface motion, are presented.

4.4.1 Structure-split

As aforementioned, for a monolithic structure-split formulation the fluid degrees of freedom express the interface motion. The coupling of ALE displacement at the interface d_{Γ}^g to the interface motion is expressed in terms of interface fluid velocities. The discrete coupling of embedded fluid velocity and the structural displacement at the interface, given in (4.42), is used to eliminate the structural interface d_{Γ}^s . Solving (4.42) for the structural interface displacement and replacing C_{SF} and C_{FS} with the identity matrix leads to

$$\Delta d_{\Gamma,i+1}^{s,n+1} = \tau \Delta u_{\Gamma,i+1}^{ff,n+1} + \delta_{i0} \Delta t u_{\Gamma}^{ff,n} - \delta_{i0} \Delta d_{\Gamma,p}^s. \quad (4.53)$$

Using the balance of linear momentum of the structural interface degrees of freedoms (second row of (4.52)) and the equation above results in

$$\begin{aligned} \lambda^{n+1} = & -\frac{a}{1-a} \lambda^n + \frac{1}{1-a} (r_{\Gamma}^{s,n+1} + S_{\Gamma\Gamma} \Delta d_{\Gamma,i+1}^{s,n+1} + \tau S_{\Gamma\Gamma} \Delta u_{\Gamma,i+1}^{ff,n+1}) \\ & + \delta_{i0} \frac{1}{1-a} (\Delta t S_{\Gamma\Gamma} u_{\Gamma}^{ff,n} - S_{\Gamma\Gamma} \Delta d_{\Gamma,p}^s). \end{aligned} \quad (4.54)$$

The formulation (4.54) is used to recover the Lagrange multiplier unknown at the end of each time step. Using equations (4.53) and (4.54), the Lagrange multipliers can be condensed from the linear system. Then, the final condensed Jacobian, incremental solution vector and residual become

$$J_i^{\text{FSI},n+1} = \begin{bmatrix} S_{\text{II}} & & \tau S_{\text{I}\Gamma} & & \\ & F_{\text{II}}^{\text{ff}} & F_{\text{II}}^{\text{ff}} + \tau F_{\text{II}}^{\text{g}} & & F_{\text{II}}^{\text{g}} \\ \frac{1-b}{1-a} S_{\Gamma\text{I}} & F_{\Gamma\text{I}}^{\text{ff}} & \frac{1-b}{1-a} \tau S_{\Gamma\text{I}\Gamma} + F_{\Gamma\text{I}}^{\text{ff}} + \tau F_{\Gamma\text{I}}^{\text{g}} & & F_{\Gamma\text{I}}^{\text{g}} \\ & & \tau A_{\text{I}\Gamma} & & A_{\text{II}} \end{bmatrix}_i^{n+1}, \quad (4.55a)$$

$$\Delta x_{i+1}^{n+1} = \begin{bmatrix} \Delta d_{\Gamma}^s \\ \Delta u_{\Gamma}^{\text{ff}} \\ \Delta u_{\Gamma}^{\text{ff}} \\ \Delta d_{\Gamma}^g \end{bmatrix}_{i+1}^{n+1} \quad (4.55b)$$

and

$$\begin{aligned} r_i^{\text{FSI},n+1} = & \begin{bmatrix} r_{\Gamma}^s \\ r_{\Gamma}^{\text{ff}} \\ r_{\Gamma}^{\text{ff}} + \frac{1-b}{1-a} r_{\Gamma}^s \\ 0 \end{bmatrix}_i^{n+1} + \begin{bmatrix} 0 \\ 0 \\ (b - a \frac{1-b}{1-a}) \lambda^n \\ 0 \end{bmatrix} \\ & + \delta_{i0} \begin{bmatrix} \Delta t S_{\text{I}\Gamma} u_{\Gamma}^{\text{ff},n} - S_{\text{I}\Gamma} \Delta d_{\Gamma,p}^s \\ \Delta t F_{\text{II}}^{\text{g}} u_{\Gamma}^{\text{ff},n} \\ \Delta t F_{\Gamma\text{I}}^{\text{g}} u_{\Gamma}^{\text{ff},n} + \Delta t \frac{1-b}{1-a} S_{\Gamma\text{I}\Gamma} u_{\Gamma}^{\text{ff},n} - \frac{1-b}{1-a} S_{\Gamma\text{I}\Gamma} \Delta d_{\Gamma,p}^s \\ \Delta t A_{\text{I}\Gamma} u_{\Gamma}^{\text{ff},n} \end{bmatrix}. \end{aligned} \quad (4.55c)$$

4.4.2 Fluid-split

The other possibility to describe the interface motion are the structural displacements, i.e. a fluid-split formulation. In a fluid-split formulation the interface motion is expressed by structural interface displacements d_{Γ}^s . Again, discrete kinematic coupling condition (4.42), which is equal to the last row of the linear system (4.52) will be used to eliminate the fluid interface velocities u_{Γ}^{ff} . The equation (4.42) can be expressed by fluid velocities at the interface as

$$\Delta u_{\Gamma,i+1}^{\text{ff},n+1} = \frac{1}{\tau} \left(\Delta d_{\Gamma,i+1}^{\text{s},n+1} + \delta_{i0} (\Delta d_{\Gamma,p}^{\text{s}} - \Delta t u_{\Gamma}^{\text{ff},n}) \right), \quad (4.56)$$

at which the matrices C_{SF} and C_{FS} are replaced with the identity matrix, as described in Section 4.4. By replacing the equation above in the linear momentum of the fluid interface degrees of freedom (forth row of (4.52)), the unknown Lagrange multipliers can be expressed by

$$\begin{aligned} \lambda^{n+1} = & -\frac{b}{1-b} \lambda^n - \frac{1}{1-b} \left(r_{\Gamma}^{\text{ff},n+1} + \left(\frac{1}{\tau} F_{\Gamma\Gamma}^{\text{ff}} + F_{\Gamma\Gamma}^{\text{g}} \right) \Delta d_{\Gamma,i+1}^{\text{s},n+1} \right. \\ & + F_{\Gamma\Gamma}^{\text{ff}} \Delta u_{\Gamma,i+1}^{\text{ff},n+1} + F_{\Gamma\Gamma}^{\text{g}} \Delta d_{\Gamma,i+1}^{\text{g},n+1} \left. \right) - \delta_{i0} \frac{1}{1-b} \left(\left(\frac{1}{\tau} F_{\Gamma\Gamma}^{\text{ff}} + F_{\Gamma\Gamma}^{\text{g}} \right) \Delta d_{\Gamma,p}^{\text{s}} \right. \\ & \left. - \frac{\Delta t}{\tau} F_{\Gamma\Gamma}^{\text{ff}} u_{\Gamma}^{\text{ff},n} \right). \end{aligned} \quad (4.57)$$

The equation (4.57) is used to recover the Lagrange multiplier solution at the end of each time step. Using equations (4.56) and (4.57), the saddle-point structure of the linear system can be eliminated. The resulting condensed linear system with structure degrees of freedom at the interface is given as

$$J_i^{\text{FSI},n+1} = \begin{bmatrix} S_{\text{II}} & S_{\Gamma} & & & \\ S_{\Gamma\Gamma} & S_{\Gamma\Gamma} + \frac{1-a}{1-b} \left(\frac{1}{\tau} F_{\Gamma\Gamma}^{\text{ff}} + F_{\Gamma\Gamma}^{\text{g}} \right) & \frac{1-a}{1-b} F_{\Gamma\Gamma}^{\text{ff}} & \frac{1-a}{1-b} F_{\Gamma\Gamma}^{\text{g}} & \\ & \frac{1}{\tau} F_{\Gamma\Gamma}^{\text{ff}} + F_{\Gamma\Gamma}^{\text{g}} & F_{\Gamma\Gamma}^{\text{ff}} & F_{\Gamma\Gamma}^{\text{g}} & \\ & & & & A_{\text{II}} \end{bmatrix}_i^{n+1}, \quad (4.58a)$$

$$\Delta x_{i+1}^{n+1} = \begin{bmatrix} \Delta d_{\Gamma}^{\text{s}} \\ \Delta d_{\Gamma}^{\text{s}} \\ \Delta u_{\Gamma}^{\text{ff}} \\ \Delta d_{\Gamma}^{\text{g}} \end{bmatrix}_{i+1}^{n+1} \quad (4.58b)$$

and

$$\begin{aligned} r_i^{\text{FSI},n+1} = & \begin{bmatrix} r_{\Gamma}^{\text{s}} \\ r_{\Gamma}^{\text{s}} + \frac{1-a}{1-b} r_{\Gamma}^{\text{ff}} \\ r_{\Gamma}^{\text{ff}} \\ 0 \end{bmatrix}_i^{n+1} + \begin{bmatrix} 0 \\ (-a + b \frac{1-a}{1-b}) \lambda^n \\ 0 \\ 0 \end{bmatrix} \\ & + \delta_{i0} \begin{bmatrix} 0 \\ -\frac{\Delta t}{\tau} \frac{1-a}{1-b} F_{\Gamma\Gamma}^{\text{ff}} u_{\Gamma}^{\text{ff},n} + \frac{1-a}{1-b} \left(\frac{1}{\tau} F_{\Gamma\Gamma}^{\text{ff}} + F_{\Gamma\Gamma}^{\text{g}} \right) \Delta d_{\Gamma,p}^{\text{s}} \\ \left(\frac{1}{\tau} F_{\Gamma\Gamma}^{\text{ff}} + F_{\Gamma\Gamma}^{\text{g}} \right) \Delta d_{\Gamma,p}^{\text{s}} - \frac{\Delta t}{\tau} F_{\Gamma\Gamma}^{\text{ff}} u_{\Gamma}^{\text{ff},n} \\ A_{\text{II}} d_{\Gamma,p}^{\text{s}} \end{bmatrix}. \end{aligned} \quad (4.58c)$$

In the forthcoming section, the challenge of solving derived monolithic systems, structure-split or fluid-split formulation, in combination of moving embedded fluid and fixed-grid background fluid is discussed and in order to deal with this issue a new approach is proposed.

4.5 Relaxing ALE approach

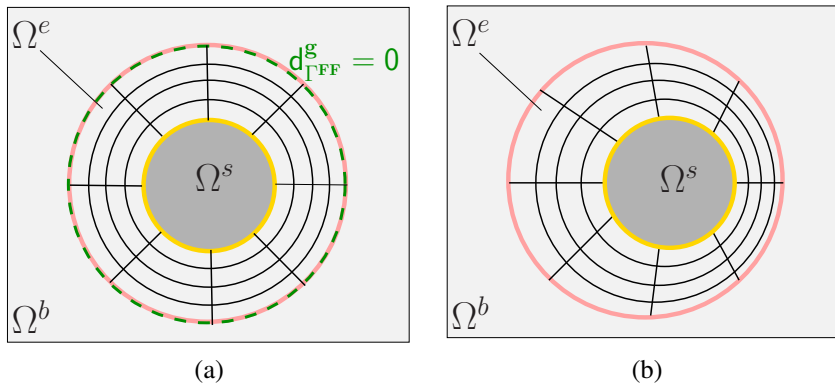
The structure-split or fluid-split monolithic linear systems, (4.55) or (4.58), respectively, have to be solved in every Newton iteration step i of the current time step t^{n+1} . This results in a new incremental solution vector Δx_{i+1}^{n+1} , which includes among other values the embedded fluid velocities at the interface $\Delta u_{\Gamma,i+1}^{e,n+1}$ (for a structure-split), or the structure displacements at the interface $\Delta d_{\Gamma,i+1}^{s,n+1}$ (for a fluid-split), and the new interior displacements of the ALE field $\Delta d_{i,i+1}^{g,n+1}$. This brings in the following complexities in the order specified:

- Having a new interior ALE displacement $\Delta d_{i,i+1}^{g,n+1}$ implies that the position of the internal fluid-fluid interface Γ^{FF} also changes in the newton step $i + 1$. The new position of the fluid-fluid interface yields new physical and void/fictitious parts of background fluid, Ω^b or Ω^{b-} , respectively.
- In order to obtain the new physical background fluid mesh related to the new position of fluid-fluid interface Γ^{FF} , which is relevant for the Newton step $i + 1$, the cut algorithm needs to be applied. As described in Section 3.2, the cut algorithm decomposes the background fluid elements into new volume-cells and the associated boundary segments. Subsequently, new degrees of freedom of background fluid mesh are provided. Moreover, the degrees of freedom that are located in the void/fictitious background fluid subdomain with respect to the new position of fluid-fluid interface are removed.
- This leads to the inconsistency due to the combination of fixed-grid background fluid subdomain and moving embedded fluid, described in Section 3.8, since integrals on the background fluid subdomain Ω^b in the new Newton step $i + 1$ involve values from the last iteration step i , which have changed their number of degrees of freedom; some new degrees of freedom are arisen and some are disappeared, if the associated nodes have changed their positions from the fictitious fluid subdomain Ω^{b-} to the physical background fluid subdomain Ω^b and vice versa.
- Thus, the missing values from the Newton step i , like $\Delta u_i^{b,n+1}$ and $\Delta \dot{u}_i^{b,n+1}$, which are not available and are required in the Newton step $i + 1$, have to be reconstructed. The XFEM time-integration approach described in Section 3.8, which is based on the interpolation of the values from the embedded fluid mesh to the background fluid mesh, provides the missing values.

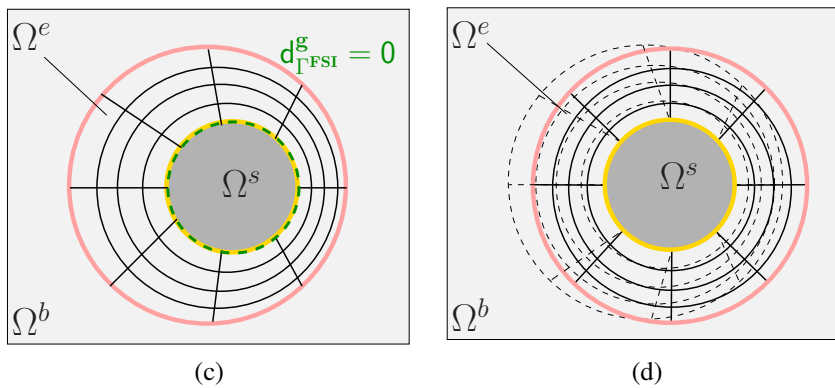
In summary, the whole process described above implies that the size and the degrees of freedom associated with the global linear system, (4.55) or (4.58), would change in every Newton step. Furthermore, the reconstructed values of background fluid subdomain, $\Delta \tilde{u}_i^{b,n+1}$ and $\Delta \tilde{\dot{u}}_i^{b,n+1}$, which affect the values of the right hand side of the linear system at the new Newton step, r_{i+1}^{FSI} , bring in a perturbation in the new Newton step, which would prevent any convergence or result in a poor convergence behavior of the Newton-Raphson scheme.

As a remedy to this problem, in the following, a novel approach stated as monolithic *relaxing ALE approach* is introduced. The key idea is to keep the position of internal fluid-fluid interface Γ^{FF} within the present Newton-Raphson loop unchanged and update its position at the end of the time step in order to avoid alteration of the degrees of freedom within the Newton loop. The

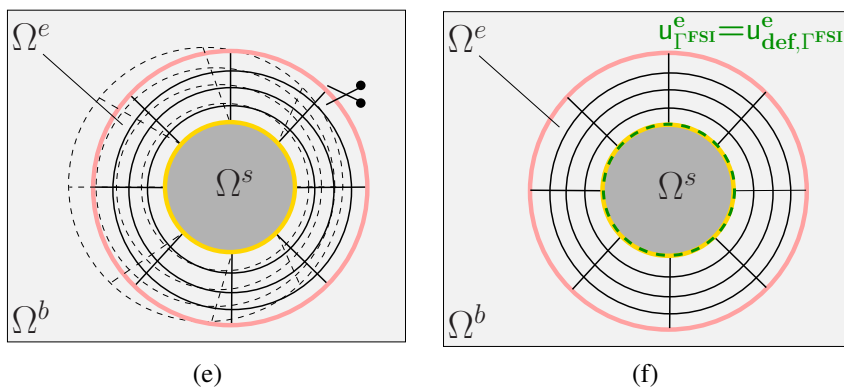
Phase I: Solve the nonlinear FSI problem on a deformed mesh



Phase II: Relax the ALE mesh



Phase III: Update the fluid field



--- Constrained Interface — Γ^{FF} — Γ^{FSI} ✂ Cut algorithm

Figure 4.3: Relaxing ALE approach: **(a)** Fix the position of Γ^{FF} . **(b)** Solve the nonlinear monolithic FSI system without moving Γ^{FF} . **(c)** Fix the position of Γ^{FSI} . **(d)** Solve the ALE problem separately to relax the ALE mesh. **(e)** Cut and assign new DOFs to background fluid subdomain and perform XFEM time-integration approach. **(f)** Set the velocities at Γ^{FSI} to the solution obtained on the deformed mesh and solve one step pure fluid-fluid problem.

algorithm can be divided into three main phases: solve the nonlinear FSI problem on a deformed mesh (Phase I), relax the ALE field (Phase II) and, finally, update the fluid solution (Phase III). The monolithic relaxing ALE approach is illustrated in Figure 4.3.

In Phase I, first, before solving the linear system, zero values are prescribed on the fluid-fluid interface mesh displacement $d_{\Gamma^{FF}}^g$ in order to avoid new position of Γ^{FF} within the current time step t^{n+1} , see Figure 4.3a. With this additional constraint, the nonlinear monolithic FSI problem is solved, see Figure 4.3b. This results in a solution of monolithic FSI problem on a deformed mesh, indicated by

$$\mathbf{x}_{\text{def}}^{n+1} = \begin{bmatrix} d_{\text{def}}^s \\ \mathbf{u}_{\text{def}}^b \\ \mathbf{u}_{\text{def}}^e \\ d_{\text{def}}^g \end{bmatrix}^{n+1}. \quad (4.59)$$

All problems mentioned above are avoided since the position of fluid-fluid interface Γ^{FF} is not changing within the Newton loop (see Figures 4.3a and 4.3b). In Phase II, the ALE mesh is updated in order to reach its final position. In a manner of speaking it "relaxes" itself from its deformed position. For this purpose, first, zero values are prescribed on the fluid-structure interface degrees of freedom of the embedded mesh displacement, $d_{\Gamma^{FSI}}^g = 0$, to keep the position of the fluid-structure interface unchanged, see Figure 4.3c. Afterwards, with the additional constraint, the linear system of the ALE mesh

$$[\mathbf{A}]_i^{n+1} [\Delta d^g]_{i+1}^{n+1} = 0. \quad (4.60)$$

is solved separately, in order to obtain the final mesh displacement d^g , see Figure 4.3d.

Since after the second phase of the algorithm, the final position of fluid-fluid interface Γ^{FF} is reached, the cut algorithm needs to be applied to the background fluid. It decomposes the background fluid elements into new volume-cells, and, consequently, the new physical background fluid subdomain Ω^b is obtained. With the DOF-management algorithm described in Section 3.2.2, new degrees of freedom are assigned to the volume-cells. Moreover, the missing values of the newly arisen degrees of freedom are reconstructed with the XFEM time-integration approach described in Section 3.8. This part of Phase III is illustrated in Figure 4.3e.

Afterwards, in the next part of Phase III, the fluid solution has to be updated. In the phase II of the algorithm, the position of the embedded fluid mesh except for fluid-structure interface Γ^{FSI} has been changed. Additionally, in the first part of the Phase III, due to the new position of fluid-fluid interface Γ^{FF} , a new physical background fluid mesh is obtained. Thus, the solution of the whole fluid field needs to be updated. Hereby, first, in order to keep the values on the fluid-structure interface obtained in the phase I unchanged, the velocities at the fluid-structure interface $\mathbf{u}_{\Gamma^{FSI}}^e$ are set to the solution of fluid-structure interface velocities on the deformed mesh $\mathbf{u}_{\text{def},\Gamma^{FSI}}^e$. Afterwards, the pure fluid-fluid problem

$$\begin{bmatrix} \mathbf{F}_{uu}^{\text{ff}} & \mathbf{F}_{up}^{\text{ff}} \\ \mathbf{F}_{pu}^{\text{ff}} & \mathbf{F}_{pp}^{\text{ff}} \end{bmatrix}_i^{n+1} \begin{bmatrix} \Delta \mathbf{u}^{\text{ff}} \\ \Delta p^{\text{ff}} \end{bmatrix}_{i+1}^{n+1} = - \begin{bmatrix} r_u^{\text{ff}} \\ r_p^{\text{ff}} \end{bmatrix}_i^{n+1} \quad (4.61)$$

with the given position of embedded fluid mesh, is solved separately, see Figure 4.3f. The linear system (4.61) is a short version of the linear system of the embedded fluid formulation (3.144)

and the superscript $(\cdot)^{\text{ff}}$ indicates the contributions of background and embedded fluid subdomains. Solving (4.61) results in the final fluid solutions $u^{b,n+1}$ and $u^{e,n+1}$.

To sum up, in this section, a new FSI approach is proposed to avoid the problems of solving the monolithic FSI system in combination of moving embedded fluid and fixed-grid background fluid, as mentioned above. The key idea is that the position of the internal fluid-fluid interface Γ^{FF} within the present Newton-Raphson loop stays unchanged and it is updated at the end of the time step. The monolithic relaxing ALE approach is shown in Algorithm 1.

Algorithm 1 Monolithic relaxing ALE approach within one time step t^{n+1}

- 1: **Phase I:** Solve the nonlinear FSI problem on a deformed mesh
- 2: **a)** Set $d_{\Gamma^{\text{FF}}}^g = 0$ to fix the position of fluid-fluid interface.
- 3: **b)** Solve linear monolithic FSI problem

$$J_{\text{def},i}^{\text{FSI},n+1} \Delta x_{\text{def},i+1}^{n+1} = -r_{\text{def},i}^{\text{FSI},n+1}, \quad (4.62)$$

$$x_{\text{def},i+1}^{n+1} = x_{\text{def},i}^{n+1} + \Delta x_{\text{def},i+1}^{n+1}. \quad (4.63)$$

→ FSI solution on deformed mesh: $u_{\text{def}}^b, u_{\text{def}}^e, d_{\text{def}}^s, d_{\text{def}}^g$

- 4: **Phase II:** Relax the ALE mesh
- 5: **a)** Set $d_{\Gamma^{\text{FSI}}}^g = 0$ to keep the position of fluid-structure interface.
- 6: **b)** Solve the ALE problem

$$\left[A \right]_i^{n+1} \left[\Delta d^g \right]_{i+1}^{n+1} = 0 \quad (4.64)$$

separately.

- 7: **Phase III:** Update the fluid field
- 8: **a)** Cut the background fluid with the new position of Γ^{FF} .
- 9: **b)** Assign new DOFs to elements and volume-cells of background fluid mesh.
- 10: **c)** Obtain the missing values of new DOFs via XFEM time-integration approach.
- 11: **d)** Set $u_{\Gamma^{\text{FSI}}}^e = u_{\text{def},\Gamma^{\text{FSI}}}^e$ to keep the values at the fluid-structure interface Γ^{FSI} unchanged.
- 12: **e)** Set the solution on the deformed mesh $u_{\text{def}}^{\text{ff}}$ as the starting solution.
- 13: **f)** Solve the pure fluid-fluid problem

$$\left[\begin{array}{cc} F_{wu}^{\text{ff}} & F_{up}^{\text{ff}} \\ F_{pu}^{\text{ff}} & F_{pp}^{\text{ff}} \end{array} \right]_i^{n+1} \left[\begin{array}{c} \Delta u^{\text{ff}} \\ \Delta p^{\text{ff}} \end{array} \right]_{i+1}^{n+1} = - \left[\begin{array}{c} r_u^{\text{ff}} \\ r_p^{\text{ff}} \end{array} \right]_i^{n+1}. \quad (4.65)$$

→ final fluid solutions $u^{b,n+1}$ and $u^{e,n+1}$.

4.6 Numerical examples

In this section, the proposed relaxing ALE hybrid FSI approach is validated and the ability of the method is demonstrated. For this purpose, first, a simple pseudo one-dimensional FSI problem with analytical solution is considered. For further validations, the results of proposed relaxing ALE hybrid FSI approach are compared with the results of well-established monolithic

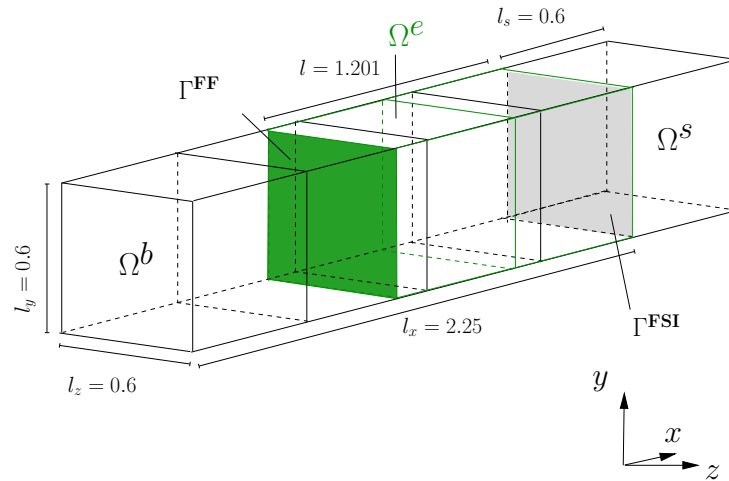


Figure 4.4: Pseudo one-dimensional FSI example: Setup. The unit of lengths is [m].

ALE-based FSI approach (see e.g. Küttler [120] and Klöppel et al. [117]). For this purpose, FSI problems with moderate deformations are chosen, which can also be computed by classical ALE-based FSI approaches. Furthermore, other numerical examples are provided to demonstrate the potential of the proposed approach to robustly and accurately deal with complex three-dimensional FSI problems. All the 2D simulations are performed as pseudo 2D examples with one element in z -direction.

4.6.1 Pseudo one-dimensional FSI example

As a very simple example, a pseudo-1D FSI problem with analytical solution, motivated from Gerstenberger [82] and Mayr et al. [135], is considered. This example verifies the correctness of the monolithic relaxing ALE approach introduced in Section 4.5. The setup is given in Figure 4.4. In order to achieve a pseudo one-dimensional channel all displacement and velocity degrees of freedom in y - and z -direction are set to zero. Thus, the only possible movement is in x -direction. A rigid structure block Ω^s (Poisson's ratio $\nu^s = 0.3$, Young's modulus $E = 2 \cdot 10^8 \text{ N/m}^2$) with a time dependent Dirichlet boundary condition

$$\bar{d}_x^s(t) = -t^3 \quad (4.66)$$

on its dry side pushes the fluid out of the channel. It moves the embedded fluid subdomain Ω^e and the fluid-fluid interface Γ^{FF} into the background fluid. Therefore, the physical background fluid subdomain Ω^b gets smaller during the simulation time. At the outflow of the background fluid subdomain a zero Neumann boundary condition is prescribed.

Considering the time dependent Dirichlet boundary condition at the dry side of the structure, the velocity and acceleration fields read as

$$u_x(x, t) = \frac{\partial \bar{d}_x^s}{\partial t} = -3t^2, \quad (4.67)$$

$$a_x(x, t) = \frac{\partial^2 \bar{d}_x^s}{\partial t^2} = -6t, \quad (4.68)$$

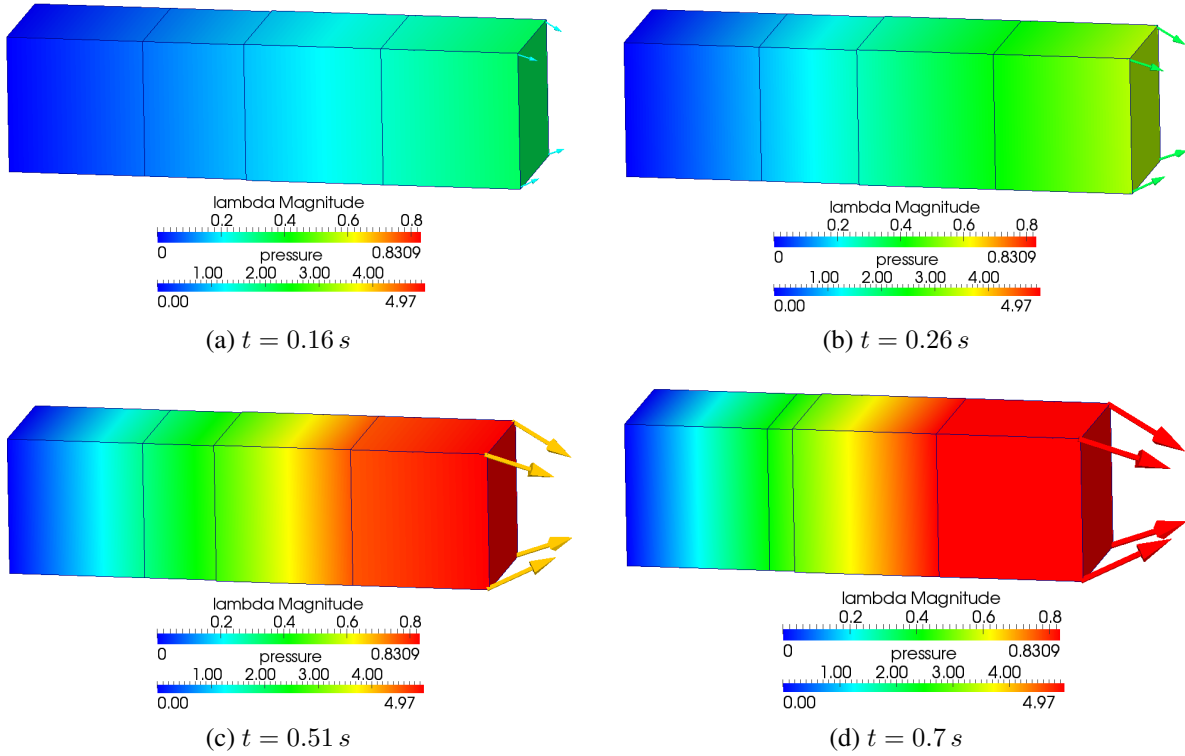


Figure 4.5: Pseudo one-dimensional FSI example: Pressure field and Lagrange multipliers at fluid-structure interface at time steps $t = 0.16$ s, $t = 0.26$ s, $t = 0.51$ s and $t = 0.7$ s.

respectively. The corresponding analytical solution for the pressure field with a zero pressure at the outflow, neglecting the body forces \mathbf{b}^f , results in

$$p(x, t) = -\rho^f a_x(x, t)x. \quad (4.69)$$

The simulation is run for $T = 0.7$ s with $\Delta t = 0.01$ s. The time step Δt is chosen small in order to minimize the temporal error. In this example, the one-step- θ time-integration scheme for the fluid field with $\theta = 1$ and $\theta = 0.5$, in combination of first and second order conversion of interface velocities and displacements, $\tau = \Delta t$ and $\tau = \frac{\Delta t}{2}$ in (4.39), respectively, is considered. For the structural time discretization the generalized- α method with $\rho_\infty = 0.8$, i.e. with numerical dissipation, is used. In this example, a fluid governed interface motion, i.e. a structure-split, is chosen. Hence, the structure field, which is the slave field in a structure-split formulation, carries the Lagrange multiplier field λ at the interface. Moreover, due to a structure-split formulation, at the interface only the fluid side carries Dirichlet boundary conditions. Thus, at the interface the fluid velocity in y - and z - directions are set to zero.

In Figure 4.5, the Lagrange multiplier and the pressure field are depicted. The Lagrange multiplier field represents the traction onto the fluid. Thus, the x -component of the Lagrange multiplier field holds the same value as the pressure at the interface. The other components are the nodal forces which prevent the structure to deform at the FSI interface in y - and z -directions.

Figures 4.6a and 4.6b, show the results of the simulation for displacement and velocity over time, together with the analytical solutions (4.66) and (4.67), respectively, evaluated at the fluid-structure interface, i.e. $x = x_{\Gamma^{\text{FSI}}}$. For all four configurations good agreement of numerical results

with the analytical solution is achieved. The solutions of the pressure field is shown in Figure 4.6c, which is plotted together with the analytical solution of the pressure field at the interface defined as

$$p(x_{\Gamma^{\text{FSI}}}, t) = \rho^f 6t \cdot (l_x - t^3), \quad (4.70)$$

with $\rho^f = 1.0 \text{ kg/m}^3$ and $l_x = 2.25 \text{ m}$, denoting the initial length of the channel. Hereby, it is assumed that due to the deformation of the structure the length of the channel decreases proportional to $-t^3$. It can be observed that using $\theta = 0.5$ in combination of the trapezoidal rule for the conversion of the interface displacements and velocities causes some oscillation in the pressure field. It has to be pointed out again that using the trapezoidal rule for conversion of interface velocities and displacements correctly preserves the volume of the fluid domain but it is not a dissipating approach, i.e. it tends to oscillate, see Förster [73]. The one-step- θ approach with $\theta = 0.5$ is likewise not dissipative. For all other configurations the analytical solution can be represented exactly. Considering the absence of viscous forces, for the analytical solution of FSI forces at the structure side of fluid-structure interface in x -direction holds

$$F^{\text{exact}}(t) = - \int_{\Gamma^{\text{FSI}}} \boldsymbol{\sigma} \cdot \mathbf{n}^e \, dx = -A \cdot p(t, x_{\Gamma^{\text{FSI}}}) \quad (4.71)$$

with $A = 0.36 \text{ m}^2$ denoting the surface area of the fluid-structure interface and \mathbf{n}^e , the outward pointing normal with respect to embedded fluid subdomain Ω^e . The resulting numerical interface forces in x -direction can be computed as the sum of Lagrange multipliers, which present the discrete nodal forces, over FSI nodes as

$$F_x = \sum_{i=0}^{n=4} \lambda_x^i. \quad (4.72)$$

In Figure 4.6d, the numerical solution of FSI forces in the x -direction and the analytical solution (4.71) are presented. As expected, like in the pressure field, oscillation is observed for the configuration with $\theta = \frac{1}{2}$ and $\tau = \frac{\Delta t}{2}$. For all other configurations the analytical FSI forces are represented exactly.

4.6.2 Two-dimensional compressing structure

The following FSI problem with moderate structural displacements validates the monolithic relaxing ALE hybrid FSI approach by comparing the results with results of the monolithic classical ALE-based FSI approach (see Klöppel et al. [117], Küttler [120] and Mayr et al. [135]). In this example, which is motivated from Gerstenberger [82], a circular structure with Neo-Hookean material law (Poisson's ratio $\nu^s = 0.0$, Young's modulus $E = 50 \text{ N/m}^2$, density $\rho^s = 1.0 \text{ kg/m}^3$) is located in the middle of a rectangular fluid domain with $\nu = 0.1 \text{ m}^2/\text{s}$ and $\rho^f = 1.0 \text{ kg/m}^3$. The setup of the example for hybrid FSI and ALE-based FSI approaches, is shown in Figures 4.7a and 4.7b, respectively. Constant velocities in opposite y -directions are prescribed on upper and lower walls, indicated as Γ_{top} and Γ_{bottom} in Figure 4.7. On both left and right walls (Γ_{left} and Γ_{right}) a zero Neumann boundary condition is applied. The structure is fixed along the central axis as well as at two additional symmetrical points in y -direction to avoid any rotations. Due to the purpose of employing a comparison of the results of both FSI approaches,

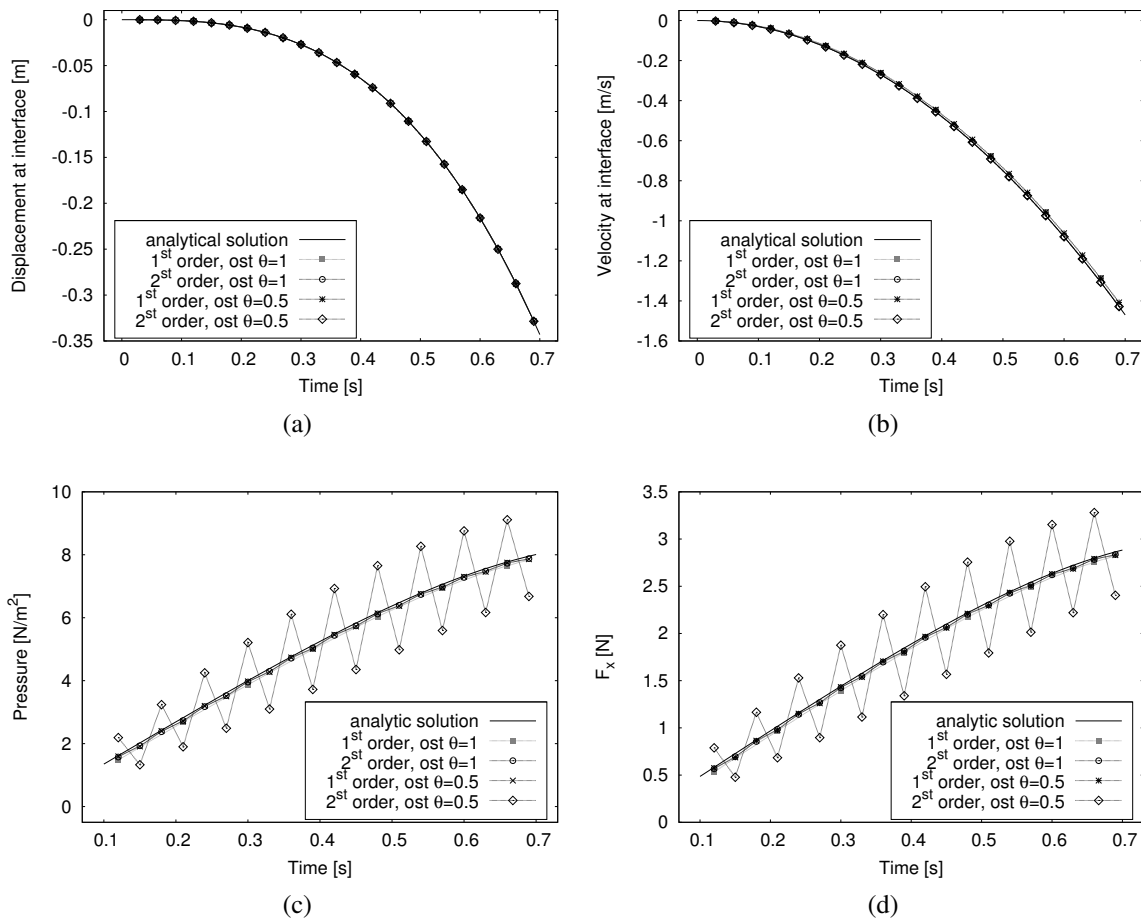


Figure 4.6: Pseudo one-dimensional FSI example: interface displacement, velocity, pressure and FSI forces over the time compared with analytical solutions.

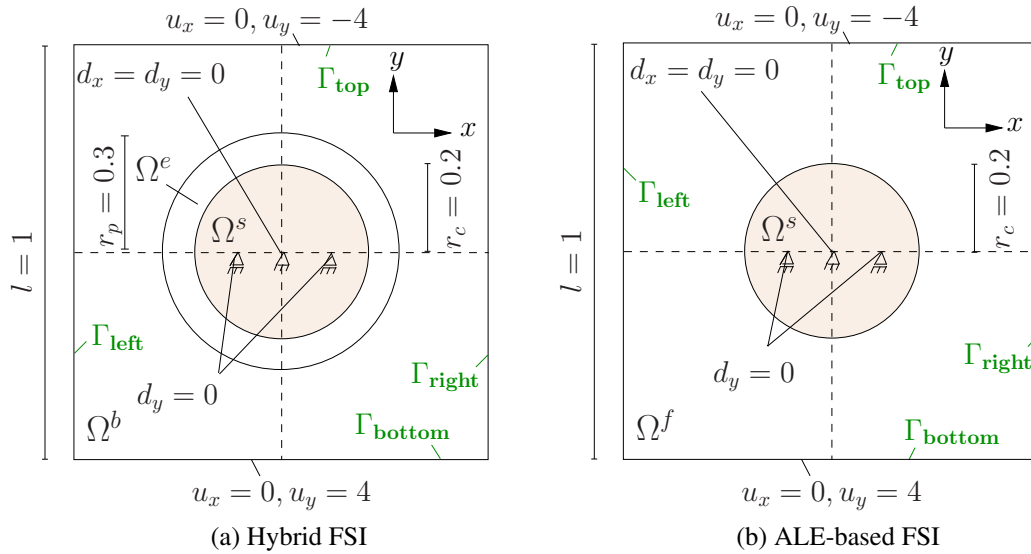


Figure 4.7: Two-dimensional compressing structure: **(a)** Setup of hybrid FSI approach and **(b)** setup of ALE-based FSI approach. The units of the lengths and displacements are $[m]$.

the same structural mesh for both FSI approaches is used. In the case of hybrid FSI approach, a fine layer of stretched fluid elements (embedded fluid domain) surrounds the circular structure, while the classical FSI approach consists of only one fluid domain. Both simulations are run for $T = 3 s$ with $\Delta t = 0.03 s$ and monolithic structure-split formulation.

In Figure 4.8, the velocity and pressure fields for both approaches in equilibrium are shown. Figures 4.8a and 4.8b show the results of the hybrid FSI approach, while in Figures 4.8c and 4.8d, the results of ALE-based FSI approach are presented. In order to compare the results of both simulations, displacement magnitude, velocity magnitude, pressure and magnitude of Lagrange multiplier field are computed for a control point P_c at the interface, depicted in Figure 4.9a, which undergoes a big deformation over the simulation time. In Figure 4.9b, the steady state solution of the magnitude of Lagrange multiplier field is depicted. The results of the validation of both simulations are plotted in Figure 4.10. Due to the elastodynamic behavior of the problem an oscillation in the computed values can be observed until the equilibrium state is reached. As it can be seen in Figure 4.10, despite different fluid meshes, a good agreement of results for the hybrid FSI and the ALE-based FSI approaches, over the simulation time is obtained.

4.6.3 Two-dimensional bending structure

Similar to the two-dimensional compressing cylinder presented in Section 4.6.2, this example validates also the monolithic relaxing ALE hybrid FSI approach by comparing the results with the results of monolithic ALE-based FSI approach. It also demonstrates the applicability of hybrid FSI approach to FSI problems with large structural deformation, where the classical ALE-based FSI approach reaches its limit. It has to be pointed out that with other material parameters of the fluid grid or other fluid grid approaches the failure of the ALE-based FSI approach could

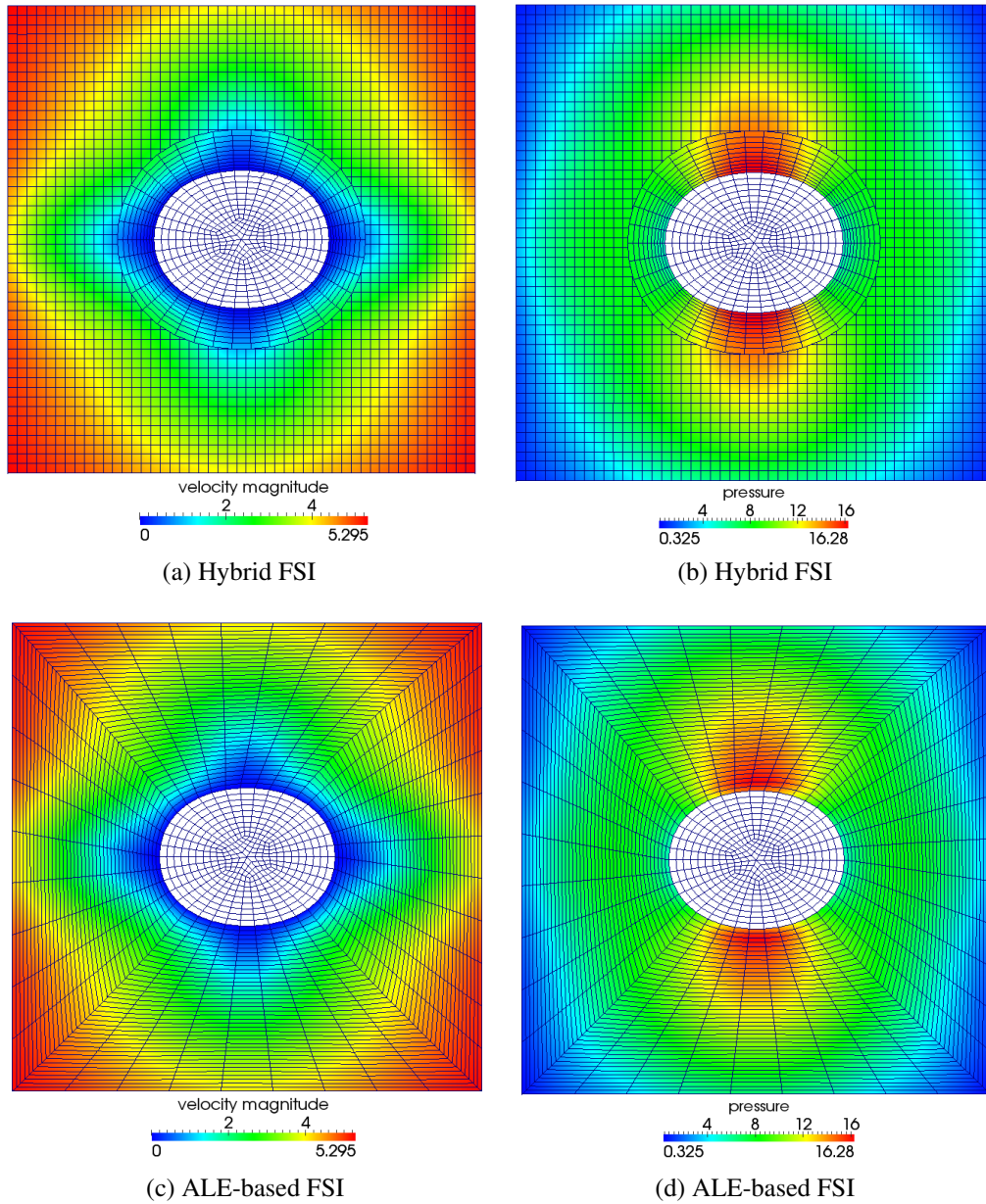


Figure 4.8: Two-dimensional compressing structure: Steady state solution of velocity and pressure fields for hybrid FSI approach ((a) and (b)) ALE-based FSI approach ((c) and (d)).

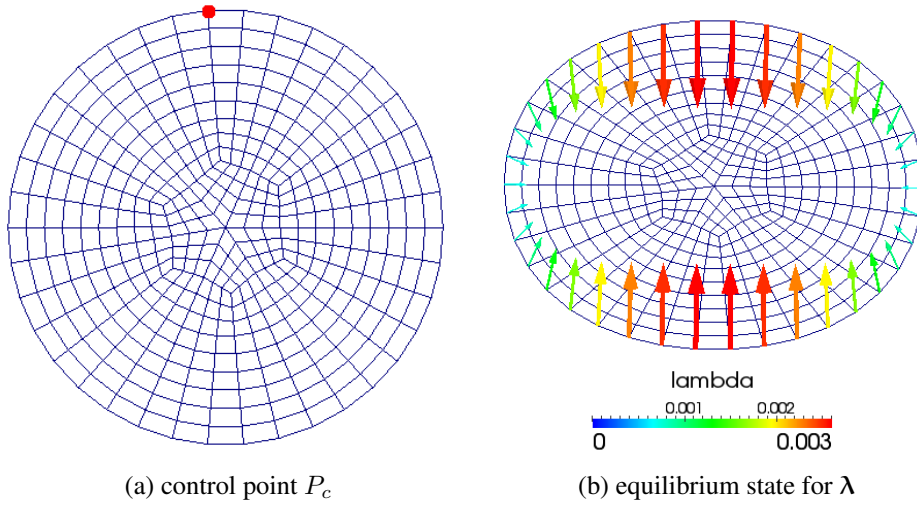


Figure 4.9: Two-dimensional compressing cylinder: (a) Control point P_c (b) The equilibrium state for Lagrange multiplier field.

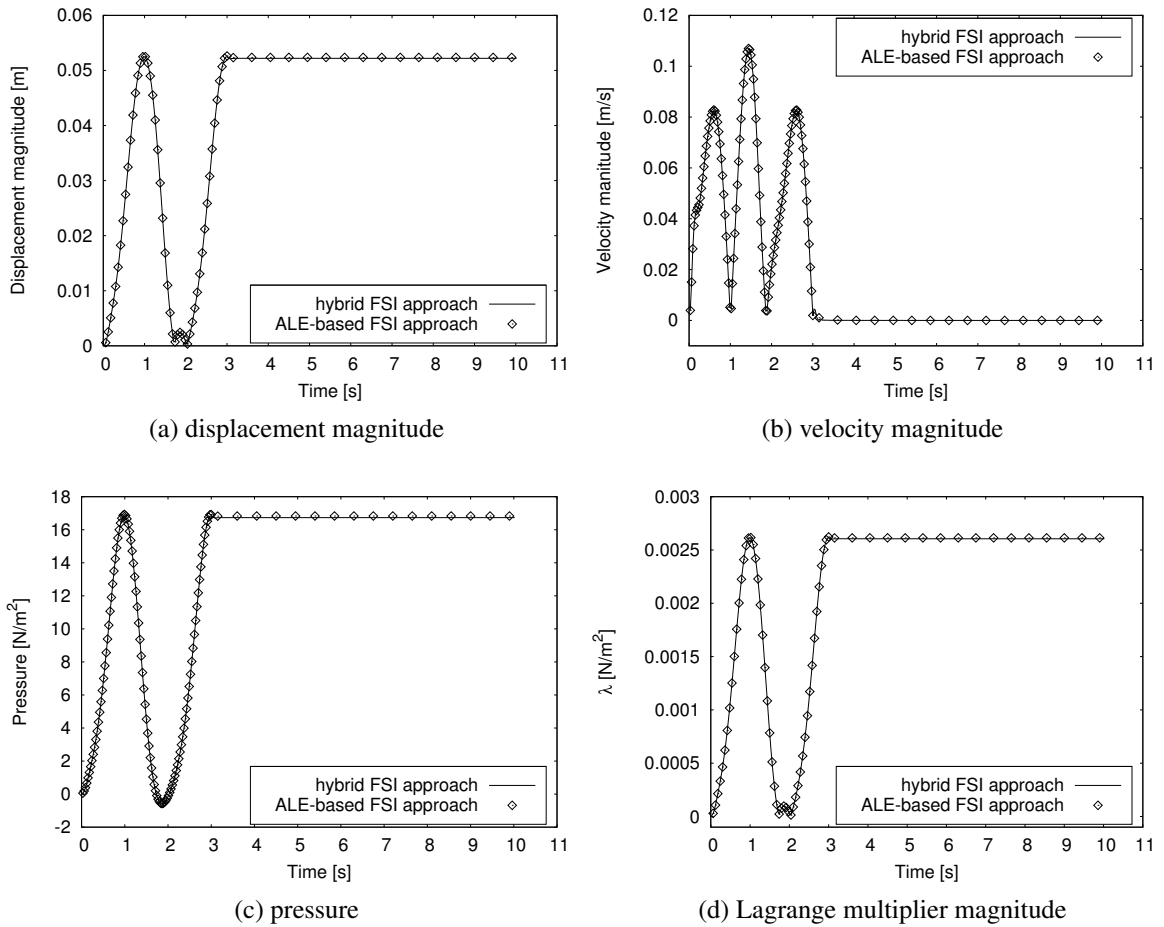


Figure 4.10: Two-dimensional compressing cylinder: Results of displacement, velocity, pressure and Lagrange multiplier at fluid-structure interface at control point P_c .

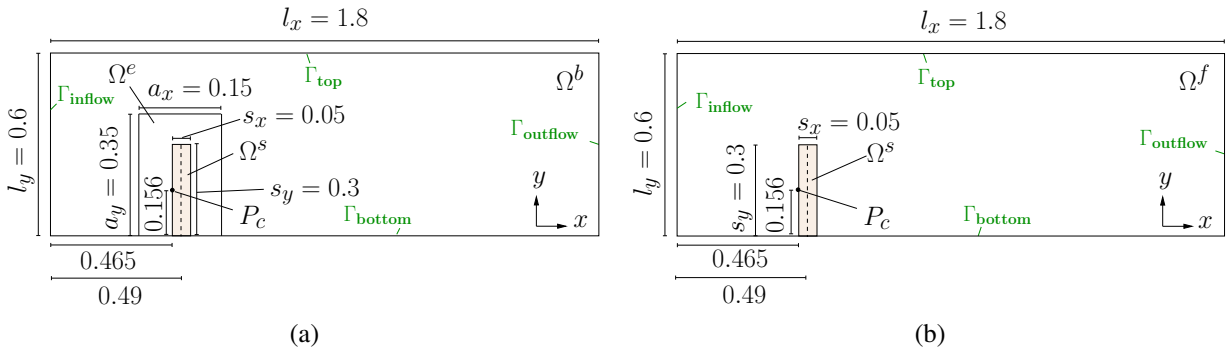


Figure 4.11: Two-dimensional bending structure: **(a)** Setup of hybrid FSI approach and **(b)** setup of ALE-based FSI approach. The unit of lengths is $[m]$.

be postponed. Furthermore, ALE-based FSI approach applied does not involve any mesh update algorithm. As an example the recent publication by Alauzet [1] shows that using a changing-topology moving mesh technique allows for handling of large structural deformations.

Due to flow through a channel a flexible structure with St.-Venant-Kirchhoff material law (Poisson's ratio $\nu^s = 0.0$, Young's modulus $E = 300 \text{ N/m}^2$, density $\rho^s = 1.0 \text{ kg/m}^3$) is deformed. The geometric setup of the hybrid FSI and the ALE-based FSI approach is depicted in Figures 4.11a and 4.11b, respectively. As it can be seen, in contrast to the hybrid FSI approach, the ALE-based FSI approach only consists of one fluid domain, stated as Ω^f in Figure 4.11b, which is described in ALE formulation. For both approaches, zero velocity at top and bottom of the channel (Γ_{top} and Γ_{bottom} in Figure 4.11) and a parabolic velocity profile at the inflow (Γ_{inflow} in Figure 4.11) with maximum velocity of $u_x^{\text{max}} = 0.3 \text{ m/s}$ are prescribed. At the outflow (Γ_{outflow} in Figure 4.11), a zero Neumann boundary condition is applied. The fluid has a kinematic viscosity of $\nu = 0.01 \text{ m}^2/\text{s}$ and a density of $\rho^f = 1.0 \text{ kg/m}^3$. In Figures 4.12a and 4.12b meshes used for hybrid FSI approach and classical FSI approach, are depicted, respectively. As shown in Figure 4.12a, in the case of hybrid approach, the structure is surrounded with a boundary layer mesh of fine stretched fluid elements (embedded fluid mesh), which is embedded in the background fluid mesh. For both simulations, the same mesh for the structure field is used. Furthermore, for both simulations a velocity governed interface motion, i.e. a structure-split formulation, is applied. The simulations are run with the time step $\Delta t = 0.005 \text{ s}$.

In Figures 4.13a and 4.13b, the steady state solution of the velocity field in x -direction and the pressure field of hybrid FSI approach are shown. The additional pressure contour lines, are depicted in Figure 4.13b, which confirm the smoothness of pressure solution over the internal fluid-fluid interface. The velocity in x -direction and pressure of classical FSI approach at the time step $t = 0.92 \text{ s}$ are shown in Figures 4.13c and 4.13d. Due to the large deformation of the structure and, consequently, distorted fluid elements, the classical FSI approach fails after $t = 0.92 \text{ s}$. In contrast, the hybrid FSI approach is not limited due to large structural deformation and does not distort any fluid elements. The distorted fluid elements of the ALE-based FSI approach can be seen at the top of the structure in Figures 4.13c and 4.13d.

In Figure 4.14, displacement and velocity magnitude, pressure field, and magnitude of Lagrange multiplier field for both simulations at the control point P_c located at the interface, which is depicted in Figures 4.11a and 4.11b, are plotted over simulation time. The line graphs clearly

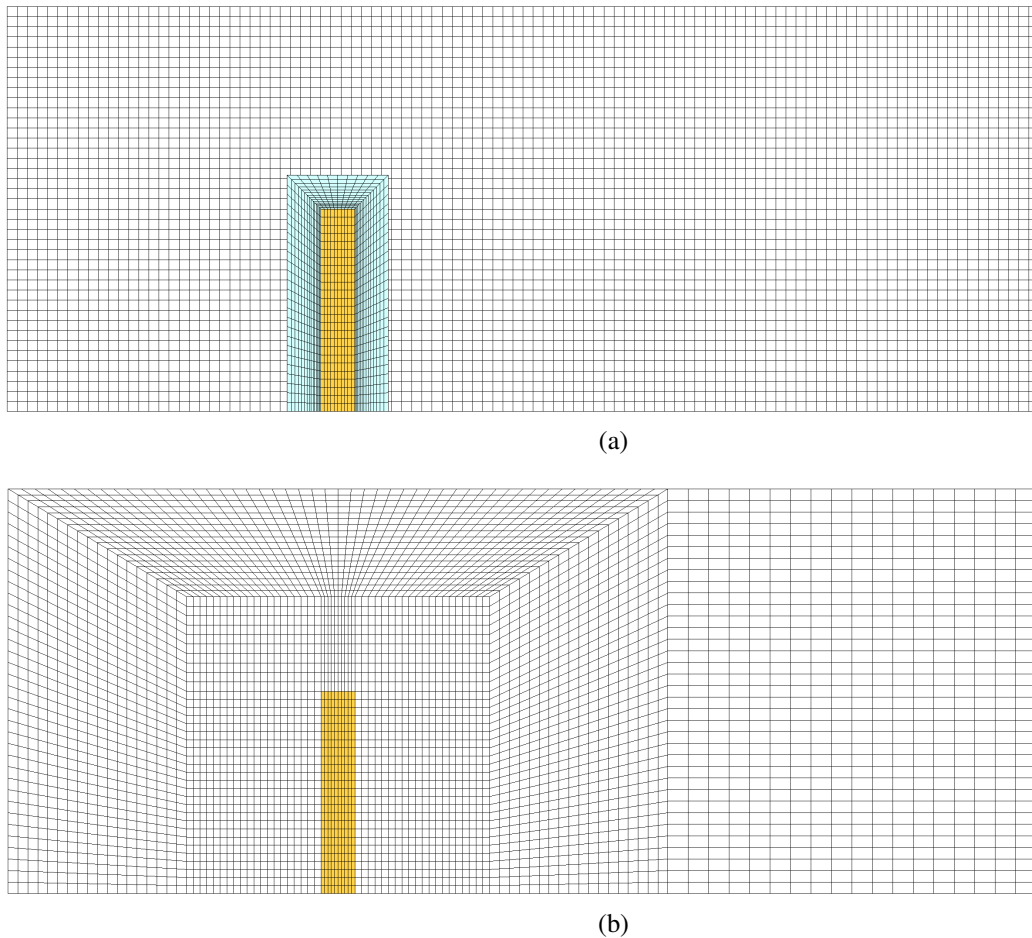


Figure 4.12: Two-dimensional bending structure: **(a)** Mesh used for hybrid FSI approach. The embedded fluid mesh is depicted in blue and the structure mesh is depicted in yellow. **(b)** Mesh used for ALE-based FSI approach. The structure mesh is depicted in yellow.

show that during the common simulation times of both methods the computed values for hybrid and ALE-based FSI approaches match very well. As it can be observed in the line graphs the computation time of ALE-based FSI approach is shorter, due to distorted fluid elements. Thus, beside good agreement of the computed results, this example demonstrates that the hybrid FSI approach is applicable to FSI problems with large structural deformation, while the classical ALE-based approach reaches its limit.

4.6.4 Three-dimensional bending structure

In this example, the relaxing ALE hybrid FSI approach is applied to a three-dimensional FSI problem. The setup of three-dimensional bending structure is similar to the setup of two-dimensional bending structure described in Section 4.6.3. Again, the flow is computed over a deforming structure. The fluid domain is a channel with dimensions $0.6\text{ m} \times 1.8\text{ m} \times 1.2\text{ m}$ with zero Dirichlet boundary condition for the velocity at the top, bottom and the side walls. A flexible structure

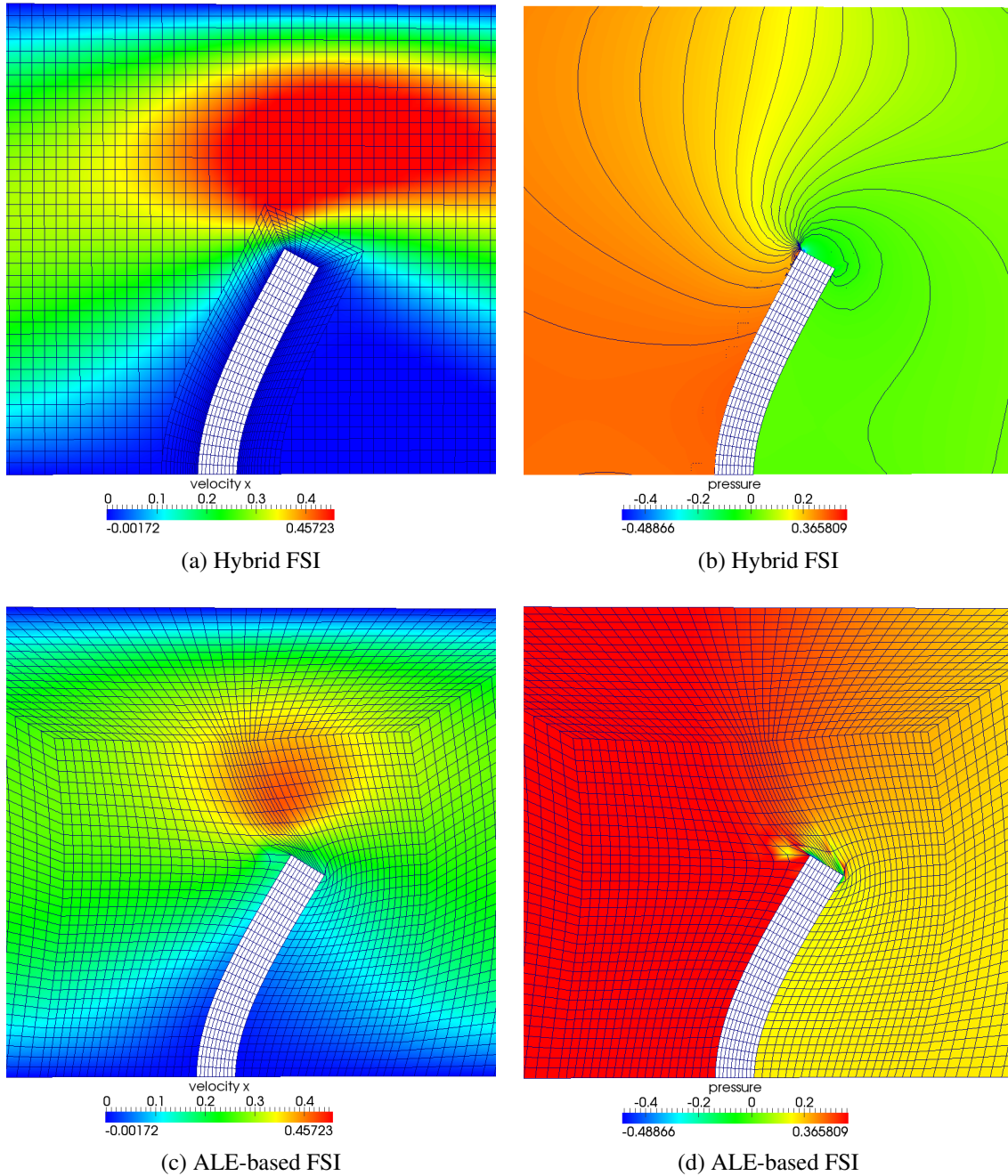


Figure 4.13: Two-dimensional bending structure: Steady state solution of velocity and pressure fields of hybrid FSI approach ((a) and (b)) versus the solution of velocity and pressure fields of classical ALE-based FSI approach at $t = 0.92 s$ ((c) and (d)).

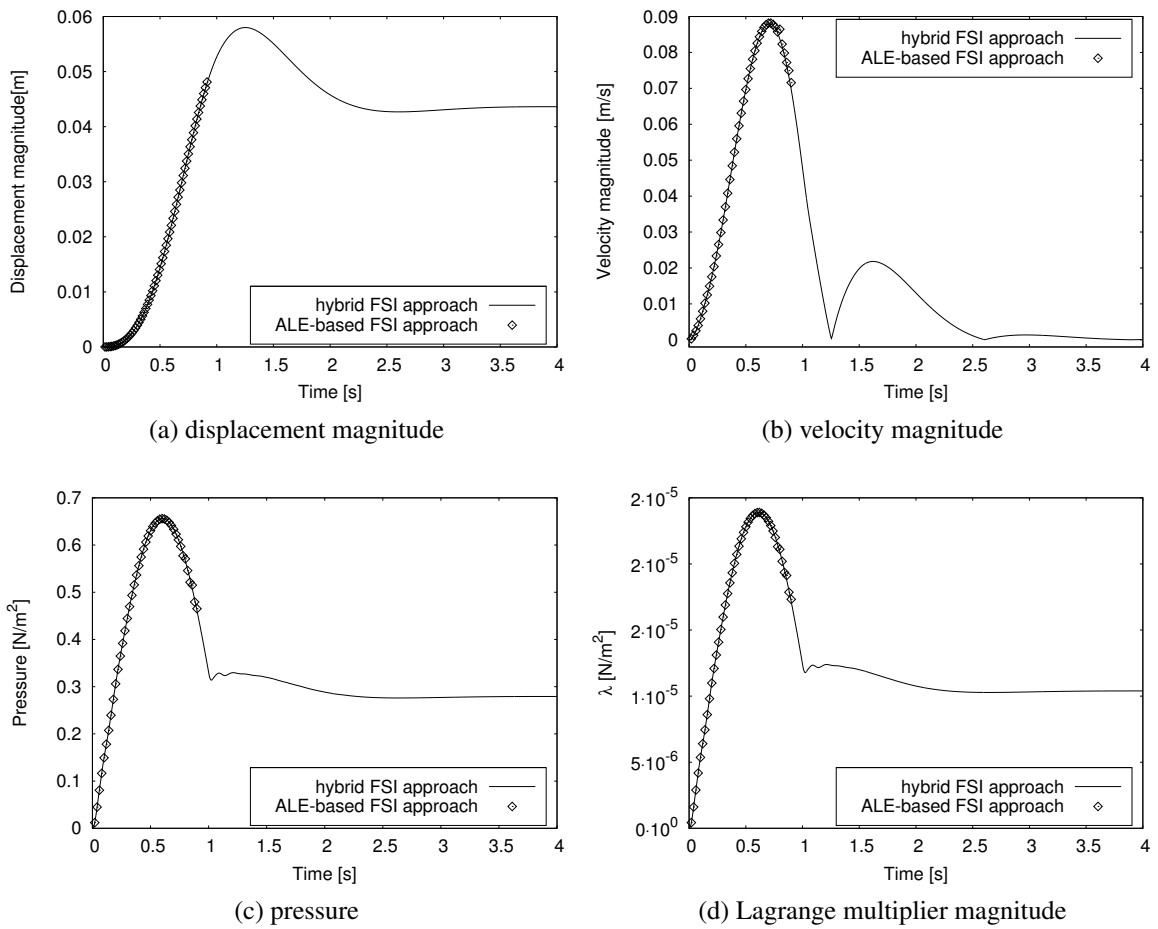


Figure 4.14: Two-dimensional bending structure: Results of displacement, velocity, pressure and Lagrange multiplier at the control point P_c .

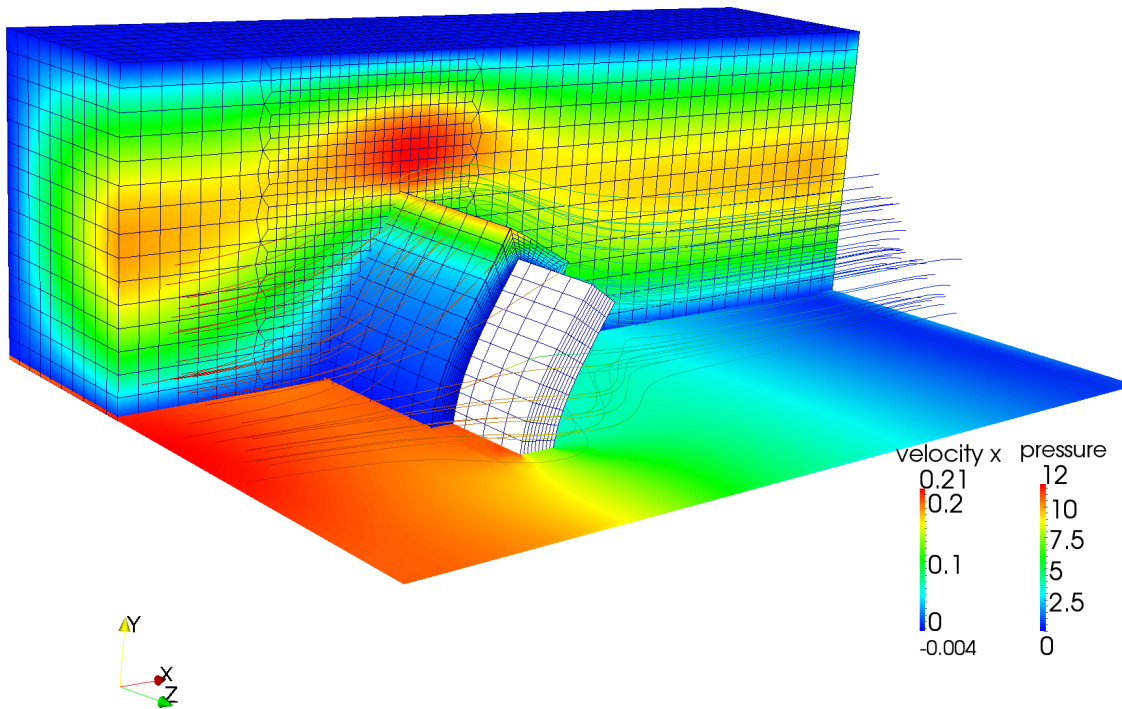


Figure 4.15: Three-dimensional bending structure at steady state: At the cross section the velocity in x -direction and at the bottom wall the pressure solution are illustrated.

$0.4\text{ m} \times 0.15\text{ m} \times 0.75\text{ m}$ with St.-Venant-Kirchhoff material law (Poisson's ratio $\nu^s = 0.3$, Young's modulus $E = 4000\text{ N/m}^2$, density $\rho^s = 250\text{ kg/m}^3$) is located in the channel, which is surrounded by a fine layer of stretched embedded fluid elements. At the inflow, a parabolic velocity profile with maximum velocity of $u_x^{\max} = 0.2\text{ m/s}$ and $u_y = u_z = 0$ is prescribed. At the outflow, a zero Neumann boundary condition is applied. The fluid has a kinematic viscosity of $\nu = 1.0\text{ m}^2/\text{s}$ and a density of $\rho^f = 0.1\text{ kg/m}^3$. The simulation is run with $\Delta t = 0.003\text{ s}$ for a structure-split formulation. Figure 4.15 illustrates the steady state solution of x -component of the velocity field at the cross section and of pressure at the bottom wall. Streamlines illustrate the flow over and around the structure colored by the pressure field.

4.6.5 Three-dimensional freely moving snake

To demonstrate the potential and the ability of the proposed approach to robustly and accurately deal with complex three-dimensional FSI problems, a freely moving thin structure is investigated. The structure is freely transported through a three-dimensional domain, while being subject to a three-dimensional deformation. The example is motivated from the 2D and 3D moving snakes with prescribed motions, given in Sections 3.9.4 and 3.9.5, respectively, which have been computed with a monolithic fluid-split formulation. However, for this example the 'snake-like' deformation of the structure is not prescribed and it is due to the flow in the channel.

In this example, a flexible thin structure with Neo-Hookean material law (Poisson's ratio $\nu^s = 0.35$, Young's modulus $E = 500\text{ N/m}^2$, density $\rho^s = 1.0\text{ kg/m}^3$) is located at the beginning of a channel. The fluid has a kinematic viscosity of $\nu = 0.01\text{ m}^2/\text{s}$ and a density of

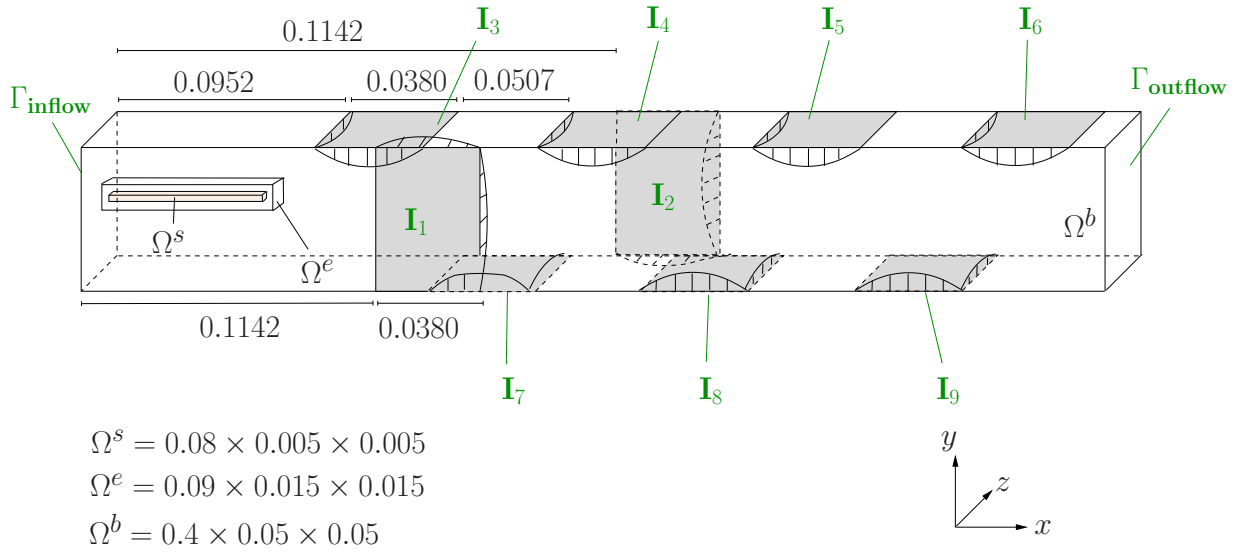
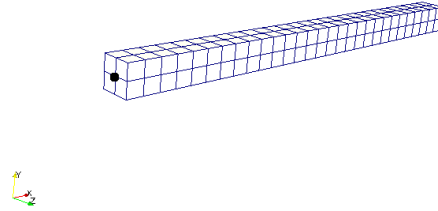
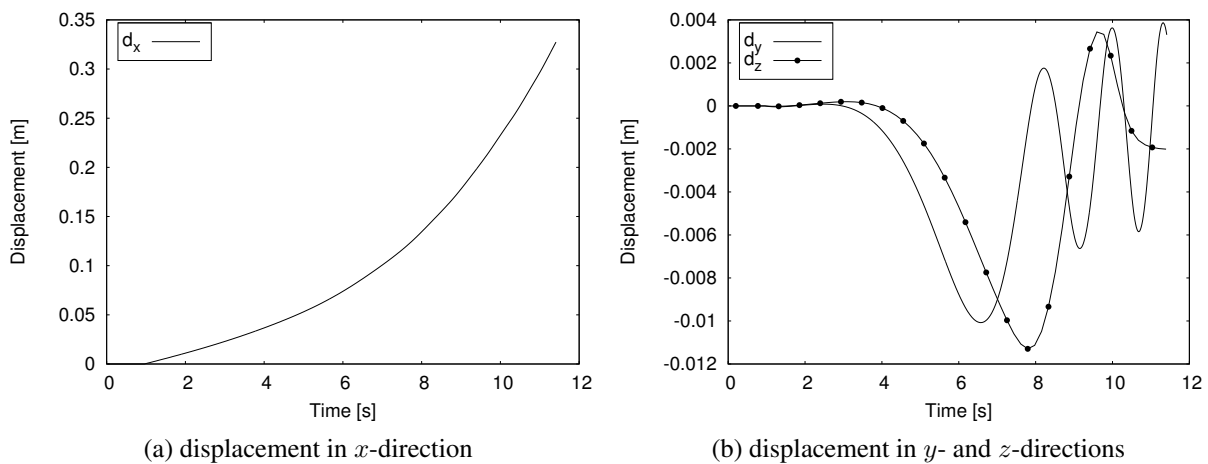


Figure 4.16: Three-dimensional freely moving snake: Setup. The unit of lengths is [m].

$\rho^f = 1.0 \text{ kg/m}^3$. The setup of the example is shown in Figure 4.16. The flexible structure Ω^s is surrounded with a fine layer of fluid elements Ω^e , which is then embedded into the background fluid Ω^b . At the inflow of the channel (Γ_{inflow} in Figure 4.16) a parabolic velocity profile with maximum velocity of $u_x^{\max} = 0.01 \text{ m/s}$ is prescribed. Zero Dirichlet boundary conditions are prescribed at the four walls of the channel and a zero Neumann boundary condition is applied at the outflow, depicted as $\Gamma_{outflow}$ in Figure 4.16. In order to simulate the 'snake-like' motion of the structure seven inlets at the top and bottom walls (I_3, I_4, \dots, I_9 in Figure 4.16) of the channel in regular distances are added. Moreover, in order to extend the deformation of the structure in the z -direction and obtain an irregular motion, two further inlets are located at the side wall of the channel (I_1 and I_2 in Figure 4.16). At the inlets at the top and bottom of the channel (I_3, I_4, \dots, I_9 in Figure 4.16), parabolic profiles with maximum velocity of $u_y^{\max} = -0.02 \text{ m/s}$ and $u_y^{\max} = 0.02 \text{ m/s}$, respectively, are prescribed. Accordingly, parabolic profiles with maximum velocities of $u_z^{\max} = 0.01 \text{ m/s}$ and $u_z^{\max} = -0.01 \text{ m/s}$ are prescribed at the horizontal inlets (I_1 and I_2 in Figure 4.16). The simulation is run for 11.16 s with $\Delta t = 0.02 \text{ s}$. During the simulation time the structure moves from its initial position to the end of the channel and undergoes a freely three-dimensional snake-like deformation, i.e. in x -, y - and z - directions, due to the crossflows. The deformation of the structure in x -direction, and in y - and z -directions over the simulation time for a control point P_s located at the interface, which is depicted in Figure 4.17, are shown in Figures 4.18a and 4.18b, respectively. Furthermore, the embedded fluid mesh in cross section is depicted in Figure 4.19.

In Figures 4.20, 4.21 and 4.22, the velocity field at the cross section and the pressure solution at the bottom wall at time steps, $t = 6.624 \text{ s}$, $t = 8.244 \text{ s}$ and $t = 10.332 \text{ s}$, respectively, are shown. In all Figures 4.20, 4.21 and 4.22, the structure is depicted at the top, and at the bottom the embedded fluid mesh at the same time step is shown. Streamlines illustrate the flow in the channel colored by the velocity field. As it can be seen in Figures 4.20, 4.21 and 4.22, as the structure moves and deforms arbitrarily in domain, the embedded fluid undergoes the same deformation of the structure during the whole simulation time. Thus, an appropriate boundary

Figure 4.17: Three-dimensional freely moving snake: Control point P_s .Figure 4.18: Three-dimensional freely moving snake: **(a)** The displacement in x -direction over the simulation time validated at the control point P_s . **(b)** The displacement in y - and z -directions over the simulation time validated at the control point P_s .

layer mesh is available in every time step around the structural surface. In Figure 4.23a, a close up view of the structure at $t = 10.332$ s is given. In Figure 4.23b, the embedded fluid mesh, colored by the pressure field, is depicted at the same time step. Figures 4.24a and 4.24b present a plane view of the structure and embedded fluid mesh at $t = 8.406$ s. Also in Figure 4.24, the velocity field is shown at the cross section and the pressure field at the bottom wall. Streamlines illustrate the flow in channel colored by velocity field.

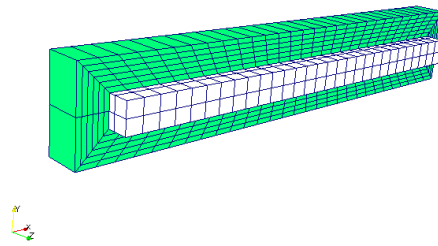


Figure 4.19: Three-dimensional freely moving snake: Embedded fluid mesh at the cross section.

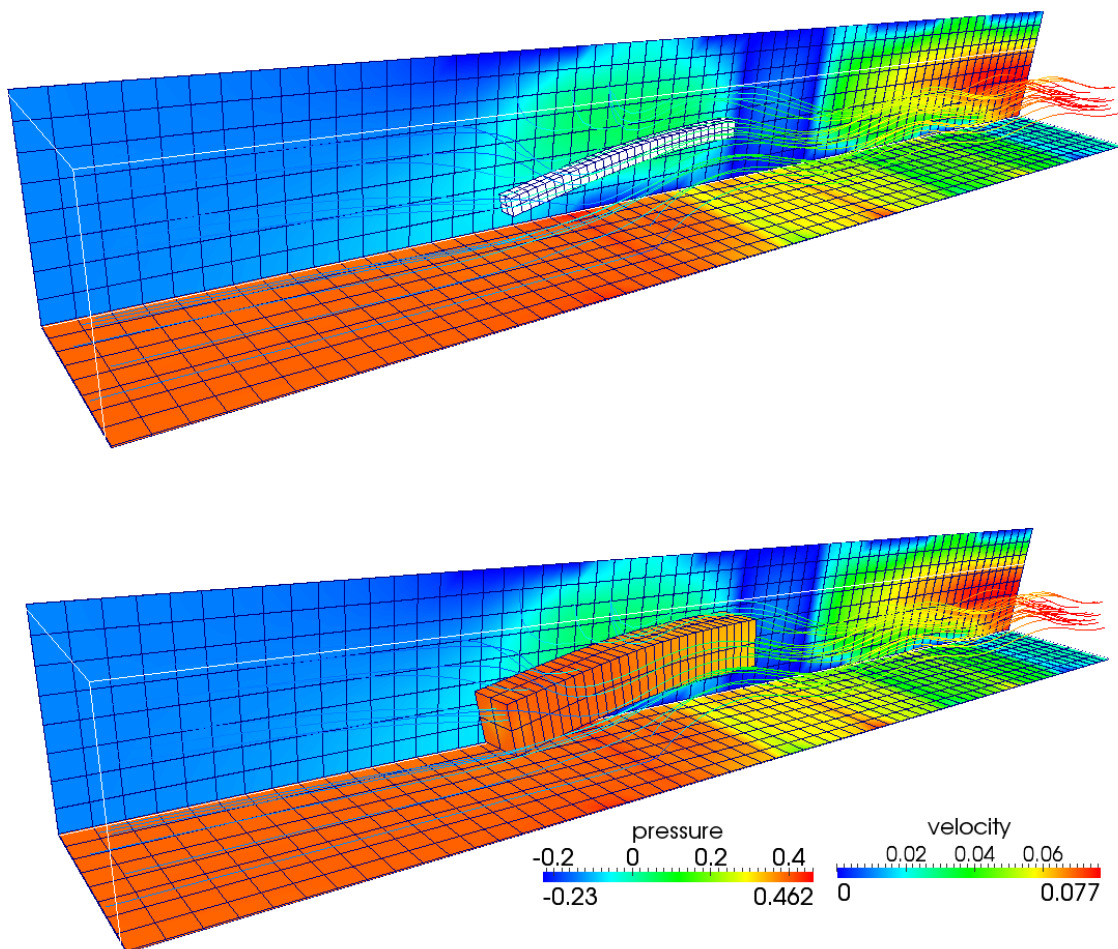


Figure 4.20: Three-dimensional freely moving snake: The velocity field is shown at the cross section and the pressure field at the bottom wall at $t = 6.624 s$. The structure is depicted at the top, while the embedded fluid mesh, colored by pressure field, is shown at the bottom. Streamlines illustrate the flow in the channel colored by velocity magnitude.

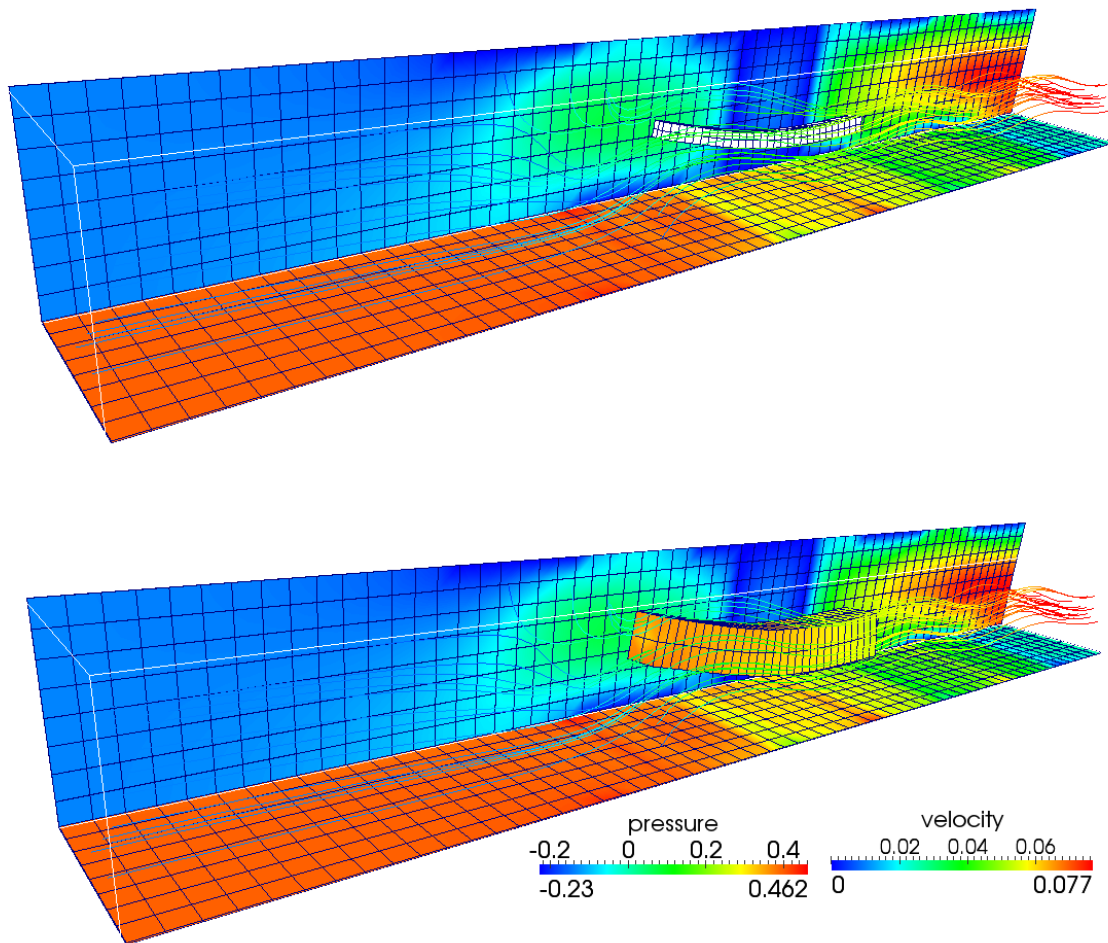


Figure 4.21: Three-dimensional freely moving snake: The velocity field is shown at the cross section and the pressure field at the bottom wall at $t = 8.244 s$. The structure is depicted at the top, while the embedded fluid mesh, colored by pressure field, is shown at the bottom. Streamlines illustrate the flow in the channel colored by velocity magnitude.

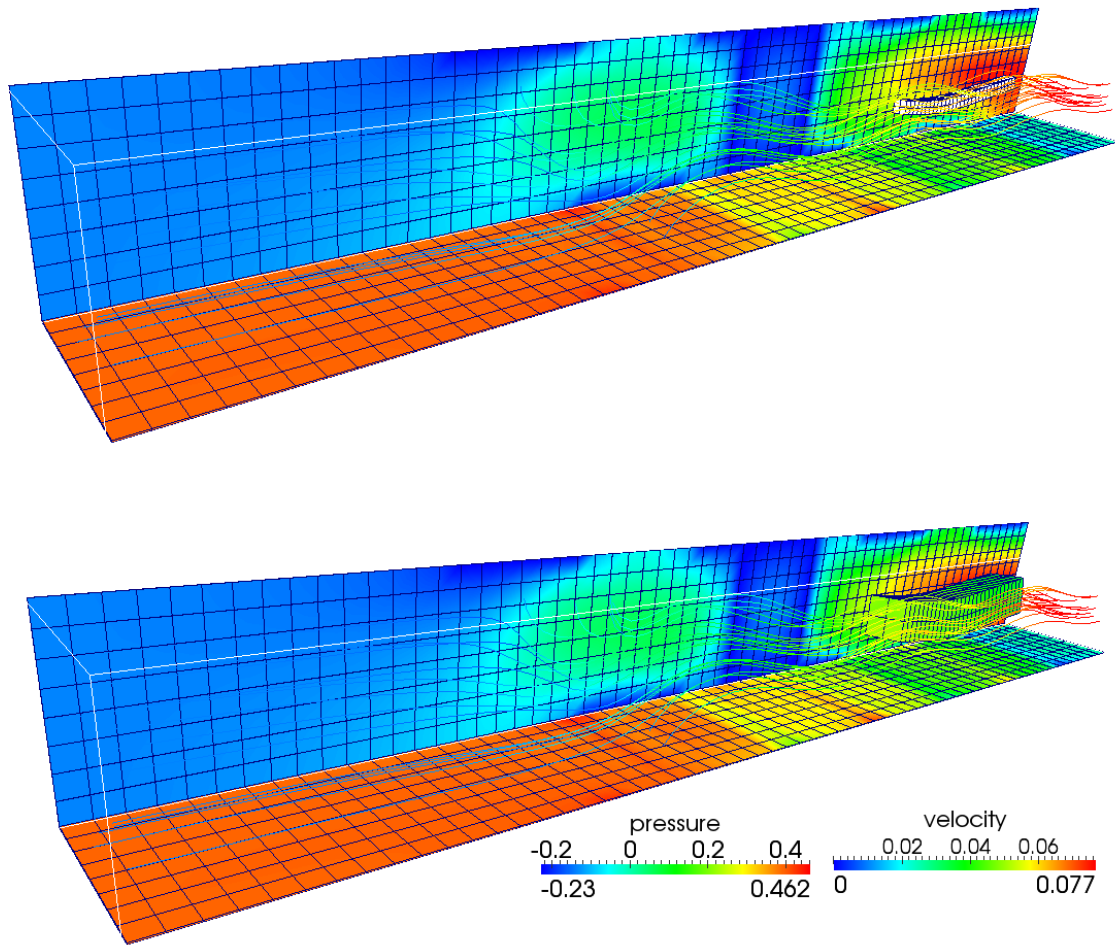
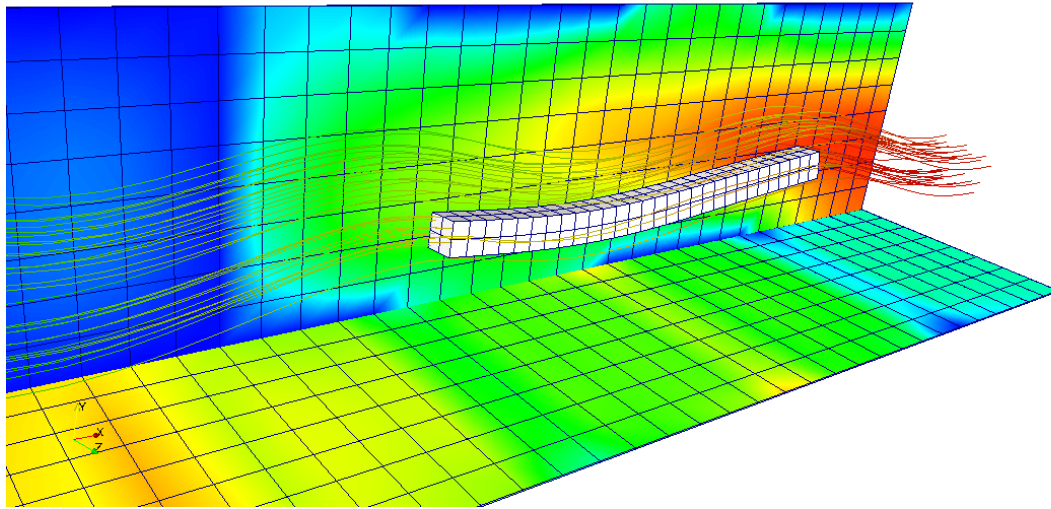
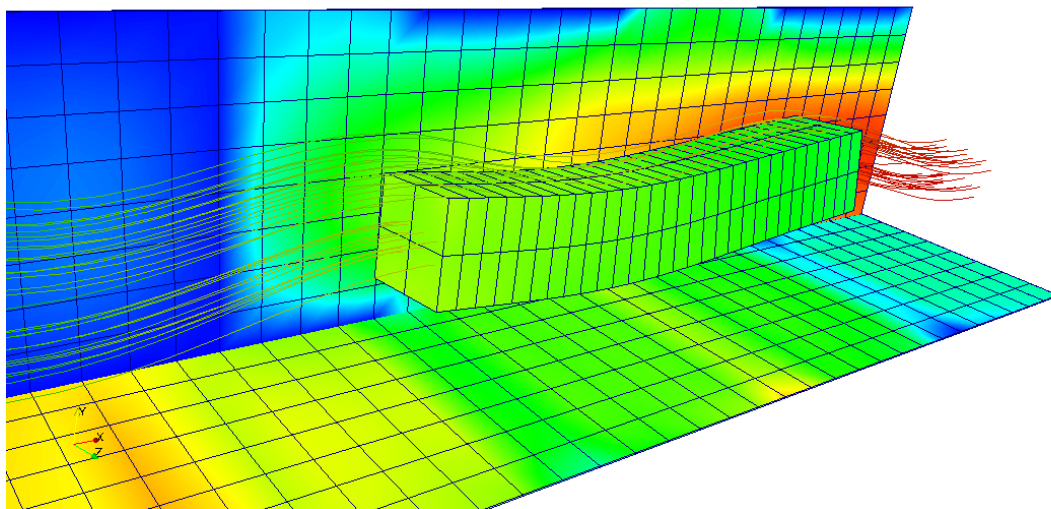


Figure 4.22: Three-dimensional freely moving snake: The velocity field is shown at the cross section and the pressure field at the bottom wall at $t = 10.332 s$. The structure is depicted at the top, while the embedded fluid mesh, colored by pressure field, is shown at the bottom. Streamlines illustrate the flow in the channel colored by velocity magnitude.

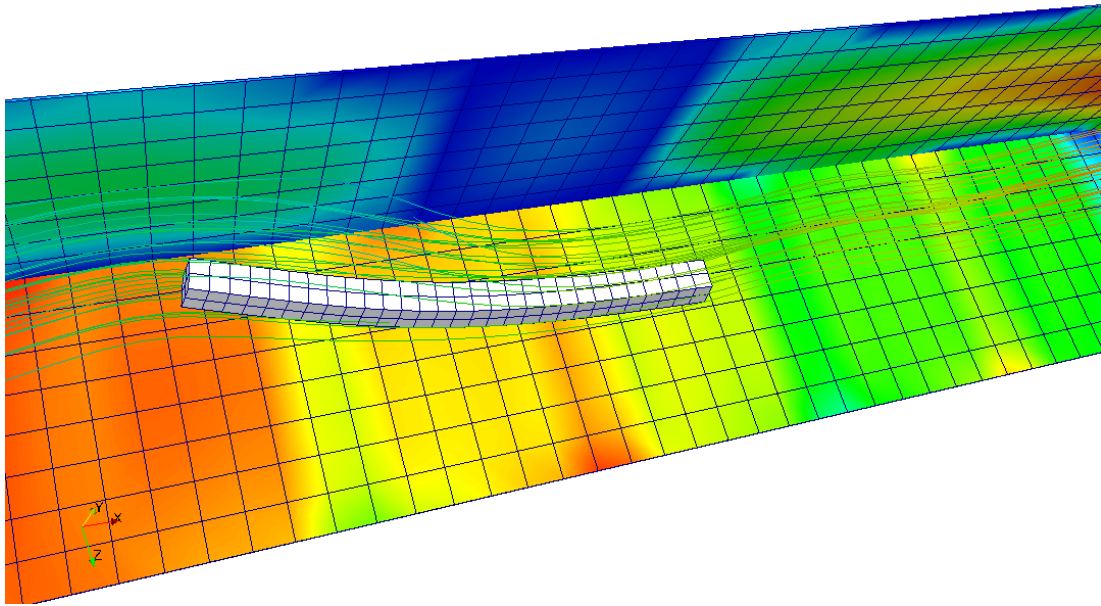


(a)

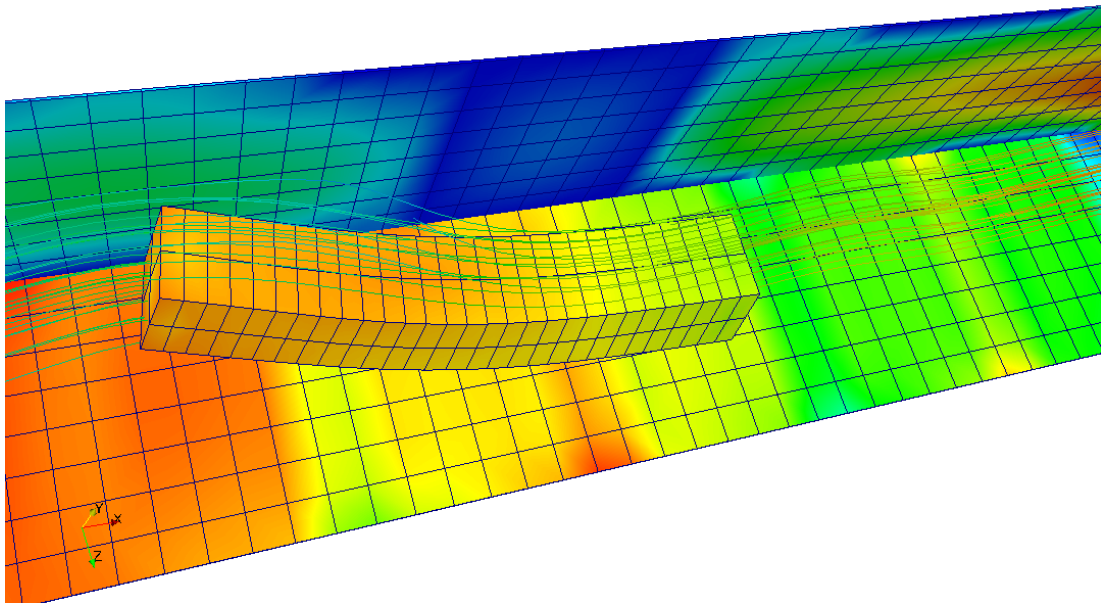


(b)

Figure 4.23: Three-dimensional freely moving snake: **(a)** Close up view of the structure field at $t = 10.332 s$. **(b)** Close up view of the embedded field mesh, colored by pressure field at $t = 10.332 s$. The velocity field is shown at the cross section and the pressure field at the bottom wall. Streamlines illustrate the flow in channel colored by velocity field.



(a)



(b)

Figure 4.24: Three-dimensional freely moving snake: **(a)** Plane view of the structure field at $t = 8.406$ s. **(b)** Plane view of the embedded field mesh, colored by pressure field at $t = 8.406$ s. The velocity field is shown at the cross section and the pressure field at the bottom wall. Streamlines illustrate the flow in channel colored by velocity field.

5 Summary and Outlook

The focus of this thesis has been the development of a fluid-structure interaction (FSI) approach, particularly suited for complex two- and three-dimensional FSI problems with incompressible flow and structures, undergoing large deformations, which provides a proper resolution of the flow features at structural surface throughout the simulation. This is an import prerequisite for achieving reliable results, particularly, for high Reynolds number flow, where steep gradients in normal direction of the surface have to be resolved. In order to achieve this task, a hybrid ALE-fixed-grid FSI approach combining the advantages of Arbitrary-Lagrangian-Eulerian (ALE)-based FSI techniques and fixed-grid FSI approaches has been developed .

In this method, the structure, described in a Lagrangian formulation, is surrounded by a surface layer of deformable fluid elements based on an ALE formulation. This deformable fluid patch, which is embedded in the fixed-grid Eulerian background fluid, moves and deforms with the structure, providing an appropriate boundary layer mesh for it, throughout the simulation. The coupling between the two fluid subdomains is weakly imposed using a stabilized formulation at the fluid-fluid interface. The structure and the moving fluid are coupled in the same way as classical ALE-based FSI approaches. Thus, the formulation has been derived in two main steps: developing a stable, robust and accurate embedded fluid formulation for stationary and moving interfaces, and the coupling of the derived embedded fluid formulation with the structure field.

In the first step, the concentration has been on the coupling between the background and embedded fluid subdomains. For this purpose, first, the background fluid subdomain has been decoupled into a physical and a fictitious/void part. In order to describe a jump from the physical values of the background fluid to zero along the fluid-fluid interface and assign DOFs to the volume-cells of cut elements, an extended finite element method (XFEM)-based formulation in combination with a DOF-management algorithm has been proposed. Afterwards, the focus has been shifted to the main challenge, development of a stable formulation for weak enforcement of coupling conditions at the fluid-fluid interface independent of the interface position or the complexity of the form of the fluid patch. In this context, three methods for weak imposition of coupling conditions, Nitsche's method, mixed/hybrid Cauchy stress-based method and mixed/hybrid viscous stress-based method, considering both variants, background and embedded sided weighting of coupling conditions, have been introduced. In this regard, the similarities and differences of the formulations and their solution behaviors, regarding stability of coupling conditions at the interface, have been discussed. Face-oriented stabilizations have been applied to control ghost values sufficiently, to balance instabilities in the interface zone for viscous as well as convective dominated flows, and to improve the system conditioning. For a better control of ghost values, in the case of embedded sided weighting of coupling conditions, and for a stable formulation, in the case of background sided weighting of coupling conditions, and to improve the system conditioning in both cases additional ghost-penalty stabilizations are added to the faces of cut elements. Furthermore, to overcome instabilities caused by the convective mass transport across the interface, additional inflow stabilization terms have been introduced.

Finally, a stabilized embedded fluid formulation has been proposed, built from the following essential ingredients: Coupling conditions on the embedded interface have been weakly imposed using an embedded sided weighting of Nitsche's formulation. The Nitsche parameter has been determined via local eigenvalue problems, which provide a good estimation for arbitrary element shapes, forms and polynomial orders. Additional face-oriented and ghost-penalty terms have been added to the cut elements. Convective mass transport inflow stabilization at the interface have been included. A detailed convergence analysis has shown the optimal error convergence of the proposed embedded fluid formulation for viscous and convective dominated flows. The proposed embedded fluid formulation has been applied to moving interfaces introducing a new XFEM time-integration approach for handling the issue of Eulerian background fluid mesh in combination with moving interfaces. The XFEM time-integration approach reconstructs the missing values of background fluid mesh at the previous time step from the embedded fluid mesh, which provides a flow field with the same physical properties at the previous time step. Results of numerical examples have shown the correctness of the proposed approach for stationary and moving interfaces independent of the interface position.

In the second step, structural equations have been coupled with the proposed embedded fluid formulation into a monolithic FSI system. The coupling of the structure field and the fluid field has been performed in the same way as ALE-based FSI approach, see e.g. Küttler [120], which allows for using coupling algorithms, originally developed for classical ALE-based FSI approaches. For the monolithic FSI system, the embedded fluid interface is an internal interface, which is hidden in the fluid system, and does not affect the FSI coupling directly. However, solving the coupled nonlinear hybrid FSI system with Newton-Raphson scheme in a straightforward way would introduce further complexities, regarding the Eulerian description of fixed-grid background fluid in combination with moving fluid patch. It would lead to a global FSI system, which changes its degrees of freedom in every Newton step. The reason is that a new position of the fluid-fluid interface gives rise to new physical and fictitious background fluid parts and, thus, new degrees of freedom arise and some degrees of freedom disappear in every Newton step. Moreover, the missing values at the previous Newton step of the fixed-grid background fluid mesh have to be reconstructed with the XFEM time-integration approach. This process would result in a perturbation in every Newton step, which would prevent any convergence or result in poor convergence behavior of the Newton-Raphson scheme. To avoid these complexities, a novel FSI approach stated as relaxing ALE approach has been proposed. The key idea of the relaxing ALE approach is that the position of the internal fluid-fluid interface does not change during the Newton-Raphson scheme and it is updated at the end of the time step in order to avoid any alteration of degrees of freedom within the Newton loop. Two- and three- dimensional numerical examples have validated the hybrid ALE-fixed-grid approach and shown the ability and potential of the hybrid FSI approach.

Several open tasks remain to make the approach robust, accurate and efficient for complex real-world problems such as modeling of biofilms, see e.g. Taherzadeh et al. [166] and Coroneo et al. [53]. In the following, the most important tasks are listed.

Using high aspect ratio elements in surface-normal direction of the structure is an efficient way to resolve high gradients. This is particularly essential for high Reynolds number flows where the gradients in the flow variables in the normal direction of structural surface are much higher than the gradients along the surface. In such a scenario, where high aspect ratio elements are used for embedded fluid subdomain, a stable imposition of coupling conditions at the fluid-fluid

interface needs further investigations. As mentioned above, in order to have a stable formulation regarding coupling conditions and to avoid problems with critical cuts at the interface, in this work, an embedded element weighting of Nitsche's method has been applied. Nitsche's parameter has been estimated via solving local eigenvalue problems on embedded fluid elements, which implicitly includes a relation of coupling surface area of embedded fluid element and its volume, as shown in equation (3.42). Thus, using elements with high aspect ratios, can increase Nitsche's parameter, which subsequently, could result in an ill-conditioned system. Hence, for such elements, it needs to be investigated if the embedded-sided weighting of Nitsche's method is still a proper choice or either a background element weighting of Nitsche's method, which is a stable formulation regarding interface coupling in combination with a ghost-penalty operator, would possibly be a more reasonable choice. Furthermore, in this context, the choice of different aspect ratios needs to be investigated, which certainly also depends on the application itself.

The XFEM time-integration approach given in this thesis has provided a stable and robust solution over the simulation time. However, due to the interpolation process of the values of embedded fluid to missing values of background fluid mesh, an interpolation-error is introduced. A temporal convergence analysis of the proposed XFEM time-integration approach would show the influence of the interpolation-error on the temporal convergence rate of the applied time-integration scheme, the one-step- θ scheme. As an example, for further convergence studies the two-dimensional Kim-Moin flow, given in Section 3.7, can be used in combination with moving embedded fluid.

Furthermore, from the implementation point of view, load balancing of the background cut elements is an important step toward having an efficient implementation. Cut elements are much more expensive, compared to elements far from the fluid-fluid interface, as there are several additional steps, which have to be performed on them. Besides the cut process itself, the integration process is more expensive, since more integration points are required for a cut element. Moreover, the ghost-penalty and face-oriented stabilizations increase the bandwidth of the matrix, and consequently the solution time. Thus, with a new distribution of the background fluid mesh, which depends on the position of fluid-fluid interface, the load of the expensive cut elements would be balanced among the processors.

The hybrid ALE-fixed-grid FSI approach has been developed based on the assumption that the embedded fluid subdomain and structure domain share the same nodes at the fluid-structure interface. However, in order to be able to deal with non-conforming meshes at the fluid-structure interface, the hybrid ALE-fixed-grid FSI approach needs to be extended to non-matching meshes at the interface. Monolithic FSI approaches for non-conforming meshes based on dual mortar method have been already proposed by Klöppel [115], Klöppel et al. [117] and Mayr et al. [135]. In these approaches, the dual mortar approach allows for the elimination of FSI Lagrange multiplier degrees of freedom from the global FSI system by condensation, such that, the resulting system matrices have the same block structure as the matrices for the conforming case.

A Appendix

A.1 Derivation of a lower bound of the Nitsche parameter for Stokes problem

In the following, an estimation of the lower bound of the Nitsche stabilization parameter α' in (3.31) for an embedded element weighting of Nitsche's method applied to Stokes problems, is derived, in order to achieve a coercive formulation of the viscous part. In the same way a lower bound of the Nitsche stabilization parameter can be derived for background element weighting of Nitsche's method. A coercivity analysis for Poisson embedded interface problems is given, e.g. in Dolbow and Harari [59].

A general setup of the problem is presented in Section 3.1, where the entire physical fluid domain is divided into background fluid subdomain Ω^b and embedded fluid subdomain Ω^e by the fluid-fluid interface Γ^{FF} , as depicted in Figure 3.1. The strong form of embedded fluid formulation for Stokes problem can be stated as

$$\nabla p^i - 2\mu \nabla \cdot \boldsymbol{\epsilon}(\mathbf{u}^i) = \mathbf{f}^i \quad \text{in } \Omega^i, \quad (\text{A.1})$$

$$\nabla \cdot \mathbf{u}^i = 0 \quad \text{in } \Omega^i, \quad (\text{A.2})$$

$$[[\mathbf{u}]] = 0 \quad \text{on } \Gamma^{\text{FF}}, \quad (\text{A.3})$$

$$[(-p\mathbf{I} + 2\mu\boldsymbol{\epsilon}(\mathbf{u})) \cdot \mathbf{n}] = 0 \quad \text{on } \Gamma^{\text{FF}}, \quad (\text{A.4})$$

for $i \in \{b, e\}$. Hereby \mathbf{n} is defined as the outward pointing normal with respect to Ω^b , i.e. $\mathbf{n} := \mathbf{n}^b = -\mathbf{n}^e$. As in Chapter 3, equal-order continuous approximations on 3D trilinear hexahedral elements for all velocity components $u_h^i, v_h^i, (i = 1, 2, 3)$ and the pressure q^h, p^h are used, such that

$$\mathbf{v}_h^b, \mathbf{u}_h^b \in V_h^b := \{\mathbf{v} \in [C^0(\Omega^b)]^3 : \mathbf{v}|_V \in [Q^1(K)]^3 \forall V \in \Omega_K^b, \forall K \in \mathcal{T}^*\}, \quad (\text{A.5})$$

$$q_h^b, p_h^b \in Q_h^b := \{q \in C^0(\Omega^b) : q|_V \in Q^1(K) \forall V \in \Omega_K^b, \forall K \in \mathcal{T}^*\}, \quad (\text{A.6})$$

$$\mathbf{v}_h^e, \mathbf{u}_h^e \in V_h^e := \{\mathbf{v} \in [C^0(\Omega^e)]^3 : \mathbf{v}|_K \in [Q^1(K)]^3 \forall K \in \mathcal{T}^e\}, \quad (\text{A.7})$$

$$q_h^e, p_h^e \in Q_h^e := \{q \in C^0(\Omega^e) : q|_K \in Q^1(K) \forall K \in \mathcal{T}^e\}. \quad (\text{A.8})$$

The discrete version of Nitsche bilinear form, $a_h((\mathbf{u}_h^b, p_h^b), (\mathbf{v}_h^e, q_h^e))$, reads as:

Find $(\mathbf{u}_h^b, p_h^b) \in V_h^b \times Q_h^b$ and $(\mathbf{u}_h^e, p_h^e) \in V_h^e \times Q_h^e$ such that $\forall (\mathbf{v}_h^b, q_h^b) \in V_h^b \times Q_h^b$ and $\forall (\mathbf{v}_h^e, q_h^e) \in V_h^e \times Q_h^e$ it holds

$$\begin{aligned}
a((\mathbf{u}_h^b, p_h^b, \mathbf{u}_h^e, p_h^e), (\mathbf{v}_h^b, q_h^b, \mathbf{v}_h^e, q_h^e)) &= (q_h^b, \nabla \cdot \mathbf{u}_h^b)_{\Omega^b} - (\nabla \cdot \mathbf{v}_h^b, p_h^b)_{\Omega^b} + (\boldsymbol{\epsilon}(\mathbf{v}_h^b), 2\mu\boldsymbol{\epsilon}(\mathbf{u}_h^b))_{\Omega^b} \\
&+ (q_h^e, \nabla \cdot \mathbf{u}_h^e)_{\Omega^e} - (\nabla \cdot \mathbf{v}_h^e, p_h^e)_{\Omega^e} + (\boldsymbol{\epsilon}(\mathbf{v}_h^e), 2\mu\boldsymbol{\epsilon}(\mathbf{u}_h^e))_{\Omega^e} \\
&+ \langle \llbracket \mathbf{v}_h \rrbracket, \{p_h \cdot \mathbf{n}\} \rangle_{\Gamma^{\text{FF}}} - \langle \llbracket \mathbf{v}_h \rrbracket, \{2\mu\boldsymbol{\epsilon}(\mathbf{u}_h) \cdot \mathbf{n}\} \rangle_{\Gamma^{\text{FF}}} \\
&- \langle \{q_h \cdot \mathbf{n}\}, \llbracket \mathbf{u}_h \rrbracket \rangle_{\Gamma^{\text{FF}}} - \langle \{2\mu\boldsymbol{\epsilon}(\mathbf{v}_h) \cdot \mathbf{n}\}, \llbracket \mathbf{u}_h \rrbracket \rangle_{\Gamma^{\text{FF}}} \\
&+ \langle \alpha' \llbracket \mathbf{v}_h \rrbracket, \llbracket \mathbf{u}_h \rrbracket \rangle_{\Gamma^{\text{FF}}}.
\end{aligned} \tag{A.9}$$

Hereby, for the embedded-sided weighting of the averaged operators, the consistency and adjoint consistency terms, third and fourth line of (A.9), become

$$\begin{aligned}
&+ \langle \llbracket \mathbf{v}_h \rrbracket, p_h^e \cdot \mathbf{n} \rangle_{\Gamma^{\text{FF}}} - \langle \llbracket \mathbf{v}_h \rrbracket, 2\mu\boldsymbol{\epsilon}(\mathbf{u}_h^e) \cdot \mathbf{n} \rangle_{\Gamma^{\text{FF}}} \\
&- \langle q_h^e \cdot \mathbf{n}, \llbracket \mathbf{u}_h \rrbracket \rangle_{\Gamma^{\text{FF}}} - \langle 2\mu\boldsymbol{\epsilon}(\mathbf{v}_h^e) \cdot \mathbf{n}, \llbracket \mathbf{u}_h \rrbracket \rangle_{\Gamma^{\text{FF}}}.
\end{aligned} \tag{A.10}$$

By replacing (\mathbf{v}_h^b, q_h^b) by (\mathbf{u}_h^b, p_h^b) and (\mathbf{v}_h^e, q_h^e) by (\mathbf{u}_h^e, p_h^e) the discrete form (A.9) can then be written as

$$\begin{aligned}
a((\mathbf{u}_h^b, p_h^b, \mathbf{u}_h^e, p_h^e), (\mathbf{u}_h^b, p_h^b, \mathbf{u}_h^e, p_h^e)) &= (p_h^b, \nabla \cdot \mathbf{u}_h^b)_{\Omega^b} - (\nabla \cdot \mathbf{u}_h^b, p_h^b)_{\Omega^b} + (\boldsymbol{\epsilon}(\mathbf{u}_h^b), 2\mu\boldsymbol{\epsilon}(\mathbf{u}_h^b))_{\Omega^b} \\
&+ (p_h^e, \nabla \cdot \mathbf{u}_h^e)_{\Omega^e} - (\nabla \cdot \mathbf{u}_h^e, p_h^e)_{\Omega^e} + (\boldsymbol{\epsilon}(\mathbf{u}_h^e), 2\mu\boldsymbol{\epsilon}(\mathbf{u}_h^e))_{\Omega^e} \\
&+ \langle \llbracket \mathbf{u}_h \rrbracket, p_h^e \cdot \mathbf{n} \rangle_{\Gamma^{\text{FF}}} - \langle \llbracket \mathbf{u}_h \rrbracket, 2\mu\boldsymbol{\epsilon}(\mathbf{u}_h^e) \cdot \mathbf{n} \rangle_{\Gamma^{\text{FF}}} \\
&- \langle p_h^e \cdot \mathbf{n}, \llbracket \mathbf{u}_h \rrbracket \rangle_{\Gamma^{\text{FF}}} - \langle 2\mu\boldsymbol{\epsilon}(\mathbf{u}_h^e) \cdot \mathbf{n}, \llbracket \mathbf{u}_h \rrbracket \rangle_{\Gamma^{\text{FF}}} \\
&+ \langle \alpha' \llbracket \mathbf{u}_h \rrbracket, \llbracket \mathbf{u}_h \rrbracket \rangle_{\Gamma^{\text{FF}}} \\
&= (\boldsymbol{\epsilon}(\mathbf{u}_h^b), 2\mu\boldsymbol{\epsilon}(\mathbf{u}_h^b))_{\Omega^b} + (\boldsymbol{\epsilon}(\mathbf{u}_h^e), 2\mu\boldsymbol{\epsilon}(\mathbf{u}_h^e))_{\Omega^e} \\
&- \langle \llbracket \mathbf{u}_h \rrbracket, 2\mu\boldsymbol{\epsilon}(\mathbf{u}_h^e) \cdot \mathbf{n} \rangle_{\Gamma^{\text{FF}}} - \langle 2\mu\boldsymbol{\epsilon}(\mathbf{u}_h^e) \cdot \mathbf{n}, \llbracket \mathbf{u}_h \rrbracket \rangle_{\Gamma^{\text{FF}}} \\
&+ \langle \alpha' \llbracket \mathbf{u}_h \rrbracket, \llbracket \mathbf{u}_h \rrbracket \rangle_{\Gamma^{\text{FF}}}.
\end{aligned} \tag{A.11}$$

Using the following definitions of the L_2 -norm of a quantity over the background fluid subdomain Ω^b , embedded fluid subdomain Ω^e and along the interface Γ^{FF}

$$\|\mathbf{w}\|_{\Omega^i} = \left(\int_{\Omega^i} \mathbf{w}^2 d\Omega^i \right)^{1/2}, \quad \text{for } i \in \{b, e\}, \tag{A.12}$$

$$\|\mathbf{w}\|_{\Gamma^{\text{FF}}} = \left(\int_{\Gamma^{\text{FF}}} \mathbf{w}^2 d\Gamma^{\text{FF}} \right)^{1/2}, \tag{A.13}$$

the bilinear form (A.11) can be written as

$$\begin{aligned}
a((\mathbf{u}_h^b, p_h^b, \mathbf{u}_h^e, p_h^e), (\mathbf{u}_h^b, p_h^b, \mathbf{u}_h^e, p_h^e)) &= 2\mu \|\boldsymbol{\epsilon}(\mathbf{u}_h^b)\|_{\Omega^b}^2 + 2\mu \|\boldsymbol{\epsilon}(\mathbf{u}_h^e)\|_{\Omega^e}^2 \\
&+ 2\mu \int_{\Gamma^{\text{FF}}} \llbracket \mathbf{u}_h \rrbracket \boldsymbol{\epsilon}(\mathbf{u}_h^e) \cdot \mathbf{n} d\Gamma^{\text{FF}} + \alpha' \|\llbracket \mathbf{u}_h \rrbracket\|_{\Gamma^{\text{FF}}}^2.
\end{aligned} \tag{A.14}$$

Employing *Young's inequality* with $\epsilon > 0$, which states: Let $a, b, \epsilon \geq 0$, then it holds

$$ab \leq \frac{a^2}{2\epsilon} + \frac{\epsilon b^2}{2}, \tag{A.15}$$

results in

$$\begin{aligned}
 a((\mathbf{u}_h^b, p_h^b, \mathbf{u}_h^e, p_h^e), (\mathbf{u}_h^b, p_h^b, \mathbf{u}_h^e, p_h^e)) &\geq 2\mu \|\boldsymbol{\epsilon}(\mathbf{u}_h^b)\|_{\Omega^b}^2 + 2\mu \|\boldsymbol{\epsilon}(\mathbf{u}_h^e)\|_{\Omega^e}^2 \\
 &\quad - \frac{1}{\epsilon} \mu \|[\![\mathbf{u}_h]\!] \|_{\Gamma^{\text{FF}}}^2 - \epsilon \mu \|\boldsymbol{\epsilon}(\mathbf{u}_h^e) \cdot \mathbf{n}\|_{\Gamma^{\text{FF}}}^2 \\
 &\quad + \alpha' \|[\![\mathbf{u}_h]\!] \|_{\Gamma^{\text{FF}}}^2,
 \end{aligned} \tag{A.16}$$

with $\epsilon > 0$. The following inverse inequality holds

$$\|\boldsymbol{\epsilon}(\mathbf{u}_h^e) \cdot \mathbf{n}\|_{\Gamma^{\text{FF}} \cap K}^2 \leq C_K^e \cdot \|\boldsymbol{\epsilon}(\mathbf{u}_h^e)\|_{\Omega^e \cap K}^2, \tag{A.17}$$

for an embedded element K adjacent to the interface Γ^{FF} , with $\Omega^e \cap K$ denoting the entire embedded fluid element K and $\Gamma^{\text{FF}} \cap K$ the boundary of K at Γ^{FF} . Furthermore, C_K^e is a constant independent of the position of the fluid-fluid interface Γ^{FF} . Considering (A.17) the bilinear form can be written over the sum of elements as

$$\begin{aligned}
 a((\mathbf{u}_h^b, p_h^b, \mathbf{u}_h^e, p_h^e), (\mathbf{u}_h^b, p_h^e, \mathbf{u}_h^e, p_h^e)) &\geq \sum_{K^b} 2\mu \|\boldsymbol{\epsilon}(\mathbf{u}_h^b)\|_{\Omega_K^b}^2 + \sum_{K^e} 2\mu \|\boldsymbol{\epsilon}(\mathbf{u}_h^e)\|_{\Omega_K^e}^2 \\
 &\quad - \sum_K \frac{1}{\epsilon} \mu \|[\![\mathbf{u}_h]\!] \|_{\Gamma_K^{\text{FF}}}^2 - \sum_{K^e} \epsilon \mu C_K^e \|\boldsymbol{\epsilon}(\mathbf{u}_h^e)\|_{\Omega_K^e}^2 + \sum_K \alpha' \|[\![\mathbf{u}_h]\!] \|_{\Gamma_K^{\text{FF}}}^2 \\
 &= \sum_{K^b} 2\mu \|\boldsymbol{\epsilon}(\mathbf{u}_h^b)\|_{\Omega_K^b}^2 + \sum_{K^e} (2\mu - \epsilon \mu C_K^e) \|\boldsymbol{\epsilon}(\mathbf{u}_h^e)\|_{\Omega_K^e}^2 \\
 &\quad + \sum_K \left(-\frac{1}{\epsilon} \mu + \alpha'\right) \|[\![\mathbf{u}_h]\!] \|_{\Gamma_K^{\text{FF}}}^2.
 \end{aligned} \tag{A.18}$$

Hereby, K^b and K^e denote the elements of background and embedded fluid subdomains, respectively. Considering

$$2\mu - \epsilon \mu C_K^e \geq C > 0, \tag{A.19}$$

with C is a constant greater than 0, the value of ϵ can be chosen as $\epsilon = \frac{1}{C_K^e}$. Then, the bilinear form (A.18) can be estimated as

$$\begin{aligned}
 a((\mathbf{u}_h^b, p_h^b, \mathbf{u}_h^e, p_h^e), (\mathbf{u}_h^b, p_h^b, \mathbf{u}_h^e, p_h^e)) &\geq \sum_{K^b} 2\mu \|\boldsymbol{\epsilon}(\mathbf{u}_h^b)\|_{\Omega_K^b}^2 + \sum_{K^e} \mu \|\boldsymbol{\epsilon}(\mathbf{u}_h^e)\|_{\Omega_K^e}^2 \\
 &\quad + \sum_K (\alpha' - C_K^e \mu) \|[\![\mathbf{u}_h]\!] \|_{\Gamma_K^{\text{FF}}}^2.
 \end{aligned} \tag{A.20}$$

Thus, the coercivity of the bilinear is ensured when

$$\alpha' > C_K^e \mu. \tag{A.21}$$

Therefore, the Nitsche stabilization parameter α' can be defined as

$$\alpha' := \delta C_K^e \mu, \tag{A.22}$$

where δ is a user-defined constant, which has to be greater than 1.

A.2 Convergence study with two-dimensional Kim-Moin flow

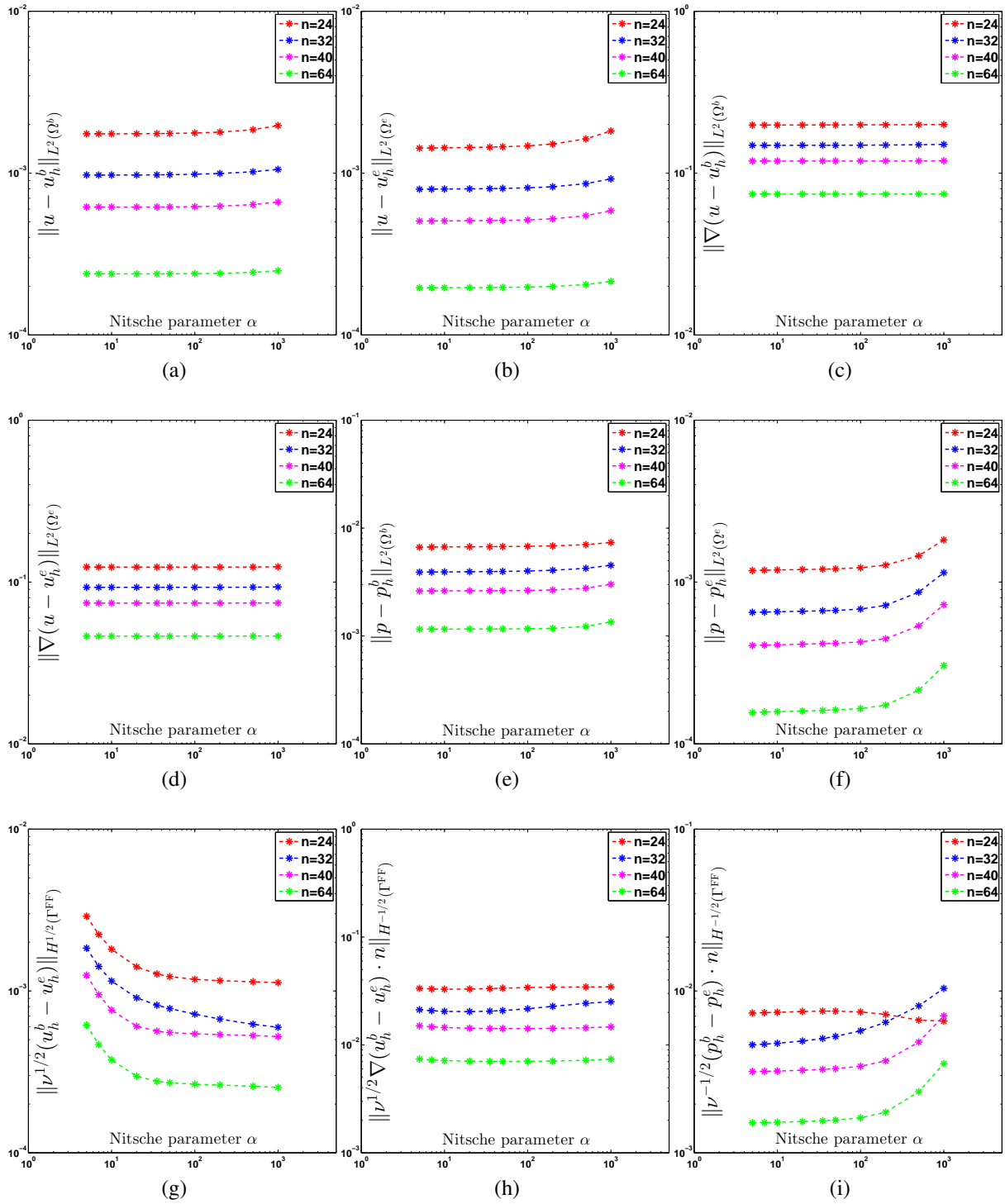


Figure A.1: Stationary Kim-Moin-flow: Error-norms for varying Nitsche parameter α .

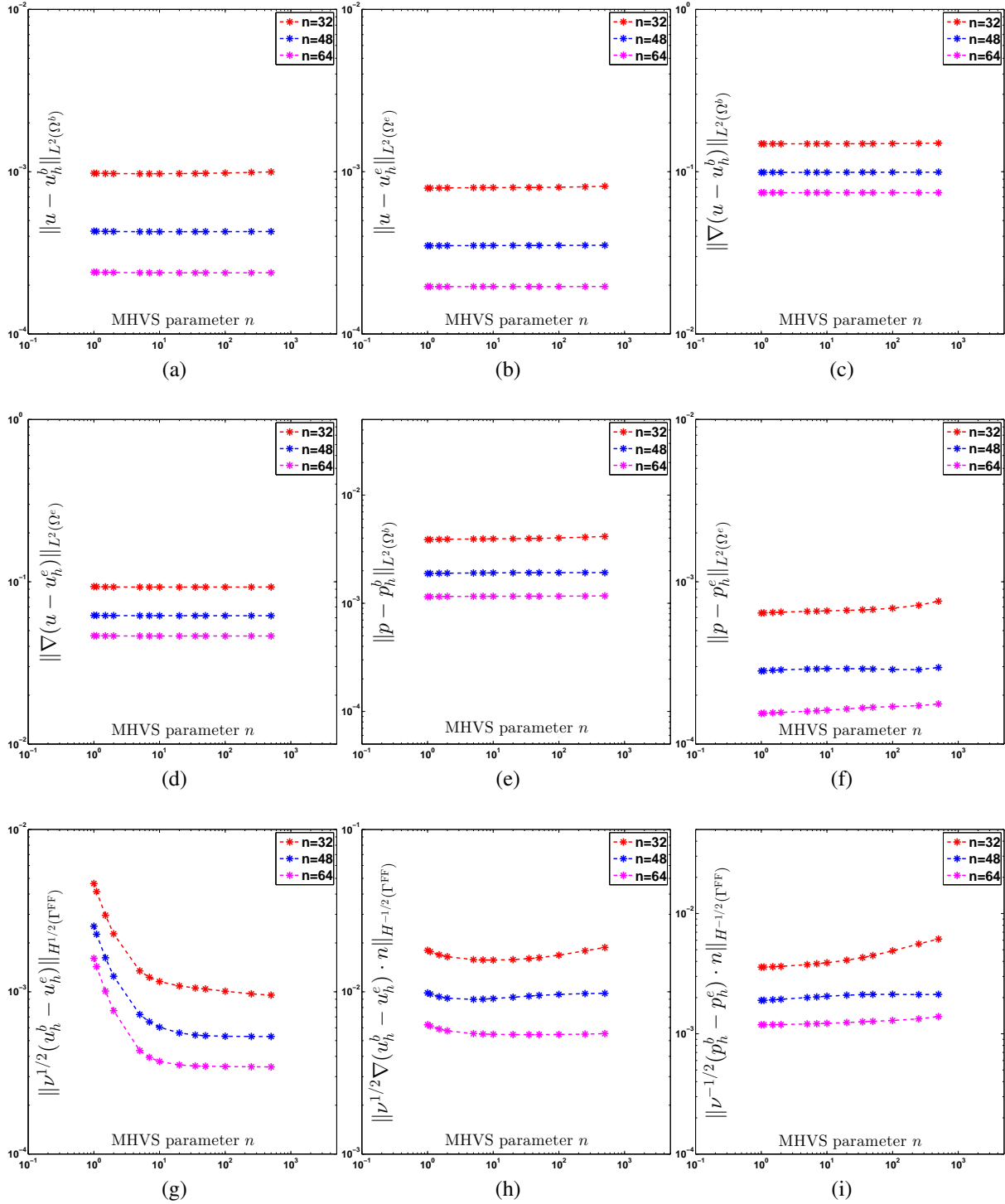


Figure A.2: Stationary Kim-Moin flow: Error-norms for varying MHVS parameter n .

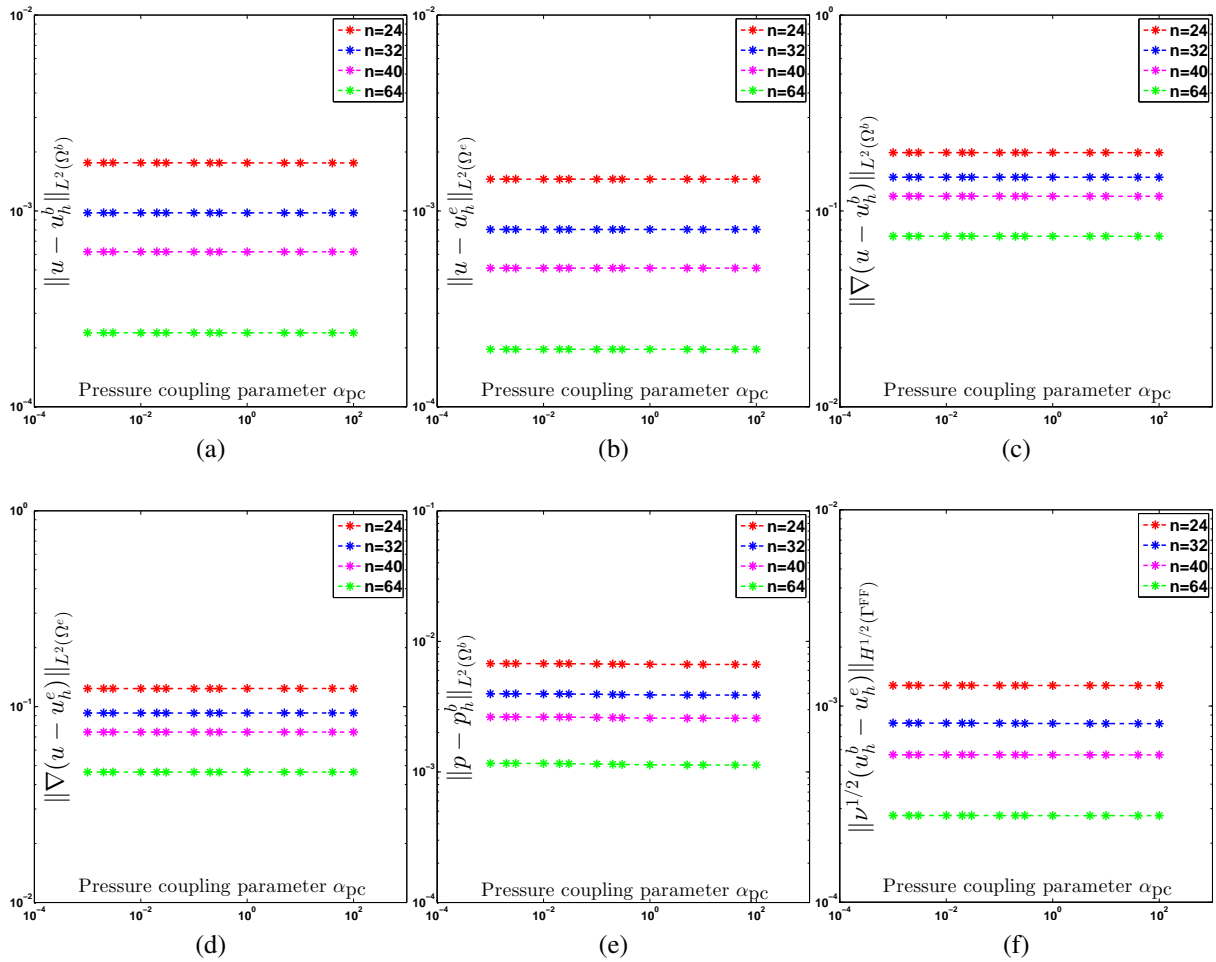


Figure A.3: Stationary Kim-Moin flow: Error-norms for varying interface pressure coupling parameter α_{pc} .

Bibliography

- [1] F. Alauzet, A changing-topology moving mesh technique for large displacements, *Engineering with Computers* **30**, 175–200, 2014.
- [2] C. Annavarapu, M. Hautefeuille, and J. Dolbow, A robust Nitsche’s formulation for interface problems, *Computer Methods in Applied Mechanics and Engineering* **225-228**, 44–54, 2012.
- [3] D. Arnold, F. Brezzi, B. Cockburn, and L. Marini, Unified analysis of Discontinuous Galerkin Methods for Elliptic Problems, *SIAM Journal on Numerical Analysis* **39**, 1749–1779, 2002.
- [4] F. Baaijens, A fictitious domain/mortar element method for fluid-structure interaction, *International Journal for Numerical Methods in Fluids* **35**, 743–761, 2001.
- [5] I. Babuška, Error-bounds for finite element method, *Numerische Mathematik* **16**, 322–333, 1971.
- [6] I. Babuška, The finite element method with Lagrangian multipliers, *Numerische Mathematik* **20**, 179–192, 1973.
- [7] I. Babuška and U. Banerjee, Stable Generalized Finite Element Method (SGFEM), *Computer Methods in Applied Mechanics and Engineering* **201-204**, 91–111, 2012.
- [8] I. Babuška and J. Melenk, The partition of unity finite element method, *International Journal for Numerical Methods in Engineering* **40**, 727–758, 1997.
- [9] I. Babuška, G. Caloz, and J. Osborn, Special finite element methods for a class of second order elliptic problems with rough coefficients, *SIAM Journal on Numerical Analysis* **31**, 945–981, 1994.
- [10] J. Baiges and R. Codina, The fixed-mesh ALE approach applied to solid mechanics and fluid-structure interaction problems, *International Journal for Numerical Methods in Engineering* **81**, 1529–1557, 2010.
- [11] J. Baiges, R. Codina, F. Henke, S. Shahmiri, and W. Wall, A symmetric method for weakly imposing Dirichlet boundary conditions in embedded finite element meshes, *International Journal for Numerical Methods in Engineering* **90**, 636–658, 2012.
- [12] G. Barrenechea and F. Valentin, An unusual stabilized finite element method for a generalized Stokes problem, *Numerische Mathematik* **92**, 653–677, 2002.

- [13] J. Batina, Unsteady Euler algorithm with unstructured dynamic mesh for complex-aircraft aerodynamic analysis, *AIAA Journal* **29**, 327–333, 1991.
- [14] Y. Bazilevs and T. Hughes, Weak imposition of Dirichlet boundary conditions in fluid mechanics, *Computers & Fluids* **36**, 12–26, 2007.
- [15] Y. Bazilevs and T. Hughes, NURBS-based isogeometric analysis for the computation of flows about rotating components, *Computational Mechanics* **43**, 143–150, 2008.
- [16] E. Béchet, N. Moës, and B. Wohlmuth, A stable lagrange multiplier space for stiff interface conditions within the extended finite element method, *International Journal for Numerical Methods in Engineering* **78**, 931–954, 2009.
- [17] R. Becker, Mesh adaptation for Dirichlet flow control via Nitsche’s method, *Communications in Numerical Methods in Engineering* **18**, 669–680, 2002.
- [18] R. Becker and M. Braack, A finite element pressure gradient stabilization for the Stokes equations based on local projections, *CALCOLO* **38**, 173–199, 2001.
- [19] R. Becker, E. Burman, and P. Hansbo, A Nitsche extended finite element method for incompressible elasticity with discontinuous modulus of elasticity, *Computer Methods in Applied Mechanics and Engineering* **198**, 3352 – 3360, 2009.
- [20] M. Behr and T. Tezduyar, The Shear-Slip Mesh Update Method, *Computer Methods in Applied Mechanics and Engineering* **174**, 261 – 274, 1999.
- [21] M. Behr and T. Tezduyar, Shear-slip mesh update in 3d computation of complex flow problems with rotating mechanical components, *Computer Methods in Applied Mechanics and Engineering* **190**, 3189 – 3200, 2001.
- [22] T. Belytschko and T. Black, Elastic crack growth in finite elements with minimal remeshing, *International Journal for Numerical Methods in Engineering* **45**, 601–620, 1999.
- [23] T. Belytschko, J. Kennedy, and D. Schoeberle, Quasi-Eulerian finite element formulation for fluid structure interaction, *Journal of Pressure Vessel Technology* **109**, 62–69, 1980.
- [24] T. Belytschko, R. Gracie, and G. Ventura, A review of extended/generalized finite element methods for material modeling, *Modelling and Simulation in Materials Science and Engineering* **17**, 043001, 2009.
- [25] T. Belytschko and J. Kennedy, Computer models for subassembly simulation, *Nuclear Engineering and Design* **49**, 17–38, 1978.
- [26] M. Braack and E. Burman, Local Projection Stabilization for the Oseen Problem and its Interpretation as a Variational Multiscale Method, *SIAM Journal on Numerical Analysis* **43**, 2544–2566, 2006.
- [27] M. Braack, E. Burman, V. John, and G. Lube, Stabilized finite element methods for the generalized Oseen problem, *Computer Methods in Applied Mechanics and Engineering* **196**, 853–866, 2007.

-
- [28] F. Brezzi, On the existence, uniqueness and approximation of saddle-point problems arising from lagrangian multipliers, *ESAIM: Mathematical Modelling and Numerical Analysis - Modélisation Mathématique et Analyse Numérique* **8**, 129–151, 1974.
- [29] F. Brezzi and M. Fortin, *Mixed and hybrid finite element methods*, Springer Series in Computational Mathematics, Springer, 2002.
- [30] A. Brooks and T. Hughes, Streamline upwind/Petrov-Galerkin formulations for convection dominated flows with particular emphasis on the incompressible Navier-Stokes equations, *Computer Methods in Applied Mechanics and Engineering* **32**, 199–259, 1982.
- [31] E. Burman, A unified analysis for conforming and nonconforming stabilized finite element methods using interior penalty, *SIAM Journal on Numerical Analysis* **43**, 2012–2033, 2005.
- [32] E. Burman, Interior penalty variational multiscale method for the incompressible Navier-Stokes equation: Monitoring artificial dissipation, *Computer Methods in Applied Mechanics and Engineering* **196**, 4045–4058, 2007.
- [33] E. Burman, A penalty-free nonsymmetric Nitsche-type method for the weak imposition of boundary conditions, *SIAM Journal on Numerical Analysis* **50**, 1959–1981, 2012.
- [34] E. Burman and M. Fernández, A finite element method with edge oriented stabilization for the time-dependent Navier-Stokes equations: space discretization and convergence, Rapport de recherche RR-5630, INRIA, 2005.
- [35] E. Burman and M. Fernández, Finite element methods with symmetric stabilization for the transient convection-diffusion-reaction equation, *Computer Methods in Applied Mechanics and Engineering* **198**, 2508–2519, 2009.
- [36] E. Burman and P. Hansbo, Edge stabilization for Galerkin approximations of convection-diffusion-reaction problems, *Computer Methods in Applied Mechanics and Engineering* **193**, 1437–1453, 2004.
- [37] E. Burman and P. Hansbo, Edge stabilization for the generalized stokes problem: A continuous interior penalty method, *Computer Methods in Applied Mechanics and Engineering* **195**, 2393–2410, 2006.
- [38] E. Burman and P. Hansbo, Fictitious domain methods using cut elements: III. A stabilized nitsche method for stokes' problem, *ESAIM: Mathematical Modelling and Numerical Analysis*, 2011.
- [39] E. Burman and P. Hansbo, Fictitious domain finite element methods using cut elements: II. A stabilized Nitsche method, *Applied Numerical Mathematics* **62**, 328–341, 2012.
- [40] E. Burman and P. Zunino, A domain decomposition method based on weighted interior penalties for advection-diffusion-reaction problems, *SIAM* **44**, 1612–1638, 2006.

- [41] E. Burman, M. Fernández, and P. Hansbo, Edge Stabilization for the Incompressible Navier-Stokes Equations: a Continuous Interior Penalty Finite Element Method, Rapport de recherche RR-5349, INRIA, 2004.
- [42] E. Burman, M. Fernández, and P. Hansbo, Continuous interior penalty finite element method for Oseen's equations, *SIAM Journal on Numerical Analysis* **44**, 1248–1274, 2006.
- [43] L. Cattaneo, L. Formaggia, G. Iori, A. Scotti, and P. Zunino, Stabilized extended finite elements for the approximation of saddle point problems with unfitted interfaces, *Calcolo*, 1–30, 2014.
- [44] P. Causin, J. Gerbeau, and F. Nobile, Added-mass effect in the design of partitioned algorithms for fluid-structure problems, *Computer Methods in Applied Mechanics and Engineering* **194**, 4506–4527, 2005.
- [45] J. Chessa and T. Belytschko, An extended finite element method for two-phase fluids: Flow simulation and modeling, *American Society of Mechanical Engineers* **70**, 10–17, 2003.
- [46] J. Chessa and T. Belytschko, Arbitrary discontinuities in space-time finite elements by level sets and X-FEM, *International Journal for Numerical Methods in Engineering* **61**, 2595–2614, 2004.
- [47] J. Chessa and T. Belytschko, A local space-time discontinuous finite element method, *Computer Methods in Applied Mechanics and Engineering* **195**, 1325–1343, 2006.
- [48] J. Chessa, P. Smolinski, and T. Belytschko, The extended finite element method (XFEM) for solidification problems, *International Journal for Numerical Methods in Engineering* **53**, 1959–1977, 2002.
- [49] J. Chung and G. Hulbert, A time integration algorithm for structural dynamics with improved numerical dissipation: the generalized- α method, *Journal of applied mechanics* **60**, 371–375, 1993.
- [50] F. Cirak and R. Radovitzky, A Lagrangian-Eulerian shell-fluid coupling algorithm based on level sets, *Computers & Structures* **83**, 491 – 498, 2005.
- [51] R. Codina and J. Baiges, Approximate imposition of boundary conditions in immersed boundary methods, *International Journal for Numerical Methods in Engineering* **80**, 1379–1405, 2009.
- [52] R. Codina, G. Houzeaux, H. Coppola-Owen, and J. Baiges, The fixed-mesh ALE approach for the numerical approximation of flows in moving domains, *Journal of Computational Physics* **228**, 1591–1611, 2009.
- [53] M. Coroneo, L. Yoshihara, and W. Wall, Biofilm growth: A multi-scale and coupled fluid-structure interaction and mass transport approach, *Biotechnology and Bioengineering*, published online, 2014.

-
- [54] M. Crisfield, *Non-linear finite element analysis of solids and structures, Volume 2: advanced topics*, Wiley, 1997.
- [55] M. Crisfield, *Non-linear finite element analysis of solids and structures, Volume 1*, Wiley, 1998.
- [56] C. Daux, N. Moës, J. Dolbow, N. Sukumar, and T. Belytschko, Arbitrary branched and intersecting cracks with the extended finite element method, *International Journal for Numerical Methods in Engineering* **48**, 1741–1760, 2000.
- [57] J. De Hart, G. Peters, P. Schreurs, and F. Baaijens, A two-dimensional fluid-structure interaction model of the aortic valve, *Journal of Biomechanics* **33**, 1079–1088, 2000.
- [58] C. Degand and C. Farhat, A three-dimensional torsional spring analogy method for unstructured dynamic meshes, *Computers & Structures* **80**, 305–316, 2002.
- [59] J. Dolbow and I. Harari, An efficient finite element method for embedded interface problems, *International Journal for Numerical Methods in Engineering* **78**, 229–252, 2009.
- [60] J. Dolbow, N. Moës, and T. Belytschko, An extended finite element method for modeling crack growth with frictional contact, *Computer Methods in Applied Mechanics and Engineering* **190**, 6825 – 6846, 2001.
- [61] J. Dolbow and L. Franca, Residual-free bubbles for embedded Dirichlet problems, *Computer Methods in Applied Mechanics and Engineering* **197**, 3751 – 3759, 2008.
- [62] J. Donea and A. Huerta, *Finite element methods for flow problems*, Wiley, 2003.
- [63] J. Donea, S. Giuliani, and J. Halleux, An arbitrary lagrangian-eulerian finite element method for transient dynamic fluid-structure interactions, *Computer Methods in Applied Mechanics and Engineering* **33**, 689–723, 1982.
- [64] J. Donea, A. Huerta, J.-P. Ponthot, and A. Rodríguez-Ferran, *Arbitrary Lagrangian-Eulerian Methods*, John Wiley & Sons, Ltd, 2004.
- [65] J. Douglas and T. Dupont, Interior penalty procedures for elliptic and parabolic Galerkin methods, In R. Glowinski and J. Lions (eds.), *Computing Methods in Applied Sciences*, Volume 58 of *Lecture Notes in Physics*, pages 207–216, 1976.
- [66] A. Ehrl, A. Popp, V. Gravemeier, and W. Wall, A dual mortar approach for mesh tying within a variational multiscale method for incompressible flow, *International Journal for Numerical Methods in Fluids*, *accepted*, 2010.
- [67] A. Embar, J. Dolbow, and I. Harari, Imposing Dirichlet boundary conditions with Nitsche’s method and spline-based finite elements, *International Journal for Numerical Methods in Engineering* **83**, 877–898, 2010.
- [68] C. Farhat, *CFD-Based Nonlinear Computational Aeroelasticity*, John Wiley & Sons, Ltd, 2004.

- [69] C. Farhat, C. Degand, B. Koobus, and M. Lesoinne, Torsional springs for two-dimensional dynamic unstructured fluid meshes, *Computer Methods in Applied Mechanics and Engineering* **163**, 231–245, 1998.
- [70] R. Fedkiw, T. Aslam, B. Merriman, and S. Osher, A Non-oscillatory Eulerian Approach to Interfaces in Multimaterial Flows (the Ghost Fluid Method), *Journal of Computational Physics* **152**, 457 – 492, 1999.
- [71] M. Fernández and M. Moubachir, A Newton method using exact jacobians for solving fluid-structure coupling, *Computers & Structures* **83**, 127–142, 2005.
- [72] J. Ferziger and M. Peric, *Computational methods for fluid dynamics*, Springer, 2002.
- [73] C. Förster, *Robust methods for fluid-structure interaction with stabilized finite elements*, PhD thesis, Universität Stuttgart, 2007.
- [74] C. Förster, W. Wall, and E. Ramm, Artificial added mass instabilities in sequential staggered coupling of nonlinear structures and incompressible viscous flows, *Computer Methods in Applied Mechanics and Engineering* **196**, 1278 – 1293, 2007.
- [75] L. Franca and F. Valentin, On an improved unusual stabilized finite element method for the advective-reactive-diffusive equation, *Computer Methods in Applied Mechanics and Engineering* **190**, 1785–1800, 2000.
- [76] J. Freund and R. Stenberg, On weakly imposed boundary conditions for second order problems, In *Proceedings of the Ninth Int. Conf. Finite Elements in Fluids, Venice*, pages 327–336, 1995.
- [77] T.-P. Fries and T. Belytschko, The extended/generalized finite element method: An overview of the method and its applications, *International Journal for Numerical Methods in Engineering* **84**, 253–304, 2010.
- [78] T.-P. Fries and A. Zilian, On time integration in the XFEM, *International Journal for Numerical Methods in Engineering* **79**, 69–93, 2009.
- [79] P. Gamnitzer, *Residual-based variational multiscale methods for turbulent flows and fluid-structure interaction*, PhD thesis, Technische Universität München, 2010.
- [80] P. Gamnitzer and W. Wall, An ALE-Chimera method for large deformation fluid structure interaction, In P. Wesseling, E. Oñate, and J. Périaux (eds.), *European Conference on Computational Fluid Dynamics, Proc. of the ECCOMAS CFD 2006*. TU Delft, 2006.
- [81] M. Gee, U. Küttler, and W. Wall, Truly monolithic algebraic multigrid for fluid-structure interaction, *International Journal for Numerical Methods in Engineering* **85**, 987–1016, 2011.
- [82] A. Gerstenberger, *An XFEM based fixed-grid approach for fluid-structure interaction*, PhD thesis, Technische Universität München, 2010.

- [83] A. Gerstenberger and W. Wall, Enhancement of fixed-grid methods towards complex fluid-structure interaction applications, *International Journal for Numerical Methods in Fluids* **57**, 1227–1248, 2008.
- [84] A. Gerstenberger and W. Wall, An eXtended finite element method/Lagrange multiplier based approach for fluid-structure interaction, *Computer Methods in Applied Mechanics and Engineering* **197**, 1699–1714, 2008.
- [85] A. Gerstenberger and W. Wall, An embedded Dirichlet formulation for 3D continua, *International Journal for Numerical Methods in Engineering* **82**, 537–563, 2010.
- [86] R. Glowinski, T.-W. Pan, and J. Periaux, A fictitious domain method for Dirichlet problem and applications, *Computer Methods in Applied Mechanics and Engineering* **111**, 283–303, 1994.
- [87] R. Glowinski, T.-W. Pan, T. Hesla, and D. Joseph, A distributed Lagrange multiplier/fictitious domain method for particulate flows, *International Journal of Multiphase Flow* **25**, 755 – 794, 1999.
- [88] V. Gravemeier, *The Variational Multiscale Method for Laminar and Turbulent Incompressible Flow*, PhD thesis, Universität Stuttgart, 2003.
- [89] P. Gresho and R. Sani, *Incompressible Flow and the Finite Element Method, Volume 2*, John Wiley And Sons LTD, 2000.
- [90] M. Griebel and M. Schweitzer, A Particle-Partition of Unity Method Part V: Boundary Conditions, In S. Hildebrandt and H. Karcher (eds.), *Geometric Analysis and Nonlinear Partial Differential Equations*, pages 519–542, Springer Berlin Heidelberg, 2003.
- [91] S. Groß and A. Reusken, An extended pressure finite element space for two-phase incompressible flows with surface tension, *Journal of Computational Physics* **224**, 40 – 58, 2007.
- [92] A. Hansbo and P. Hansbo, An unfitted finite element method, based on Nitsche’s method, for elliptic interface problems, *Computer Methods in Applied Mechanics and Engineering* **191**, 5537 – 5552, 2002.
- [93] A. Hansbo, P. Hansbo, and M. Larson, A finite element method on composite grids based on Nitsche’s method, *ESAIM: Mathematical Modelling and Numerical Analysis* **37**, 495–514, 2003.
- [94] P. Hansbo, Nitsche’s method for interface problems in computational mechanics, *GAMM-Mitteilungen* **28**, 183–206, 2005.
- [95] P. Hansbo and M. Larson, Discontinuous Galerkin methods for incompressible and nearly incompressible elasticity by Nitsche’s method, *Computer Methods in Applied Mechanics and Engineering* **191**, 1895 – 1908, 2002.

- [96] P. Hansbo and A. Szepessy, A velocity-pressure streamline diffusion finite element method for the incompressible Navier-Stokes equations, *Computer Methods in Applied Mechanics and Engineering* **84**, 175 – 192, 1990.
- [97] I. Harari and T. Hughes, What are C and h?: Inequalities for the analysis and design of finite element methods, *Computer Methods in Applied Mechanics and Engineering* **97**, 157–192, 1992.
- [98] M. Hautefeuille, C. Annavarapu, and J. Dolbow, Robust imposition of Dirichlet boundary conditions on embedded surfaces, *International Journal for Numerical Methods in Engineering* **90**, 40–64, 2012.
- [99] M. Heil, An efficient solver for the fully coupled solution of large-displacement fluid-structure interaction problems, *Computer Methods in Applied Mechanics and Engineering* **193**, 1–23, 2004.
- [100] M. Heil, A. Hazel, and J. Boyle, Solvers for large-displacement fluid-structure interaction problems: segregated versus monolithic approaches, *Computational Mechanics* **43**, 91–101, 2008.
- [101] F. Henke, *An extended finite element method for turbulent premixed combustion*, PhD thesis, Technische Universität München, 2013.
- [102] F. Henke, M. Winklmaier, V. Gravemeier, and W. A. Wall, A semi-lagrangean time-integration approach for extended finite element methods, *International Journal for Numerical Methods in Engineering* **98**, 174–202, 2014.
- [103] M. Heroux, R. Bartlett, V. Howle, R. Hoekstra, J. Hu, T. Kolda, R. Lehoucq, K. Long, R. Pawlowski, E. Phipps, et al., An overview of the Trilinos project, *ACM Transactions on Mathematical Software (TOMS)* **31**, 397–423, 2005.
- [104] C. Hirt, A. Amsden, and J. Cook, An arbitrary Lagrangian-Eulerian computing method for all flow speeds, *Journal of Computational Physics* **14**, 227–253, 1974.
- [105] J.-M. Hong, T. Shinar, M. Kang, and R. Fedkiw, On boundary condition capturing for multiphase interfaces, *Journal of Scientific Computing* **31**, 99–125, 2007.
- [106] G. Houzeaux and R. Codina, Transmission conditions with constraints in finite element domain decomposition methods for flow problems, *Communications in Numerical Methods in Engineering* **17**, 179–190, 2001.
- [107] G. Houzeaux and R. Codina, A Chimera method based on a Dirichlet/Neumann(Robin) coupling for the Navier-Stokes equations, *Computer Methods in Applied Mechanics and Engineering* **192**, 3343–3377, 2003.
- [108] T. Hughes, W. Liu, and T. Zimmermann, Lagrangian-Eulerian finite element formulation for incompressible viscous flows, *Computer Methods in Applied Mechanics and Engineering* **29**, 329–349, 1981.

-
- [109] T. Hughes, *The Finite Element Method-Linear Static and Dynamic Finite Element Analysis*, Dover Publication, 2000.
- [110] T. Hughes and G. Wells, Conservation properties for the Galerkin and stabilised forms of the advection-diffusion and incompressible navier-stokes equations, *Computer Methods in Applied Mechanics and Engineering* **194**, 1141–1159, 2005.
- [111] T. Hughes, L. Franca, and M. Balestra, A new finite element formulation for computational fluid dynamics: V. Circumventing the Babuška-brezzi condition: a stable Petrov-Galerkin formulation of the stokes problem accommodating equal-order interpolations, *Computer Methods in Applied Mechanics and Engineering* **59**, 85 – 99, 1986.
- [112] H. Ji and J. Dolbow, On strategies for enforcing interfacial constraints and evaluating jump conditions with the extended finite element method, *International Journal for Numerical Methods in Engineering* **61**, 2508–2535, 2004.
- [113] M. Kang, R. Fedkiw, and X. Liu, A boundary condition capturing method for multiphase incompressible flow, *Journal of Scientific Computing* **15**, 323–360, 2000.
- [114] J. Kim and P. Moin, Application of a fractional-step method to incompressible Navier-Stokes equations, *Journal of Computational Physics* **59**, 308–323, 1985.
- [115] T. Klöppel, *A finite element model for the human red blood cell*, PhD thesis, Technische Universität München, 2012.
- [116] T. Klöppel and W. Wall, A novel two-layer, coupled finite element approach for modeling the nonlinear elastic and viscoelastic behavior of human erythrocytes, *Biomechanics and Modeling in Mechanobiology* **10**, 445–459, 2011.
- [117] T. Klöppel, A. Popp, U. Küttler, and W. Wall, Fluid-structure interaction for non-conforming interfaces based on a dual mortar formulation, *Computer Methods in Applied Mechanics and Engineering* **200**, 3111–3126, 2011.
- [118] A. Kölke and A. Legay, An enriched space-time finite element method for fluid-structure interaction-Part II: thin flexible structures, *Proceedings III ECCM, Solid Struct Coupling Prob Eng, Lisbon Portugal*, 5–8, 2006.
- [119] R. Kruse. Enforcing coupling conditions on embedded interfaces using stress-based Lagrange multipliers in the XFEM for incompressible flow, Master’s thesis, Technische Universität München, 2013.
- [120] U. Küttler, *Effiziente Lösungsverfahren für Fluid-Struktur-Interaktions-Probleme*, PhD thesis, Technische Universität München, 2009.
- [121] U. Küttler and W. Wall, Fixed-point fluid-structure interaction solvers with dynamic relaxation, *Computational Mechanics* **43**, 61–72, 2008.
- [122] U. Küttler and W. Wall, Vector extrapolation for strong coupling fluid-structure interaction solvers, *Computational Mechanics* **43**, 61–72, 2009.

- [123] U. Küttler, M. Gee, C. Förster, A. Comerford, and W. Wall, Coupling strategies for biomedical fluid–structure interaction problems, *International Journal for Numerical Methods in Biomedical Engineering* **26**, 305–321, 2010.
- [124] W. Lai, D. Rubin, and E. Krembl, *Introduction to Continuum Mechanics*, Butterworth-Heinemann, 2009.
- [125] P. Le Tallec and J. Mouro, Fluid structure interaction with large structural displacements, *Computer Methods in Applied Mechanics and Engineering* **190**, 3039 – 3067, 2001.
- [126] L. Lee and R. Leveque, An immersed interface method for incompressible Navier-Stokes equations, *SIAM Journal on Scientific Computing* **25**, 832–856, 2003.
- [127] A. Legay and A. Kölke, An enriched space-time finite element method for fluid-structure interaction-Part I: prescribed structural displacement, *Proceedings III ECCM, Solid Struct Coupling Prob Eng, Lisbon Portugal*, 5–8, 2006.
- [128] A. Legay, J. Chessa, and T. Belytschko, An Eulerian-Lagrangian method for fluid-structure interaction based on level sets, *Computer Methods in Applied Mechanics and Engineering* **195**, 2070 – 2087, 2006.
- [129] R. Leveque and D. Calhoun, Cartesian grid methods for fluid flow in complex geometries, In L. Fauci and S. Gueron (eds.), *Computational Modeling in Biological Fluid Dynamics*, Volume 124 of *The IMA Volumes in Mathematics and its Applications*, pages 117–143, Springer New York, 2001.
- [130] R. Löhner, J. Cebal, F. Camelli, S. Appanaboyina, J. Baum, E. Mestreau, and O. Soto, Adaptive embedded and immersed unstructured grid techniques, *Computer Methods in Applied Mechanics and Engineering* **197**, 2173 – 2197, 2008.
- [131] A. Massing, M. Larson, and A. Logg, Efficient implementation of finite element methods on non-matching and overlapping meshes in 3D, *Submitted*, 2012.
- [132] A. Massing, M. Larson, A. Logg, and M. Rognes, A stabilized nitsche fictitious domain method for the stokes problem, *ArXiv e-prints*, 2012.
- [133] A. Massing, M. Larson, A. Logg, and M. Rognes, An overlapping mesh finite element method for a fluid-structure interaction problem, *arXiv preprint arXiv:1311.2431*, 2013.
- [134] A. Massing, M. Larson, A. Logg, and M. Rognes, A stabilized Nitsche overlapping mesh method for the Stokes problem, *Numerische Mathematik*, 1–29, 2014.
- [135] M. Mayr, , T. Klöppel, W. Wall, and M. Gee, A temporal consistent monolithic approach to fluid-structure interaction enabling single field predictors, *SIAM Journal on Scientific Computing*, *submitted*, 2014.
- [136] R. Meakin and N. Suhs, Unsteady aerodynamic simulation of multiple bodies in relative motion, *AIAA paper* **1996**, 89–1996–CP, 1989.

-
- [137] J. Melenk and I. Babuška, The partition of unity finite element method: Basic theory and applications, *Computer Methods in Applied Mechanics and Engineering* **139**, 289 – 314, 1996.
- [138] R. Mittal and G. Iaccarino, Immersed boundary methods, *Annual Review of Fluid Mechanics* **37**, 239–2361, 2005.
- [139] N. Moës, J. Dolbow, and T. Belytschko, A finite element method for crack growth without remeshing, *International Journal for Numerical Methods in Engineering* **46**, 131–150, 1999.
- [140] N. Moës, E. Béchet, and M. Tourbier, Imposing dirichlet boundary conditions in the extended finite element method, *International Journal for Numerical Methods in Engineering* **67**, 1641–1669, 2006.
- [141] D. Mok and W. Wall, Partitioned analysis schemes for the transient interaction of incompressible flows and nonlinear flexible structures, *Trends in computational structural mechanics*, 689–698, 2001.
- [142] H. Mourad, J. Dolbow, and I. Harari, A bubble-stabilized finite element method for dirichlet constraints on embedded interfaces, *International Journal for Numerical Methods in Engineering* **69**, 772–793, 2007.
- [143] S. Mousavi and N. Sukumar, Numerical integration of polynomials and discontinuous functions on irregular convex polygons and polyhedrons, *Computational Mechanics* **47**, 535–554, 2011.
- [144] J. Nitsche, Über ein Variationsprinzip zur Lösung von Dirichlet-Problemen bei Verwendung von Teilräumen, die keinen Randbedingungen unterworfen sind, *Abhandlungen aus dem Mathematischen Seminar der Universität Hamburg* **36**, 9–15, 1971.
- [145] C. Peskin, Numerical analysis of blood flow in the heart, *Journal of Computational Physics* **25**, 220–252, 1977.
- [146] C. Peskin, The immersed boundary method, *Acta Numerica* **11**, 479–517, 2002.
- [147] U. Rasthofer, F. Henke, W. Wall, and V. Gravemeier, An extended residual-based variational multiscale method for two-phase flow including surface tension, *Computer Methods in Applied Mechanics and Engineering* **200**, 1866 – 1876, 2011.
- [148] J. N. Reddy, On penalty function methods in the finite-element analysis of flow problems, *International Journal for Numerical Methods in Fluids* **2**, 151–171, 1982.
- [149] A. Reusken, Analysis of an extended pressure finite element space for two-phase incompressible flows, *Computing and Visualization in Science* **11**, 293–305, 2008.
- [150] J. Sanders, J. Dolbow, and T. Laursen, On methods for stabilizing constraints over enriched interfaces in elasticity, *International Journal for Numerical Methods in Engineering* **78**, 1009–1036, 2009.

- [151] H. Sauerland and T.-P. Fries, The extended finite element method for two-phase and free-surface flows: A systematic study, *Journal of Computational Physics* **230**, 3369 – 3390, 2011.
- [152] M. Schäfer and S. Turek, Volume 52, Article, Benchmark Computations of Laminar Flow Around a Cylinder, pages 547–566, *Flow simulation with High-Performance Computers II, Notes on Numerical Fluid Mechanics*, E. Hirschel (ed.), Vieweg, 1996.
- [153] B. Schott. Enforcing interface conditions with Nitsche’s method in XFEM, Master’s thesis, Technische Universität München, 2010.
- [154] B. Schott and W. Wall, A new face-oriented stabilized XFEM approach for 2D and 3D incompressible Navier-Stokes equations, *Computer Methods in Applied Mechanics and Engineering* **276**, 233–265, 2014.
- [155] B. Schott, U. Rasthofer, V. Gravemeier, and W. Wall, Nitsche-type extended variational multiscale method for incompressible two-phase flow., *International Journal for Numerical Methods in Engineering*, submitted, 2014.
- [156] S. Shahmiri, B. Schott, and W. Wall, A face-oriented stabilized XFEM-based embedding mesh approach for 3D incompressible Navier-Stokes equations, *In preparation*.
- [157] S. Shahmiri, A. Gerstenberger, and W. Wall, An XFEM-based embedding mesh technique for incompressible viscous flows, *International Journal for Numerical Methods in Fluids* **65**, 166–190, 2011.
- [158] A. Simone, Partition of unity-based discontinuous elements for interface phenomena: computational issues, *Communications in Numerical Methods in Engineering* **20**, 465–478, 2004.
- [159] J. Steger, F. Dougherty, and J. Benek, A Chimera grid scheme, *Advances in Grid Generation (Ghia, Ghia eds.)*. **ASME FED-5**, 59–69, 1983.
- [160] T. Strouboulis, I. Babuška, and K. Copps, The design and analysis of the generalized finite element method, *Computer Methods in Applied Mechanics and Engineering* **181**, 43 – 69, 2000.
- [161] T. Strouboulis, K. Copps, and I. Babuška, The generalized finite element method, *Computer Methods in Applied Mechanics and Engineering* **190**, 4081–4193, 2001.
- [162] Y. Sudhakar and W. Wall, Quadrature schemes for arbitrary convex/concave volumes and integration of weak form in enriched partition of unity methods, *Computer Methods in Applied Mechanics and Engineering* **258**, 39–54, 2013.
- [163] Y. Sudhakar, W. Wall, and J. Moitinho de Almeida, An accurate and easy-to-implement method for integration over arbitrary polyhedra: application to Embedded Interface Methods, Preprint submitted to Elsevier, 2013.

-
- [164] N. Sukumar, N. Mos, B. Moran, and T. Belytschko, Extended finite element method for three-dimensional crack modelling, *International Journal for Numerical Methods in Engineering* **48**, 1549–1570, 2000.
- [165] N. Sukumar, D. Chopp, N. Moës, and T. Belytschko, Modeling holes and inclusions by level sets in the extended finite-element method, *Computer Methods in Applied Mechanics and Engineering* **190**, 6183 – 6200, 2001.
- [166] D. Taherzadeh, C. Picioreanu, U. Küttler, A. Simone, W. Wall, and H. Horn, Computational study of the drag and oscillatory movement of biofilm streamers in fast flows, *Biotechnology and Bioengineering* **105**, 600–610, 2010.
- [167] C. Taylor and P. Hood, A numerical solution of the Navier-Stokes equations using the finite element technique, *Computers & Fluids* **1**, 73–100, 1973.
- [168] T. Tezduyar, S. Mittal, S. Ray, and R. Shih, Incompressible flow computations with stabilized bilinear and linear equal-order-interpolation velocity-pressure elements, *Computer Methods in Applied Mechanics and Engineering* **95**, 221 – 242, 1992.
- [169] F. Van der Bos and V. Gravemeier, Numerical simulation of premixed combustion using an enriched finite element method, *Journal of Computational Physics* **228**, 3605 – 3624, 2009.
- [170] R. Van Loon, P. Anderson, F. Baaijens, and F. van de Vosse, A three-dimensional fluid-structure interaction method for heart valve modelling, *Comptes Rendus Mécanique* **333**, 856 – 866, 2005.
- [171] M. Vázquez, G. Houzeaux, and R. Codina, Chimera type domain decomposition methods applied to fractional step finite element schemes for incompressible flows, In *Proceedings of the ECCOMAS 2000 Computational Fluid Dynamics Conference*, 2000.
- [172] W. Wall, *Fluid-Struktur-Interaktion mit stabilisierten Finiten Elementen*, PhD thesis, Universität Stuttgart, 1999.
- [173] W. Wall and M. Gee, BACI: a parallel multiphysics simulation environment, Technical report, Institute for Computational Mechanics, Technische Universität München, 2010.
- [174] W. Wall, A. Gerstenberger, P. Gamnitzer, C. Förster, and E. Ramm, Large deformation fluid structure interaction - advances in ALE methods and new fixed-grid approaches, *Springer Berlin Heidelberg* **53**, 195–232, 2006.
- [175] W. Wall, P. Gamnitzer, and A. Gerstenberger, Fluid-structure interaction approaches on fixed grids based on two different domain decomposition ideas, *International Journal of Computational Fluid Dynamics* **22**, 411–427, 2008.
- [176] X. Wang and W. Liu, Extended immersed boundary method using FEM and RKPM, *Computer Methods in Applied Mechanics and Engineering* **193**, 1305–1321, 2004.

- [177] Z. Wang and V. Parthasarathy, A fully automated Chimera methodology for multiple moving body problems, *International Journal for Numerical Methods in Fluids* **33**, 919–938, 2000.
- [178] B. Wohlmuth, A mortar finite element method using dual spaces for the lagrange multiplier, *SIAM Journal on Numerical Analysis* **38**, 989–1012, 2000.
- [179] P. Wriggers, *Nichtlineare Finite-Element-Methoden*, number XI, Springer, 2004.
- [180] Q. Xiao and B. Karihaloo, Improving the accuracy of XFEM crack tip fields using higher order quadrature and statically admissible stress recovery, *International Journal for Numerical Methods in Engineering* **66**, 1378–1410, 2006.
- [181] Z. Yu, A DLM/FD method for fluid/flexible-body interactions, *Journal of Computational Physics* **207**, 1 – 27, 2005.
- [182] L. Zhang, A. Gerstenberger, X. Wang, and W. Liu, Immersed finite element method, *Computer Methods in Applied Mechanics and Engineering* **193**, 2051–2067, 2004.
- [183] O. Zienkiewicz and R. Taylor, *The finite element method - for solid and structural mechanics*, Butterworth-Heinemann, 2005.
- [184] O. Zienkiewicz, R. Taylor, and P. Nithiarasu, *The finite element method - for fluid dynamics*, Butterworth-Heinemann, 2005.
- [185] A. Zilian and A. Legay, The enriched space-time finite element method (EST) for simultaneous solution of fluid-structure interaction, *International Journal for Numerical Methods in Engineering* **75**, 305–334, 2008.

Lebenslauf

Name:	Shadan Shahmiri
Geburtsdatum:	21. April 1982
Geburtsort:	Teheran–Iran
Nationalität:	Deutsch–Iranisch
1988–1992:	Grundschule, Teheran
1992–1995:	Mittelschule, Teheran
1995–1999:	Gymnasium, Teheran
1999:	Abitur, Teheran
2001–2002:	Studienkolleg, Hamburg
2002:	Feststellungsprüfung
2002–2009:	Studium an der Technischen Universität Hamburg-Harburg (TUHH) Studiengang: Informatik-Ingenieurwesen Studienschwerpunkt: Wissenschaftliches Rechnen, Technische Dynamik
2008:	Diplomarbeit am Institut für Materialforschung, Karlsruher Institut für Technologie (KIT)
2006:	Auslandsstudium an der Macquarie University Sydney, Australien
2009–2014:	Wissenschaftliche Mitarbeiterin am Institut für Numerische Mechanik, Technische Universität München (TUM)

Reports of the Institute for Computational Mechanics at Technische Universität München

- 22 (2014) Shadan Shahmiri:**
A hybrid ALE-fixed-grid approach for fluid-structure interaction.
- 21 (2014) Caroline Danowski:**
Computational modelling of thermo-structure interaction with application to rocket nozzles.
- 20 (2014) Kei Müller:**
Simulation of self-assembly and mechanics of transiently crosslinked, semiflexible biopolymer networks.
- 19 (2014) Mahmoud Ismail:**
Reduced dimensional modeling of the entire human lung.
- 18 (2013) Florian Henke:**
An extended finite element method for turbulent premixed combustion.
- 17 (2012) Markus Gitterle:**
A dual mortar formulation for finite deformation frictional contact problems including wear and thermal coupling.
- 16 (2012) Andreas Maier:**
Computational modeling of rupture risk in abdominal aortic aneurysms.
- 15 (2012) Georg Bauer:**
A coupled finite element approach for electrochemical systems.
- 14 (2012) Alexander Popp:**
Mortar methods for computational contact mechanics and general interface problems.
- 13 (2012) Thomas Klöppel:**
A finite element model for the human red blood cell.
- 12 (2012) Sophie Rausch:**
Computational and experimental modeling of lung parenchyma.
- 11 (2011) Christian Cyron:**
Micromechanical continuum approach for the analysis of biopolymer networks.
- 10 (2011) Lena Wiechert:**
Computational modeling of multi-field and multi-scale phenomena in respiratory mechanics.

- 9 (2010) Peter Gamnitzer:**
Residual-based variational multiscale methods for turbulent flows and fluid-structure interaction.
- 8 (2010) Axel Gerstenberger:**
An XFEM based fixed grid approach to fluid-structure interaction.
- 7 (2009) Ulrich Küttler:**
Effiziente Lösungsverfahren für Fluid-Struktur-Interaktions-Probleme.
- 6 (2009) Moritz Frenzel:**
Advanced structural finite element modeling of arterial walls for patient-specific geometries.
- 5 (2007)* Christiane Förster:**
Robust methods for fluid-structure interaction with stabilised finite elements.
- 4 (2004)* Tobias Erhart:**
Strategien zur Numerischen Modellierung transienter Impaktvorgänge bei nichtlinearem Materialverhalten.
- 3 (2004)* Michael Gee:**
Effiziente Lösungsstrategien in der nichtlinearen Schalenmechanik.
- 2 (2003)* Volker Gravemeier:**
The variational multiscale method for laminar and turbulent incompressible flow.
- 1 (2001)* Daniel Mok:**
Partitionierte Lösungsverfahren in der Strukturmechanik und der Fluid-Struktur-Interaktion.

*This dissertation was supervised by Prof. Dr.-Ing. Wolfgang A. Wall at Institute for Structural Mechanics at the University of Stuttgart and is published in the respective report series.